LINEAR AND NONLINEAR RESPONSES OF A MODEL ATMOSPHERE TO LARGE SCALE TOPOGRAPHY AND DIABATIC HEATING

Submitted by

ZHAO-CHONG LEI

for the degree of

DOCTOR OF PHILOSOPHY

University of Edinburgh

1986

ABSTRACT

Linear and nonlinear steady-state, baroclinic, primitive equation, numerical models of forced stationary waves in the atmosphere are developed. Newtonian cooling, Rayleigh friction and biharmonic horizontal diffusion are included in both models. The vertical as well as horizontal structure is described by truncated series of analytical orthogonal functions. The steady-state, convergent, nonlinear solution is obtained by using Newton-Raphson iteration, and the transform method is used to evaluate the nonlinear terms in the governing equations.

The Eliassen-Palm (EP) cross-section and the three-dimensional wave activity flux, which was derived by Plumb (1985) for linear, quasi-geostrophic stationary waves on a zonal flow, are used as diagnostics for the vertical and horizontal propagation of the waves, the interaction between the mean flow and the waves, and the significance of the nonlinearity.

Comparison of nonlinear model solutions with corresponding linear model solutions, and the diagnostic analyses show that the nonlinear effects are significant and of primary importance in simulation of the stationary waves in the real atmosphere. The model's nonlinear response to the Northern Hemispheric topography and the actual diabatic heating is, in general, consistent with the observed climatological stationary waves in the northern winter and makes a substantial improvement over the

deficiencies of the linear solution. It is also shown that nonlinear effects are important for investigating wave propagation and the interaction between the zonal mean flow and the stationary waves.

Results of the numerical experiments suggest that the Tibetan Plateau plays the most important role in the maintenance of orographically forced stationary waves in the northern winter, while the orographic effect of the Rocky mountains or the Greenland Plateau seems to be of secondary importance.

The stationary waves induced by the actual thermal forcing in winter have a comparable amplitude and more baroclinic nature than those produced by the Northern Hemispheric orographic forcing.

The mid-latitude orographic forcing, especially that by the Tibetan Plateau, makes a substantial contribution to the maintenance of the cyclonic circulation over the eastern tropical and sub-tropical Pacific in the upper troposphere. On the other hand, the longitudinal variation of diabatic heating in the tropics has a significant influence on the wintertime stationary waves in middle and high latitudes.

CONTENTS

CHAPTER 1

INTRODUCTION

From monthly or seasonally averaged weather maps it is clear that in addition to the transient eddies in the atmosphere, there are planetary scale waves which remain stationary with respect to the earth. These stationary planetary waves are responsible for the climatic variation around a latitude circle. For example, Reiter (1963) described a great deal of evidence which shows the meridional position of the jet stream is related to the stormy cyclogenetic belts near the ground. He has also suggested that the quasi-stationary troughs in the lee of the two large mountain ranges in the Northern Hemisphere (namely Tibetan Plateau and Rocky Mountains) have a very obvious effect upon the arrangement of climatic zones. Particularly, an anomalous pattern of climate around the globe is usually associated with an abnormal variation of the stationary waves. Such relationships have been found by a number of meteorologists, e.g., Namias (1966) related the drought in the northeastern United States during 1962-65 to the contemporary upper-level wind patterns and the implied storm tracks and air masses. Some weather forecasters have noticed that the variation of the stationary waves could not only be used to explain the climatic change over a large region, they have also some predictive value in operational long-range weather forecasting (see, e.g., Ratcliffe 1968, 1974).

The diagnoses of local, time averaged budgets of momentum and kinetic energy by Lau (1978, 1979a) showed that stationary waves play a dominant role in the balances, whereas the effects of the transient eddies were seen to be of secondary importance. The study clearly suggested that a better understanding of the stationary wave structure and its maintenance is of primary concern in our effort to provide a comprehensive description of the general circulation.

The existence of stationary disturbances in the general circulation has been attributed primarily to two categories of forcing: a) the geographical distribution of topographic variations of the Earth's surface, and b) the differential mean diabatic heating at the boundaries and within the atmosphere, which mainly results from the contrast between the surface thermal properties of the continents and oceans. The problem of explaining the atmospheric stationary waves is complicated by a number of interaction processes, which are little understood so far, such as the interactions between various scales of eddies, mid-latitude and tropical regions, the surface and the atmosphere and so on.

An ability faithfully to reproduce the essential features of stationary disturbances in numerical models and to interpret the results clearly, in terms of basic dynamical principles, would demonstrate the validity of the dynamical principles and parameterizations used in numerical weather prediction and general circulation models, and help improve

these models. Therefore the problem of explaining the atmospheric stationary disturbances has been one of the most important subjects of general circulation research in the period since the pioneering work of Charney and Eliassen (1949).

1.1 Historical Review

Charney and Eliassen (1949) used a barotropic model on a beta-plane, linearized about a uniform westerly zonal wind flowing over surface topography and obtained a 500 mb stationary geopotential field along 45°N which is quite consistent with the wintertime observation. It was shown that the large-scale quasi-stationary disturbances of the middle-latitude westerlies are produced by the forced ascent of the westerly current over the continental land masses. Friction was found to have an important modifying effect on the motion.

Bolin (1950) extended the analysis given by Charney and Eliassen (1949) by considering the north-south extent of the mountain ranges and width of the zonal current. He concluded that the only mountains which may be of real importance in generating planetary waves in the westerlies are the Rocky Mountains and the mountains in the interior of Asia. He also found the splitting tendency of the basic current caused by a circular mountain. This is consistent with the fact revealed in a simultaneous paper by Yeh (1950) that the Asian wintertime westerly jet is split into

two branches due to the Tibetan Plateau.

Soon after, the influence of large-scale asymmetries of non-adiabatic heating and cooling on mid-tropospheric flow was calculated to be of the same magnitude as the influence of broad mountain areas by Smagorinsky (1953).

In the following years more complicated models were used to investigate the separate or combined effects of thermal and orographic forcing. Kasahara (1966) used the time-dependent shallow-water equations in a beta-plane channel and showed that westerly flows past an obstacle, which is placed at the bottom in the middle of the channel, produced a train of planetary waves on the lee side. On the other hand, easterly flows were little disturbed by the obstacle. Derome and Wiin-Nielsen (1971) used a beta-plane quasi-geostrophic model to study the effect of the two forcings. Their calculation suggested that the stationary waves forced by the topography are in about the same position as those produced by the diabatic forcing and that the former have somewhat larger amplitudes than the latter. Egger (1976a, b) used a beta-plane, two-layer, primitive equation model for the same purpose. He found that the ridge on the windward side of the Himalayas and the strong trough over eastern Asia at 400 mb are orographically induced, whereas the heat sources play an almost dominant role over North America and determine the position of the ridge over the Atlantic.

The results for barotropic or baroclinic flow in a beta-plane channel are substantially modified when

spherical geometry and mean flow variation with latitude are taken into account. The shallow-water equations on the sphere were used to study the steady state, linear Rossby wave pattern on mean zonal flow induced by various simple mountains by Grose and Hoskins (1979). It was found that there was a tendency to a split wavetrain downstream of a mountain range. Subsequently, a linearized, steady-state, five-layer, baroclinic model was used by Hoskins and Karoly (1981) and the results showed that in the upper troposphere the thermal and orographic sources generate wavetrains which are very similar to those given by barotropic models. Huang and Gambo (1981, 1982) used a quasi-geostrophic, steady state model with a high vertical resolution (34 vertical levels) in the stratosphere and found that the topography at high latitude, such as the Greenland Plateau, plays an important role in the stationary waves responding to forcing by hemispherical topography.

Simmons (1982) used a high resolution, steady, linear, primitive equation model to examine both the extratropical and tropical response to an isolated region of steady thermal forcing in the tropics. The results was largely in agreement with those obtained from much lower resolution models by a number of authors (Egger 1977; Opsteegh and Van den dool 1980; Hoskins and Karoly 1981; Webster 1981). These results suggested that an isolated tropical region of heating may excite a wavetrain with a substantial poleward direction of propagation.

As to the nonlinear response of the model atmosphere to topography and heat sources, Ashe (1979) using a steady, two layer linear balance equation model, and Frederikson and Sawford (1981) using nonlinear and linear spherical barotropic models, found that the nonlinear effect is very important for the heating solution as well as the topography solution. The stationary flow field simulated by the nonlinear model is in better agreement with the observed field than that of the linear model. It was shown by Wu (1984) that there exists a critical mountain height, which is only about one kilometre: only if the mountain height is less than this critical value, can the deflection effect of the mountain be neglected and the response be regarded as approximately linear. Therefore most of the atmospheric response to large-scale mountains must be nonlinear.

General circulation models have been used to try to isolate the role of mountains (Manabe and Terpstra, 1974; Kasahara et al., 1973) and anomalous thermal sources (Rowntree, 1972; Chervin et al., 1980). By using the multi-level general circulation model at GFDL, Manabe and Terpstra (1974) found that the stationary waves computed in the 'mountain' case were closer to those observed than the counterpart in the 'no-mountain' case, particularly in the upper troposphere. The thermal forcing effect was more important in the lower troposphere. Kasahara et al. (1973) used the NCAR atmospheric general circulation model and found that there was enhanced vertical transport of

wave energy, particularly for zonal wavenumber one, in the stratosphere when mountains were included. They found that the orographical forcing was dominant in determining the stratospheric circulation, but the thermal forcing was more important in determining the tropospheric circulation. It has been pointed out (see, Karoly, 1980; Held, 1983) that the difference between the mountain and no-mountain circulations cannot be interpreted as simply due to the mechanical diversion of flow by the mountains, since the insertion of the mountains has some effect on the distribution of the diabatic heating as well. In a complex general circulation model there are so many feedback processes which link together all model variables that it is not possible to isolate the various factors affecting the structure of stationary disturbances.

For the extratropical and tropical response to an isolated tropical thermal forcing, a time-dependent, nonlinear primitive equation model has been utilized by Grose et al. (1984). The response can be characterized by two distinct components: a quasi-stationary disturbance which extends eastward and poleward away from the source region, and a growing baroclinic wave propagating zonally at mid-latitudes.

The structure of the stationary waves has also been investigated in many observational studies. The traditional way of studying the general circulation was based on zonal averages. One excellent example of many such studies is the compilation of Oort and Rasmusson (1971) which included

extensive statistics of stationary waves. Van Loon et al. (1973) described the structure of the stationary waves in terms of the amplitudes and phases of the first three zonal harmonic components. During the last decade the observational studies have emphasized the longitudinal inhomogeneity of the flow (see, for example, Blackmon 1976; Blackmon et al. 1977; Lau 1978, 1979b; Lau and Wallace 1979). Some essential characteristics of the three-dimensional structure of the stationary waves in the extra-tropics of both hemispheres during both winter and summer seasons has been summarized in a review by Wallace (1983).

1.2 Present Study

The aim of this study is to develop a more precise steady-state, nonlinear, hemispherical model, in which primitive equations based on a three-dimensional spectral representation will be adopted, to investigate the atmospheric response to topographic and thermal forcings. A linearized model is also used which corresponds to the nonlinear one in all aspects except that the basic equations are linearized by the perturbation method. The solutions of the linear model can provide a reasonable initial guess for the nonlinear model, which is then solved by Newton-Raphson iteration.

Compared to previous steady-state nonlinear models (e.g., Ashe, 1979; Frederikson and Sawford, 1981) the present

nonlinear model has the following characteristics:

a) The primitive equations with a spherical geometry are used as the governing model equations, which are more precise for describing the hemispherical or global circulation;

b) A three-dimensional spectral representation is employed and therefore the resolution in all three directions can be changed easily by altering the associated truncation wavenumbers to fit the computer's capacity. Because the nonlinear model is quite expensive in computing resources, the present study used an expansion series truncated at indices 3, 11 and 4 in the zonal, meridional and vertical directions respectively. Although this is still a low resolution, the basic features of full three-dimensional propagation of wave activity should be retained;

c) The nonlinear and linear model differ only through linearization, a direct comparison for nonlinear and linear responses of the model atmosphere is therefore possible.

In Chapters 2 and 3 the nonlinear and linear models are described in detail. In both models the governing equations are the primitive equations in which Rayleigh friction, the effect of Newtonian cooling and scale selective ∇^4 smoothing are included. The vertical as well as the horizontal structure of the dependent variables is described

by a truncated series of orthogonal functions, i.e., the vertical structure is represented in terms of normalized Legendre polynomials and on the hemisphere the horizontal structure of each vertical mode is represented in terms of spherical harmonics.

The wave activity flux constitutes a useful diagnostic of the three-dimensional propagation of stationary wave activity for both the linear and nonlinear model solutions. This flux appears in a locally applicable (non-zonally-averaged) conservation relation which was derived by Plumb (1985) for quasi-geostrophic stationary waves on a zonal flow, a generalization of the Eliassen-Palm relation. In addition, the Eliassen-Palm (EP) cross-section is also used in this study to diagnose both the propagation of wave activity and the interaction between waves and the mean flow. The basic definitions and calculation procedures relevant to the three-dimensional wave activity and the EP cross-section are outlined, and the experimental design is described in Chapter 4.

In chapter 5, some preliminary experiments are done to examine both the linear and nonlinear response of the model atmosphere to forcing by idealized large-scale topography or diabatic heating. These experiments may provide an elementary understanding of the model atmosphere behaviour. Attention is particularly paid to the differences between nonlinear and linear responses. The sensitivity of the model solution to different dissipation

conditions is reported for a case where the only forcing is provided by a large scale mountain in mid-latitudes.

The forcing by the Northern Hemispheric topography and the actual diabatic heating in January 1979 is subsequently discussed in Chapter 6 for the linear solution, and in Chapter 7 for the nonlinear solution. Before the combined effect of these two categories of forcing is considered, the response to the pure orographic or thermal forcing is calculated separately. In order to investigate the relative importance of the three large scale mountains of the Northern Hemisphere (i.e., the Tibetan Plateau, Rocky mountains and the Greenland Plateau) in the maintenance of orographically forced stationary waves in the winter season, some numerical experiments are performed for the idealized cases where the topography either in North America or in Greenland is removed. The comparison between the linear solution, the nonlinear solution and the observed climatological stationary waves shows that the nonlinear effect is significant and the nonlinear model gives a more realistic result than the linear one.

Finally, some conclusions and possible extensions to the present study are put forward in Chapter 8.

CHAPTER 2

NONLINEAR PRIMITIVE EQUATION MODEL

2.1 Introduction

Since the pioneering work of Charney and Eliassen (1949), Bolin (1950) and Smagorinsky (1953), there has been a steady increase in the sophistication and accuracy of numerical models used to investigate the atmospheric response to orographic and thermal forcing. This is not only due to the progressive reduction of the approximation used in deriving the model equations and reinfinement of the model resolution, but also due to improvement of the numerical techniques used to discretize the continuous equations of the models. Until 1972 almost all sophisticated numerical models were based on finite-difference techniques, which represent the dependent variable fields in space and time on a finite difference grid. An alternative method, which represents the variable fields, in part, by truncated series of analytic spectral functions and is commonly referred to as the spectral method, has now been used in many operational weather forecasting models and general circulation studies. This method offers a number of significant advantages in global and hemispheric scale simulation and prediction as discussed in detail by Platzman (1960), Elsaesser (1966), Orszag (1970, 1974), Bourke et al. (1977) and Jarraud and Simmons (1983).

An important breakthrough in the development of the spectral method was the adaptation of the transform method in numerical spectral models, which was formulated independently by Eliasen et al. (1970) and Orszag (1970). The idea of the transform method is to transform all variable fields to an associated grid of points where all nonlinear terms can then be computed as in a classical grid point model, and then transform back to spectral space. This method has considerably reduced the requirements for storage and computation compared with the interaction coefficient method, and has made it possible to include physical processes in a straightforward way. This method is used to evaluate the nonlinear terms in the present model.

In this chapter a steady-state, primitive equation, spectral model is formulated. The model equations are specified in the next section. The spectral representation of basic variable fields and associated derivatives, and the evaluation of vertical velocity and geopotential are described in sections 2.3 and 2.4 respectively. Finally, section 2.5 gives a description of the method used to obtain the steady solution of this nonlinear model.

2.2 Model Equations

The vertical coordinate in this model is defined by

$$\sigma = 2\frac{P}{P_s} - 1 \qquad (2.1)$$

where P is pressure at any level, and P_s is the surface pressure. It may be noted that

$$\begin{cases} \sigma = 1 & \text{at } P=P_s \\ \sigma = -1 & \text{at } P=0 \end{cases} \qquad (2.2)$$

Following Machenhauer and Daley (1972), the primitive equations in this system may be written

$$\frac{\partial u}{\partial t} = -u\frac{1}{a\cos\varphi}\frac{\partial u}{\partial \lambda} - v\frac{1}{a}\frac{\partial u}{\partial \varphi} + uv\frac{\tan\varphi}{a} - \dot{\sigma}\frac{\partial u}{\partial \sigma}$$
$$+fv - \frac{1}{a\cos\varphi}\frac{\partial \phi}{\partial \lambda} - \frac{RT}{P_s}\frac{1}{a\cos\varphi}\frac{\partial P_s}{\partial \lambda} + F_\lambda \qquad (2.3)$$

$$\frac{\partial v}{\partial t} = -u\frac{1}{a\cos\varphi}\frac{\partial v}{\partial \lambda} - v\frac{1}{a}\frac{\partial v}{\partial \varphi} - u^2\frac{\tan\varphi}{a} - \dot{\sigma}\frac{\partial v}{\partial \sigma}$$
$$-fu - \frac{1}{a}\frac{\partial \phi}{\partial \varphi} - \frac{RT}{P_s}\frac{1}{a}\frac{\partial P_s}{\partial \varphi} + F_\varphi \qquad (2.4)$$

$$\frac{\partial T}{\partial t} = -u\frac{1}{a\cos\varphi}\frac{\partial T}{\partial \lambda} - v\frac{1}{a}\frac{\partial T}{\partial \varphi} - \dot{\sigma}\left[\frac{\partial T}{\partial \sigma} - \frac{R}{C_p}\frac{T}{1+\sigma}\right]$$
$$\frac{RT}{C_p}\left[\frac{1}{a\cos\varphi}\frac{\partial u}{\partial \lambda} + \frac{1}{a}\frac{\partial v}{\partial \varphi} - v\frac{\tan\varphi}{a} + \frac{\partial \dot{\sigma}}{\partial \sigma}\right] + \frac{Q}{C_p} \qquad (2.5)$$

$$\frac{1}{P_s}\frac{\partial P_s}{\partial t} = -\frac{1}{2}\int_{-1}^{1}\left[\frac{1}{a\cos\varphi}\frac{\partial u}{\partial\lambda} + \frac{1}{a}\frac{\partial v}{\partial\varphi} - v\frac{\tan\varphi}{a} + \frac{u}{P_s}\frac{1}{a\cos\varphi}\frac{\partial P_s}{\partial\lambda} + \frac{v}{P_s}\frac{1}{a}\frac{\partial P_s}{\partial\varphi}\right]d\sigma \qquad (2.6)$$

$$\dot{\sigma} = -\int_{1}^{\sigma}\left[\frac{1}{a\cos\varphi}\frac{\partial u}{\partial\lambda} + \frac{1}{a}\frac{\partial v}{\partial\varphi} - v\frac{\tan\varphi}{a} + \frac{u}{P_s}\frac{1}{a\cos\varphi}\frac{\partial P_s}{\partial\lambda} + \frac{v}{P_s}\frac{1}{a}\frac{\partial P_s}{\partial\varphi}\right]d\sigma + \frac{1-\sigma}{P_s}\frac{\partial P_s}{\partial t} \qquad (2.7)$$

$$(1+\sigma)\frac{\partial\phi}{\partial\sigma} = -RT \qquad (2.8)$$

with the following notations:

φ	latitude
λ	longitude
a	radius of the earth
t	time
u	zonal component of velocity
v	meridional component of velocity
$\dot{\sigma}$	$=d\sigma/dt$, individual time derivative of σ
T	temperature (in °K)
ϕ	geopotential
F_λ	zonal component of friction force per unit mass
F_φ	meridional component of friction force per unit mass
Q	diabatic heating per unit mass per unit time

f $=2\Omega\sin\varphi$, the coriolis parameter, Ω being angular velocity of the earth

R the gas constant for dry air

C_p specific heat at constant pressure for dry air

The equations (2.3) and (2.4) are the momentum equations and (2.5) is the thermodynamic equation, the equations (2.6) and (2.7) are referred to as "tendency equation" and "vertical velocity equation" respectively, which are obtained by vertical integration of the continuity equation using the boundary condition

$$\dot{\sigma}=0 \qquad \text{at } \sigma=1 \text{ and } \sigma=-1. \tag{2.9}$$

Finally the equation (2.8) is the hydrostatic equation, the solution of which should satisfy the boundary condition

$$\phi\Big|_{\sigma=1} = \phi_s \tag{2.10}$$

where ϕ_s is the surface geopotential.

For later convenience, the following variables are introduced:

$$\begin{cases} U = u\cos\varphi \\ V = v\cos\varphi \\ q = \ln P_s \\ S = \dfrac{a}{1-\sigma^2}\dot{\sigma} \end{cases} \tag{2.11}$$

The eqs. (2.3)—(2.8) are suitable for prediction but now we wish to find a set of equations with which to investigate the steady response of atmosphere to large scale topography and stationary diabatic heating. We assume in this connection that all partial derivatives with respect to time in these equations equal zero, and obtain the following steady-state primitive equations, which will be used as the basic equations of the nonlinear model:

$$-\frac{1}{1-\mu^2}\left(-UU^{(\lambda)}+VU^{(\mu)}\right)+SU^{(\sigma)}+2\Omega a\mu V - \phi^{(\lambda)}-RTq^{(\lambda)}-a\left(R_f+\alpha\nabla^4\right)U=0 \tag{2.12}$$

$$\frac{1}{1-\mu^2}\left(-UV^{(\lambda)}+VV^{(\mu)}\right)+SV^{(\sigma)}-\frac{\mu(U^2+V^2)}{1-\mu^2} - 2\Omega a\mu U+\phi^{(\mu)}+RTq^{(\mu)}-a\left(R_f+\alpha\nabla^4\right)V=0 \tag{2.13}$$

$$\frac{1}{1-\mu^2}\left(-UT^{(\lambda)}+VT^{(\mu)}-\kappa T\left(U^{(\lambda)}-V^{(\mu)}\right)\right)+\kappa TS^{(\sigma)} + S\left(T^{(\sigma)}+\kappa(1+\sigma)\pi\right)+\frac{aQ}{C_p}-a\left(K_t+\nu\nabla^4\right)T=0 \tag{2.14}$$

$$\int_{-1}^{1}\left(U^{(\lambda)}-V^{(\mu)}+Uq^{(\lambda)}-Vq^{(\mu)}\right)d\sigma=0 \tag{2.15}$$

$$S = - \frac{1}{(1-\mu^2)(1-\sigma^2)} \int_1^\sigma \left(U^{(\lambda)} - V^{(\mu)} + Uq^{(\lambda)} - Vq^{(\lambda)} \right) d\sigma \qquad (2.16)$$

$$(1+\sigma) \frac{\partial \phi}{\partial \sigma} = - RT \qquad (2.17)$$

Here the following notations are used:

$$\begin{cases} \mu = \text{Sin } \varphi \\ \kappa = \dfrac{R}{C_p} \\ A^{(\lambda)} = \dfrac{\partial A}{\partial \lambda} \\ A^{(\mu)} = (\mu^2-1) \dfrac{\partial A}{\partial \mu} \\ A^{(\sigma)} = (\sigma^2-1) \dfrac{\partial A}{\partial \sigma} \end{cases} \qquad (2.18)$$

where A stands for any of the variables. Additionally, we include Rayleigh friction and Newtonian cooling with spatially-varying decay rates R_f and K_t. Thus in (2.14) aQ/C_p denotes the diabatic heating rate (in K s^{-1}) excepting Newtonian cooling. Scale-selective smoothing may also be included by diffusion terms $\alpha\nabla^4$ and $\nu\nabla^4$. The specification of coefficients R_f, K_t, α and ν is described in Section 4.1. For the zonally averaged components, this dissipation is applied only to the deviation from the initial state. These zonally averaged components of the initial

state are simply those representing the basic state for the linear model.

The stationary solution of eqs. (2.12)-(2.17) ~~can~~ should be able in principle to provide an adequate representation for the atmospheric stationary waves. However, it must be noticed that there is a difference between the stationary solution and the time mean of a time varying solution. For a steady-state model, the latter case may be considered in this way: Instead of assuming $\partial U/\partial t$, $\partial V/\partial t$, $\partial T/\partial t$ and $\partial q/\partial t$ equal zero, we may take a time average for a long period (e.g., one month or longer) firstly and then let the partial derivatives of the time mean variables with respect to time equal zero. In such a formulation some forcing terms which indicate the effect of mean convergence of heat and momentum transport by transient waves will appear in eqs. (2.12)-(2.14). This will not be considered further in this study.

2.3 Spectral Representation of the Dependent Variables and Associated Derivatives

2.3.1 Normalized Orthogonal Functions

Each of the dependent variable fields in this model is represented by a truncated series in terms of orthogonal functions. As a basis for the vertical representation, the normalized Legendre polynomials with σ as argument are chosen. These are defined by

$$P_k(\sigma) = \frac{(2k+1)^{1/2}}{2^k\ k!}\frac{d^k}{d\sigma^k}(\sigma^2-1)^k \qquad (2.19)$$

The representation of horizontal structure of each vertical mode is based on the surface spherical harmonics

$$Y_{m,n}(\lambda,\mu) = P_{m,n}(\mu)\ e^{im\lambda} \qquad (2.20)$$

where the normalized associated Legendre function $P_{m,n}(\mu)$ is defined by

$$P_{m,n}(\mu) = \left[(2n+1)\frac{(n-|m|)!}{(n+|m|)!}\right]^{1/2}\frac{(1-\mu^2)^{|m|/2}}{2^n\ n!}\frac{d^{n+|m|}}{d\mu^{n+|m|}}(\mu^2-1)^n \qquad (2.21)$$

and illustrated in Fig.2.1 for m=0, 1, 2 and 3. Here |m| is the planetary wavenumber and n-|m| is the number of zeros between the poles.

With the definition above, the functions are normalized as well as orthogonal, namely

$$\frac{1}{2}\int_{-1}^{1} P_k(\sigma)\ P_l(\sigma)\ d\sigma = \begin{cases} 1 & \text{for } k=l \\ 0 & \text{for } k\neq l \end{cases}$$

$$\frac{1}{2\pi}\int_{0}^{2\pi} e^{im\lambda}\ (e^{im'\lambda})^*\ d\lambda = \begin{cases} 1 & \text{for } m=m' \\ 0 & \text{for } m\neq m' \end{cases} \qquad (2.22)$$

$$\frac{1}{2}\int_{-1}^{1} P_{m,n}(\mu)\ P_{m',n'}(\mu)\ d\mu = \begin{cases} 1 & \text{for } m=m' \text{ and } n=n' \\ 0 & \text{otherwise} \end{cases}$$

where $(e^{im'\lambda})^*$ represents the complex conjugate of $e^{im'\lambda}$.

In practice, the $P_{m,n}(\mu)$ can be calculated using the following properties:

$$P_{m,n}(\mu) = 0 \quad \text{when } n<m,$$
$$P_{-m,n}(\mu) = P_{m,n}(\mu) \qquad (2.23)$$

together with the recursion relationships:

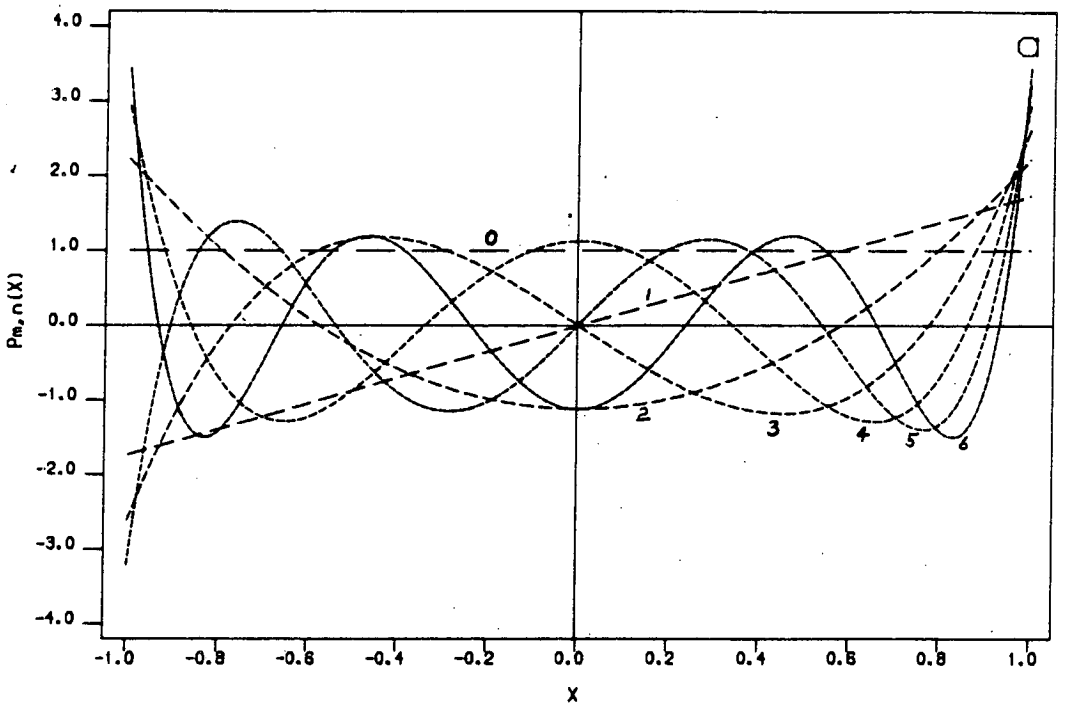
a
4.0
3.0
2.0
1.0
0.0
-1.0
-2.0
-3.0
-4.0
Pm,n(X)
0
1
2
3
4
5
6
-1.0
-0.8
-0.6
-0.4
-0.2
0.0
0.2
0.4
0.6
0.8
1.0
X

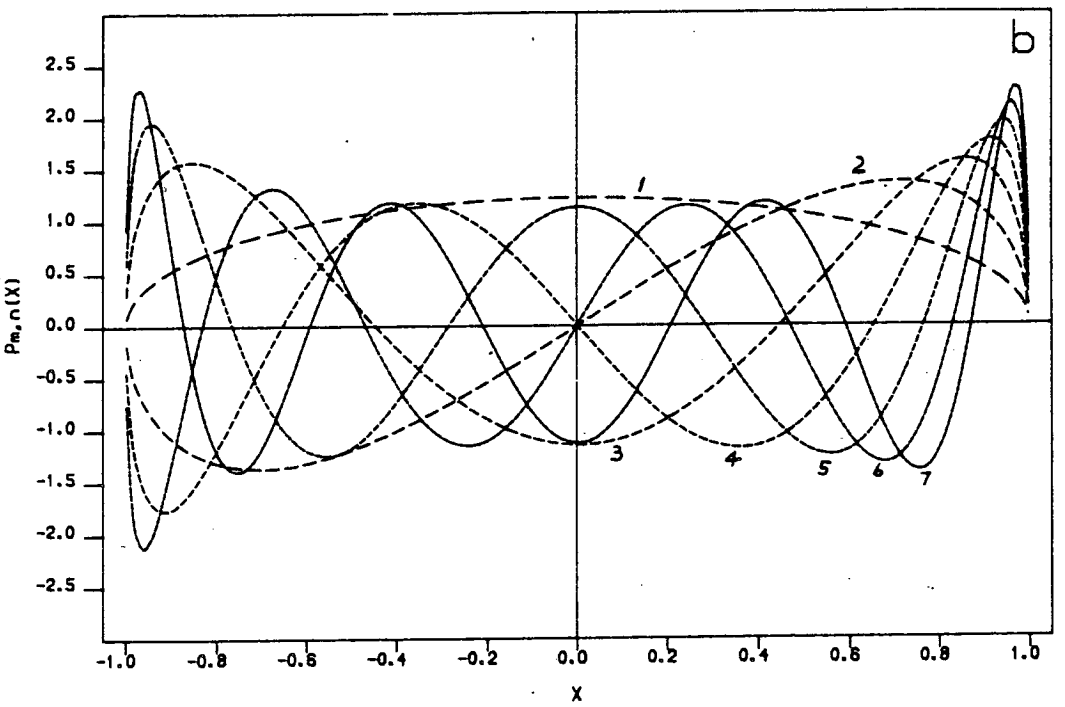
b
2.5
2.0
1.5
1.0
0.5
0.0
-0.5
-1.0
-1.5
-2.0
-2.5
Pm,n(X)
1
2
3
4
5
6
7
-1.0
-0.8
-0.6
-0.4
-0.2
0.0
0.2
0.4
0.6
0.8
1.0
X

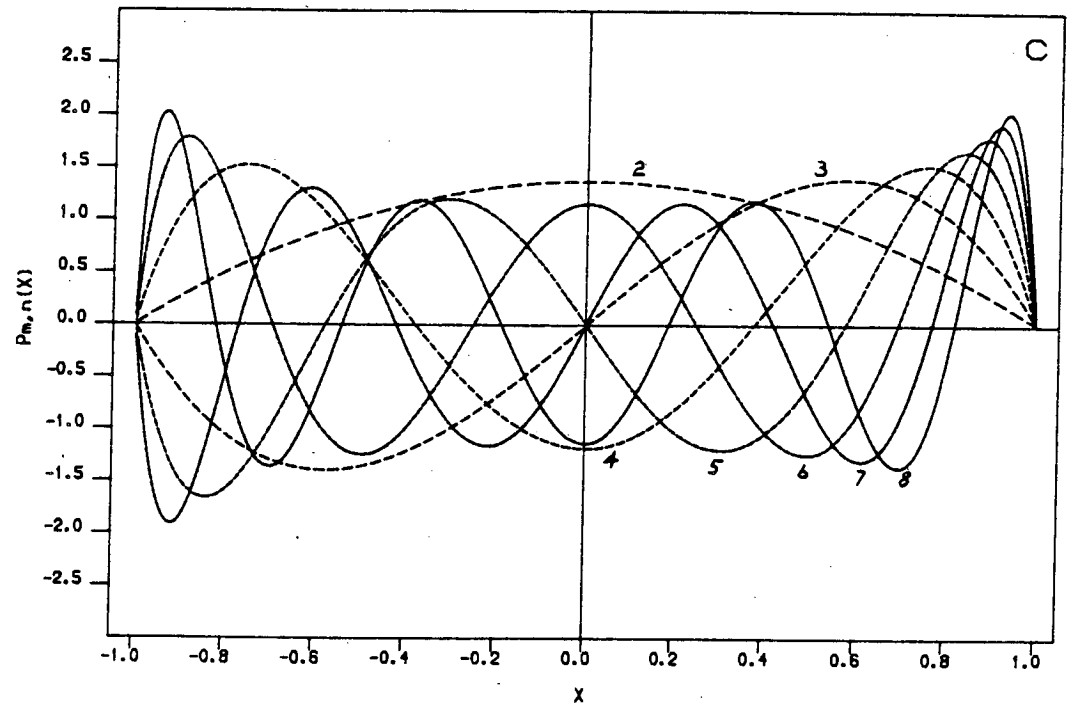

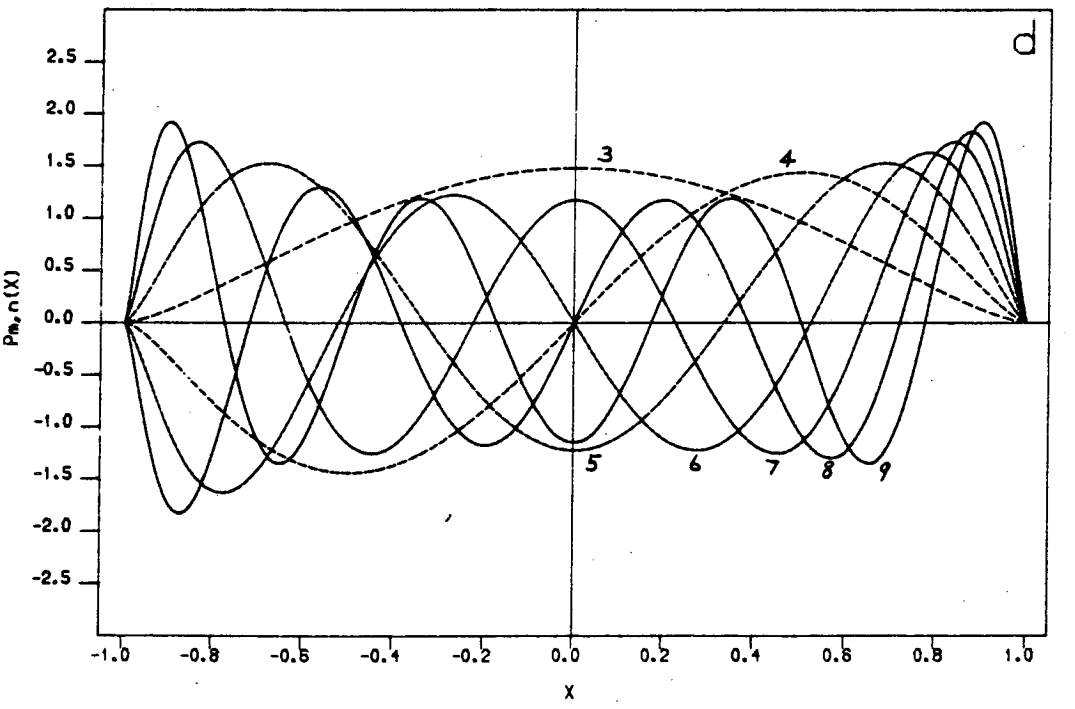

Fig.2.1 Normalized associated Legendre polynomials $P_{m,n}(x)$ for (a) m=0, (b) m=1, (c) m=2 and (d) m=3; n=m,m+1,.....,m+6. The figures marked near the curves indicate the values of n.

$$P_{m,m+1}(\mu) = (2m+3)^{1/2}\ \mu\ P_{m,m}(\mu) \qquad (2.24)$$

$$P_{m+1,m+1}(\mu) = \left[\frac{2m+3}{2m+2}\ (1-\mu^2)\right]^{1/2} P_{m,m}(\mu) \qquad (2.25)$$

$$D_{m,n+1}\ P_{m,n+1}(\mu) = \mu\ P_{m,n}(\mu) - D_{m,n}\ P_{m,n-1}(\mu) \qquad (2.26)$$

where

$$D_{m,n} = \left[\frac{n^2-m^2}{4n^2-1}\right]^{1/2}$$

The Legendre polynomials $P_k(\sigma)$ are simply a subset of the $P_{m,k}(\sigma)$, therefore similar formulae can be used for their calculation.

Another recurrence formula given by Belousov (1962) has the advantage of being mathematically stable when m and n increase, and is preferable for high resolution spectral models.

2.3.2 Spectral representation of the dependent variables

The associated Legendre polynomials have the property

$$P_{m,n}(-\mu) = (-1)^{m+n}\ P_{m,n}(\mu) \qquad (2.27)$$

This property shows that n-m must be even for a hemispherical symmetric field or odd for an antisymmetric field. Hence in our hemisphere model, using a rhomboidal truncation, the basic dependent variables are represented approximately by the following truncated series

$$U(\lambda,\mu,\sigma) = \sum_{k=0}^{L} \sum_{m=-M}^{M} \sum_{j=|m|}^{|m|+J+1}{}^{(2)} U_{k,m,j} P_k(\sigma) e^{im\lambda} P_{m,j}(\mu) \tag{2.28}$$

$$V(\lambda,\mu,\sigma) = \sum_{k=0}^{L} \sum_{m=-M}^{M} \sum_{j=|m|+1}^{|m|+J}{}^{(2)} V_{k,m,j} P_k(\sigma) e^{im\lambda} P_{m,j}(\mu) \tag{2.29}$$

$$T(\lambda,\mu,\sigma) = \sum_{k=0}^{L} \sum_{m=-M}^{M} \sum_{j=|m|}^{|m|+J-1}{}^{(2)} T_{k,m,j} P_k(\sigma) e^{im\lambda} P_{m,j}(\mu) \tag{2.30}$$

$$q(\lambda,\mu) = \sum_{m=-M}^{M} \sum_{j=|-m|}^{|m|+J-1}{}^{(2)} q_{m,j} e^{im\lambda} P_{m,j}(\mu) \tag{2.31}$$

where J has been chosen to be an odd integer. The "(2)" attached to the summation signs indicates that the summation should be taken only for each second value of the index, that is in (2.28), (2.30) and (2.31) for even values of $n-|m|$, in (2.29) for odd values of $n-|m|$.

In view of the orthogonal property of spherical harmonics and Legendre polynomials, the expansion coefficients on the right hand sides of (2.28)-(2.31) are easy to evaluate if the spatial distribution of the relevant variables is known. For example, the coefficient $U_{k,m,j}$ is the orthogonal projection of $U(\lambda,\mu,\sigma)$ on the sub-spectral space generated by $P_k(\sigma)e^{im\lambda}P_{m,j}(\mu)$. In other words,

$$U_{k,m,j} = \frac{1}{8\pi} \int_{-1}^{1} \int_{-1}^{1} \int_{0}^{2\pi} U(\lambda,\mu,\sigma) P_k(\sigma) e^{-im\lambda} P_{m,j}(\mu)\, d\lambda d\mu d\sigma \tag{2.32}$$

The expressions for $V_{k,m,j}$, $T_{k,m,j}$ and $q_{m,j}$ are analogous to that for $U_{k,m,j}$.

Each of these series may be split up as shown below for U, in which the notation for the different expansion coefficients will be used in the following text without further explanation.

$$\begin{cases} U(\lambda,\mu,\sigma) = \sum_{k=0}^{L} U_k(\lambda,\mu)\, P_k(\sigma) \\ U_k(\lambda,\mu) = \sum_{m=-M}^{M} U_{k,m}(\mu)\, e^{im\lambda} \\ U_{k,m}(\mu) = \sum_{j=|m|}^{|m|+J+1} {}^{(2)} U_{k,m,j}\, P_{m,j}(\mu) \end{cases} \tag{2.33}$$

As shown by Eliasen et al. (1970), this representation of the velocity field is identical with a velocity field represented in terms of streamfunction Ψ and velocity potential χ provided that so called "truncation relations" are employed. In order to derive these relations, let us consider the velocity field given by the following truncated series of Ψ and χ:

$$\begin{cases} \Psi = \sum_{m=-M}^{M} \sum_{j=|m|+1}^{|m|+J} {}^{(2)} \Psi_{m,j}(\sigma)\, Y_{m,j}(\lambda,\mu) \\ \chi = \sum_{m=-M}^{M} \sum_{j=|m|}^{|m|+J-1} {}^{(2)} \chi_{m,j}(\sigma)\, Y_{m,j}(\lambda,\mu) \end{cases} \tag{2.34}$$

Substituting these series into the relations

$$\begin{cases} U = \dfrac{1}{a}(\chi^{(\lambda)} + \psi^{(\mu)}) \\ \\ V = \dfrac{1}{a}(\psi^{(\lambda)} - \chi^{(\mu)}) \end{cases} \tag{2.35}$$

we obtain finally

$$\begin{cases} U = \displaystyle\sum_{m=-M}^{M} \sum_{j=|m|}^{|m|+J+1}(2) \; U_{m,j}(\sigma)\; Y_{m,j}(\lambda,\mu) \\ \\ V = \displaystyle\sum_{m=-M}^{M} \sum_{j=|m|+1}^{|m|+J}(2) \; V_{m,j}(\sigma)\; Y_{m,j}(\lambda,\mu) \end{cases} \tag{2.36}$$

where

$$\begin{cases} U_{m,j} = \dfrac{1}{a}\left[(j-1)\; D_{m,j}\; \psi_{m,j-1} + im\; \chi_{m,j} - (j+2)\; D_{m,j+1}\; \psi_{m,j+1}\right] \\ \\ V_{m,j} = \dfrac{1}{a}\left[(1-j)\; D_{m,j}\; \chi_{m,j-1} + im\; \psi_{m,j} + (j+2)\; D_{m,j+1}\; \chi_{m,j+1}\right] \end{cases} \tag{2.37}$$

and

$$D_{m,j} = \left[\frac{j^2-m^2}{4j^2-1}\right]^{1/2}$$

For each zonal wave number m, relations (2.37) forms a system of (J+2) equations, in which the (J+2) coefficients of U and V are determined by (J+1) coefficients of Ψ and χ. We therefore have a relation between the U and V coefficients, which can be obtained by elimination of the Ψ and χ coefficients. In the case of $m \neq 1$, the coefficients

$U_{m,m+J+1}$ may be expressed by the other U and V coefficients, i.e.,

$$U_{m,m+J+1} = \sum_{j=1}^{J}{}^{(2)} \left(-C_{m,j-1}\, U_{m,m+j-1} + iC_{m,j}\, V_{m,m+j}\right) \tag{2.38}$$

where

$$C_{m,j} = \prod_{i=j}^{J} K_{m,i}$$

$$K_{m,o} = -D_{m,m+1}$$

$$K_{m,i} = -\frac{(m+i)D_{m,m+i+1}}{m-K_{m,i-1}(m+i+1)D_{m,m+i}} \qquad \text{for } i>0$$

$$D_{m,n} = \left[\frac{n^2-m^2}{4n^2-1}\right]^{1/2}$$

In the special case m=0, relation (2.38) becomes

$$U_{o,j+1} = -\frac{1}{(2j+3)^{1/2}} \sum_{j=o}^{J-1}{}^{(2)} (2j+1)^{1/2}\, U_{o,j} \tag{2.39}$$

Since the spectral coefficient $\chi_{0,0}$ is an integration constant, which is usually set to be zero, the number of Ψ and χ coefficients which determine the (J+2) coefficients of U and V are reduced to J. Therefore an additional relation may be derived by elimination, that is

$$V_{o,j} = -\frac{1}{(2j+3)^{1/2}} \sum_{j=o}^{J-1}{}^{(2)} (2j+1)^{1/2}\, V_{o,j} \tag{2.40}$$

The relations (2.38), (2.39) and (2.40) are referred to as "truncation relations".

2.3.3 Evaluation of Spatial Partial Derivatives

In the spectral model the dependent variables are represented by a sum of functions that have a prescribed spatial structure. Therefore the spatial partial derivatives of the dependent variables can be easily expressed in the spectral form, for example, as indicated below for U:

$$U^{(\lambda)} = \sum_{k=0}^{L} \sum_{m=-M}^{M} \sum_{j=|m|}^{|m|+J+1} (2)\ im\, U_{k,m,j}\, P_k(\sigma)\, e^{im\lambda}\, P_{m,j}(\mu) \qquad (2.41)$$

$$U^{(\mu)} = \sum_{k=0}^{L} \sum_{m=-M}^{M} \sum_{j=|m|}^{|m|+J+1} (2)\ U_{k,m,j}\, P_k(\sigma)\, e^{im\lambda}\, H_{m,j}(\mu) \qquad (2.42)$$

$$U^{(\sigma)} = \sum_{k=0}^{L} \sum_{m=-M}^{M} \sum_{j=|m|}^{|m|+J+1} (2)\ U_{k,m,j}\, H_k(\sigma)\, e^{im\lambda}\, P_{m,j}(\mu) \qquad (2.43)$$

where

$$H_{m,n}(\mu) = (\mu^2-1)\frac{dP_{m,n}(\mu)}{d\mu}$$

$$= n\, D_{m,n+1}\, P_{m,n+1}(\mu) - (n+1)\, D_{m,n}\, P_{m,n-1}(\mu) \tag{2.44}$$

$$H_k(\sigma) = (\sigma^2-1)\frac{dP_k(\sigma)}{d\sigma}$$

$$= k D_{o,k+1}\, P_{k+1}(\sigma) - (k+1)\, D_{o,k}\, P_{k-1}(\sigma) \tag{2.45}$$

$$D_{m,n} = \left[\frac{n^2-m^2}{4n^2-1}\right]^{1/2} \tag{2.46}$$

Since spherical harmonics $Y_{m,n}$ are eigenfunctions of the equation

$$\nabla^2 Y + bY = 0 \tag{2.47}$$

where ∇^2 is the two-dimensional Laplacian operator on the sphere, i.e.,

$$\nabla^2 \equiv \frac{1}{a^2}\left\{\frac{1}{1-\mu^2}\frac{\partial^2}{\partial\lambda^2} + \frac{\partial}{\partial\mu}\left[(1-\mu^2)\frac{\partial}{\partial\mu}\right]\right\} \tag{2.48}$$

and the eigenvalues are given by

$$b = \frac{n(n+1)}{a^2} \tag{2.49}$$

the diffusion term in (2.12) can be evaluated by the following expression:

$$\alpha\nabla^4 U = \frac{\alpha}{a^4}\sum_{k=0}^{L}\sum_{m=-M}^{M}\sum_{j=|m|}^{|m|+J+1}{}^{(2)}\; j^2(j+1)^2 U_{k,m,j} P_k(\sigma) e^{im\lambda} P_{m,j}(\mu) \tag{2.50}$$

2.4 Vertical Integration of Continuity and Hydrostatic Equation

2.4.1 Evaluation of Vertical Velocity

The remaining quantities to be calculated in terms of the spectral coefficients of U, V, T and q are vertical velocity S and geopotential ϕ as well as their partial derivatives. Evaluation of S and ϕ involves the vertical integration of the continuity and hydrostatic equations respectively. S is determined from eq. (2.16). Substituting the vertical expansions of U and V in (2.16), integrating the finite series term by term and using eq. (2.15) we obtain

$$S = \frac{1}{1-\mu^2} \sum_{k=1}^{L} \left(U_k^{(\lambda)} - V_k^{(\mu)} + U_k q^{(\lambda)} - V_k q^{(\mu)} \right) K_k(\sigma) \qquad (2.51)$$

where

$$K_k(\sigma) = \frac{1}{\sigma^2 - 1} \int_1^{\sigma} P_k(\sigma)\, d\sigma \qquad (2.52)$$

$K_k(\sigma)$ are found to be polynomials in σ of degree k-1. The formula for evaluating $S^{(\sigma)}$ may be derived from (2.51) directly, that is

$$S^{(\sigma)} = \frac{1}{1-\mu^2} \sum_{k=2}^{L} \left(U_k^{(\lambda)} - V_k^{(\mu)} + U_k q^{(\lambda)} - V_k q^{(\mu)} \right) G_k(\sigma) \qquad (2.53)$$

where

$$G_k(\sigma) = (\sigma^2-1)\frac{dK_k(\sigma)}{d\sigma}$$

$$= P_k(\sigma) - \frac{2\sigma}{\sigma^2-1}\int_1^\sigma P_k(\sigma)\,d\sigma \qquad (2.54)$$

is a polynomial in σ of degree k. The lower index in (2.53) is 2 because $G_1(\sigma)\equiv 0$.

2.4.2 Evaluation of Geopotential

The geopotential field ϕ is determined from the temperature field by integrating the hydrostatic equation (2.17) with the lower boundary condition (2.10). Thus

$$\phi = \phi_s - R\int_1^\sigma \frac{T}{1+\sigma}\,d\sigma \qquad (2.55)$$

Substituting the vertical expansion of T in (2.55) and integrating term by term we have

$$\phi = \phi_s - R\sum_{k=0}^{L} T_k\, I_k(\sigma) \qquad (2.56)$$

where

$$I_k(\sigma) = \int_1^\sigma \frac{P_k(\sigma)}{1+\sigma}\,d\sigma \qquad (2.57)$$

$I_k(\sigma)$ is not a polynomial in σ, but may be calculated

approximately by numerical integration for each vertical level σ_k ($\sigma_k \neq 0$). The Gauss-Legendre quadrature described in section 2.6.3 is used to calculate $I_k(\sigma_k)$.

A temperature correction procedure suggested by Machenhauer and Daley (1972) leads to another scheme of evaluating geopotential and insures there are no spurious energy sources introduced during time integration. That correction procedure is not necessary in the present steady-state model where no time integration is performed.

2.5 Method of Solution

2.5.1 General Description

Since vertical velocity and geopotential fields can be diagnosed explicitly from U, V and q fields with use of (2.16) and (2.17) as described in section 2.4, we may consider that the equations (2.12), (2.13), (2.14) and (2.15) comprise a complete system of four equations and four unknowns, U, V, T and q.

Let the left hand side of (2.12), (2.13), (2.14) and (2.15) be $f_1(\lambda,\mu,\sigma)$, $f_2(\lambda,\mu,\sigma)$, $f_3(\lambda,\mu,\sigma)$, and $f_4(\lambda,\mu)$ respectively. These functions include a number of nonlinear terms. When each field is represented by finite series, a nonlinear term involves multiplication of two series, which is very time-consuming if it is calculated by the interaction coefficient method. The transform method is far superior to the interaction coefficient method for handling the

nonlinear terms if there are very many components in the system. With this method, we transform firstly the representation of each field from spectral form to a certain spatial grid of points, then the two fields are multiplied at each point to form a nonlinear term. Finally these functions are calculated by adding all individual terms together at grid points. Then they must be transformed back to spectral space. This is done by making an orthogonal projection of f_1, f_2, f_3 and f_4 on the sub spectral space generated by $P_l(\sigma)e^{im'\lambda}P_{m',n}(\mu)$ with respect to various combinations of index value of l, m' and n, namely

$$F^{(I)}_{l,m',n} = \frac{1}{8\pi}\int_{-1}^{1}\int_{-1}^{1}\int_{0}^{2\pi} f_I(\lambda,\mu,\sigma)P_l(\sigma)e^{-im'\lambda}P_{m',n}(\mu)d\lambda d\mu d\sigma \qquad (I = 1,2,3) \tag{2.58}$$

$$F^{(4)}_{m',n} = \frac{1}{4\pi}\int_{-1}^{1}\int_{0}^{2\pi} f_4(\lambda,\mu)\, e^{-im'\lambda}\, P_{m',n}(\mu)\, d\lambda\, d\mu \tag{2.59}$$

The projections $F_{l,m,n}$ and $F_{m,n}$ are functions of unknown spectral coefficients $U_{k,m,j}$, $V_{k,m,j}$, $T_{k,m,j}$ and $q_{m,j}$. The problem raised in this nonlinear model is to seek a set of spectral coefficients for U, V, T and q, which satisfies the following equations

$$\begin{cases} F^{(I)}_{l,m',n} = 0 \qquad (I=1,2,3) \\ F^{(4)}_{m',n} = 0 \end{cases} \tag{2.60}$$

If we choose the projection indices l, m' and n in

correspondence with the variable indices k, m and j, a complete system may be comprised.

The method for evaluating the integrals in (2.58) and (2.59) will be described in the next section. The structure of the computational grid will be discussed in section 2.5.3.

The steady-state solution of the nonlinear equation system (2.60) for a prescribed forcing function (topography, diabatic heating or both) is obtained in terms of an iteration procedure, which is described in section 2.5.4. The January mean statistics calculated from the FGGE IIIb (ECMWF) analysis, and the linear model's solution corresponding to the same forcing are used as an initial guess for the basic state and the disturbance portion respectively.

2.5.2 Numerical Integration

The triple integral (2.58) may be split up into three single integrals, i.e.

$$g_I(\mu,\sigma;m') = \frac{1}{2\pi}\int_0^{2\pi} f_I(\lambda,\mu,\sigma)\, e^{-im'\lambda}\, d\lambda \qquad (2.61)$$

$$h_I(\sigma;m',n) = \frac{1}{2}\int_{-1}^{1} g_I(\mu,\sigma;m')\, P_{m',n}(\mu)\, d\mu \qquad (2.62)$$

$$F^{(I)}_{l,m',n} = \frac{1}{2}\int_{-1}^{1} h_I(\sigma;m',n)\, P_l(\sigma)\, d\sigma \qquad (2.63)$$

The integral (2.61) can be calculated very efficiently with use of the fast Fourier transform (FFT) method, which was developed by Cooley and Tukey (1965). The number of

operations required for the FFT method applied over N points is of order $N\log_2 N$, while for the direct method, it is of order N^2. The FFT method is much faster than the direct method, especially for large values of N. Of course, this method can also be used to calculate the summation for m in (2.28)-(2.31) in order to transform the spectral coefficients into grid point values.

The Gauss-Legendre formula has been used to calculate the integrals in (2.57), (2.58), (2.47) and (2.52). this formula may be written

$$\int_{-1}^{1} f(x)\, dx = \sum_{i=1}^{N} w_i\, f(x_i) \qquad (2.64)$$

where the abscissas x_i's are sample points, which are the zero points of the Legendre polynomial $P_N(x)$. The weighting coefficients w_i can be found by

$$w_i = \frac{2(1-x_i^2)(2N-1)}{(N\, P_{N-1}(x_i))^2} \qquad (2.65)$$

In order to find the sample points x_i, Newton iteration is used to solve the nonlinear equation

$$P_N(x_i) = 0 \qquad (2.66)$$

In this iteration procedure, if the (k)th estimate of x_i is given by $x_i^{(k)}$ then the next estimate $x_i^{(k+1)}$ is obtained by

$$x_i^{(k+1)} = x_i^{(k)} - \frac{P_N(x_i^{(k)})}{P'_N(x_i^{(k)})} \qquad (2.67)$$

where the derivative $P'_N(x_i^{(k)})$ may be calculated by using the recurrence formula

$$P'_N(x) = \frac{N(P_{N-1}(x)-xP_N(x))}{1-x^2} \qquad (2.68)$$

The initial guess $x_i^{(0)}$ has been taken as

$$x_i^{(0)} = \sin\left[\frac{\pi(i-0.5)}{N} - \frac{\pi}{2}\right] \qquad (2.69)$$

In real calculation only half of the points are required to be found in this way due to symmetry. If the sample points in the meridional direction are μ_j (j=1,2,...,N), then $\varphi_j = \arcsin(\mu_j)$ where μ_j's are called Gaussian latitudes. In the vertical direction the sample points σ_k are called Gaussian levels.

For evaluating the integrals in (2.52) and (2.57) a substitution of independent variable can be made in order to transform the integral intervals into a standard one. For example, (2.52) can be transformed into

$$K_l(\sigma) = \frac{1}{2(\sigma+1)} \int_{-1}^{1} P_l\left[\frac{\sigma+1}{2} + \frac{\sigma-1}{2}\, t\right] dt \qquad (2.70)$$

Applying the Gauss-Legendre quadrature formula (2.64) to this integral, for each Gaussian level σ_k we have

$$K_l(\sigma_k) = \frac{1}{2(\sigma_k+1)} \sum_{i=1}^{n} w_i\, P_l(x_i) \qquad (2.71)$$

where

$$x_i = \frac{\sigma_k+1}{2} + \frac{\sigma_k-1}{2}\, t_i \qquad (2.72)$$

and t_i are the zeros of the Legendre polynomial $P_N(t)$, that is,

$$P_N(t_i) = 0.$$

2.5.3 Computational Grid

The physical space grid points are the intersections of N_1 equally spaced meridians where $\lambda=\lambda_i$, the N_2 Gaussian latitude circles where $\mu=\mu_j$, and the N_3 Gaussian levels where $\sigma=\sigma_k$. The total number of grid points is determined by the product of N_1, N_2 and N_3, each of which should be determined so that the Fourier transform and Gauss-Legendre quadrature formula become exact for the integrals involved in the computation of the nonlinear terms in order to avoid aliasing. The following two criteria ~~conclusion~~ are useful to determine the minimum values of N_1, N_2 and N_3: a) The Gauss-Legendre quadrature formula (2.64) is exact for all polynomials with degree smaller than or equal to 2N-1; and b) The trapezoidal quadrature formula

$$\frac{1}{2\pi}\int_0^{2\pi} f(x)dx = \frac{1}{N}\sum_{i=1}^{N} f\left[\frac{2\pi}{N}i\right] \qquad (2.73)$$

is exact for any function which is a truncated Fourier series with minimum wavenumber smaller than or equal to N-1. As explained by Eliasen et al. (1970), Machenhauer and Rasmussen (1972), and Machenhauer and Daley (1972), for all nonlinear terms, except those which include S and $S^{(\sigma)}$, the grid point numbers N_1, N_2 and N_3 should satisfy

$$\begin{cases} N_1 \geq 3M + 1 \\ N_2 \geq \frac{3}{2}J + M + 1 \\ N_3 \geq \frac{3}{2}L + \frac{1}{2} \end{cases} \tag{2.74}$$

where M, J and L denote truncation indices as represented in (2.28)-(2.31).

Much larger values of N_1 and N_2 must be used for those terms which include S and $S^{(\sigma)}$ since it is seen from (2.51) and (2.53) that S and $S^{(\sigma)}$ are quadratic in variables which vary in the horizontal directions. For these terms N_1 and N_2 should satisfy

$$\begin{cases} N_1 \geq 4M + 1 \\ N_2 \geq 2(M+J) + \frac{3}{2} \end{cases} \tag{2.75}$$

It should be noticed that the terms which require the largest values of N_1 and N_2 determine the minimum values which must be used for all the terms. It is, however, possible to reduce the minimum values to those given by (2.74) if S and $S^{(\sigma)}$ are truncated before they are used in the computation of the nonlinear terms in (2.12)-(2.14).

Different very low resolutions have been used during testing of the model program, finally the truncation indices are increased and fixed with M=3, J=11 and L=4 to fit the computational resource available. This is intended to represent the vertical and horizontal propagation of the ultralong stationary planetary waves which have been generally considered to be forced by topography and land-sea heating contrasts. Although it is still a low

resolution model, the experimental results show that it has the ability to simulate the essential features of full three-dimensional propagation of the stationary planetary wave activity. Corresponding to these truncation indices a fixed computational grid of points is used to calculate the nonlinear terms, in which there are 10 and 11 points in the longitudinal and latitudinal direction respectively on a hemisphere, and 7 levels in the vertical direction. The vertical levels used in the Gauss-Legendre quadrature formula are given in Table 2.1, where P_k is pressure at k level, which is calculated by assuming surface pressure equal to 1000 mb and gives a rough idea only.

Table 2.1: Vertical Levels

k	σ_k	P_k (mb)
1	-0.9491079	25.45
2	-0.7415312	129.23
3	-0.4058452	297.08
4	0.0000000	500.00
5	0.4058452	702.92
6	0.7415312	870.77
7	0.9491079	974.55

2.5.4 Newton-Raphson Iteration

Newton-Raphson iteration, the steepest-descent method and a variable metric method for minimization described by

Fletcher and Powell (1963) have been coded and used to solve the nonlinear equation system (2.60). It was found that the Newton-Raphson procedure is the most efficient one for this particular problem. The convergence of variable metric method is also quite rapid, but it is much more complex than the Newton-Raphson iteration. Therefore only the Newton-Raphson method is described here. More details can be found in standard mathematics texts, see, e.g., Gill et al. (1981).

We consider a system of N equations for N unknowns. For the sake of notation, we shall discuss the case N=2, which can be easily extended to arbitrary N. Given the nonlinear equations

$$\begin{cases} f_1(x,y) = 0 \\ f_2(x,y) = 0 \end{cases} \tag{2.76}$$

and an initial guess x_0, y_0 for the solution, at the neighbourhood of this initial guess, f_1 and f_2 can then be represented approximately by the following linear function

$$\begin{cases} f_1(x,y) \approx f_1(x_o,y_o) + (x-x_o)\dfrac{\partial f_1}{\partial x}(x_o,y_o)+(y-y_o)\dfrac{\partial f_1}{\partial y}(x_o,y_o) \\ f_2(x,y) \approx f_2(x_o,y_o) + (x-x_o)\dfrac{\partial f_2}{\partial x}(x_o,y_o)+(y-y_o)\dfrac{\partial f_2}{\partial y}(x_o,y_o) \end{cases} \tag{2.77}$$

In fact these expressions are obtained by truncating the

Taylor series expansions. Thus we can obtain a linear equation system

$$\begin{cases} \dfrac{\partial f_1}{\partial x}(x_o, y_o)\ \Delta x + \dfrac{\partial f_1}{\partial y}(x_o, y_o)\ \Delta y = -f_1\ (x_o, y_o) \\ \dfrac{\partial f_2}{\partial x}(x_o, y_o)\ \Delta x + \dfrac{\partial f_2}{\partial y}(x_o, y_o)\ \Delta y = -f_2\ (x_o, y_o) \end{cases} \tag{2.78}$$

where $\Delta x = x - x_0$, and $\Delta y = y - y_0$. We assume the determinant of the Jacobian matrix

$$J = \begin{bmatrix} \dfrac{\partial f_1}{\partial x} & \dfrac{\partial f_1}{\partial y} \\ \dfrac{\partial f_2}{\partial x} & \dfrac{\partial f_2}{\partial y} \end{bmatrix} \tag{2.79}$$

is not equal to zero at the neighbourhood of the solution. If the initial guess is reasonably good, the determinant of the coefficient matrix of (2.78) should also be nonzero. Δx and Δy can hence be easily found by elimination. From the definition of Δx and Δy we may write

$$\begin{cases} x_1 = x_o + \Delta x \\ y_1 = y_o + \Delta y \end{cases} \tag{2.80}$$

Then we may replace x_o and y_o with x_1 and y_1 and repeat the above procedure. The iteration process is terminated when

$$\max\ (\ \delta x,\ \ \delta y\ )\ <\ \varepsilon \tag{2.81}$$

where

$$\delta x = \frac{|x_{k+1} - x_k|}{|x_k|} \quad , \quad \delta y = \frac{|y_{k+1} - y_k|}{|y_k|} \quad ,$$

or

$$\max \left(|f_1|, \ |f_2| \right) < \delta \quad . \tag{2.82}$$

ε and δ are prescribed tolerance errors. Newton-Raphson iteration is a second-order process, which converges very rapidly if a reasonably good initial guess is given. *In the experiments we have done, 3-5 iterations are usually required for $\varepsilon = 10^{-4}$ and $\delta = 10^{-6}$.*

Scaling often has a significant influence on the performance of this kind of iteration algorithm. One method of scaling is to transform the variables from their original representation, which may reflect the physical nature of the problem, to variables that have certain desirable properties, e.g., the variables are all of similar magnitude in the region of interest. In the model program, only a linear transformation of variables has been used, which is of the form

$$\mathbf{X}_{new} = \mathbf{D}\, \mathbf{X}_{old} + \mathbf{V} \tag{2.83}$$

where **X** is the solution vector, **D** is a diagonal matrix and **V** a constant vector. Since the solution of linear model produces a reasonable initial guess for the nonlinear solution, so the elements of **D** and **V** are chosen according to the linear solution. For example, if the variable X_i represent a zonal mean component, it is expected that this variable only changes its value slightly after the iteration

procedure, e.g., only increase or decrease 20% of its initial value $X_i^{(0)}$. One possible scaling would be to define a new variable X'_i, given by

$$X'_i = \frac{X_i - X_i^{(0)}}{0.2X_i^{(0)}}$$

Thus we may choose the associated diagonal element of **D** as

$$d_{i,i} = \frac{1.}{0.2X_i^{(0)}}$$

and the associated element of **V** as

$$V_i = 5$$

For a variable X_j which represents wave component, it may lie in a larger range than X_i and then we choose

$$d_{j,j} = \frac{1}{X_j^{(0)}}$$

and

$$V_j = 1.$$

CHAPTER 3

LINEAR PRIMITIVE EQUATION MODEL

3.1 Introduction

In chapter two we have discussed the numerical techniques for solving the steady-state primitive equations governing large-scale atmospheric motions. As previously mentioned, the iteration procedure for solving the nonlinear equation system requires a reasonably good initial guess. An unrealistic initial guess may cause difficulties for the iterative algorithm. The solution of a linearized model is easily obtained and hence provides a first approximation to the solution of the nonlinear problem, which can be used as an initial guess of the nonlinear solution. At the same time a direct comparison between the linear and nonlinear responses to various forcing functions is possible. This enables us to gain more physical insight into the fundamental nature of atmospheric motions.

The perturbation method is used to simplify the complicated nonlinear system of equations. In this method all field variables are divided into two parts, a basic state portion which is assumed to be independent of longitude (and possibly time also in some problems) and a perturbation portion which is the local deviation of the field from the basic state. For example, if [u] denotes a longitudinally averaged zonal velocity and u^* is the deviation from the average, then the complete zonal

velocity field is

$$u(\lambda,\mu,\sigma) = [u](\mu,\sigma) + u^*(\lambda,\mu,\sigma). \tag{3.1}$$

Thus the inertial acceleration term in the momentum equation, $u(\partial u/a\cos\varphi\partial\lambda)$, can be written

$$u\frac{\partial u}{a\cos\varphi\ \partial\lambda} = \{[u]+u^*\}\frac{\partial\{[u]+u^*\}}{a\cos\varphi\ \partial\lambda}$$

$$= [u]\frac{\partial u^*}{a\cos\varphi\ \partial\lambda} + u^*\frac{\partial u^*}{a\cos\varphi\ \partial\lambda} \tag{3.2}$$

According to the assumptions of the perturbation theory, the second term on the right hand side of (3.2) is much smaller than the first term and therefore can be neglected.

By neglecting all terms which are nonlinear in the perturbation, the nonlinear governing equations are reduced to linear differential equations in the perturbation variables. The linear model equations derived in this way will be described in the next section. Sections 3.3 and 3.4 describe the basic state and the method of solution respectively.

3.2 Model Equations

The linearized primitive equations, corresponding to (2.12)-(2.17) in the nonlinear model, may be written

$$\frac{1}{1-\mu^2}\left\{-[U]U^{*(\lambda)}+V^*[U]^{(\mu)}\right\} + S^*[U]^{(\sigma)} + 2\Omega a\mu\ V^* - \phi^{*(\lambda)}$$

$$-R[T]q^{*(\lambda)} - a(R_f+\alpha\nabla^4)U^* = 0 \tag{3.3}$$

$$\frac{1}{1-\mu^2}\left\{-[U]V^{*(\lambda)}-2\mu[U]U^{*}\right\}-2\Omega a\mu\,U^{*}+\phi^{*(\mu)}+R[T]q^{*(\mu)}$$

$$+RT^{*}[q]^{(\mu)}+RT^{*}[q]^{(\mu)}-a(R_f+\alpha\nabla^4)\,V^{*}=0 \tag{3.4}$$

$$\frac{1}{1-\mu^2}\left\{-[U]T^{*(\lambda)}+V^{*}[T]^{(\mu)}-\kappa[T]\{U^{*(\lambda)}-V^{*(\mu)}\}\right\}$$

$$+S^{*}\left\{[T]^{(\sigma)}+\kappa(1+\sigma)[T]\right\}+\kappa[T]\,S^{*(\sigma)}$$

$$+\frac{aQ}{C_p}-a(K_t+\nu\nabla^4)\,T^{*}=0 \tag{3.5}$$

$$\int_{-1}^{1}\left\{U^{*(\lambda)}-V^{*(\mu)}+[U]q^{*(\lambda)}-V^{*}[q]^{(\mu)}\right\}d\sigma=0 \tag{3.6}$$

$$S^{*}=-\frac{1}{(1-\mu^2)(1-\sigma^2)}\int_{1}^{\sigma}\left\{U^{*(\lambda)}-V^{*(\mu)}+[U]q^{*(\lambda)}-V^{*}[q]^{(\mu)}\right\}d\sigma \tag{3.7}$$

$$(1+\sigma)\frac{\partial\phi^{*}}{\partial\sigma}=-RT^{*} \tag{3.8}$$

where a pair of square brackets indicates the longitudinal average, and a superscript asterisk indicates the local deviation from this average. Other notations have the same meaning as those in the nonlinear model of Chapter two.

In Chapter two U, V, T and q fields are represented by truncated series of orthogonal functions. The normalized Legendre polynomials and the surface spherical harmonics are chosen as the basis functions in the vertical and

horizontal directions respectively. In this linear model these field variables are divided into a basic state portion and a perturbation portion, the basic state corresponds to those components with zonal wavenumber m=0 and the perturbation portion corresponds to those components with m≠0. For example, zonal velocity $U=[U]+U^*$ is represented by

$$[U] = \sum_{k=0}^{L} \sum_{j=0}^{J+1}{}^{(2)} U_{k,0,j} P_k(\sigma) P_{0,j}(\mu) \qquad (3.9)$$

and

$$U^* = \sum_{k=0}^{L} \sum_{\substack{m=-M \\ (m\neq 0)}}^{M} \sum_{j=|m|}^{|m|+J+1}{}^{(2)} U_{k,m,j} P_k(\sigma) e^{im\lambda} P_{m,j}(\mu) \qquad (3.10)$$

The expressions for V, T and q are analogous to those for U. Since the basic state is prescribed in this model, only those spectral coefficients for perturbation are unknowns.

The truncation relation (2.34) is still employed to make the velocity field consistent with that represented by truncated series of streamfunction and velocity potential. The method for evaluating the geopotential, vertical velocity and various spatial derivatives is the same ~~to~~ as that in the nonlinear model.

3.3 Basic State

The zonal mean temperature field (Fig. 3.1) was calculated for January 1979 based on the ECMWF FGGE IIIb analysis.

The zonal means were taken on pressure surfaces. They differ insignificantly from the means taken on sigma surfaces if there is no topography assumed. The zonally averaged logarithm of surface pressure was approximately calculated by

$$[q] = \ln P_o - \frac{[h_o]}{H} \tag{3.11}$$

where $[h_o]$ is the zonally averaged topography height, $P_o = 1000$ mb and scale height H=8000 m. Then the zonal mean eastward wind component (Fig. 3.2) were determined by the following nonlinear equations

$$-\frac{\mu}{1-\mu^2}[U]^2 - 2\Omega a\mu[U] + [\phi]^{(\mu)} + R[T][q]^{(\mu)} = 0 \tag{3.12}$$

$$(1+\sigma)\frac{\partial[\phi]}{\partial\sigma} = -R[T] \tag{3.13}$$

This system of equations is solved with the aid of the transform method and Newton-Raphson iteration, the fundamentals of which have been described in Chapter two. Therefore the basic state prescribed in this linear model is well balanced.

3.4 Method of Solution

The following procedures have been taken in order to obtain a linear algebraic equation system:

a) add the diagnostic equations for vertical velocity

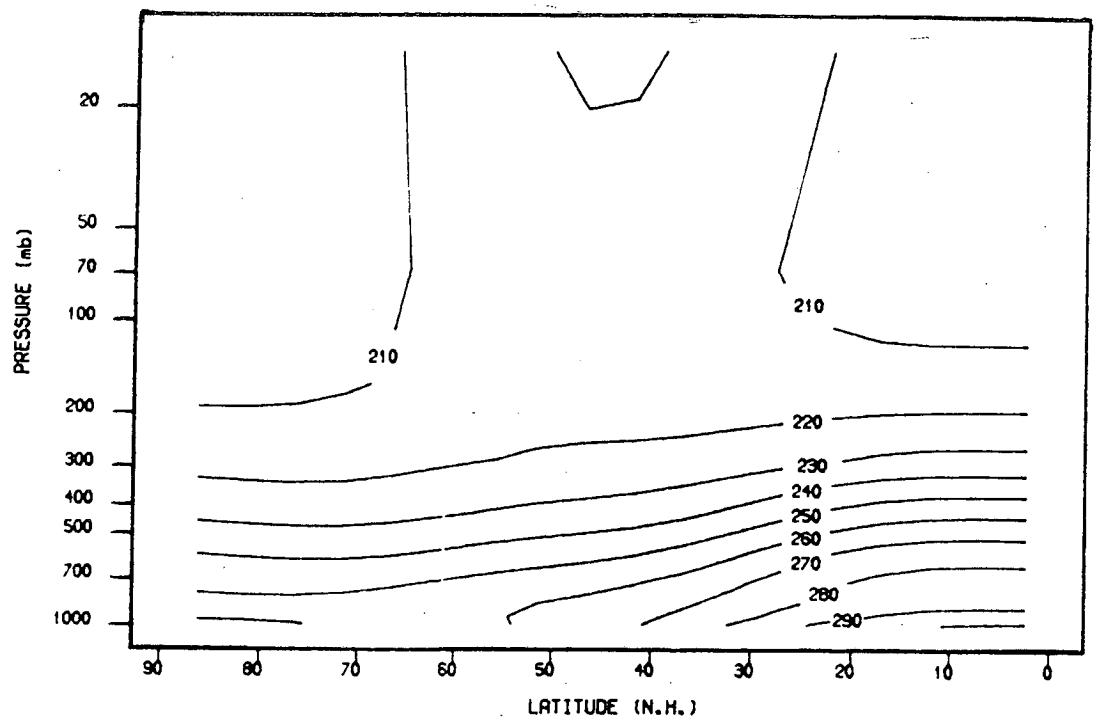

Fig.3.1 The zonal mean temperature in January 1979. Contours are at intervals of 10 K.

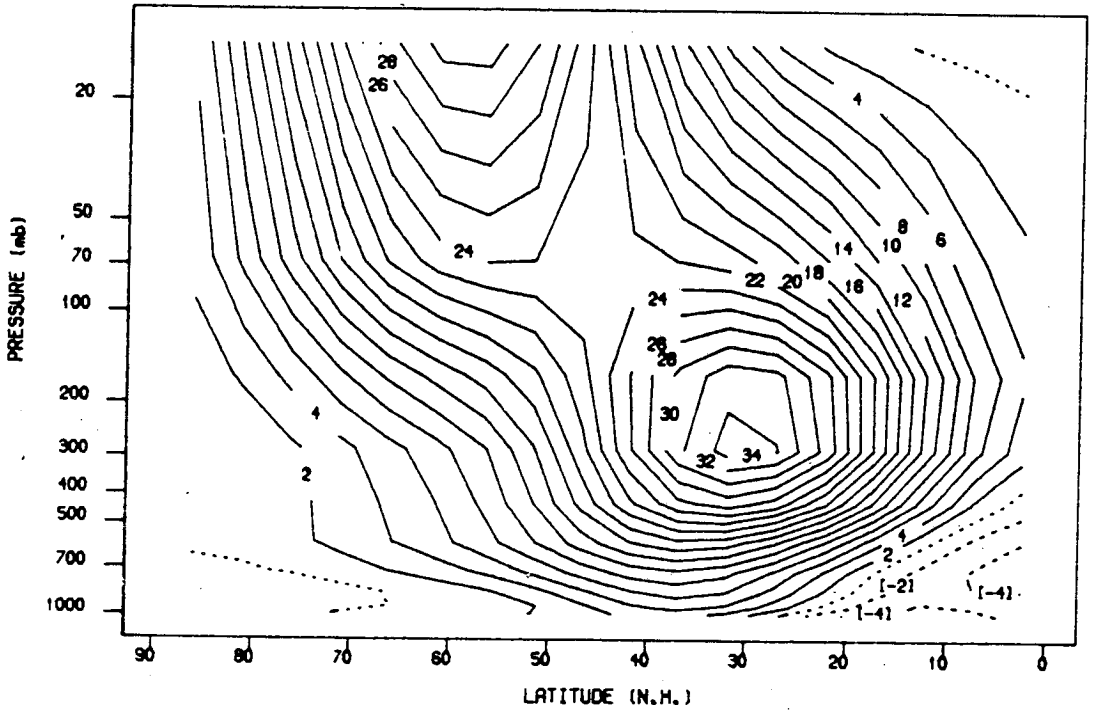

Fig.3.2 The zonal mean flow in January 1979. Contours are at intervals of 2 m s^{-1}.

and geopotential to eqs. (3.3)-(3.6) to yield a complete system for unknown variables U^*, V^*, T^*, q^* and diagnostic varibles ϕ^* and S^*;

b) insert the spectral expressions of the unknown variable fields into those equations;

c) make an orthogonal projection on the sub-spectral space generated by $P_l(\sigma)e^{im\lambda}P_{m,n}(\mu)$ with respect to various combinations of index values of l and n.

After laborious manipulation, the linear equations for each zonal wavenumber m may be written in the form

$$\begin{bmatrix} X1 & X2 & X3 & X4 \\ Y1 & Y2 & Y3 & Y4 \\ T1 & T2 & T3 & T4 \\ C1 & C2 & C3 & C4 \end{bmatrix} \begin{bmatrix} U \\ V \\ T \\ Q \end{bmatrix} = \begin{bmatrix} F1 \\ F2 \\ F3 \\ 0 \end{bmatrix} \tag{3.14}$$

where **U** is the column vector with the element $U_{k,m,j}$ ($k=0,1,\ldots\ldots,L$; $j=m,m+2,\ldots\ldots,m+J-1$.) and **V**, **T**, **Q** are similar column vectors. **0** is a zero column vector. The elements of the coefficient matrix and the other column vectors in the right side may be expressed as

$$X1_{l,n;k,j} = -\frac{1}{4}\int_{-1}^{1}\int_{-1}^{1}\left\{\frac{im}{1-\mu^2}[U] + aR_f + \frac{\alpha k^2(k+1)^2}{a^3}\right\} P_{m,j}P_kP_{m,n}P_l\,d\mu d\sigma$$

$$+\delta'_{k,o}\,im\,\frac{1}{4}\int_{-1}^{1}\int_{-1}^{1}\frac{1}{1-\mu^2}[U]^{(\sigma)}P_{m,j}K_kP_{m,n}P_l\,d\mu d\sigma \tag{3.15}$$

$$X2_{l,n;k,j} = \frac{1}{4}\int_{-1}^{1}\int_{-1}^{1}\frac{1}{1-\mu^2}[U]^{(\mu)}\,P_{m,j}P_k P_{m,n}P_l\,d\mu d\sigma$$

$$-\delta'_{k,o}\,\frac{1}{4}\int_{-1}^{1}\int_{-1}^{1}\frac{1}{1-\mu^2}[U]^{(\sigma)}H_{m,j}K_k P_{m,n}\,P_l\,d\mu d\sigma$$

$$-\delta'_{k,o}\,\frac{1}{4}\int_{-1}^{1}\int_{-1}^{1}\frac{1}{1-\mu^2}[U]^{(\sigma)}[q]^{(\mu)}\,P_{m,j}K_k P_{m,n}P_l\,d\mu d\sigma$$

$$+\delta_{k,j}\;\;\Omega a\int_{-1}^{1}\mu\;P_{m,j}P_{m,n}\,d\mu \qquad (3.16)$$

$$X3_{l,n;k,j} = \varepsilon_{k,l}\,\delta_{j,n}\;imR \qquad (3.17)$$

$$X4_{l,n;j} = \frac{im}{4}\int_{-1}^{1}\int_{-1}^{1}\left\{\frac{1}{1-\mu^2}[U]^{(\sigma)}\bar{U}^{*} - R[T]\right\}P_{m,j}P_{m,n}P_l\,d\mu d\sigma \qquad (3.18)$$

$$Y1_{l,n;k,j} = -\frac{1}{2}\int_{-1}^{1}\int_{-1}^{1}\frac{1}{1-\mu^2}\mu[U]P_{m,j}\;P_k P_{m,n}P_l\;\;d\mu d\sigma$$

$$-\delta_{k,l}\;\;\Omega a\int_{-1}^{1}\mu\;P_{m,j}P_{m,n}\;d\mu \qquad (3.19)$$

$$Y2_{l,n;k,j} = -\frac{1}{4}\int_{-1}^{1}\int_{-1}^{1}\left\{\frac{im}{1-\mu^2}[U] + aR_f + \frac{\alpha K^2(K+1)^2}{a^3}\right\}P_{m,j}P_k P_{m,n}P_l\;d\mu\;d\sigma \qquad (3.20)$$

$$Y3_{l,n;k,j} = \delta_{k,1}\, R\, \frac{1}{2} \int_{-1}^{1} [q]^{(\mu)}\, P_{m,j}\, P_{m,n}\, d\mu$$

$$+\varepsilon_{k,1}\left\{-\delta_{j,n-1}(n-1)RD_{m,n} - \delta_{j,n+1}(n+2)RD_{m,n+1}\right\}$$

(3.21)

$$Y4_{l,n;j} = \frac{R}{4} \int_{-1}^{1}\int_{-1}^{1} [T]H_{m,j}P_{m,n}P_{l}\, d\mu\, d\sigma \qquad (3.22)$$

$$T1_{l,n;k,j} = -\frac{im\kappa}{4}\int_{-1}^{1}\int_{-1}^{1}\frac{1}{1-\mu^2}[T]\, P_{m,j}P_{k}P_{m,n}P_{l}\, d\mu\, d\sigma$$

$$+\delta'_{k,o}\frac{im}{4}\int_{-1}^{1}\int_{-1}^{1}\frac{1}{1-\mu^2}\left\{[T]^{(\sigma)} + \kappa(1+\sigma)[T]\right\}$$

$$P_{m,j}K_{k}P_{m,n}P_{l}\, d\mu\, d\sigma$$

$$+\delta'_{k,o}\delta'_{k,1}\frac{im\kappa}{4}\int_{-1}^{1}\int_{-1}^{1}\frac{1}{1-\mu^2}[T]P_{m,j}G_{k}P_{m,n}P_{l}\, d\mu\, d\sigma$$

(3.23)

$$T2_{l,n;k,j} = \frac{1}{4}\int_{-1}^{1}\int_{-1}^{1}\frac{[T]^{(\mu)}}{1-\mu^2}\, P_{m,j}P_{k}P_{m,n}P_{l}\, d\mu\, d\sigma$$

$$+\frac{\kappa}{4}\int_{-1}^{1}\int_{-1}^{1}\frac{1}{1-\mu^2}[T]\, H_{m,j}P_{k}P_{m,n}P_{l}\, d\mu\, d\sigma$$

$$-\delta'_{k,o}\frac{1}{4}\int_{-1}^{1}\int_{-1}^{1}\frac{1}{1-\mu^2}\left\{[T]^{(\sigma)}+\kappa(1+\sigma)[T]\right\}$$

$$H_{m,j}K_{k}P_{m,n}P_{l}\, d\mu\, d\sigma$$

$$-\delta'_{k,o}\,\frac{1}{4}\int_{-1}^{1}\int_{-1}^{1}\frac{1}{1-\mu^2}\left\{[T]^{(\sigma)}+\kappa(1+\sigma)[T]\right\}$$
$$[q]^{(\mu)}P_{m,j}K_kP_{m,n}P_l\,d\mu\,d\sigma$$

$$-\delta'_{k,o}\delta'_{k,1}\,\frac{\kappa}{4}\int_{-1}^{1}\int_{-1}^{1}\frac{1}{1-\mu^2}[T]H_{m,j}G_kP_{m,n}P_l\,d\mu\,d\sigma$$

$$-\delta'_{k,o}\delta'_{k,1}\,\frac{\kappa}{4}\int_{-1}^{1}\int_{-1}^{1}\frac{1}{1-\mu^2}[T][q]^{(\mu)}$$
$$P_{m,j}G_kP_{m,n}P_l\,d\mu\,d\sigma \qquad (3.24)$$

$$T3_{l,n;k,j} = -\frac{1}{4}\int_{-1}^{1}\int_{-1}^{1}\left\{\frac{im}{1-\mu^2}[U]+ak_t+\frac{\nu k^2(k+1)^2}{a^3}\right\}$$
$$P_{m,j}P_kP_{m,n}P_l\,d\mu d\sigma \qquad (3.25)$$

$$T4_{l,n;j} = \frac{im}{4}\int_{-1}^{1}\int_{-1}^{1}\frac{1}{1-\mu^2}\left\{[T]^{(\sigma)}+\kappa(1+\sigma)[T]\right\}$$
$$\bar{U}^{*}P_{m,j}P_{m,n}P_l\,d\mu\,d\sigma$$
$$+\frac{im\kappa}{4}\int_{-1}^{1}\int_{-1}^{1}\frac{1}{1-\mu^2}[T]\,\bar{U}^{**}P_{m,j}P_{m,n}P_l\,d\mu d\sigma \qquad (3.26)$$

$$C1_{n;k,j} = \delta_{k,o}\,\delta_{j,n}\,im \qquad (3.27)$$

$$C2_{n;k,j} = -\delta_{k,o}\,\frac{1}{2}\int_{-1}^{1}[q]^{(\mu)}\,P_{m,j}\,P_{m,n}\,d\mu$$

$$-\,\delta_{k,o}\left\{\delta_{j,n-1}(n-1)\,D_{m,n} - \delta_{j,n+1}(n+2)\,D_{m,n+1}\right\} \tag{3.28}$$

$$C3_{n;k,j} = 0 \tag{3.29}$$

$$C4_{n;j} = \frac{im}{2}\int_{-1}^{1} U_{o,o}\,P_{m,j}\,P_{m,n}\,d\mu \tag{3.30}$$

$$F1_{l,n} = \delta_{l,o}\;im\;\phi_{s\;m,n} \tag{3.31}$$

$$F2_{l,n} = -\delta_{l,o}\left\{(n-1)\,D_{m,n}\,\phi_{s\;m,n-1} - (n+2)\,D_{m,n+1}\,\phi_{s\;m,n+1}\right\} \tag{3.32}$$

$$F3_{l,n} = -\frac{a\,Q_{l,m,n}}{C_p} \tag{3.33}$$

where

$$\bar{U}^{*} = \sum_{k=1}^{L} U_{k,o}\,K_k(\sigma) \tag{3.34}$$

$$\bar{U}^{**} = \sum_{k=2}^{L} \phi_{k,o}\,G_k(\sigma) \tag{3.35}$$

$$U_{o,o} = \frac{1}{2}\int_{-1}^{1}[U]\,d\sigma \tag{3.36}$$

$$\varepsilon_{k,l} = \frac{1}{2}\int_{-1}^{1} I_k(\sigma)P_l(\sigma)\,d\sigma \tag{3.37}$$

$$\delta_{l,k} = \begin{cases} 1 & \text{when } l=k \\ 0 & \text{otherwise} \end{cases}$$

$$\delta'_{l,k} = \begin{cases} 0 & \text{when } l=k \\ 1 & \text{otherwise} \end{cases}$$

$$l = 0,1,2,\ldots,L$$

$$n = \begin{cases} m+1,m+3,\ldots,m+J & \text{for (3.19)—(3.22) and (3.32)} \\ m,m+2,\ldots,m+J-1 & \text{for (3.15)—(3.18), (3.23)—(3.31) and (3.33)} \end{cases}$$

$$k = 0,1,2,\ldots,L$$

$$j = \begin{cases} m+1,m+3,\ldots,m+J & \text{for (3.16), (3.20), (3.24) and (3.28)} \\ m,m+2,\ldots,m+J-1 & \text{otherwise} \end{cases}$$

We can see from the above expressions that the elements of the coefficient matrix are mainly calculated by evaluating the integrals with respect to μ and σ. If the basic state is represented by truncated series, these integrals can be calculated exactly in terms of the Gauss-Legendre quadrature formula described in section 2.5.2.

The linear equation system (3.14) can be easily solved by matrix inversion, e.g., Gauss elimination. The solution for several zonal wavenumbers is just a linear superimposition of solutions for every individual wavenumber.

CHAPTER 4

DIAGNOSTICS AND EXPERIMENTAL DESIGN

Since the work of Andrews and McIntyre (1976), the Eliassen-Palm (EP) cross-sections have been increasingly used as a diagnostic both of the propagation of wave activity and of the interaction between waves and mean flow (e.g., Edmon et al., 1980; Dunkerton et al., 1981; Palmer, 1981). Since the EP flux is a zonally-averaged quantity it can provide insight only into zonally-averaged latitudinal and vertical wave propagation characteristics. Besides the EP cross-section, a three dimensional wave activity flux, which was derived by Plumb (1985) for linear, quasi-geostrophic stationary waves on a zonal flow, is used in this study to diagnose the propagation of wave activity for both linear and nonlinear model solutions. The basic definitions and calculation procedures relevant to the wave activity flux and the EP cross-section are outlined in Sections 4.1 and 4.2 respectively. Finally the experimental design is described in Section 4.3.

4.1 Stationary Wave Activity Flux

4.1.1 Basic Definitions

For plotting convenience we use 'pressure height' z as vertical coordinate, which is defined by

$$z = - H \ln \frac{P}{P_o} \qquad (4.1)$$

where H is a constant scale height and set to 8 km, and P_o is a standard constant pressure, taken to be 1000 mb. In an isothermal atmosphere, in which the temperature was equal to gH/R everywhere, z would be equal to geometric height, measured from the level at which $P=P_o$. With this coordinate, the quasi-geostrophic approximation to the wave activity flux for linear, stationary waves on a zonal flow (Plumb, 1985) may be written as

$$\mathbf{F} = \begin{bmatrix} F_\lambda \\ F_\varphi \\ F_z \end{bmatrix}$$

$$= \frac{P}{P_o} \cos\varphi \begin{bmatrix} \frac{1}{2a^2\cos^2\varphi} \left\{ \frac{\partial\Psi^*}{\partial\lambda} \frac{\partial\Psi^*}{\partial\lambda} - \Psi^* \frac{\partial^2\Psi^*}{\partial\lambda^2} \right\} \\ \frac{1}{2a^2\cos\varphi} \left\{ \frac{\partial\Psi^*}{\partial\lambda} \frac{\partial\Psi^*}{\partial\varphi} - \Psi^* \frac{\partial^2\Psi^*}{\partial\lambda\partial\varphi} \right\} \\ \frac{2\Omega^2\sin^2\varphi}{N^2 a \cos\varphi} \left\{ \frac{\partial\Psi^*}{\partial\lambda} \frac{\partial\Psi^*}{\partial z} - \Psi^* \frac{\partial^2\Psi^*}{\partial\lambda\partial z} \right\} \end{bmatrix}$$

(4.2)

where Ψ is the streamfunction for nondivergent geostrophic flow, an asterisk indicates deviation from the zonal mean, Ω the angular velocity of the earth and N the buoyancy frequency.

The wave activity flux **F** exhibits all the advantages of the EP flux as an indicator of the propagation of wave activity. Plumb (1985) summarized the properties of **F** as the following:

a) **F** is a conservable measure of the flux of wave activity. This means that **F** is nondivergent for steady, conservative linear waves.

b) For westerly flows, the convergence of **F** indicates the piling-up of wave activity, while divergence of **F** indicates its export.

c) In the limit of almost-plane waves, **F** is a phase-independent quantity which is parallel to the group velocity.

d) If zonal averages are taken, **F** reduces to the EP flux, except for the addition of a zonal component which is of no particular consequence for the zonally-averaged case.

e) The divergence of **F**, and therefore the generation or dissipation of wave activity, is directly related to nonconservative effects or nonlinerity. In addition, boundaries may also be sources or sinks of the flux.

It is worth noting that the conservation relation for wave activity (Plumb, 1985) was based on a linearized equation system for small perturbations to a steady zonal flow, but we may formally render it valid at finite amplitude by incorporating nonlinear effects into the term which originally represents sources and sinks of potential vorticity due to nonconservative effects. This suggests that a comparison of wave activity fluxes evaluated from linear solution and from nonlinear solution may contribute to diagnoses of nonlinear effects.

4.1.2 Evaluation Procedure

The wave activity flux is evaluated by using the formula (4.2) where all derivatives are taken on pressure height surface, i.e., isobaric surface. Therefore a computational grid on 9 vertical levels with pressure equal to 850, 700, 500, 400, 300, 250, 200, 150 and 100 mb, is used for evaluating the flux. On each level the grid consists of the intersections of 32 equally spaced meridians and 36 Gaussian latitudes, thus the horizontal derivatives may be evaluated by a spectral method similar to that described in Section 2.3.3. The calculation procedure is outlined as follows:

(1) Calculate the velocity components U and V at grid points by using (2.28) and (2.29) where σ is not only a function of P but also a function of λ and φ.

(2) Calculate the streamfunction Ψ which is represented by

$$\Psi = \sum_{m=-M}^{M} \sum_{j=|m|+1}^{|m|+J(2)} \Psi_{m,j} e^{im\lambda} P_{m,j}(\mu) \qquad (4.3)$$

where the spectral coefficients

$$\Psi_{m,j} = -\frac{a}{j(j+1)} \frac{1}{4\pi} \int_{-1}^{1} \int_{0}^{2\pi} \frac{1}{1-\mu^2} \left[U(\mu) + V(\lambda) \right] e^{-im\lambda} P_{m,j}(\mu) \, d\lambda d\mu \qquad (4.4)$$

Since some grid points on the lowest one or two levels may be located under the ground if topography is inserted into the model, an approximation is made for simplicity: if the value of the integrand at a grid point is unknown, it will

be dropped out from the summation of the Fourier transformation and then the total number of grid points along that latitude circle, by which the summation is divided (see, e.g., (2.73)), is decremented by one correspondingly.

(3) Calculate the wave activity flux by using (4.2).

4.2 EP Cross-Section

With the pressure height z as vertical coordinate, the quasi-geostrophic approximation to the Eliassen-Palm (EP) wave flux may be defined as

$$\mathbf{E} = \begin{bmatrix} E_\varphi \\ E_z \end{bmatrix} \tag{4.5}$$

where

$$E_\varphi = \varrho_o \exp(-\frac{z}{H}) a^{-1} \left[\frac{\partial \Psi^*}{\partial \lambda} \frac{\partial \Psi^*}{\partial \varphi}\right] \tag{4.5a}$$

$$E_z = \varrho_o \exp(-\frac{z}{H}) 4\Omega^2 \sin^2\varphi N^{-2} \left[\frac{\partial \Psi^*}{\partial \lambda} \frac{\partial \Psi^*}{\partial z}\right] \tag{4.5b}$$

Here square brackets denote zonal mean and

$$\varrho_o = \frac{P_o}{gH} \tag{4.6}$$

is the standard density. This definition is consistent with that of Dunkerton et al. (1981), but slightly different from that of Edmon et al. due to the use of z coordinate defined by (4.1).

As mentioned in the last section, if zonal averages are taken, F_φ and F_z reduce to E_φ and E_z respectively. According to the definitions (4.2) and (4.5) we have

$$\begin{cases} E_\varphi = \varrho_o \; a \; [F_\varphi] \\ E_z = \varrho_o \; a \; [F_z] \end{cases} \tag{4.7}$$

where brackets denote zonal mean and the factor $\varrho_o a$ is simply a constant.

EP flux has the fundamental advantage that its divergence

$$\nabla \cdot \mathbf{E} = \frac{1}{a \cos\varphi} \frac{\partial}{\partial \varphi}(E_\varphi \cos\varphi) + \frac{\partial}{\partial z}(E_z) \tag{4.8}$$

is zero under 'nonacceleration conditions' (steady, conservative waves on a steady mean flow). Thus an EP cross-section, in which **E** is represented by arrows and $\nabla \cdot \mathbf{E}$ by contours, displays information not only about the net direction of wave propagation, but also about the locations where nonacceleration conditions are violated.

The graphical conventions follow, in essence, those of Edmon et al. (1980), with appropriate modifications for the pressure height coordinate. The volume element for integrating (4.8) over a zonally symmetric portion of the atmosphere is

$$dv = 2\pi a^2 \cos\varphi \, d\varphi \, dz \tag{4.9}$$

From (4.8) and (4.9)

$$\int \nabla \cdot \mathbf{E} \, dv = \int \Delta \, d\varphi \, dz \tag{4.10}$$

where

$$\Delta = \frac{\partial}{\partial\varphi}\left\{2\pi a \cos\varphi\ E_\varphi\right\} + \frac{\partial}{\partial z}\left\{2\pi a^2 \cos\varphi\ E_z\right\} \qquad (4.11)$$

Δ is the natural form of the divergence of **E** for contouring in the (φ,z) plane and the arrows will be drawn with horizontal and vertical components proportional to the quantities within the curly brackets in (4.11), that is

$$\left\{\hat{E}_\varphi,\ \hat{E}_z\right\} = 2\pi a^2 \cos\varphi \left\{a^{-1}\ E_\varphi,\ E_z\right\}$$

$$= 2\pi a^3\ \varrho_o \cos\varphi \left\{a^{-1}[F_\varphi], [F_z]\right\} \qquad (4.12)$$

In order to calculate the horizontal and vertical arrow components as measured on the diagram, $[F_\varphi]$ and $[F_z]$ are evaluated in $m^2 s^{-2}$ and then multiplied by $d_1 a^{-1}\cos\varphi$ and $d_2\cos\varphi$ respectively, where d_1 and d_2 are scale factors proportional to the distances occupied on the diagram by 1 radians or 57.3° of latitude, and one metre of pressure height. Thus the eq. (4.10) implies that the pattern of arrows will look nondivergent in the (φ,z) plane if and only if $\nabla\bullet\mathbf{E}$ is zero.

4.3 Experimental Design

4.3.1 Forcing Functions

Orographic forcing is included into the model by means of the lower boundary condition (2.10). Thermal forcing is presented explicitly in the thermodynamic equation. In Chapter 5 some idealized cases of forcing function are tested for both linear and nonlinear models. The aim of these tests is not only to check if the program codes are correct, ~~it~~ they also provide a preliminary understanding of the model atmosphere behaviour. Then the response of the model atmosphere to actual topography or/and diabatic heating in January is investigated. The Northern Hemisphere smoothed topography on the FGGE grid is used to obtain a spectral representation of the actual topography. The vertically integrated heating rates for January 1979 prepared from NMC FGGE Level IIIa operational data set and also ECMWF FGGE Level IIIb analysis by Johnson et al. (1985) are used as the horizontal distribution of diabatic heating and its vertical variation is given by

$$\begin{cases} \left[\sin \dfrac{\pi(\sigma-\sigma_1)}{(\sigma_2-\sigma_1)} \right]^2, & \sigma_1 < \sigma < \sigma_2 \\ 0 \qquad \text{otherwise} \end{cases} \tag{4.13}$$

where $\sigma_1 = -0.84$ and $\sigma_2 = 1$. This vertical profile of diabatic heating is similar to those used by Grose et al. (1984) and Simmons (1982) (The latter discussed the sensitivity to the vertical distribution.)

4.3.2 Dissipation Parameters

It is necessary to include some appropriate dissipation processes in a steady-state model in order to remove the sensitivity implied by resonance. This is done in this model by means of Newtonian cooling and Rayleigh friction with spatially varying decay rates. The vertical distribution of Rayleigh friction coefficient, R_f, and Newtonian cooling coefficient, K_t, are similar in nature to those of Simmons (1982). R_f was set to $(20\ d)^{-1}$ above $\sigma=0.6$ but increased below this level linearly with pressure to reach a value of $(2\ d)^{-1}$ at the surface ($\sigma=1$). This is expected to represent boundary layer drag in the absence of an Ekman layer in the model. K_t was set to $(20\ d)^{-1}$ below $\sigma=-0.6$ but increased linearly above this level with the logarithm of the pressure to reach a value of $(5.3\ d)^{-1}$ at the highest model level ($\sigma=-0.9491$). These dissipations are enhanced in the polar region by multiplying the above coefficients by $(\cos\varphi_o/\cos\varphi)^2$ when φ is greater than φ_o, where φ_o was set to 60^0. This is intended to remove the resonance which may occur in polar region when some wave activity source region is located in high latitude (tests using the nonlinear model showed that insufficient dissipation in the polar region may lead to failure of the iteration procedure convergence).

Singular-line dissipation is included by increasing the above decay rates to $\{2([u]/\cos\varphi)^2\ d\}^{-1}$, where [u] is the zonal mean flow in ms^{-1}, whenever they are less than this

value.

Both the coefficients of biharmonic horizontal diffusion, α and ν, were set to 1.169×10^{17} $m^4 s^{-1}$. Linear diffusion of the form $\alpha\nabla^4$ is very simply included in a spectral model and has a known scale selectivity. The e-folding diffusive time at total wavenumber n (the order of the associated Legendre function $P_{m,n}(\mu)$ in the spectral expansion) is given by

$$\tau(n) = \frac{a^4}{\alpha n^2 (n+1)^2} \qquad (4.14)$$

where a is the radius of the earth. Table 4.1 shows the scale selectivity of the diffusion formulation used in the model.

Table 4.1: e-folding dissipation time as a function of total wavenumber

n	τ (day)
1	53778.9
2	5975.4
3	1493.9
4	537.8
5	239.0
6	121.9
7	68.6
8	41.5
9	26.6
10	17.8
11	12.3
12	8.8
13	6.5
14	4.9

All dissipation parameters described above have been used for both linear and nonlinear models in order to make their results more comparable. The value of these parameters was set firstly according to Simmons (1982) and Grose et al. (1984) and tested for actual topography and thermal forcing, a small modification, i.e., the enhanced dissipation in the polar region, was then chosen to enable the model solution to be a close approximation to the observed climatological stationary waves in the winter season and meet the requirement of convergence of the nonlinear model. Then these parameters are fixed for all other experiments except those for sensitivity tests described in Section 5.1.3.

4.3.3 Graphics

The following diagrams have been plotted for each experiment but only some of them are shown in this thesis:

1) Contour maps for topography height and horizontal variation of diabatic heating rate.
2) Contour maps for streamfunction, which represents the rotational components of stream field, with horizontal velocity vectors superimposed at 700, 500, 200 and 100 mb levels.
3) Wave activity flux maps at 850, 700, 500 and 200 mb, in which arrows represent horizontal component and contours vertical component.
4) Latitude-height projection of **F** at selected

longitudes, usually through centre of the forcing.

5) Longitude-height projection of **F** at selected latitudes, usually through centre of forcing.

6) EP cross-section.

7) Longitudinal cross-sections for the departure from the zonal mean of geopotential height and vertical velocity in the pressure system which is calculated by

$$\omega \equiv \frac{dP}{dt}$$

$$= \frac{u}{a\cos\varphi}\left[\frac{\partial P}{\partial \lambda}\right]_{\sigma} + \frac{v}{a}\left[\frac{\partial P}{\partial \varphi}\right]_{\sigma} + \dot{\sigma}\frac{\partial P}{\partial \sigma}$$

$$= \frac{\sigma+1}{2}\left\{\frac{u}{\cos\varphi}\frac{\partial P_s}{\partial \lambda} + \frac{v}{a}\frac{\partial P_s}{\partial \varphi}\right\} + \frac{\dot{\sigma} P_s}{2} \qquad (4.15)$$

or, using the notations introduced in Chapter 2 it can be written

$$\omega = \frac{\exp(q)}{2a}\left\{\frac{1+\sigma}{1-\mu^2}\left(Uq^{(\lambda)} - Vq^{(\mu)}\right) + (1-\sigma^2)\,S\right\} \qquad (4.16)$$

CHAPTER 5

PRELIMINARY EXPERIMENTS FOR BOTH MODELS

Before we discuss the response of a model atmosphere to forcing by the actual Northern Hemispheric topography and the mean diabatic heating in January 1979, we examine in this chapter the response of a model atmosphere to forcing by idealized topography or diabatic heating. These preliminary experiments for both linear and nonlinear models may provide us an elementary understanding of the model atmosphere behaviour.

In section 5.1 we consider the case in which there is no stationary heat source included in the model and an idealized large scale mountain in middle latitudes is assumed. The results of a sensitivity test for different values of dissipation parameters are also described. In section 5.2 a similar idealized mountain is moved from mid-latitudes to high latitudes, this is intended to simulate the effects of the Greenland Plateau on the hemispheric stationary waves. Finally sections 5.3 and 5.4 discuss the response to an idealized thermal forcing where no topography is inserted into the model and the diabatic heating region is located in middle and low latitudes respectively.

5.1 Response to a Large Scale Mountain in Mid-latitudes

In this experiment there is no stationary asymmetrical heat source included in the model and the stationary waves are induced only by an idealized large scale mountain in mid-latitudes. The surface geopotential is specified by

$$\phi_s = \begin{cases} g_o A \left[\sin\frac{\pi(\varphi-\varphi_1)}{(\varphi_2-\varphi_1)} \sin\frac{\pi(\lambda-\lambda_1)}{(\lambda_2-\lambda_1)} \right]^2, & \varphi_1<\varphi<\varphi_2,\ \lambda_1<\lambda<\lambda_2 \\ 0 \quad \text{otherwise} \end{cases} \tag{5.1}$$

where $g_o \equiv 9.80665\ ms^{-2}$ is the global average of the acceleration due to gravity at mean sea level. Before inserting this topography into the model, it is transformed into an expansion in truncated series similar as (2.30) with truncation indices M=3, J=11 and L=4. This is illustrated in Fig. 5.1 for the values A=2500 m, $\varphi_1=20^\circ$, $\varphi_2=50^\circ$, $\lambda_1=30^\circ$ and $\lambda_2=150^\circ$.

5.1.1 Linear Solution

The perturbation stream fields at the 700 mb and 200 mb levels for the linear response to an idealized large scale mountain in mid-latitudes (as shown in Fig. 5.1) are displayed in Figs.5.2 and 5.3 respectively. At 700 mb there is an anticyclonic circulation in the upslope region to the northwest of the mountain top and a cyclonic circulation in the downslope region to the northeast of the mountain top

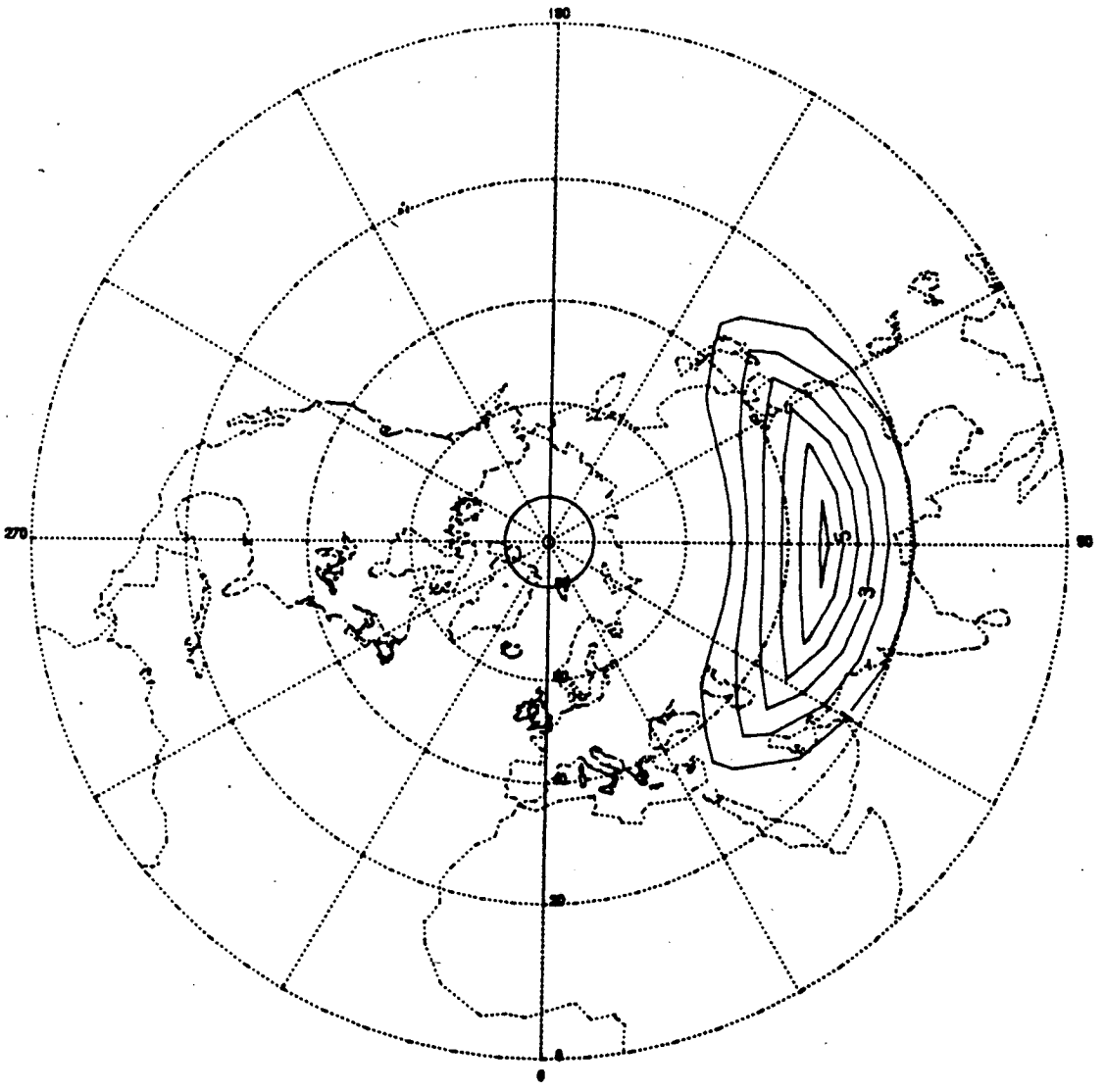

Fig. 5.1 The horizontal distribution of surface geopotential height, expressed as truncated series of spherical harmonics, for an idealized mountain in the mid-latitudes. Contours represent the geopotential height/(300m). The zero contours have been suppressed for clarity.

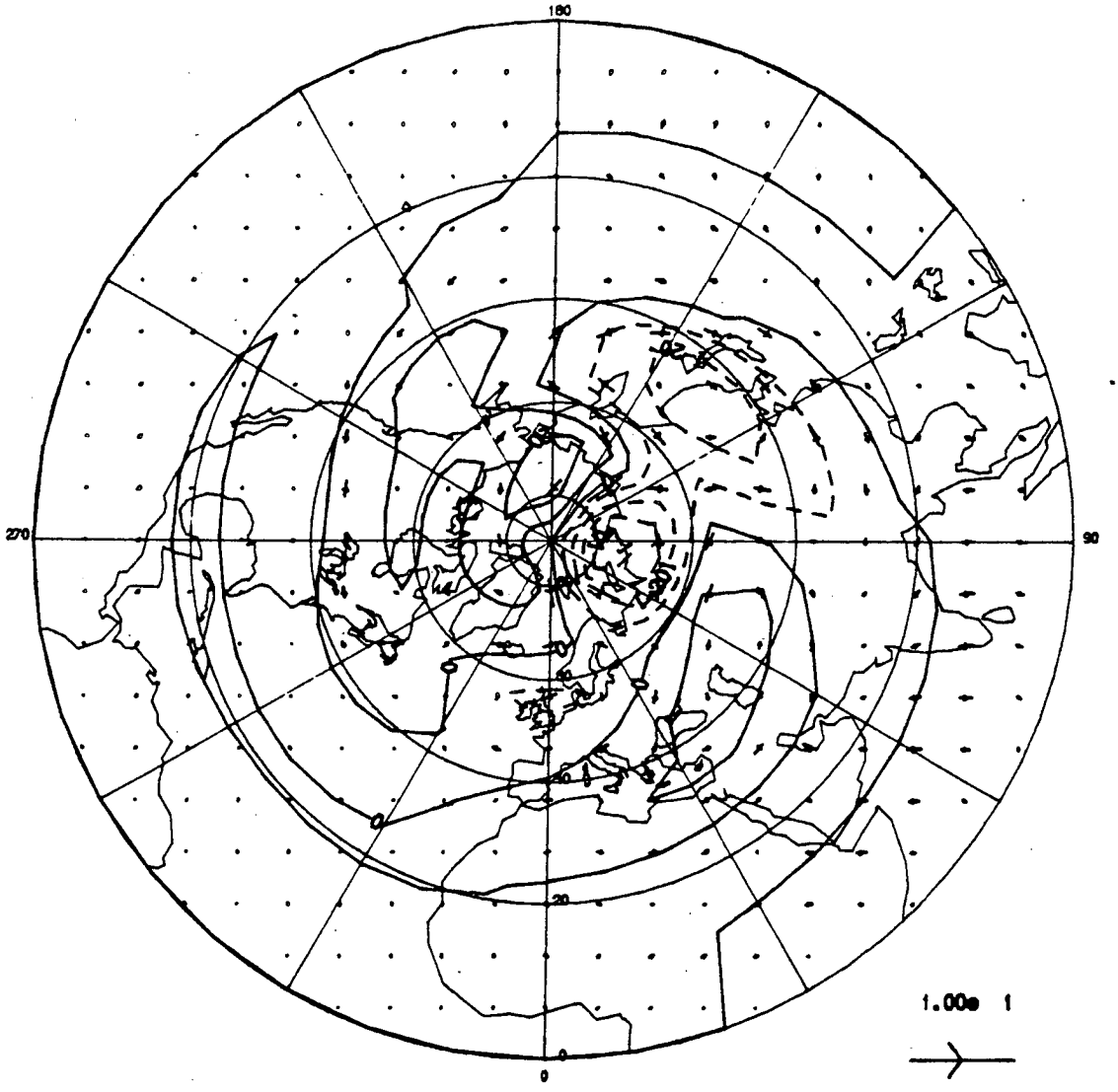

Fig. 5.2 700 mb perturbation stream field for the linear response to an idealized topography in mid-latitudes. Contours represent the perturbation streamfunction/($10^5 m^2 s^{-1}$) with an interval of 10 units. The negative contours are dashed. Vectors represent the horizontal velocity. An arrow scale for velocity in units of ms^{-1} is indicated at bottom right, where exponents are plotted as a character @ followed by an integer (e.g., 1.00@1 ≡ 1.00×10^1).

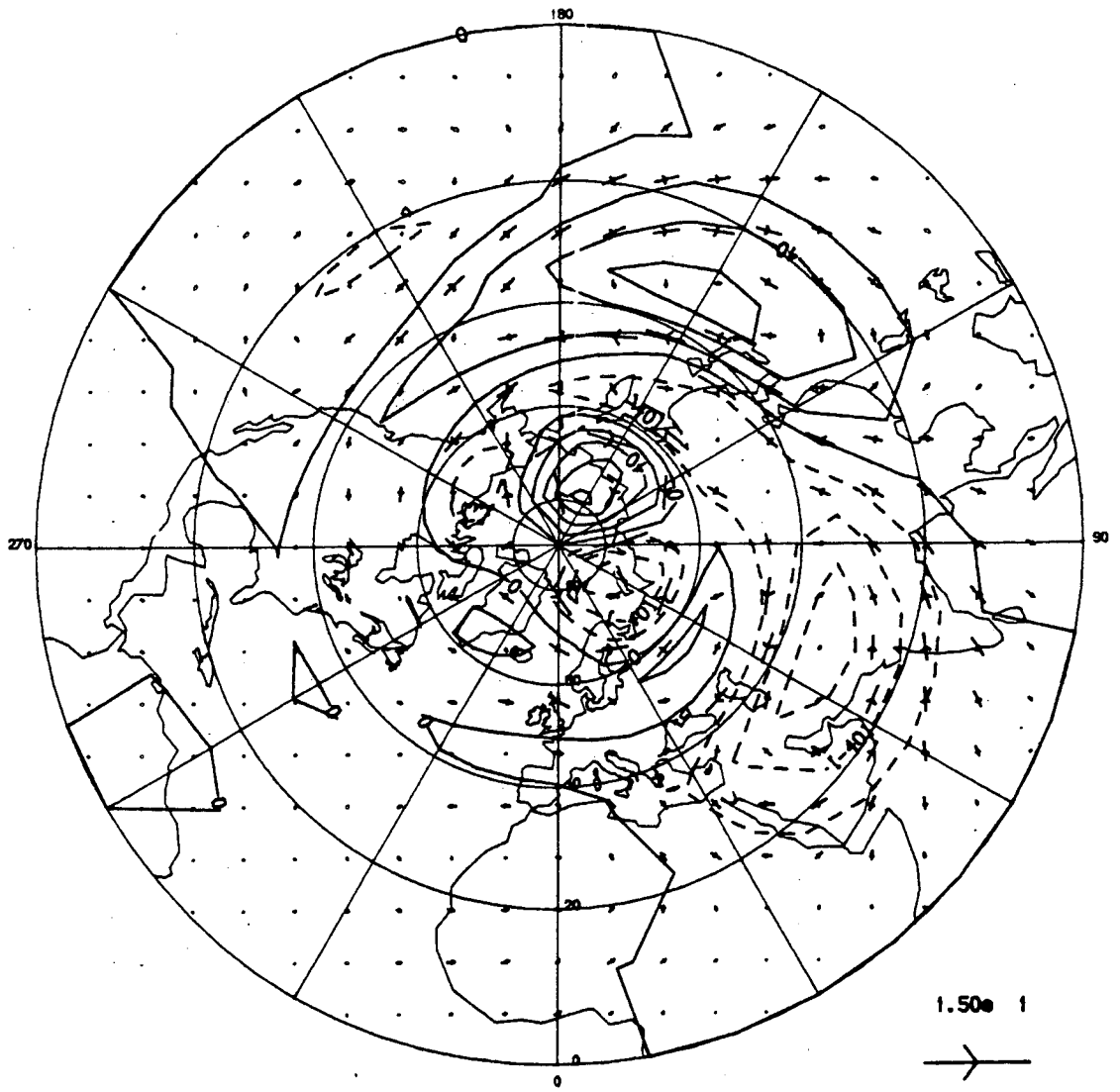

Fig. 5.3 As Fig. 5.2, but for 200 mb. Contours are at intervals of 20 units.

(it is worth noting that the westerly winds poleward of 30°N, see Fig. 3.2, produce an upslope region to the west of the mountain, whereas the low level easterly winds on the equatorward side produce an upslope region to the east of the mountain). Another anticyclonic circulation is located farther downstream and extends to high latitudes. At 200 mb the subtropical response is much stronger than at the lower level, an anticyclonic circulation is centred 60° east of the mountain top while a cyclonic circulation is centred 30° west of the mountain top. The rotational (nondivergent) component of velocity field is dominant at middle and high latitudes, whereas the divergent (irrotational) component mainly concentrates in the tropical region. The longitudinal cross-sections of perturbation geopotential height and vertical velocity at 35°N are shown in Figs. 5.4 and 5.5. In Fig. 5.4 the upstream ridge and the downstream trough of the mountain appear clearly at the low levels. At the upper levels a major trough is found over the mountain associated with a ridge to the east. All these systems are inclined slightly to the west with increasing height up to the tropopause. In Fig. 5.5 the vertical velocity field is dominated by upward motion (ω is negative) over and to the west of the mountain and a downward motion (ω is positive) to the east of the mountain. This is consistent with the β-plane channel barotropic theory (Hoskins and Karoly, 1981), which says for long wavelengths the β term in the vorticity equation is dominant and there is a cyclone over the mountain ridge.

Figs. 5.6 and 5.7 illustrate the wave activity flux **F** at the 850 mb and 500 mb levels. The major feature highlighted by these figures is a wavetrain propagating upward, eastward and predominantly equatorward from the northern slope of the mountain. At low level there is also a smaller and less intense wavetrain propagating poleward from the northwest and the southeast of the mountain. As explained by Plumb (1985) the divergence of **F** from a topographic source does not necessarily coincide with the highest topography. The locations of the apparent origins of the wavetrain extend to some distance downstream of the mountain. This can be seen more clearly from the longitudinal section of **F** at 45°N (not shown here). The latitudinal and vertical components of **F** reduce to EP flux when they are zonally averaged. The corresponding EP cross-section is plotted in Fig. 5.8, which shows the greatest EP flux is near the lower surface in the middle latitudes (40-60°N). The strongest convergence of the EP flux is at the same location, whereas a secondary maximum convergence is found in the middle troposphere at high latitudes (about 75°N).

5.1.2 Nonlinear Solution

Comparing the perturbation stream field for the nonlinear solution (Figs. 5.9 and 5.10) with the counterpart for the linear solution, we find the obvious difference is in the sub-tropical region at the lower level and in high

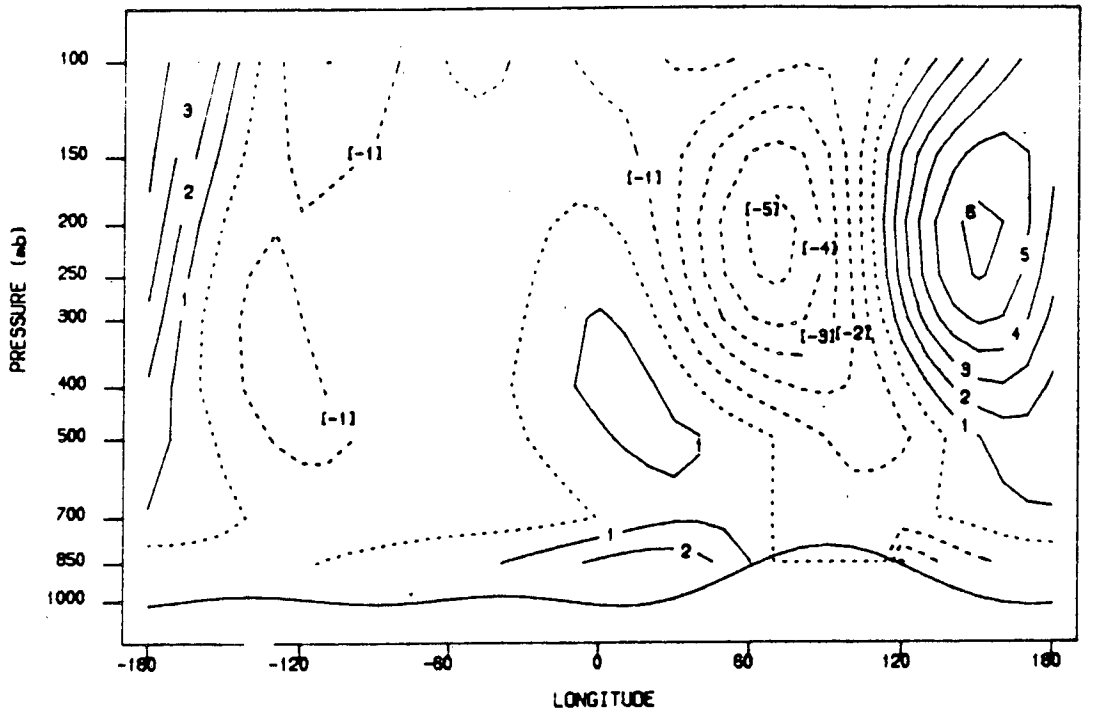

Fig. 5.4 Longitudinal cross-section of perturbation geopotential height at 35°N for the linear response to an idealized topography in mid-latitude. Contour interval is 1 dam. The surface pressure at 35 °N is superimposed.

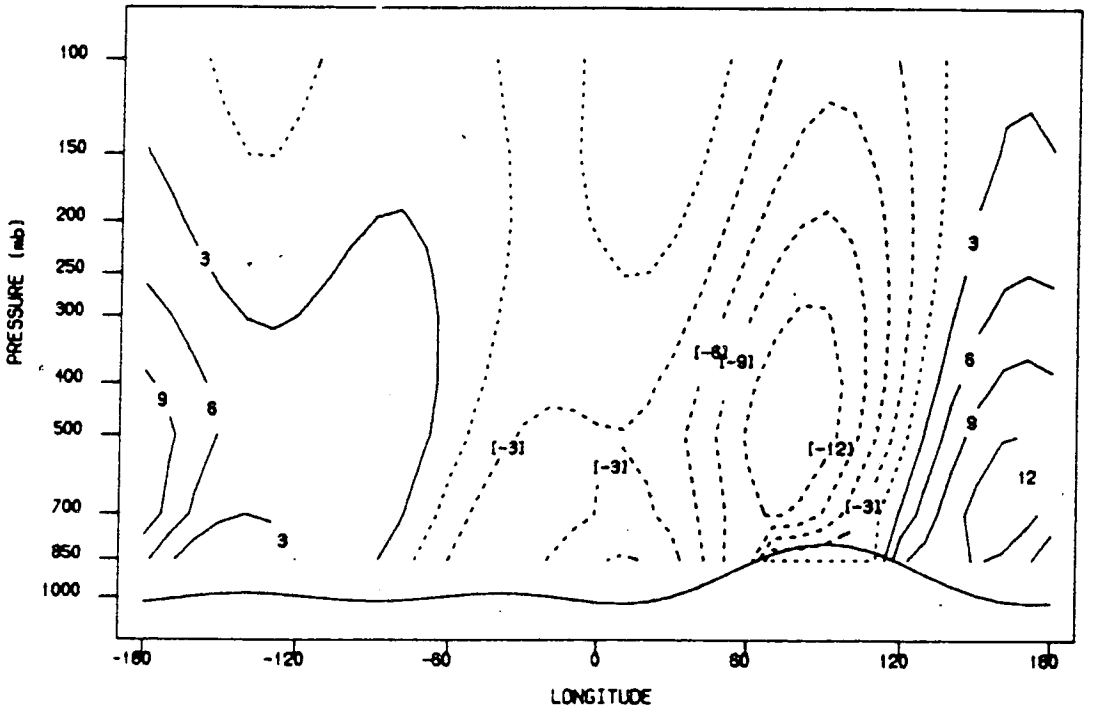

Fig. 5.5 As Fig. 5.4 but for perturbation vertical velocity ω. Contour interval is 3 mb day^{-1}.

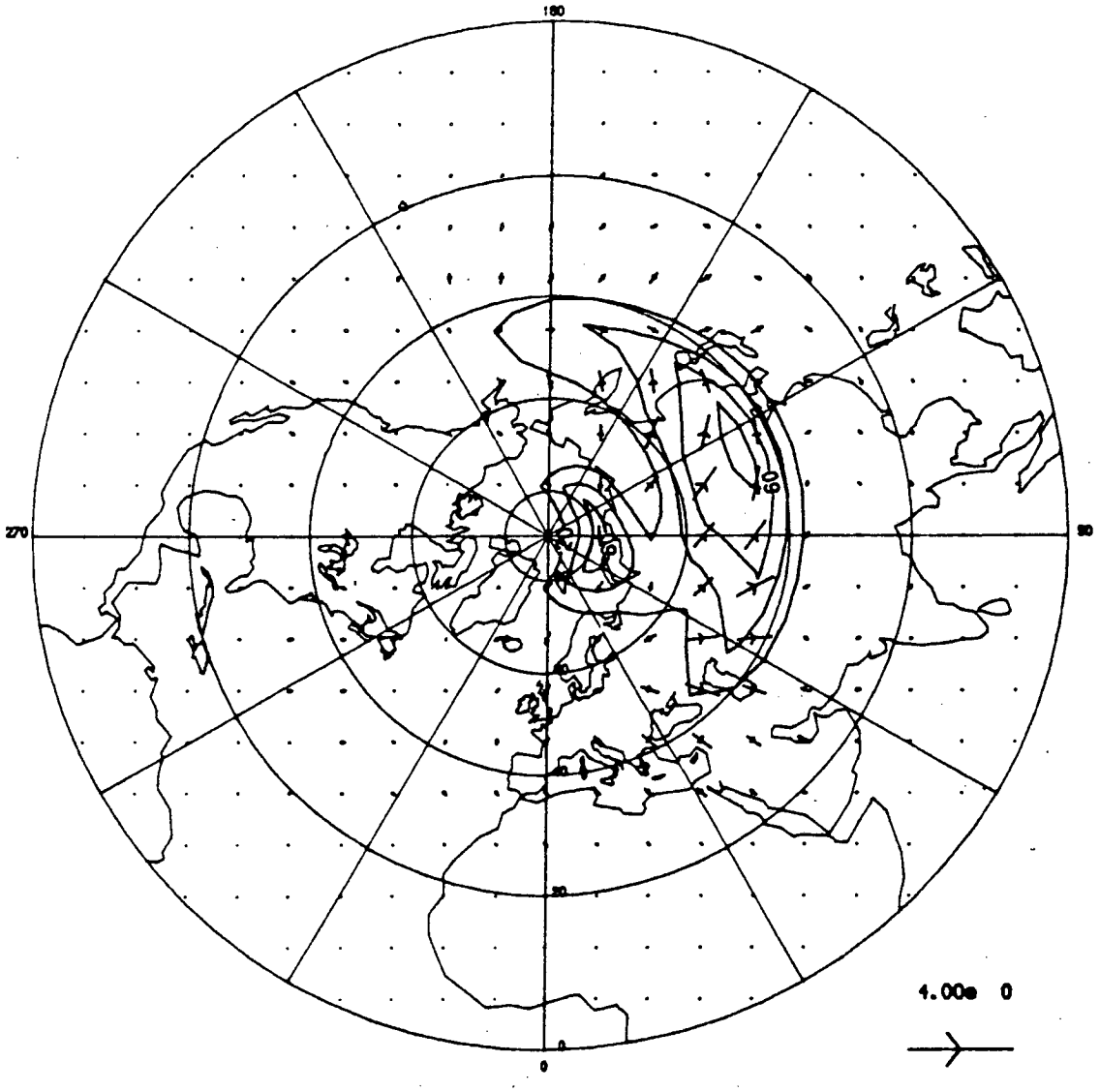

Fig. 5.6 Wave activity flux **F** at 850 mb for the linear response to an idealized topography in mid-latitudes. Contours denote the vertical component $F_z/(10^{-3} m^2 s^{-2})$ with an interval of 20 units (positive upward). Arrows denote the horizontal component with a scale plotted at bottom right (unit: $m^2 s^{-2}$).

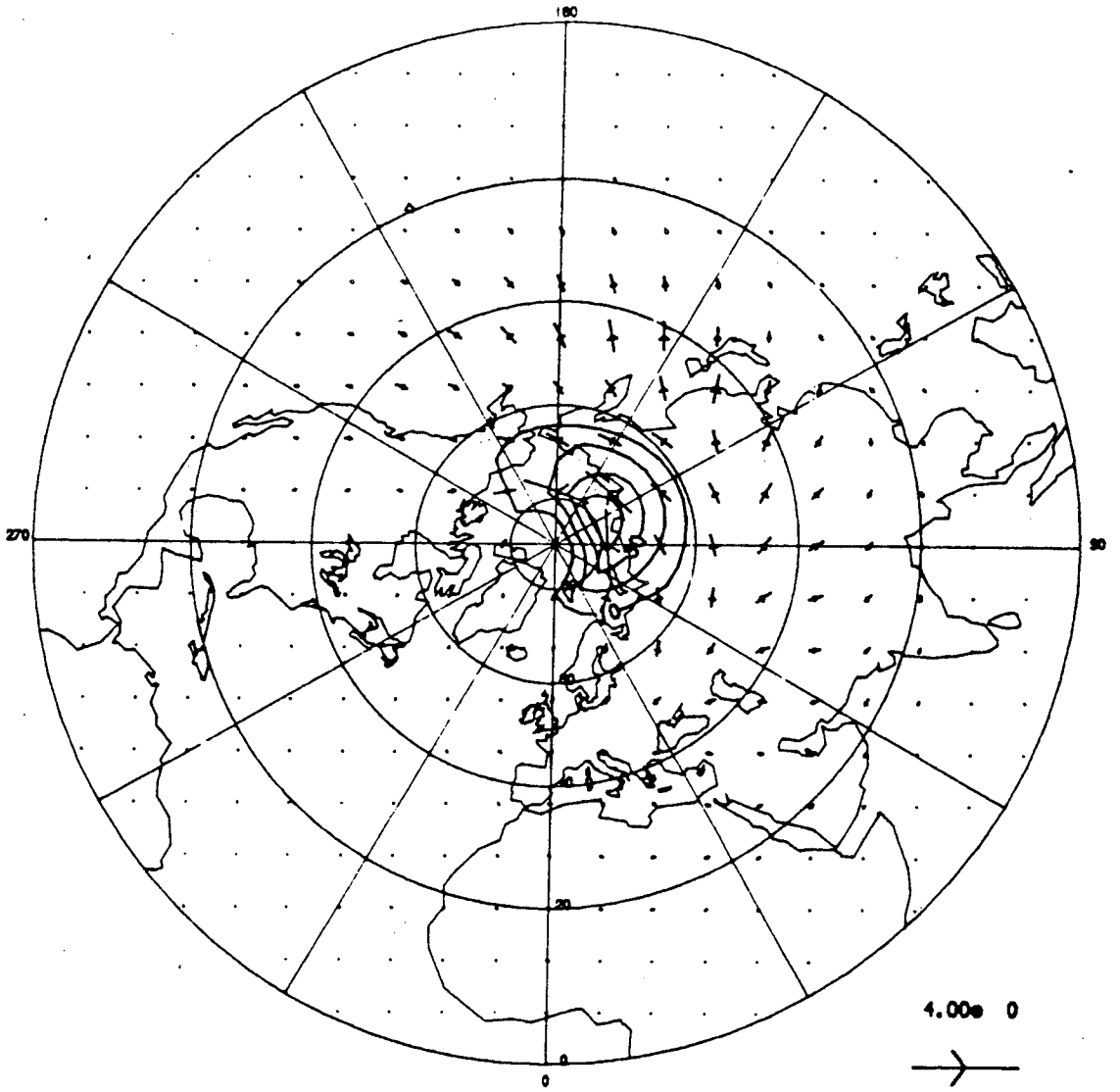

Fig. 5.7 As Fig. 5.6, but for 500 mb. Contours are at intervals of 10 units.

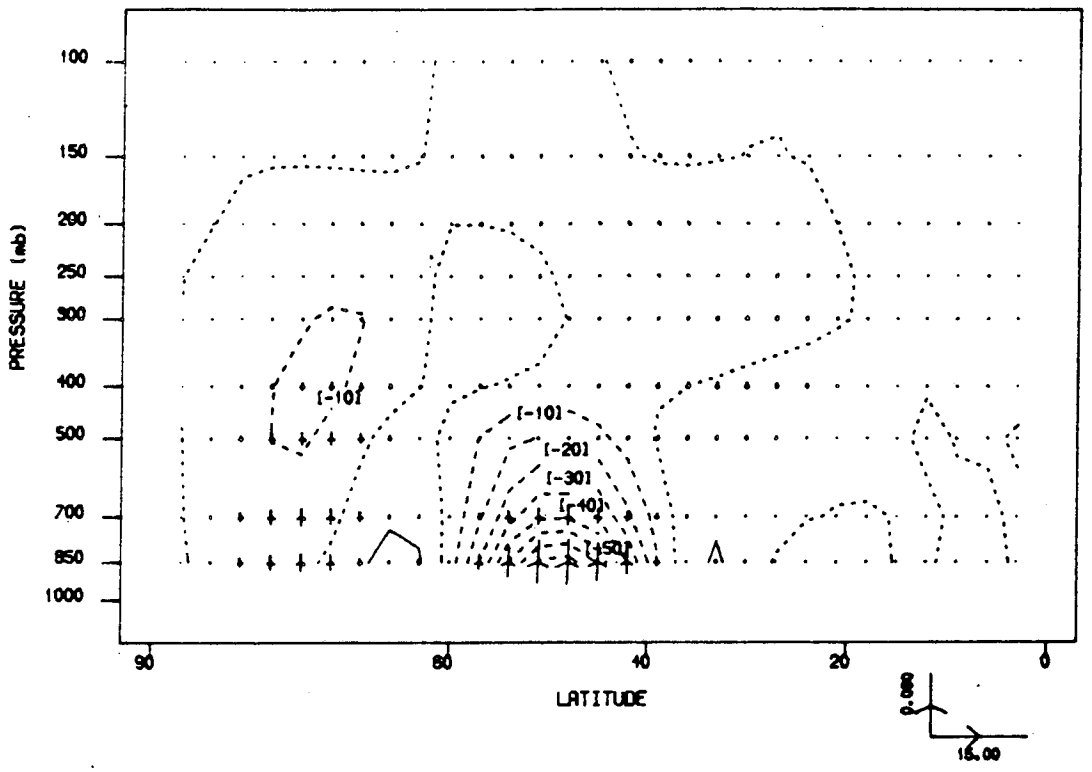

Fig. 5.8 EP cross-section for the linear response to an idealized topography in mid-latitudes. An arrow scale is plotted at bottom right. The numerical values marked on the scales are to be multiplied by $2\pi a^2 \rho_o$ $m^2 s^{-2}$ for $\hat{E}_\varphi$, and $2\pi a^3 \rho_o$ $m^2 s^{-2}$ for $\hat{E}_z$ respectively. The contours represent the quantity Δ defined by (4.11); the numerical values marked on the contours to be multiplied by $2\pi a^3 \rho_o \times 10^{-7}$ ms^{-2}. The contour interval is 10 units.

latitudes at the upper level. If we consider the assumptions of the perturbation theory (see, e.g., Holton, 1979) and note that the basic state flow (Fig. 3.2) is weak in the polar and tropical regions as well as in the lower troposphere at mid-latitudes, we may expect that the orographically forced disturbances should be highly nonlinear in these regions due to the weak basic flow. At 700 mb low latitudes the upslope anticyclonic circulation and the downslope cyclonic circulation are evident for the nonlinear solution (Fig. 5.9) but their linear counterparts is not clear. On the other hand at 200 mb the high latitude response for the nonlinear solution is significantly weakened. The longitudinal cross-section of geopotential height at 35°N for the nonlinear solution (Fig. 5.11) is similar to that for linear solution, but the upper level response is greatly weakened and the westward tilt of phase with height occurs only below 300 mb level. In addition the nonlinear solution has a weaker vertical velocity field in the same section (Fig. 5.12). These results suggest that the nonlinearity for the response to this idealized large scale mountain is significant, especially in high or low latitudes. This can be seen also in the wave activity flux maps (Fig. 5.13-5.14) and EP cross-section (Fig. 5.15).

The first point to note from Fig. 5.15 is that the vertical component of EP flux in high latitudes is substantially weakened compared with the linear results, especially at low levels. Another interesting feature shown by Fig. 5.15 is that there is an apparent source of EP flux

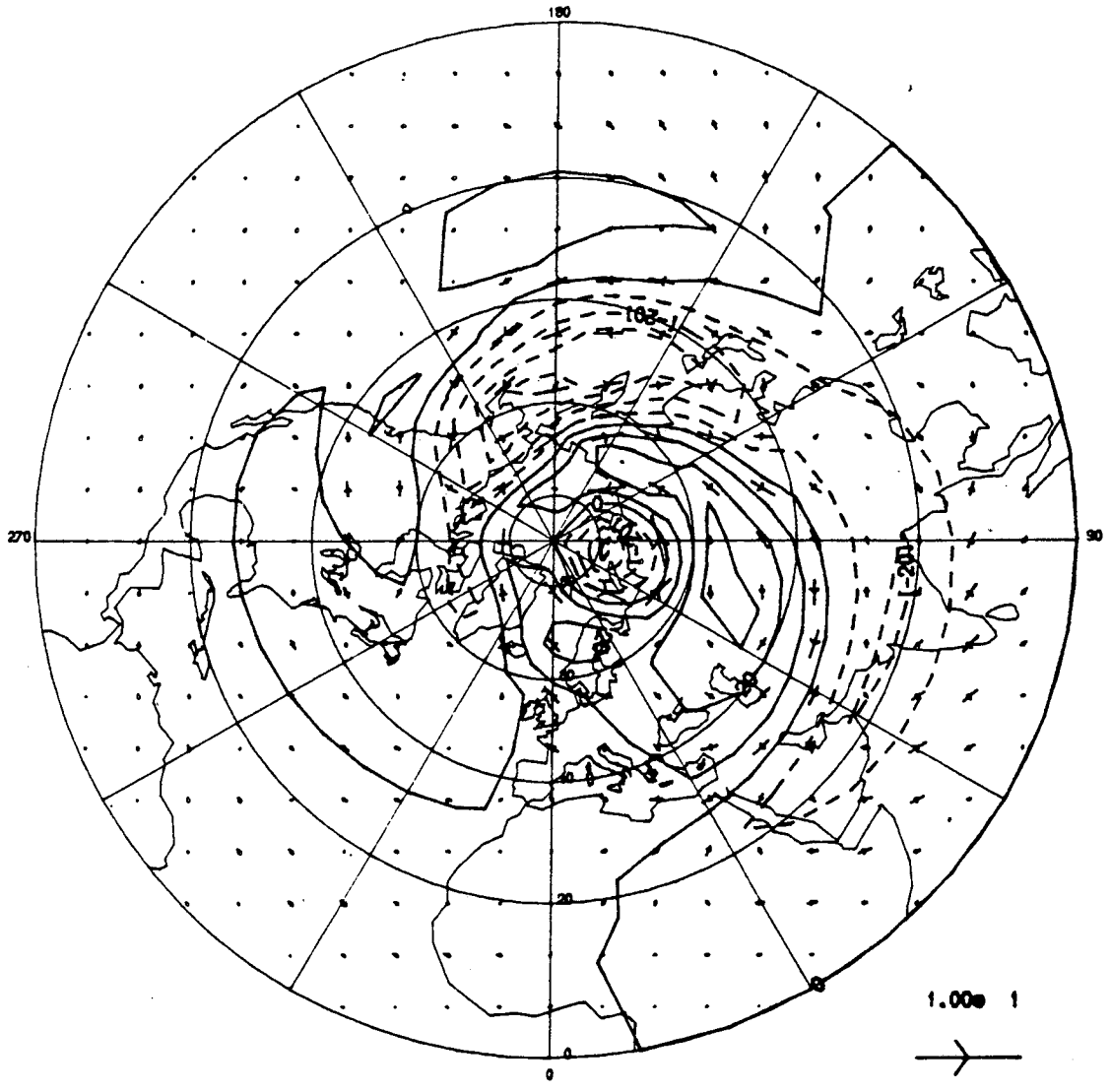

Fig. 5.9 700 mb perturbation stream field as in Fig. 5.2, but for the nonlinear response.

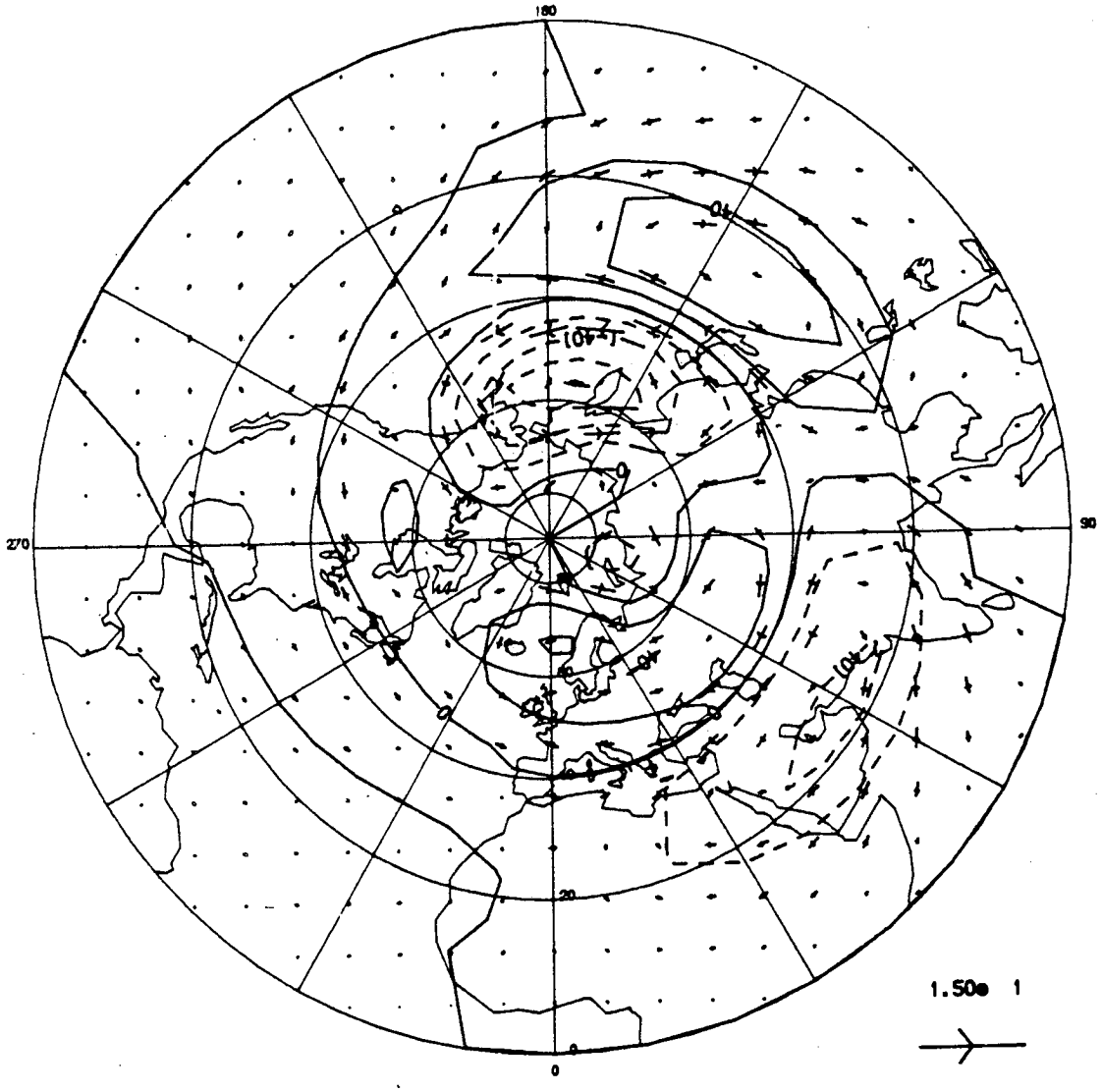

Fig. 5.10 200 mb perturbation stream field as in Fig. 5.3, but for the nonlinear response.

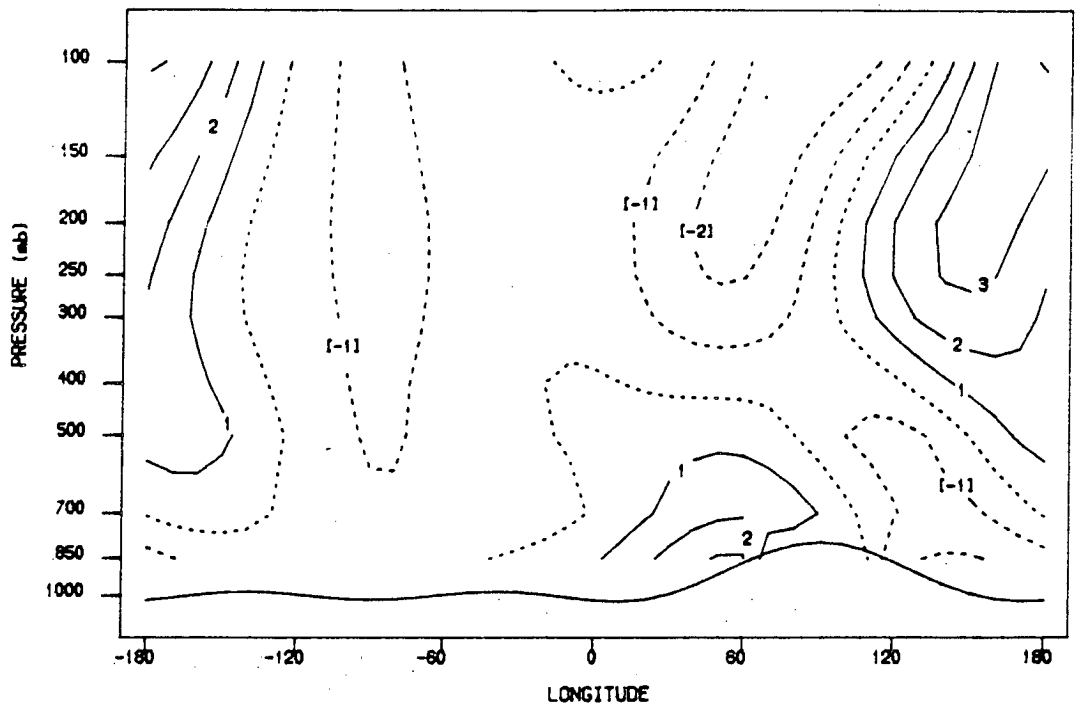

Fig. 5.11 Longitudinal cross-section of perturbation geopotential height at 35°N as in Fig. 5.4, but for the nonlinear response.

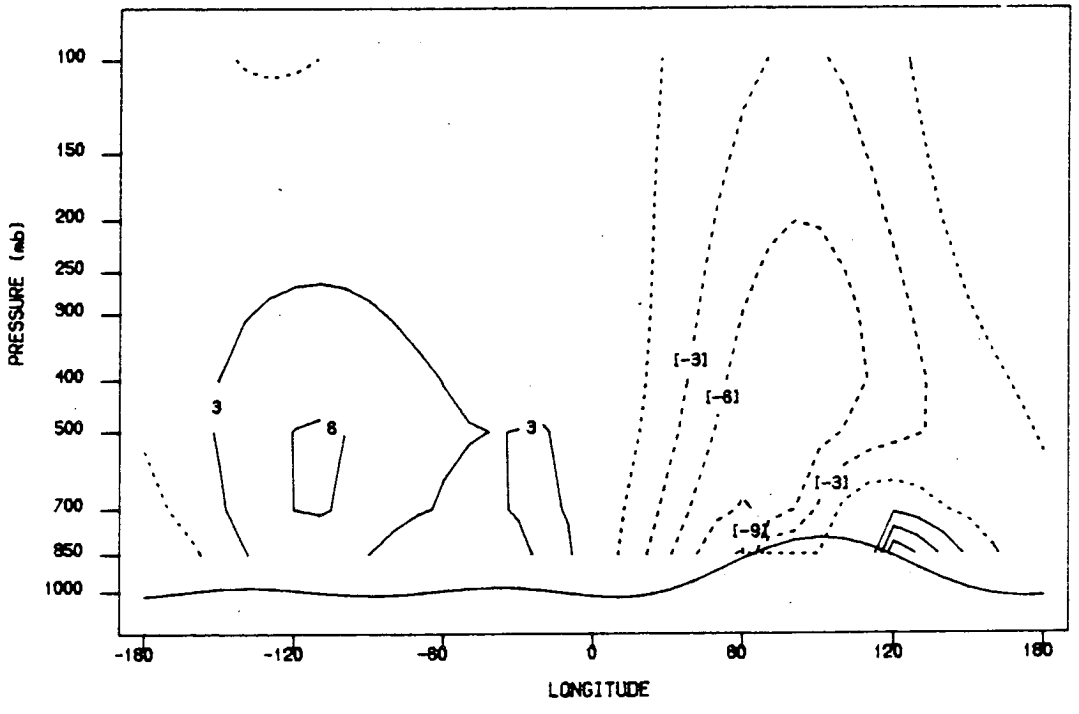

Fig. 5.12 As Fig. 5.5, but for the nonlinear response.

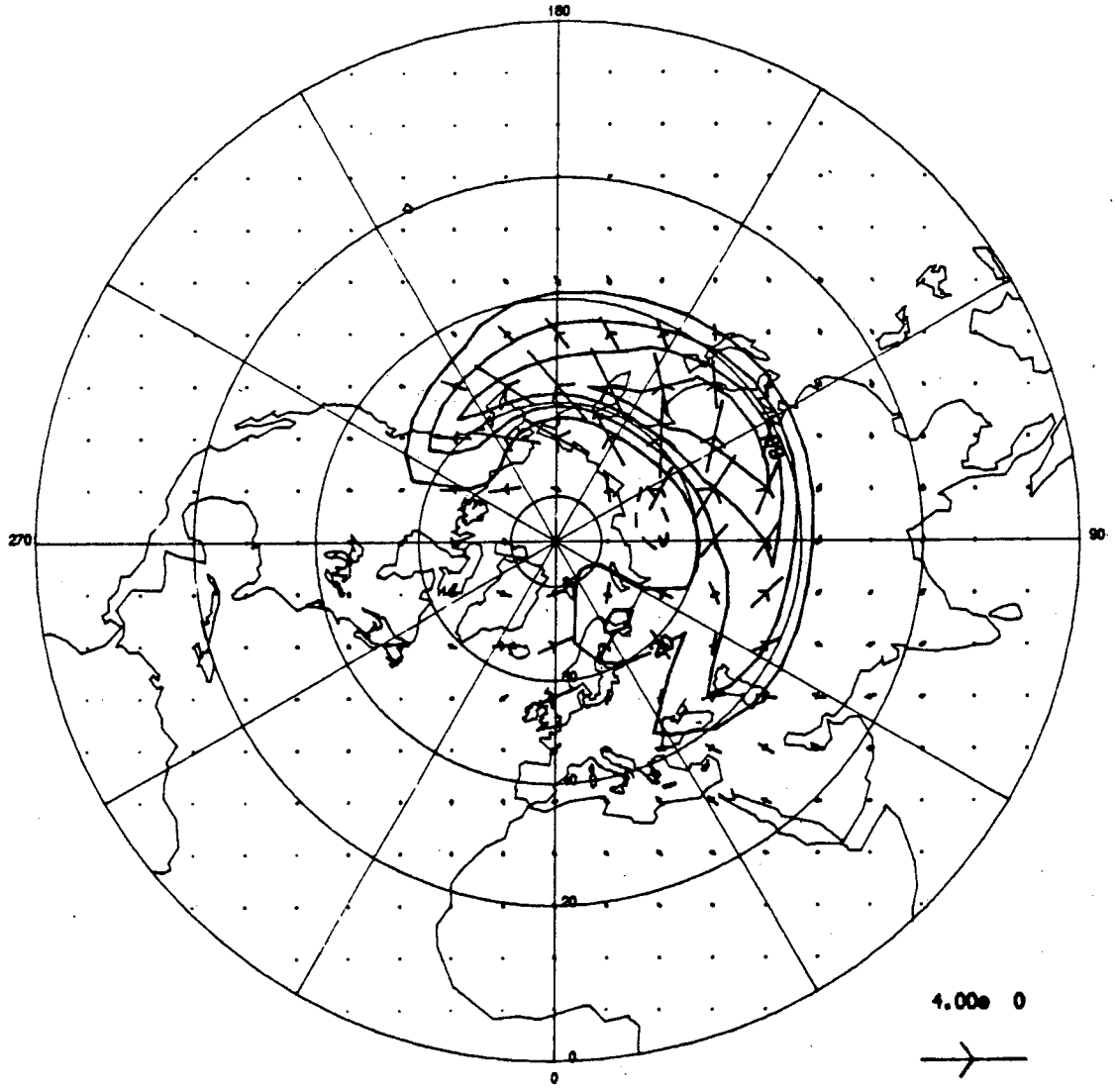

Fig. 5.13 850 mb wave activity flux as in Fig. 5.6, but for the nonlinear response.

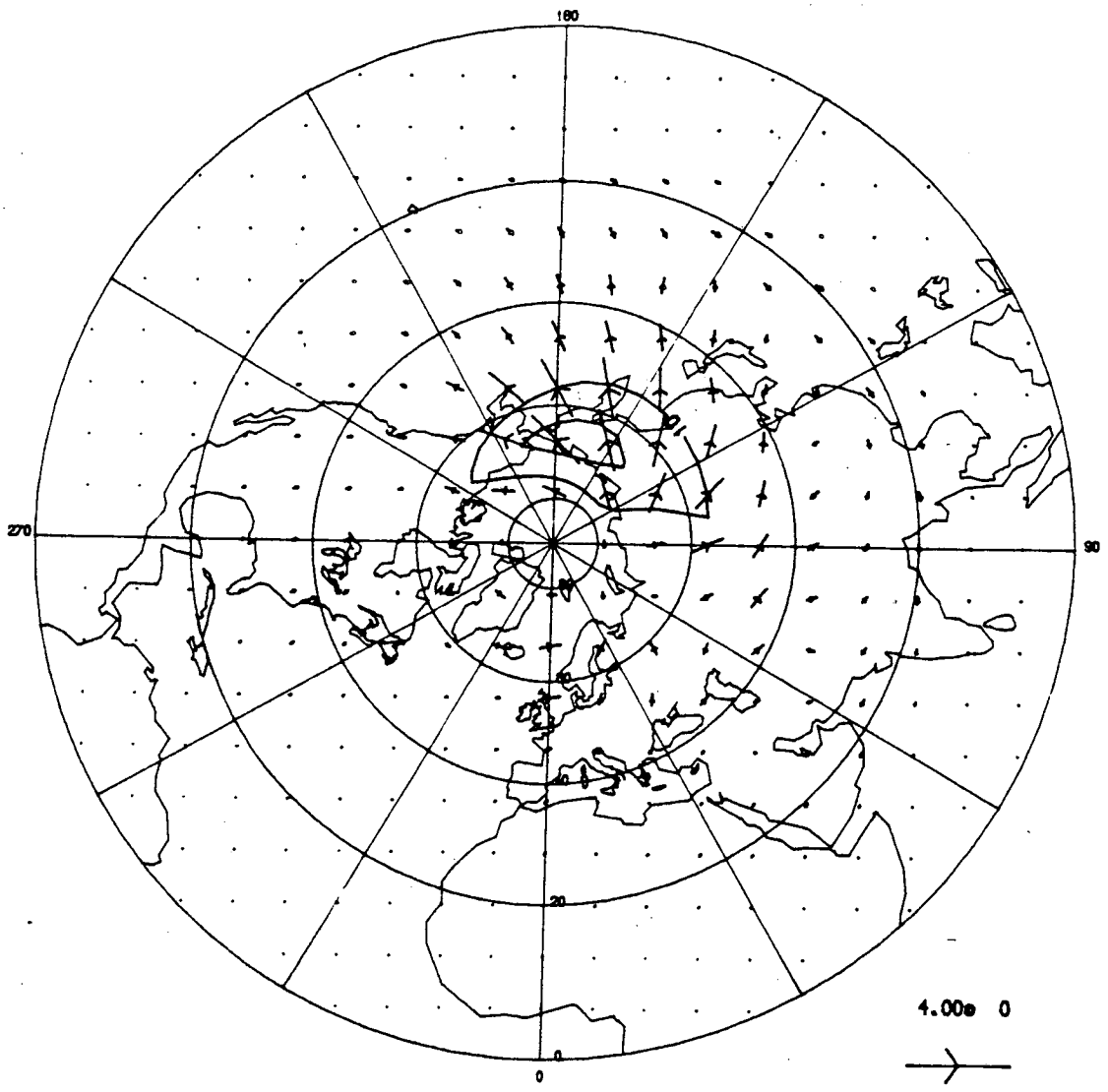

Fig. 5.14 500 mb wave activity flux as in Fig. 5,7, but for the nonlinear response.

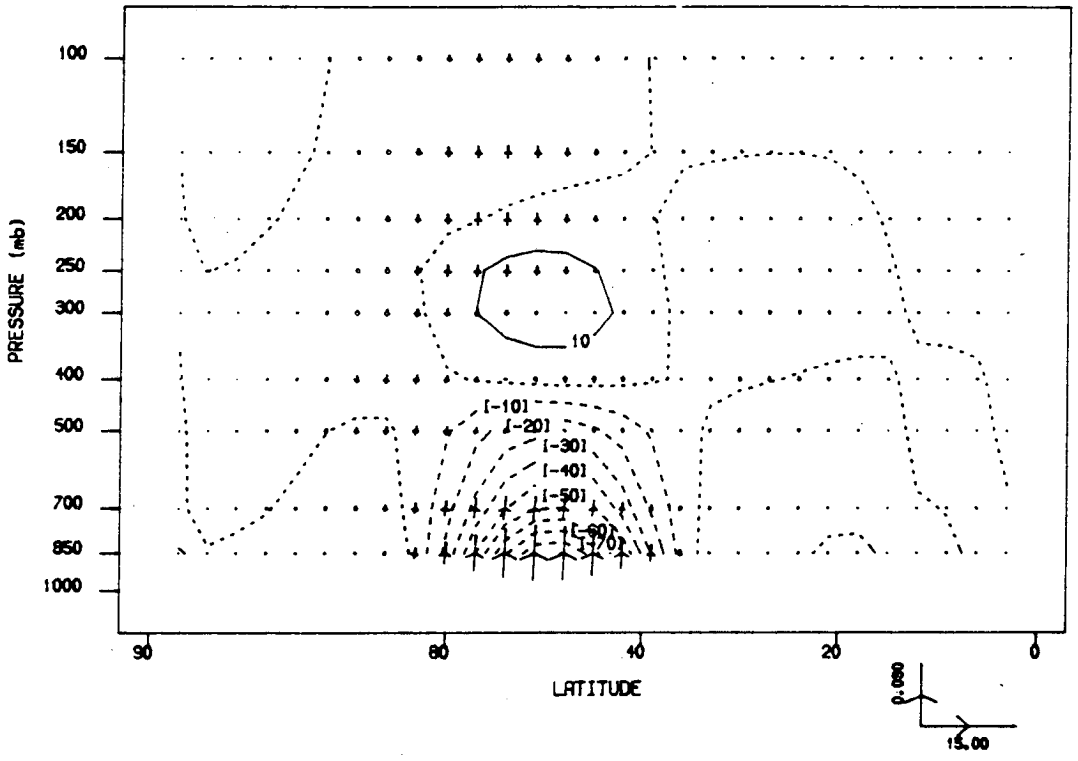

Fig. 5.15 EP cross-section as in Fig. 5.8, but for the nonlinear response.

in the upper troposphere in middle latitudes. Since it was not predicted by the linear model before and there is no diabatic heating process included in the model, this net upper tropospheric source of EP flux associated with orographically forced stationary waves must arise from the nonlinear effect. Associated with this source region more wave activity is propagating vertically into the stratosphere in the nonlinear solution than that in the linear solution.

5.1.3 Sensitivity to the dissipation parameters

Some sensitivity studies were performed for different specifications of dissipation parameters, they are

Case A: R_f and k_t are increased everywhere by 50% of their normal value specified in section 4.3.2.

Case B: R_f and k_t are decreased everywhere by 50% of their normal value.

Case C: Set the biharmonic horizontal diffusion coefficients, α and γ, equal to zero.

Case D: Remove the enhanced dissipation in the polar region, i.e., R_f and k_t are independent of latitude.

In each case all parameters other than those described above are kept unchanged. Cases A, B and C were performed for both the linear and nonlinear models, but case D was performed for the linear model only.

From cases A and B, we find that neither increasing nor decreasing the value of R_f and k_t by 50% changes obviously

the pattern of stationary waves forced by topography, but the amplitude of the wave patterns is usually increased (decreased) when R_f and k_t are decreased (increased). This can be seen, for example, from Figs. 5.16 and 5.17 for the linear solution; Similar results were obtained for the nonlinear response but are not shown here. The pattern of wave activity flux and EP flux is also remarkably insensitive in these two cases (not shown here), but their amplitudes are evidently affected.

Again in case C where the biharmonic horizontal diffusion is completely removed, the pattern of perturbation stream field has not been modified evidently, only small changes in the amplitude are produced (not shown here). A possible cause for this insensitivity to the diffusion parameters is due to the high truncation of this model, while these parameters have a much stronger effect on the wave components with smaller horizontal scale (see eq.(4.14)).

Since the linear and nonlinear models developed in this study have a low resolution and no transient wave effect included explicitly, it is impossible to simulate accurately the stationary waves in the real atmosphere. The main subject of this study is qualitatively investigating the wave patterns excited by topography and thermal forcing, we may therefore consider the sensitivity of amplitude of the model atmospheric response to dissipation parameters as unimportant. In order to compare the response to different forcing, all dissipation parameters are fixed after this section.

If the enhanced dissipation in polar latitudes is removed (case D), the response is much stronger, especially in high latitudes than before. For example, comparing Fig. 5.18 with Fig. 5.3 shows that the amplitude of wave pattern in high latitudes at 200 mb is increased by a factor of more than 3. There is an evident source of EP flux in middle and upper troposphere between 66°N and 80°N (Fig. 5.19). It is difficult to relate this source region of EP flux with the orographical forcing in middle latitudes. No convergent solution was obtained for the nonlinear model in this case by using the iteration procedures mentioned in section 2.5.4, but this does not preclude the possibility of its existence.

5.2 Response to a Large Scale Mountain in High Latitudes

In this experiment we move the idealized topography to high latitudes in order to simulate, to a certain extent, the effect of the Greenland Plateau. The surface geopotential is still represented in the form of (5.1) and reset at $\varphi_1=55°$, $\varphi_2=85°$, $\lambda_1=-90°$ and $\lambda_2=0°$ (where the amplitude A is still equal to 2500 m).

5.2.1 Linear Solution

Since in the lower troposphere in polar regions there is a weak easterly in the model's basic flow (Fig. 3.2), the vertical structure of the perturbation stream field for the linear response to an idealized large scale mountain in high

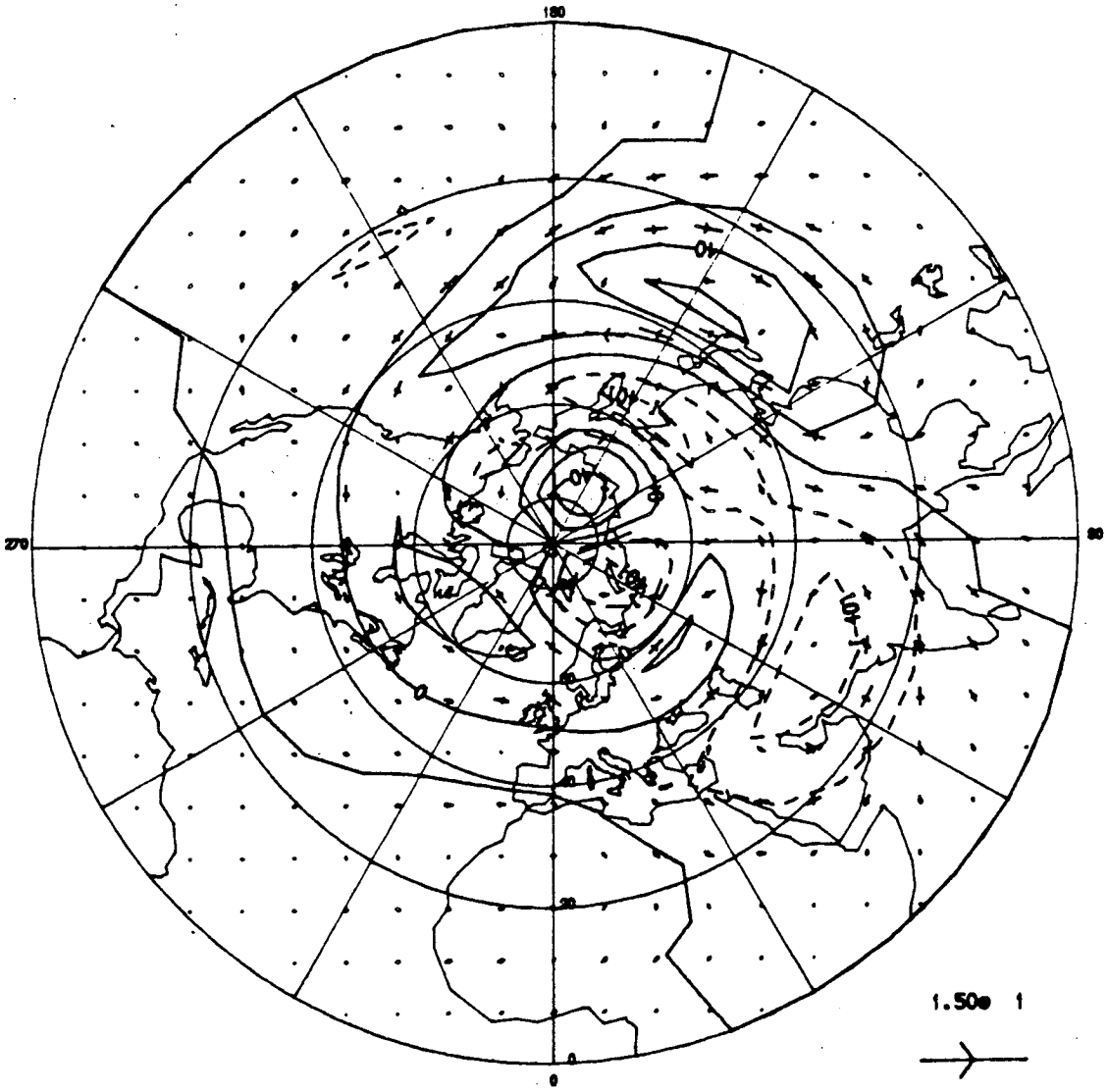

Fig. 5.16 200 mb perturbation stream field as in Fig. 5.3 except for case A, where the Rayleigh friction and Newtonian cooling coefficients are increased by 50%.

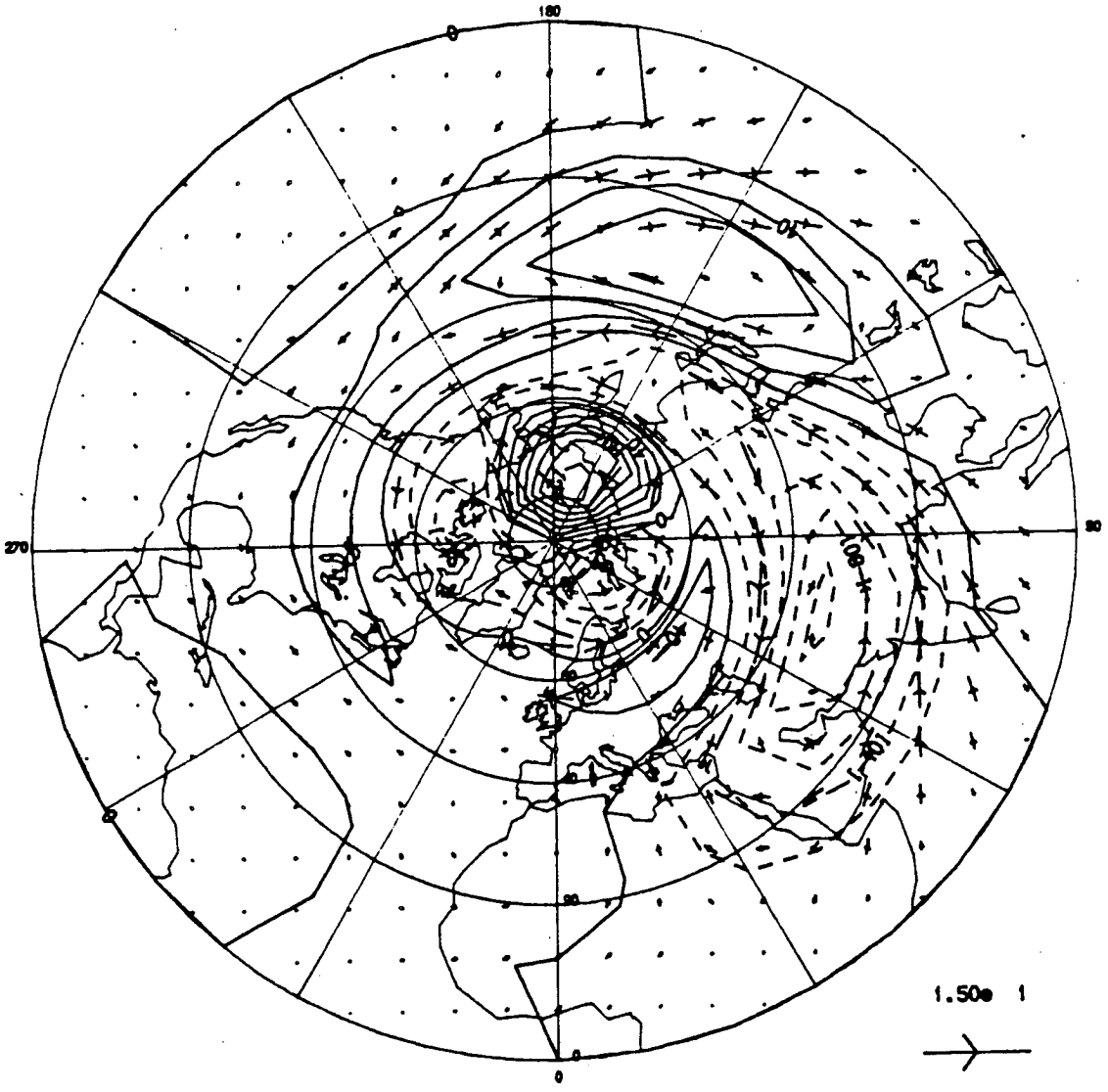

Fig. 5.17 200 mb perturbation stream field as in Fig. 5.3 except for case B, where the Rayleigh friction and Newtonian cooling coefficients are decreased by 50%.

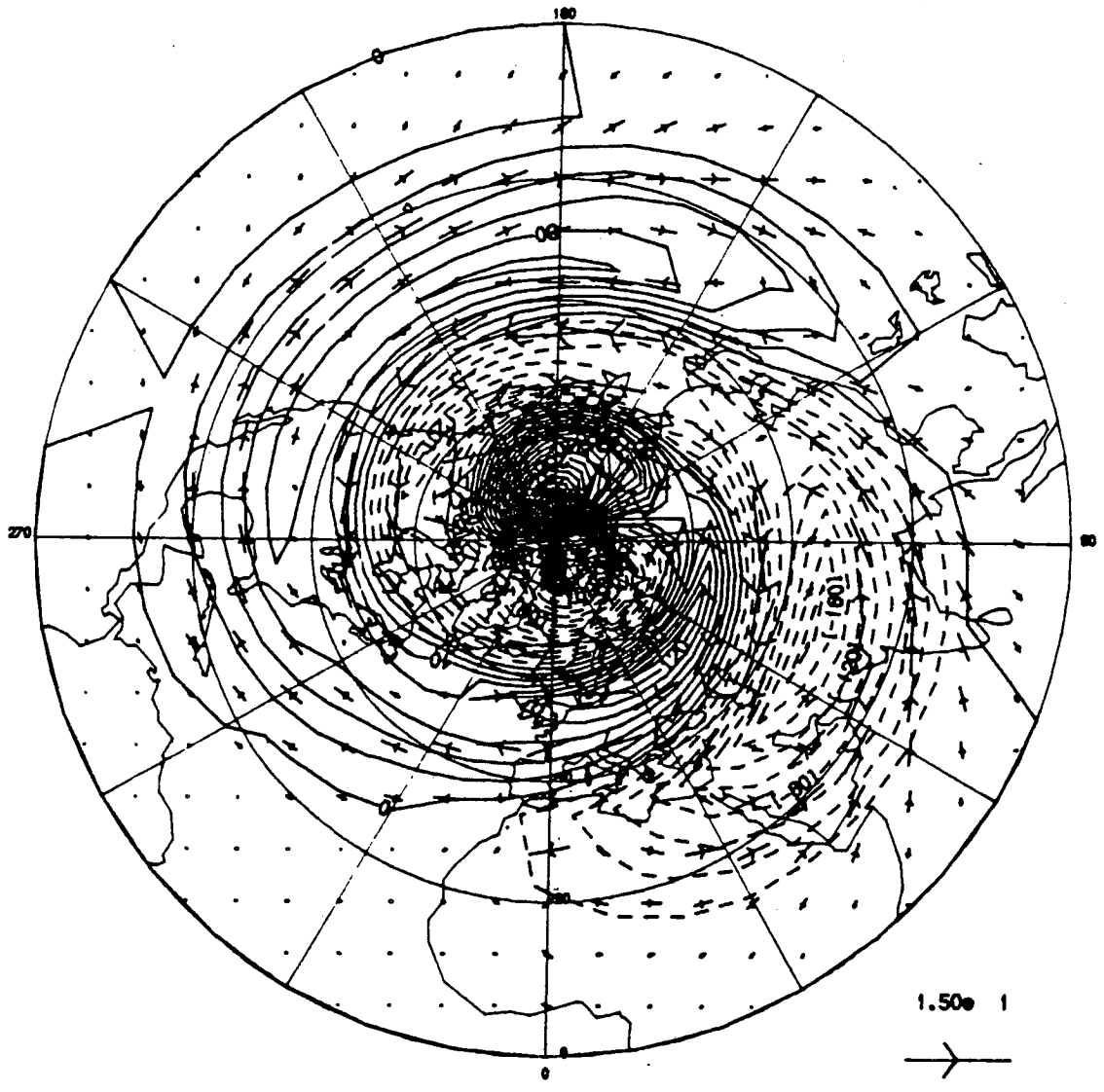

Fig. 5.18 200 mb perturbation stream field as in Fig.5.3 except for case D, where no enhanced dissipation is employed in polar latitudes.

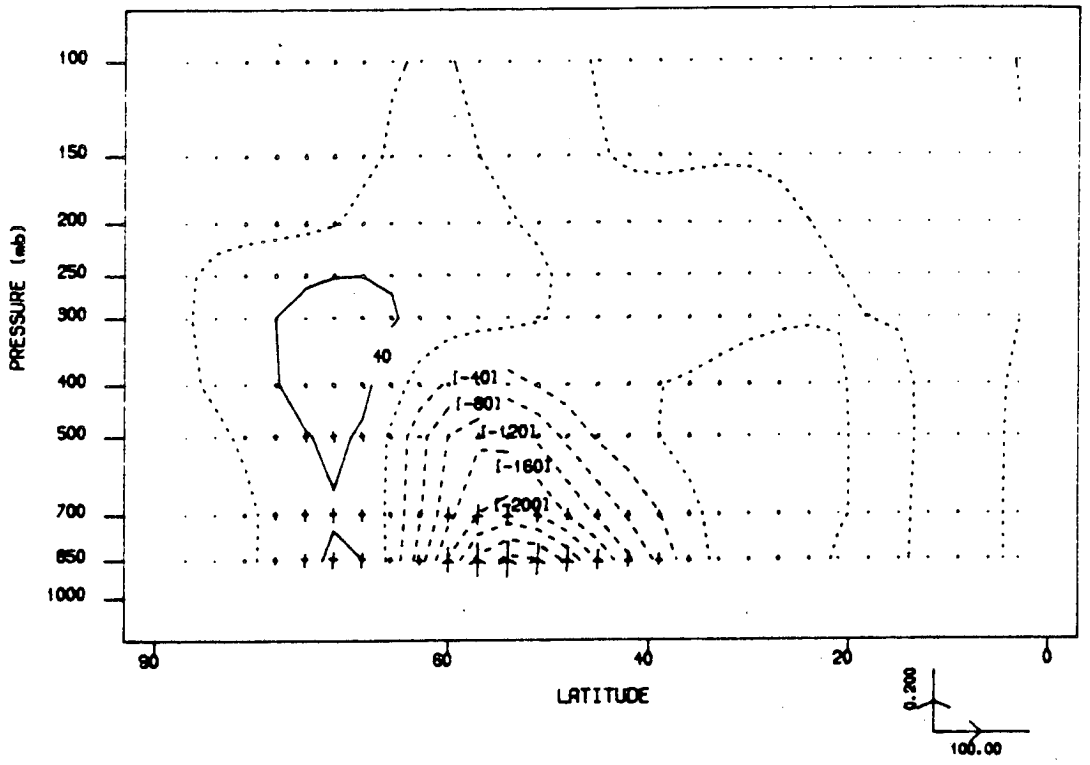

Fig. 5.19 EP cross-section as in Fig. 5.8, but for case D. Contour interval is 40 units.

latitudes is complicated. At 700 mb in polar region there is a anticyclonic circulation to the east of the mountain top and a cyclonic circulation to the west of the mountain (not shown here). At 200 mb (Fig. 5.20) a fairly strong anticyclonic circulation is over the mountain and the major wavetrain is propagating eastward and upward, while the latitudinal propagation is relatively weaker. In middle latitudes major cyclonic circulations are found in North America and North Africa and anticyclonic circulation in the Atlantic. The response in Asia and the Pacific is weak. The corresponding wave activity flux appears to originate primarily on the western side of the mountain and propagate vertically and eastward (see, for example, Fig. 5.21).

5.2.2 Nonlinear Solution

Since the basic flow in high latitudes is much weaker compared with that in middle latitudes, the difference between linear and nonlinear response to an idealized topography located in high latitudes is more evident than that in middle latitudes. Comparing Fig. 5.22 with Fig. 5.20, we find that the wavetrain for the nonlinear solution in the polar region is obviously weakened. On the other hand, the propagation equatorward of wave activity is relatively stronger than the linear solution. This is seen from the diagrams of wave activity flux (e.g., Fig. 5.23). The EP

cross-sections for linear and nonlinear response are also considerably different (compare Fig. 5.24 with Fig.5.25). The largest EP flux arrows for the nonlinear solution are even more concentrated in the southern slope of the mountain, propagate vertically and split into two branches. One branch is trapped and turns equatorward in the middle troposphere, another major branch propagates to higher levels and turns poleward. Although the vertical component of EP flux for the nonlinear solution is generally smaller than that for the linear solution, its horizontal component is relatively larger. The results of this experiment suggest that the nonlinearity is particularly important when a forcing source is located in high latitudes than in middle latitudes.

5.3 Response to Mid-latitude Heating

In this experiment we consider the case in which the only forcing is provided by an isolated region of diabatic heating located in middle latitudes and there is no topography inserted into the model. The horizontal and vertical variation of diabatic heating rate is given by

$$\frac{Q}{c_p} = \begin{cases} A \left[\sin\frac{\pi(\varphi-\varphi_1)}{(\varphi_2-\varphi_1)} \sin\frac{\pi(\lambda-\lambda_1)}{(\lambda_2-\lambda_1)} \sin\frac{\pi(\sigma-\sigma_1)}{(\sigma_2-\sigma_1)} \right]^2, \\ \qquad \varphi_1<\varphi<\varphi_2, \quad \lambda_1<\lambda<\lambda_2, \quad \sigma_1<\sigma<\sigma_2 \\ 0 \qquad \text{otherwise} \end{cases} \tag{5.2}$$

where $\varphi_1=30^\circ$, $\varphi_2=60^\circ$, $\lambda_1=90^\circ$, $\lambda_2=180^\circ$, $\sigma_1=-0.84$ and $\sigma_2=1$.

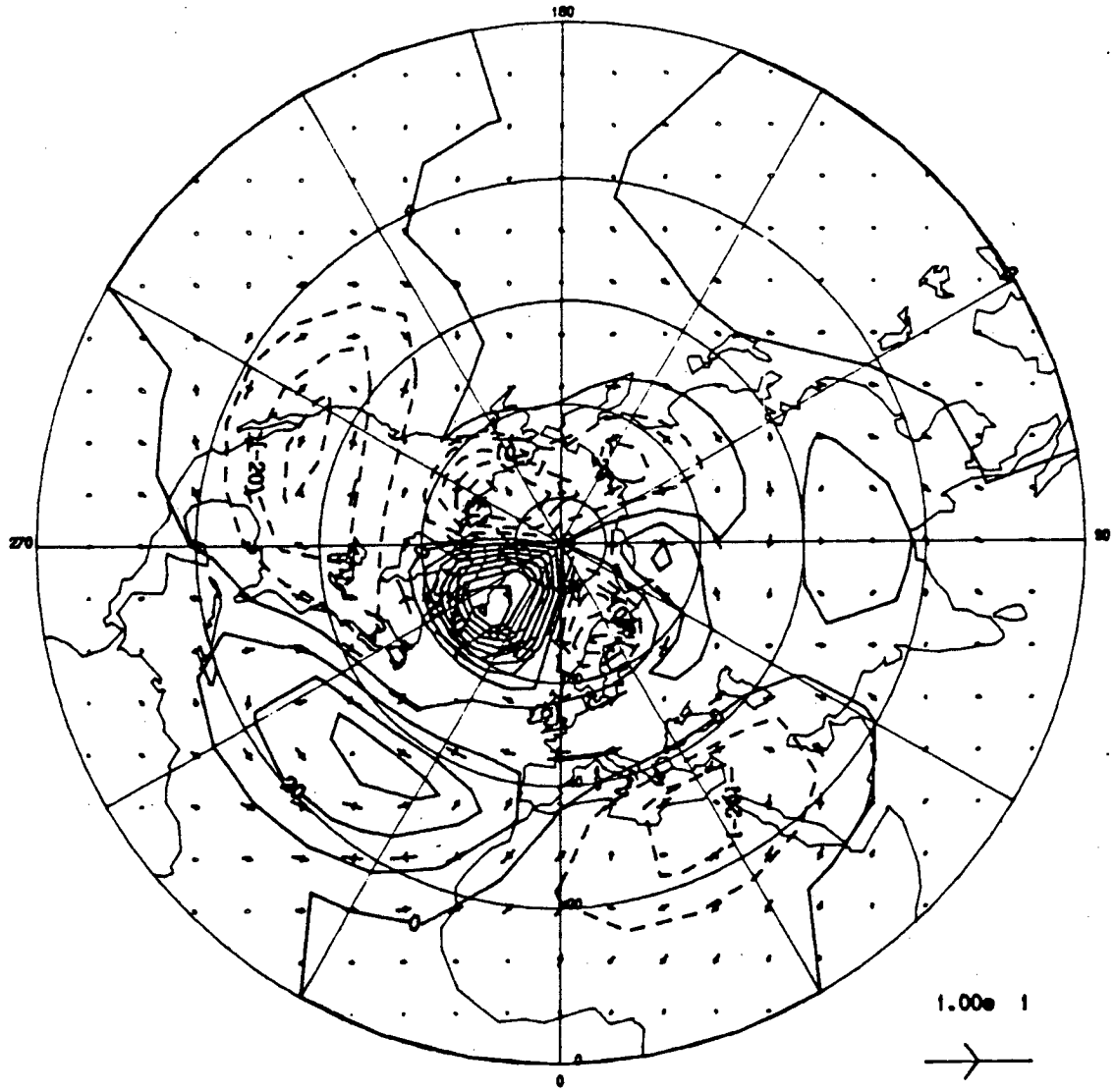

Fig. 5.20 200 mb perturbation stream field for the linear response to an idealized topography in high latitudes. Contours represent the perturbation streamfunction/($10^5 m^2 s^{-1}$) with an interval of 10 units.

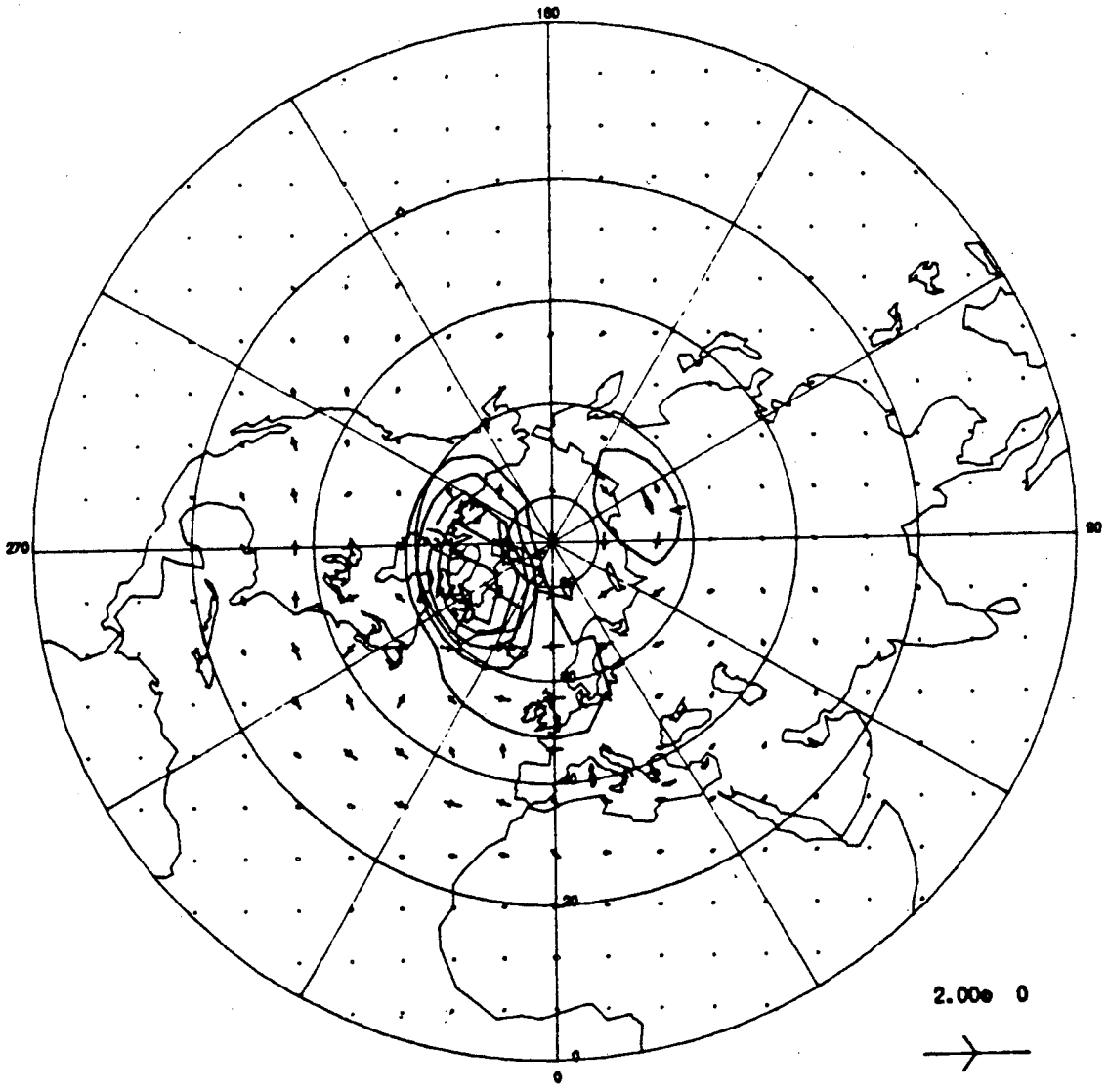

Fig. 5.21 500 mb wave activity flux as in Fig. 5.7 except for an idealized topography in high latitudes. Contours are at intervals of 4 units.

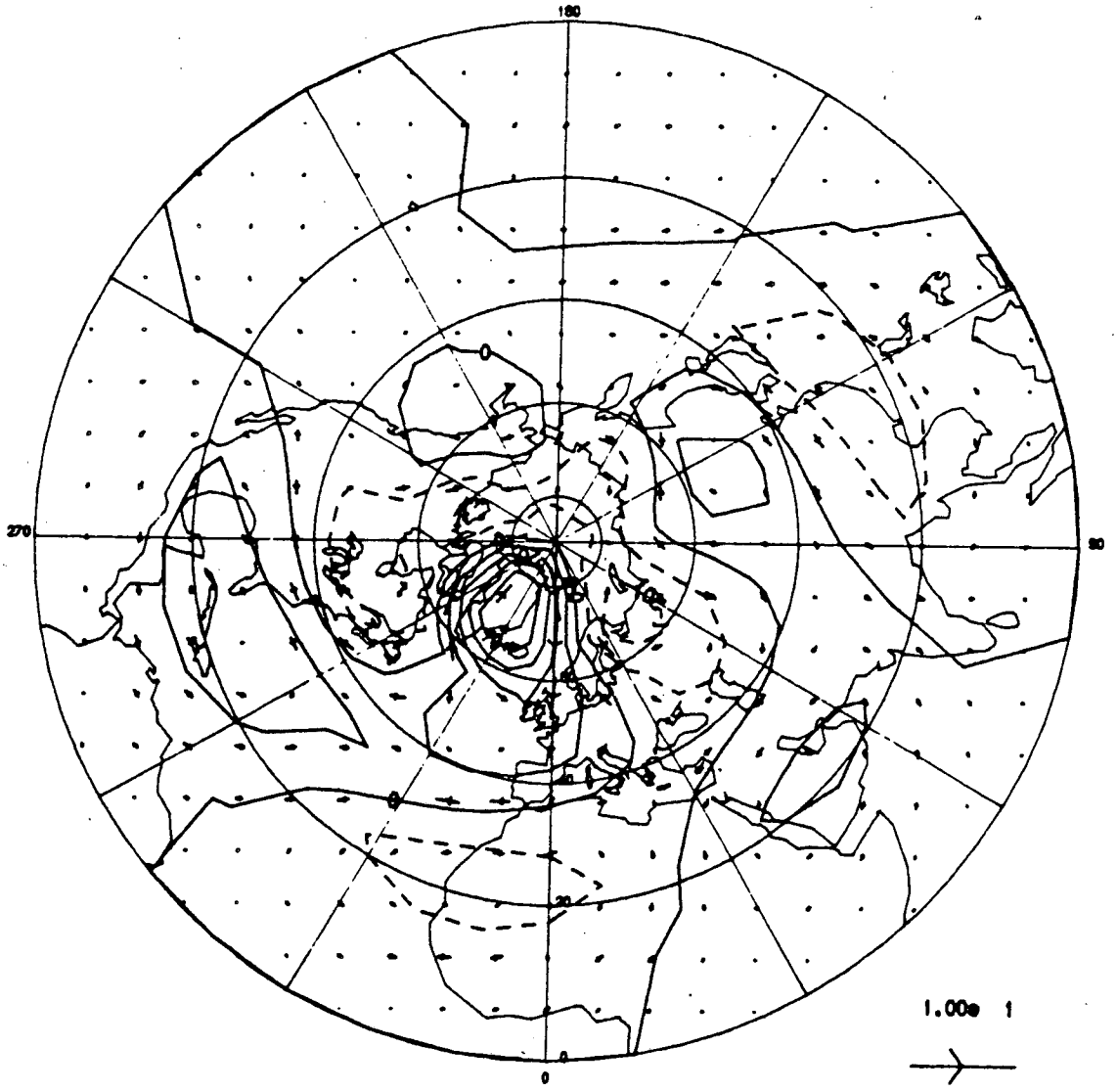

Fig. 5.22 200 mb perturbation stream field as in Fig. 5.20, but for the nonlinear solution.

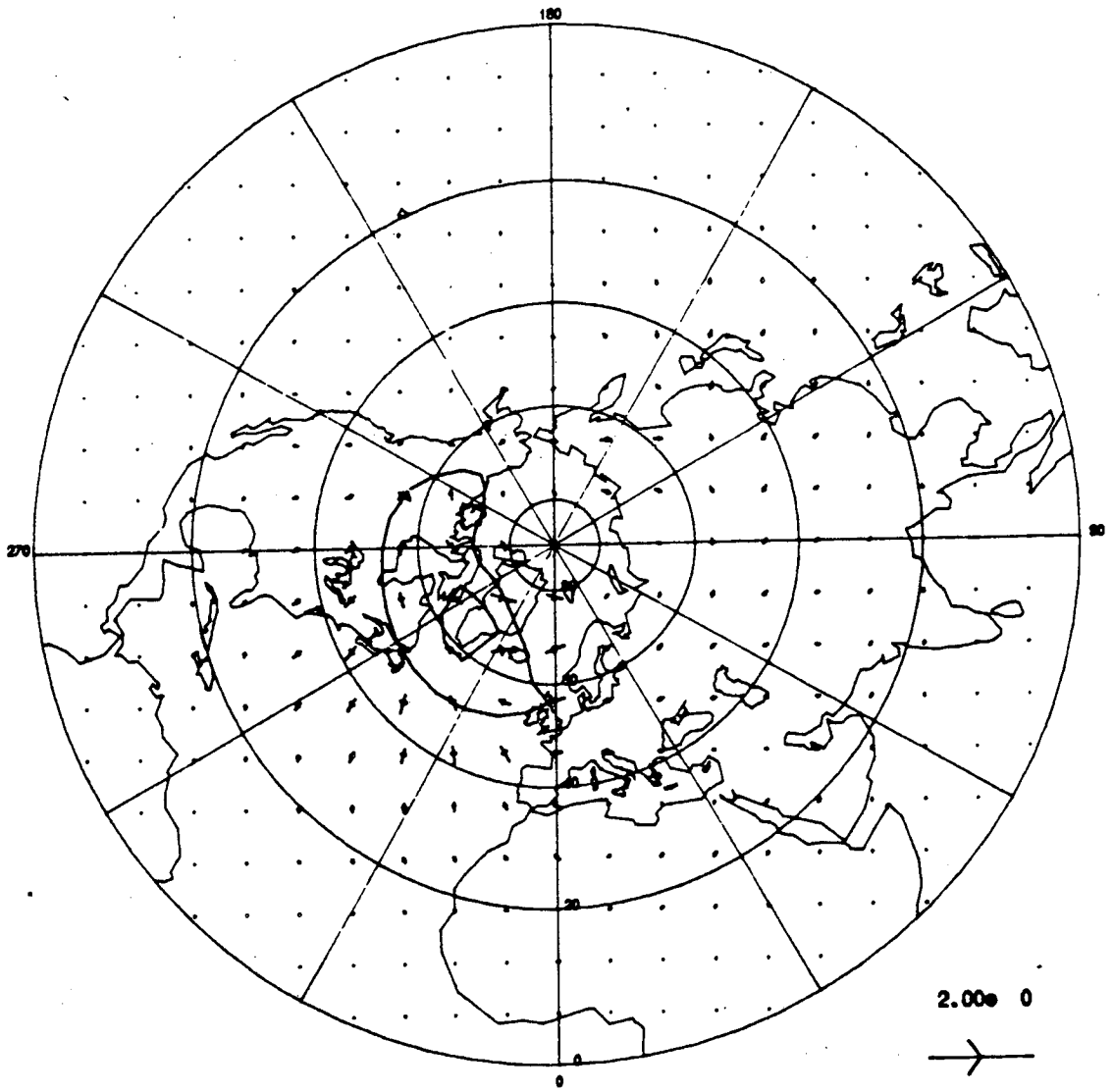

Fig. 5.23 500 mb wave activity flux as in Fig. 5.21, but for the nonlinear solution.

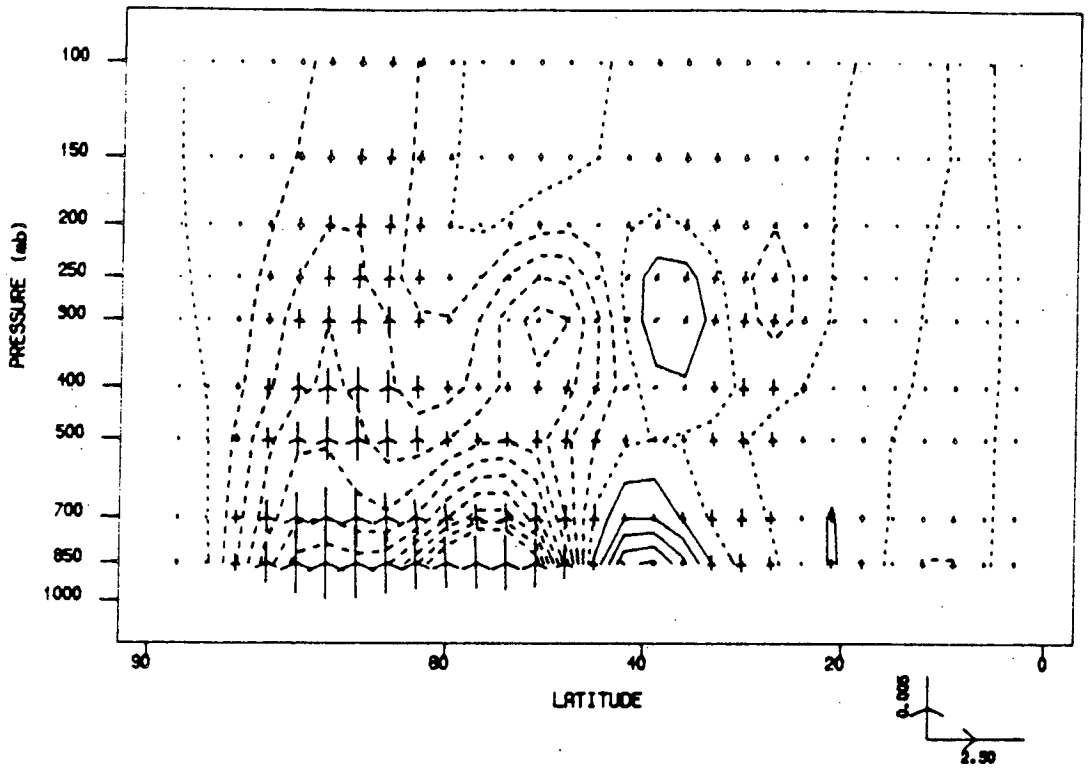

Fig. 5.24 EP cross-section for the linear response to an idealized topography in high latitudes. The graphic convention is the same as in Fig. 5.8 but the contour interval is 1 unit.

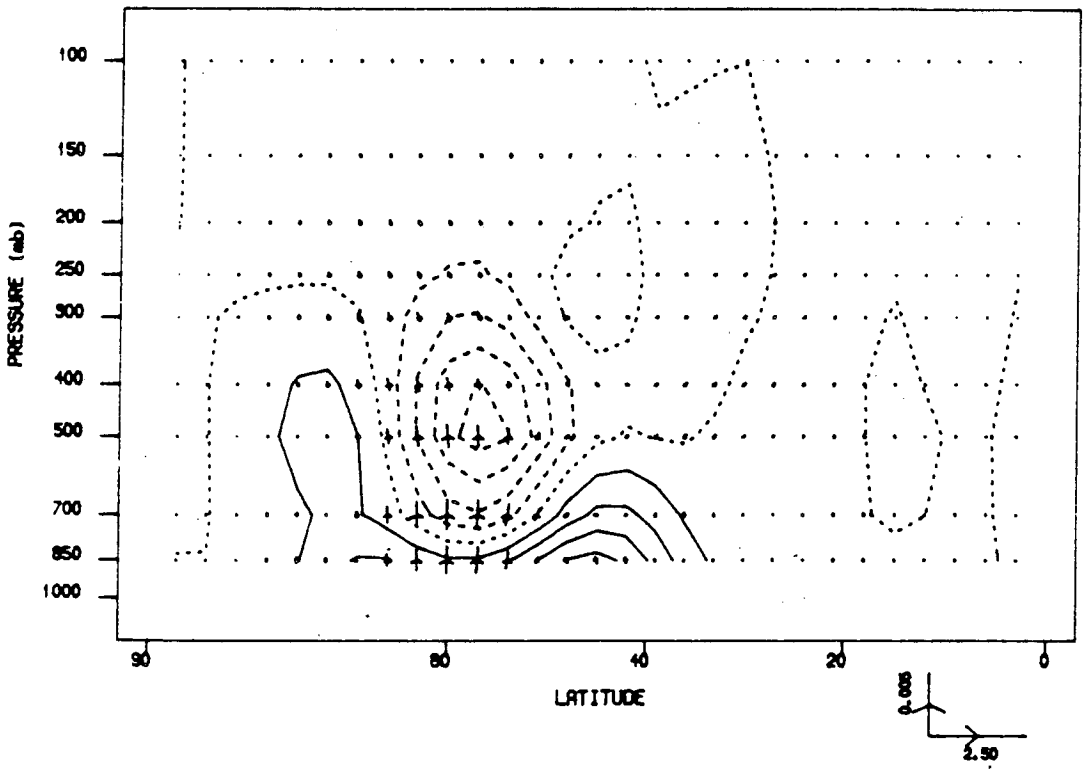

Fig.5.25 As Fig. 5.24, but for the nonlinear response.

The amplitude A is set to 5 Kd^{-1}, which implies a relatively large heating maximum value corresponding to a precipitation rate of the order of 10 mmd^{-1} (Simmons, 1982).

5.3.1 Linear Solution

The perturbation stream fields at the 700 mb and 200 mb levels are shown in Figs. 5.26 and 5.27 respectively. At low levels there is a cyclonic circulation in the heating region with a larger longitudinal extent to the east and anticyclonic circulation to the west of the heating region. At upper level the cyclonic circulation is located to the west of the heating centre and an anticyclonic circulation to the east of the heating centre. The mid-latitude response is in general consistent with the calculation by Simmons (1982), but the high latitude response is much weaker due to the way in which momentum and thermal dissipation are treated. A longitudinal cross-section of perturbation geopotential height through the heating centre (Fig. 5.28) shows the vertical structure of the wave pattern more clearly, where the westward tilt of phase with height is more evident compared with the orographic forcing case. This suggests that the stationary waves induced by the thermal forcing have a stronger baroclinic nature than those induced by the orographic forcing.

The wave activity propagates eastward in the zonal direction (see, e.g., Fig. 5.29), but in the meridional

direction it is dominated by a poleward propagation in the lower troposphere and an equatorward propagation at upper levels (see, e.g., Fig. 5.30 for a meridional cross-section of wave activity flux passed through the heating centre). In addition, the vertical variation of the vertical component of the activity flux appears somewhat different to the orographic forcing case. In the experiment described in section 5.1 the largest vertical flux is concentrated in the lower troposphere and has a much larger magnitude than that in this experiment, but their magnitudes become comparable in the upper troposphere and stratosphere. This may be due to the vertical distribution of heating rate. If the thermal forcing mainly originates from the cumulus convection, the vertical distribution of heating rate adopted in this model should be reasonable to a certain extent. This experiment suggests that the thermal forcing in the troposphere may make a considerable contribution to the maintenance of the vertically propagating stationary planetary waves in the stratosphere. This is also reflected in the associated EP cross-section (Fig. 5.31), which differs from Fig. 5.8 on the vertical distribution of vectors as well as on the pattern of contours representing the convergence of EP flux.

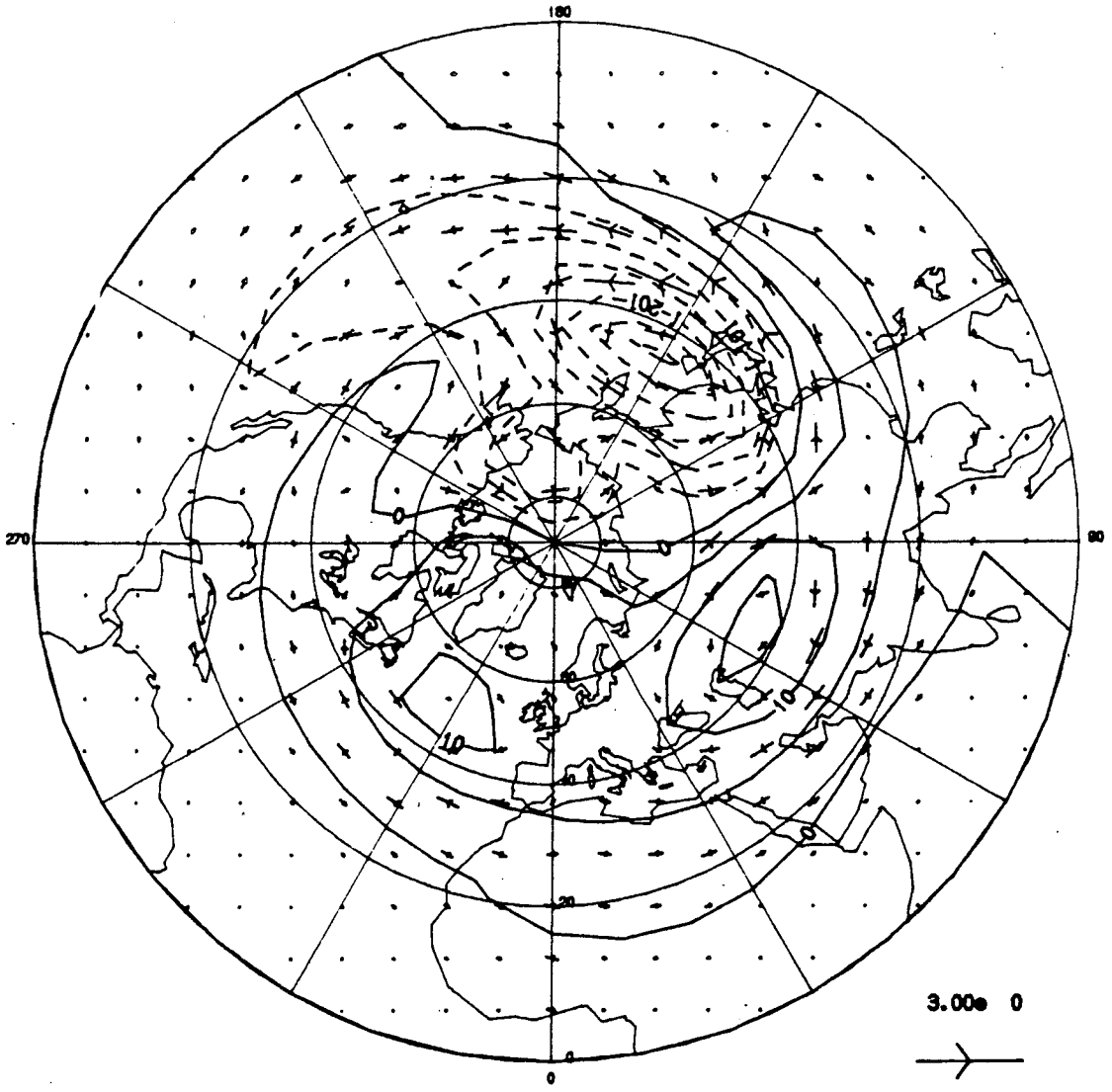

Fig. 5.26 700 mb perturbation stream field for the linear response to an idealized thermal forcing in mid-latitudes. Contour represent the perturbation streamfunction/($10^5 m^2 s^{-1}$) with an interval of 5 units.

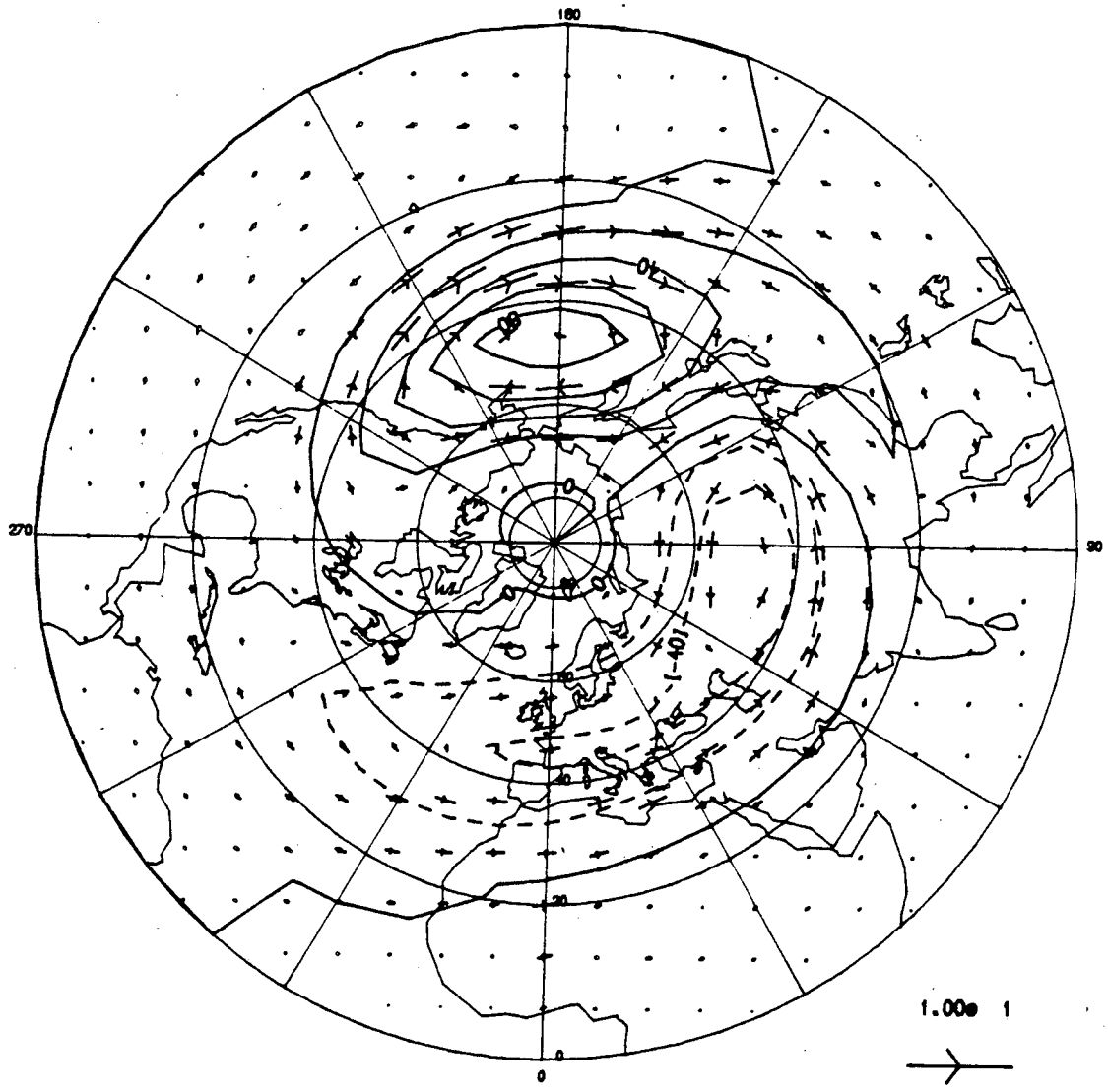

Fig. 5.27 As Fig. 5.26, but for 200 mb. Contours are at intervals of 20 units.

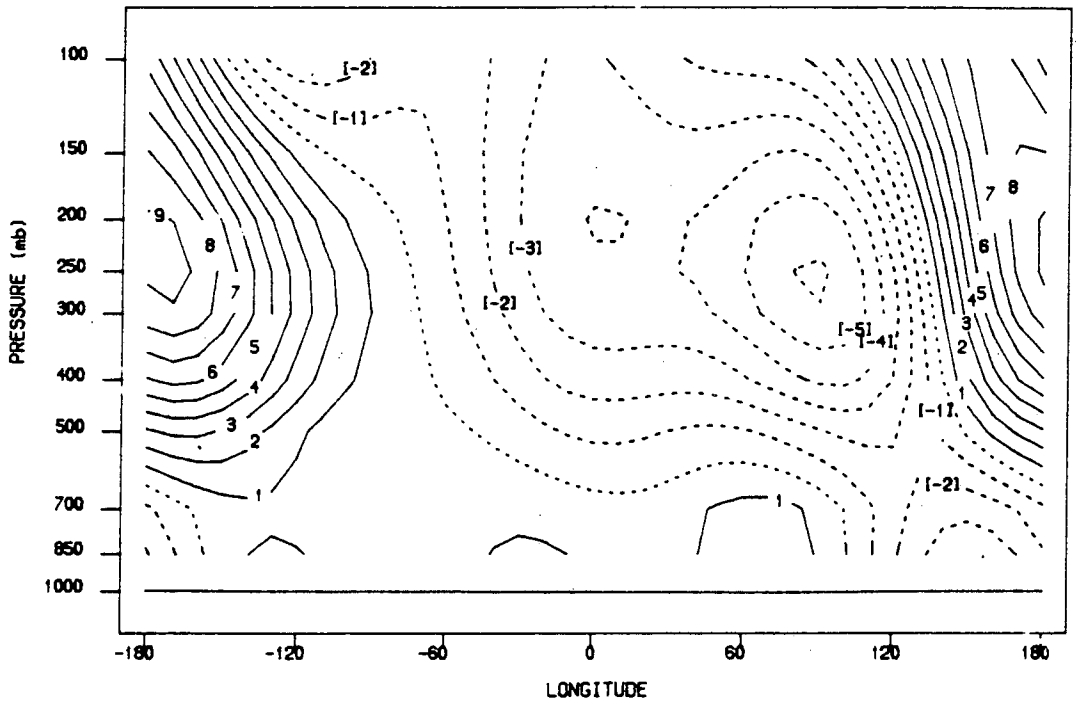

Fig. 5.28 Longitudinal cross-section of perturbation geopotential height at 45°N for the linear response to an idealized thermal forcing in mid-latitudes. Contours interval is 1 dam.

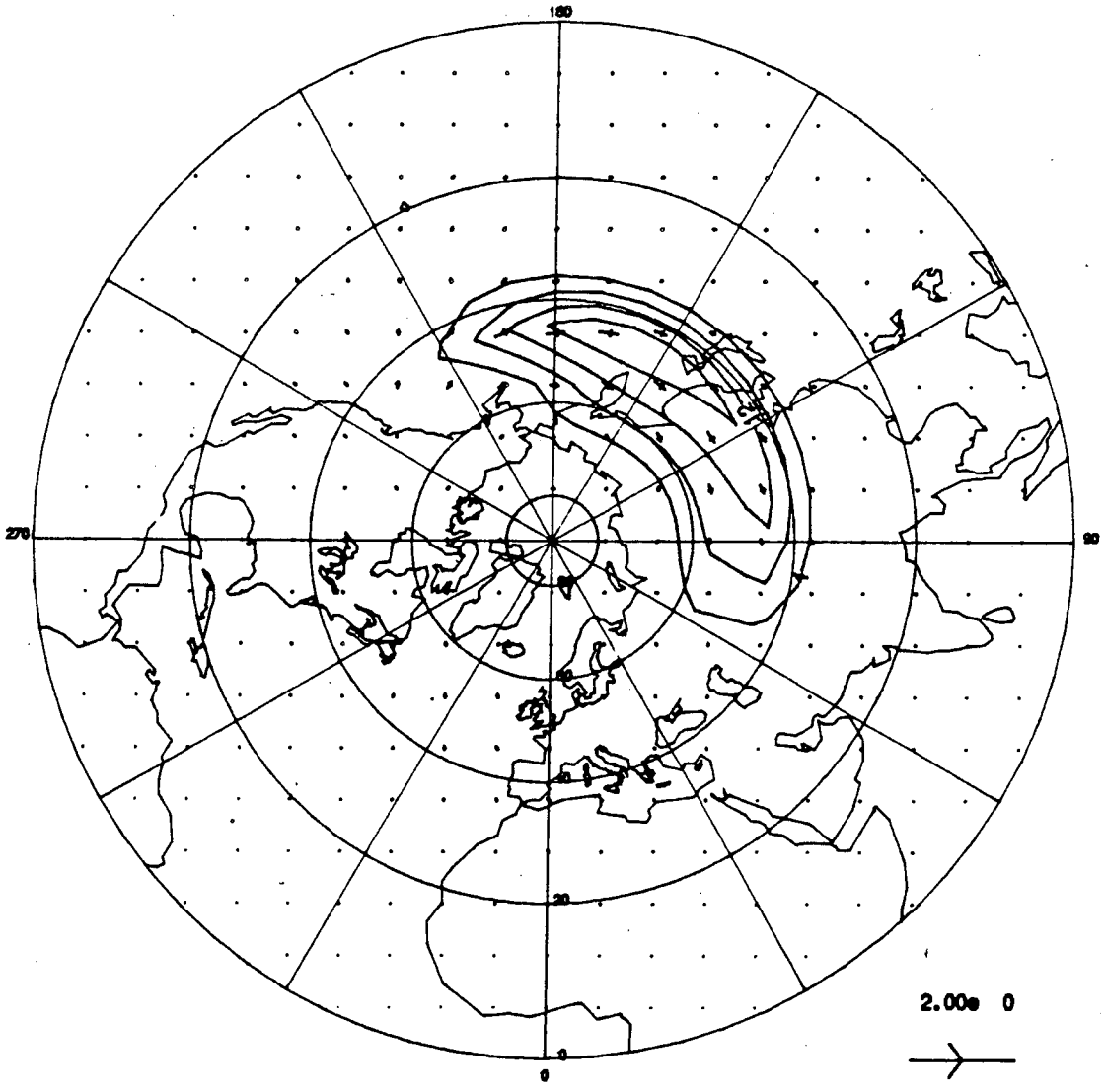

Fig. 5.29 500 mb wave activity flux for the linear response to an idealized thermal forcing in mid-latitudes. Contours represent the vertical component $F_z/(10^{-3}m^2s^{-2})$ with an interval of 5 units.

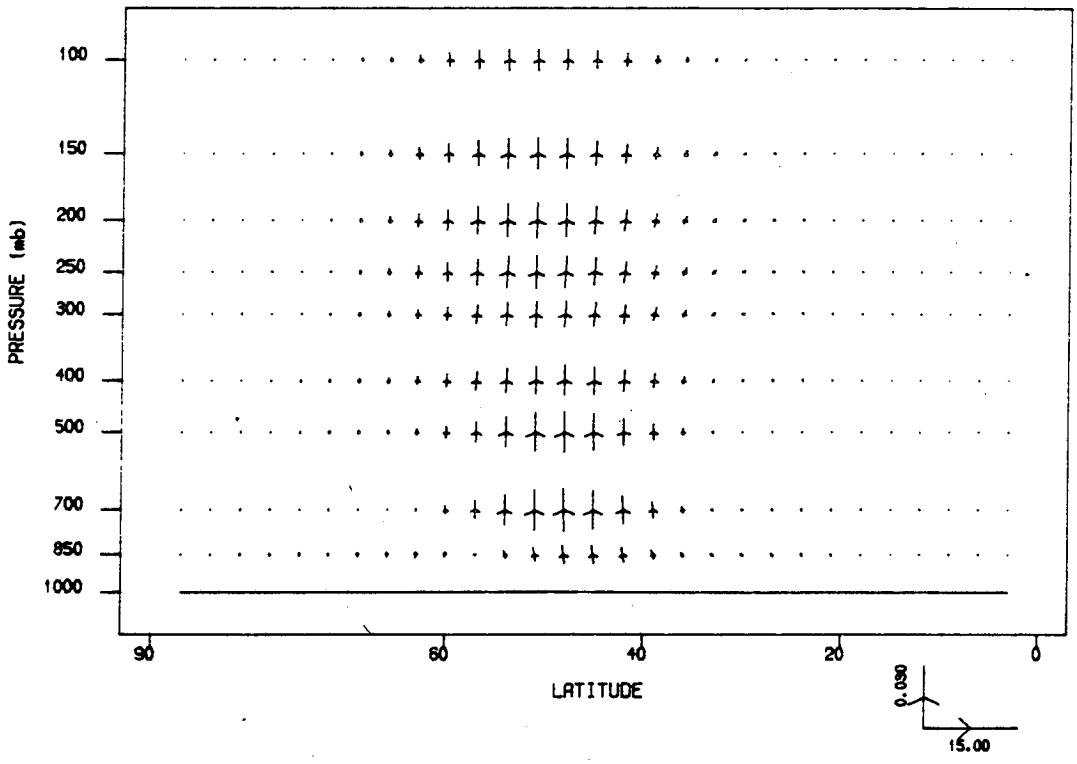

Fig. 5.30 Meridional cross-section of wave activity flux at 135°E for the linear response to an idealized thermal forcing in middle latitudes. Arrows denote the vertical and meridional components of **F** with the scale plotted at bottom right (unit: $m^2 s^{-2}$).

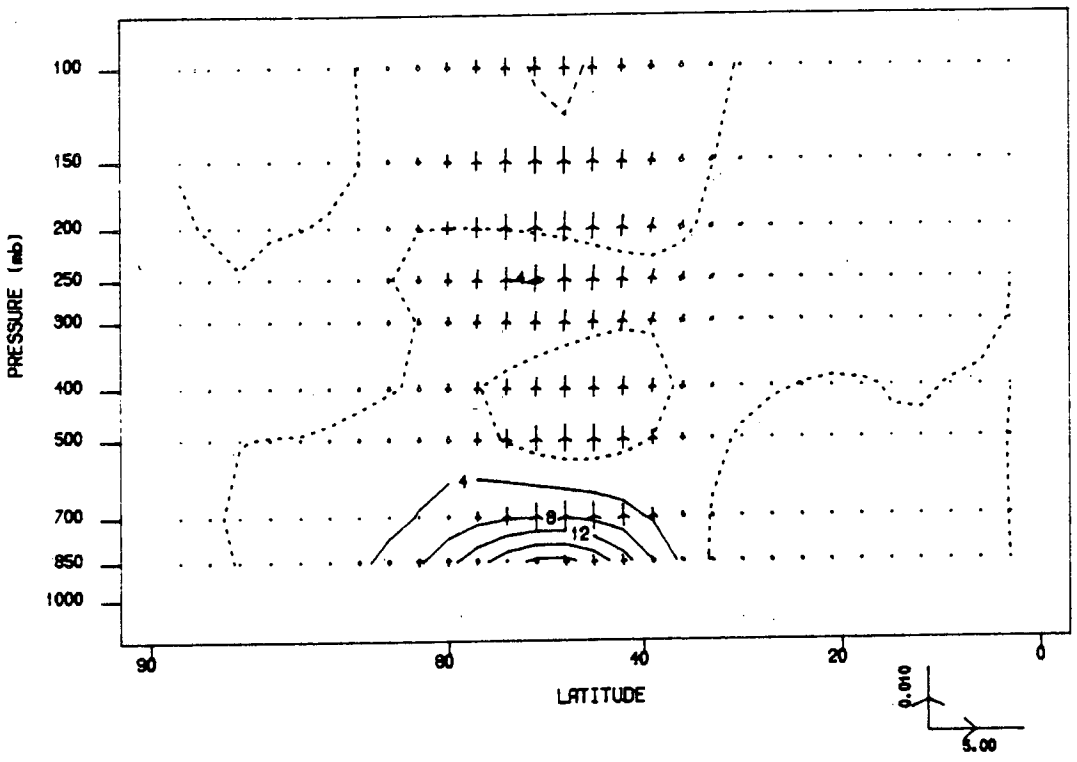

Fig. 5.31 EP cross-section for the linear response to an idealized thermal forcing in mid-latitude. The graphic convention is the same as in Fig. 5.8, but the contour interval is 4 units.

5.3.2 Nonlinear Solution

Compared with the linear solution there is no great difference found for the wave patterns at the 700 mb and 200 mb levels (they are hence not displayed here), but the wave activity flux differs from its linear counterpart. The vertical flux in the lower and middle troposphere for the nonlinear solution is much stronger than that for the linear solution. Also, the low level poleward propagation of wave activity is no longer so clear as in the linear case. In Fig. 5.32 we find a substantial equatorward propagation of wave activity at 500 mb, but a similar feature can be found only above 500 mb for the linear solution. This can also be seen in the latitudinal section of wave activity flux (Fig. 5.33) and the EP cross-section (Fig. 5.34). Corresponding to stronger vertical flux of wave activity at low levels, the convergence of EP flux at middle levels for the nonlinear solution is substantially intensified. This experiment suggests that the wave activity flux is more sensitive to nonlinearity in some circumstances than the wave patterns at the selected vertical levels.

5.4 Response to Tropical Heating

There is increasingly evidence that longitudinal variations in tropical diabatic heating can play an important role in the stationary wave structure in middle and high latitudes, as well as in the tropics (see, e.g., Simmons, 1982; Hendon

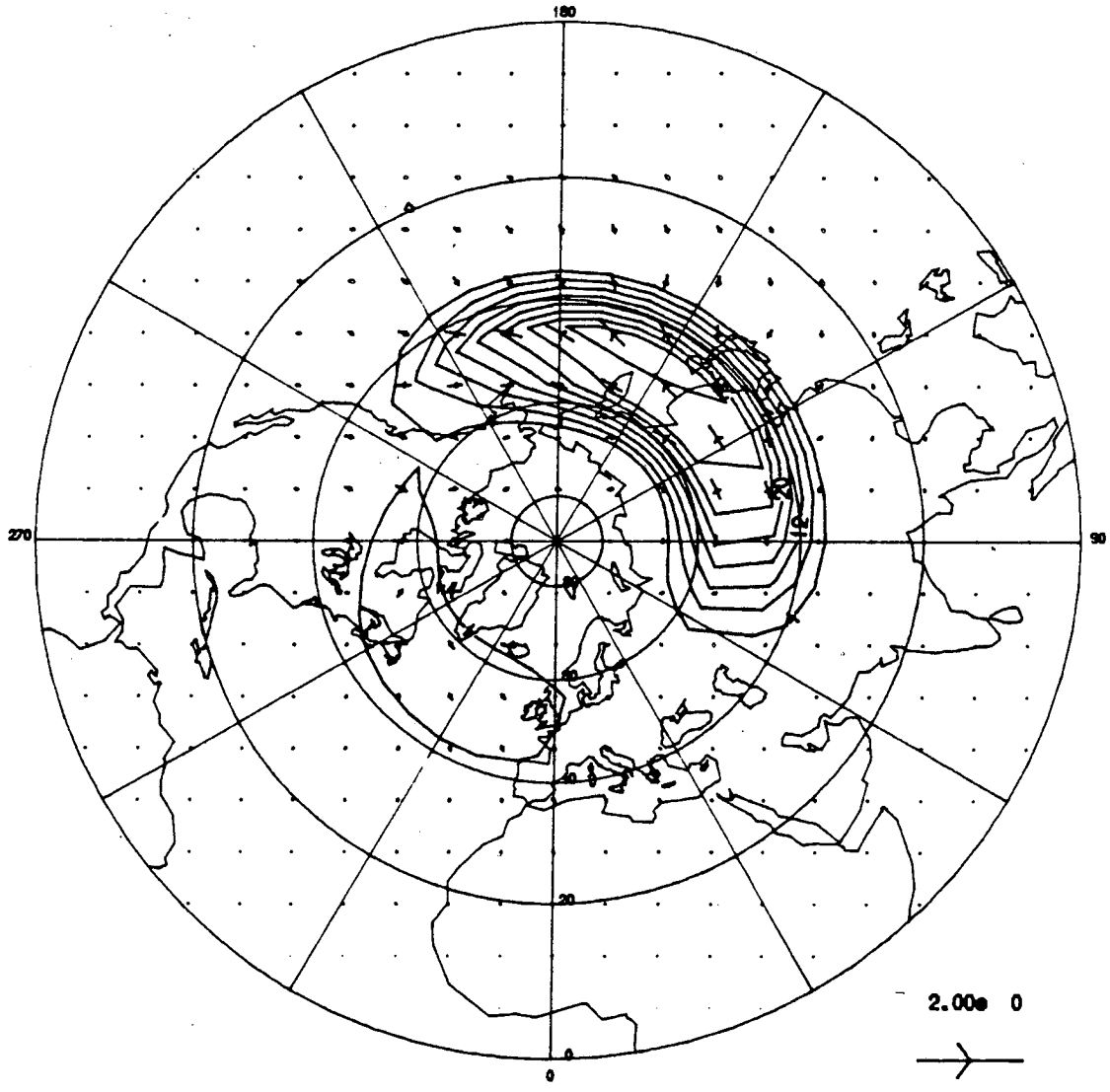

Fig. 5.32 500 mb wave activity flux as in Fig. 5.29, but for the nonlinear response.

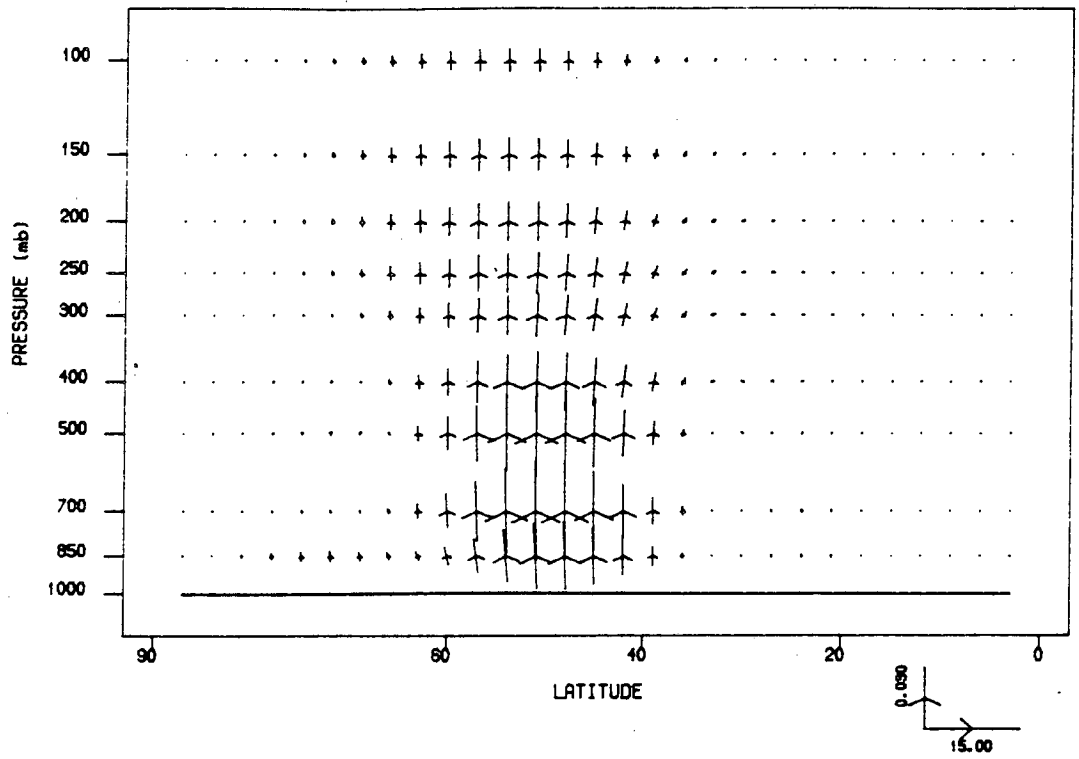

Fig. 5.33 Meridional cross-section of wave activity flux at 135°E as in Fig. 5.30, but for the nonlinear response.

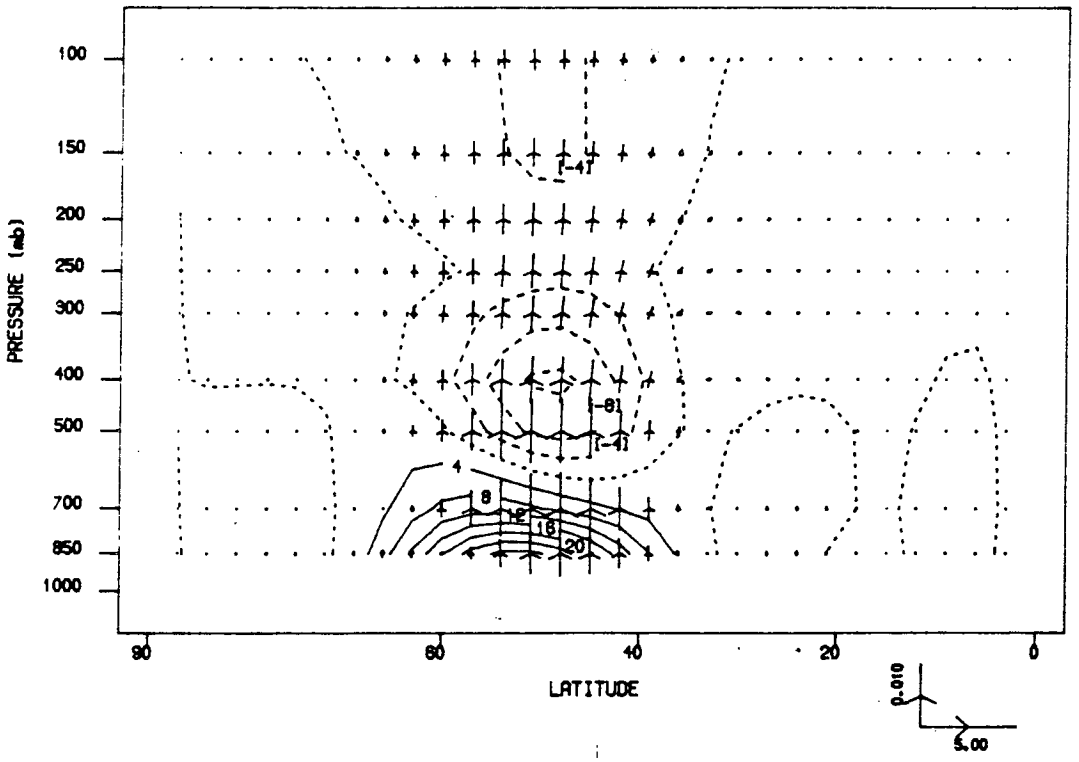

Fig. 5.34 EP cross-section as in Fig. 5.31, but for the nonlinear response.

et al, 1982; Grose et al, 1984). Therefore in this experiment we move the thermal forcing specified in the previous section to the tropical region by resetting $\varphi_1 = 0^\circ$ and $\varphi_2 = 30^\circ$ in eq. (5.2) in order to study the model atmosphere's behaviour further.

5.4.1 Linear Solution

Figs.5.35 and 5.36 show the perturbation stream field at the 700 mb and 200 mb levels for the linear solution. The extratropical response to an isolated tropical heating appears as a wavetrain propagating poleward as well as longitudinally. That the extratropical wave pattern is fairly independent of height reflects the barotropic nature of the extratropical response. These results are in general consistent with those provided by previous authors as just referenced. In contrast to the extratropical response, the tropical response itself has a baroclinic nature. The divergent (irrotational) component of horizontal velocity in the tropical region is evident, with a low level inflow to the cyclone centred to the northeast of the heating maximum and an upper-level outflow from the anticyclone. The low level cyclonic circulation spreads over the heating region, with a larger longitudinal extension to the east. The tropical response is in good qualitative agreement with the calculations by Gill (1980) and Simmons (1982). The wave activity flux differs from that for mid-latitudes thermal forcing. At low level it propagates upward and

eastward from the northern side of the heating region, in the meridional direction the flux is split into two branches propagating equatorward and poleward respectively. At upper level the wave activity flux propagates upward in the heating region and turns poleward and downward at mid-latitudes. This can be seen clearly in the EP cross-section (Fig. 5.37).

5.4.2 Nonlinear Solution

The perturbation stream fields at the 700 mb and 200 mb levels for the nonlinear solution are shown in Figs. 5.38 and 5.39 respectively. The wave pattern is in general consistent with the linear solution, but the amplitude is considerably intensified, especially for the extratropical response. Therefore the wavetrain propagating into middle and high latitudes from the tropical heating region can be seen more clearly. Similar features for the wave activity flux and the EP flux (Fig. 5.40) to the linear solution are also found, but with evident larger magnitude. In particular the poleward propagation of wave activity is stronger than in the linear solution. Just as with the high latitude topographic forcing, this experiment provides another example to suggest that the nonlinearity appears more significant when a forcing region is located somewhere with a weak basic flow than a strong basic flow.

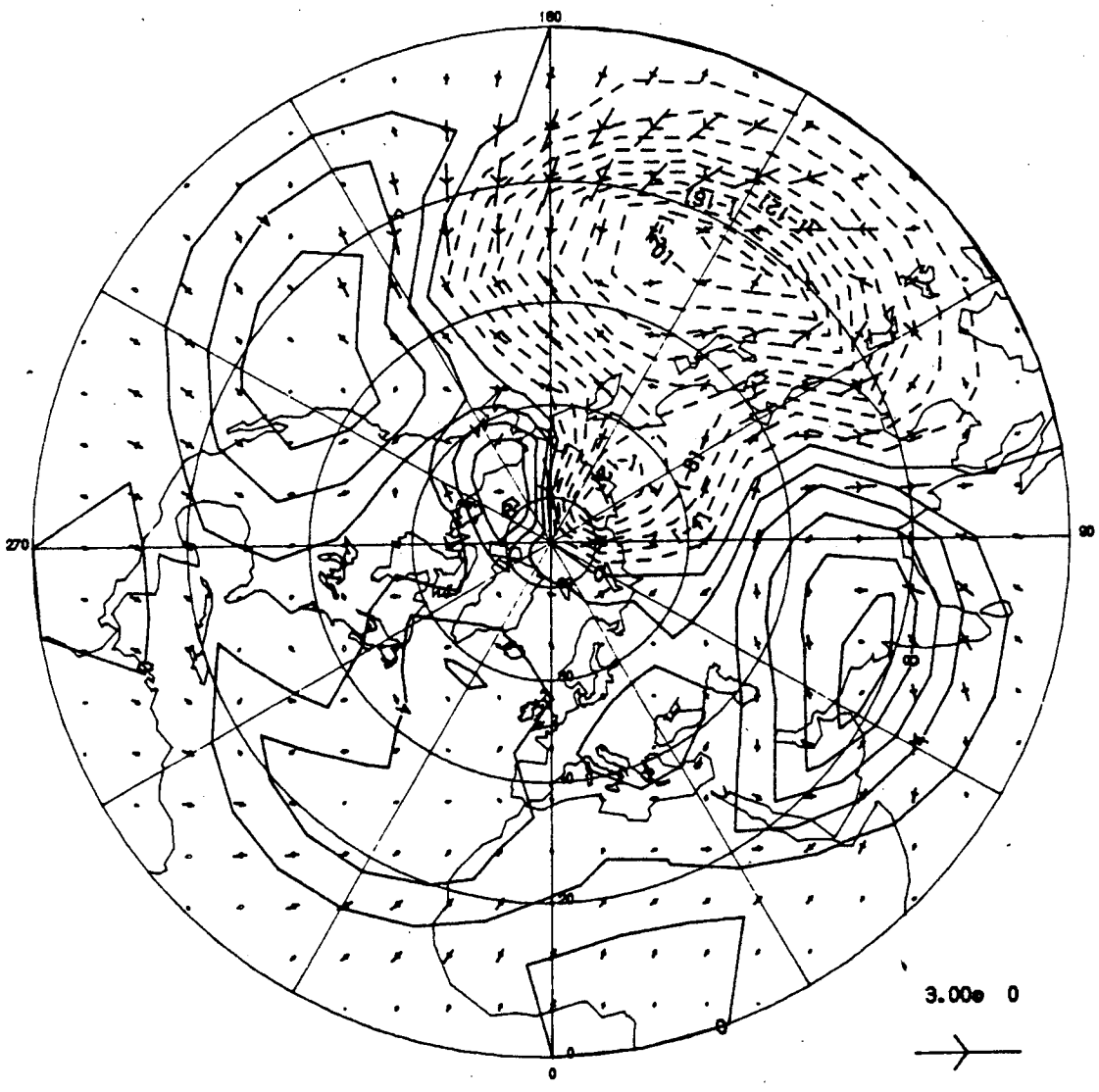

Fig. 5.35 700 mb perturbation stream field for the linear response to an idealized tropical forcing. Contours represent the perturbation streamfunction/($10^5 m^2 s^{-1}$) with an interval of 2 units.

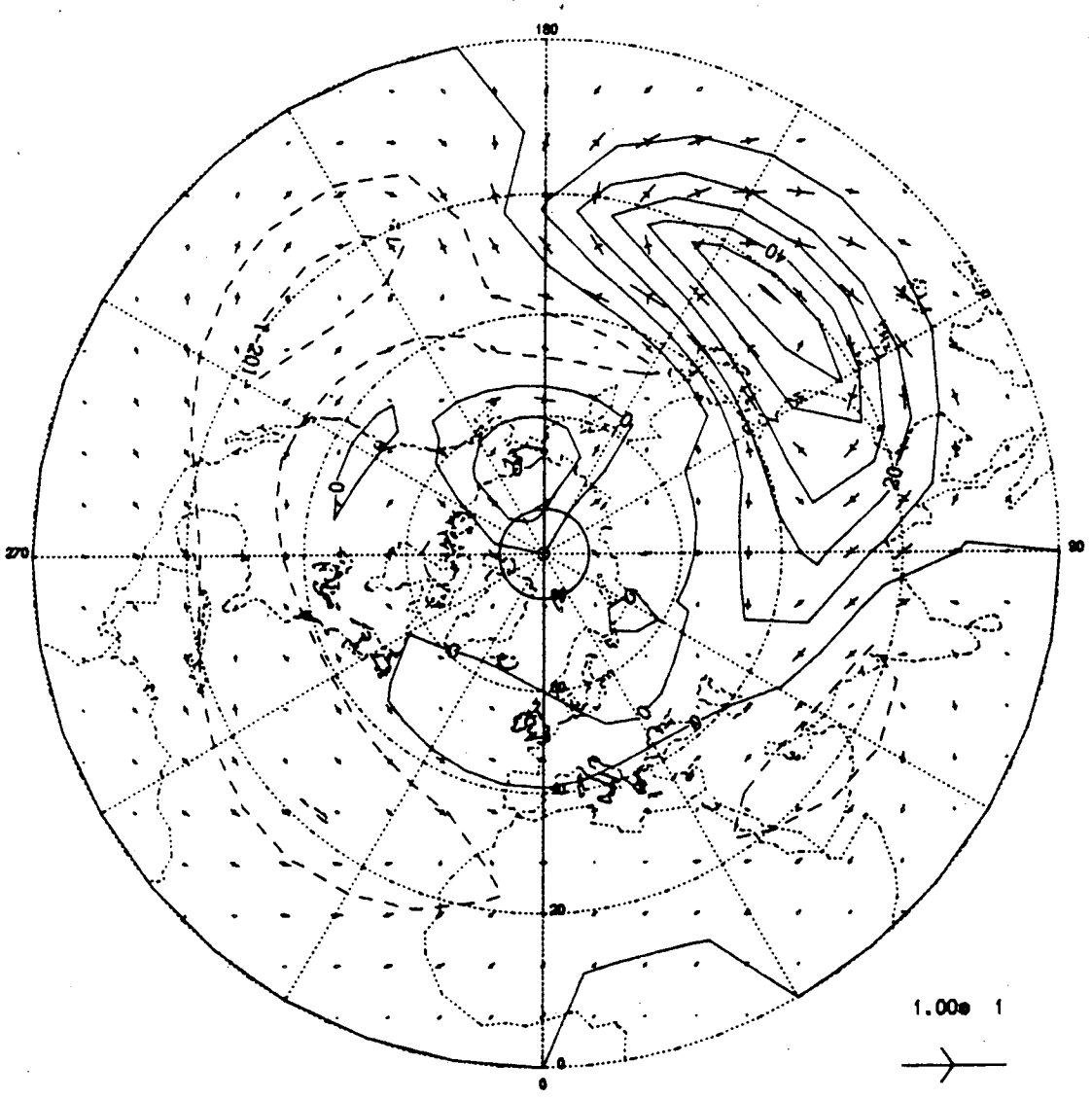

Fig.5.36 As Fig. 5.35, but for 200 mb. Contours are at intervals of 5 units.

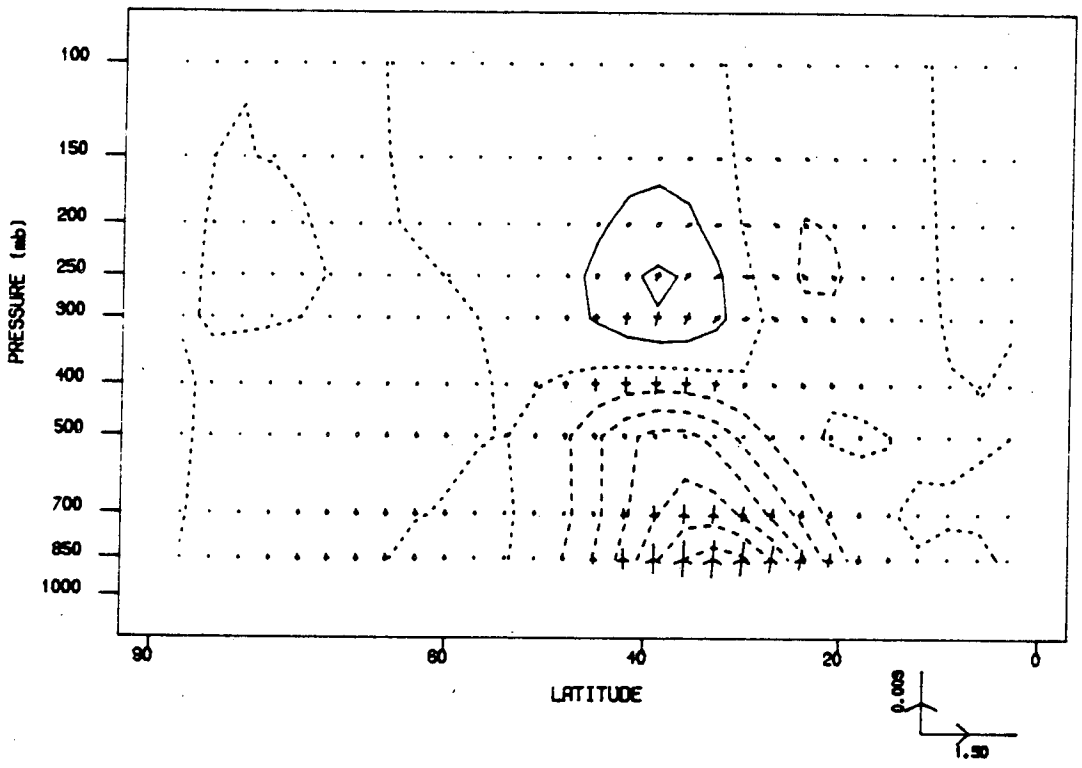

Fig. 5.37 EP cross-section for the linear response to an idealized tropical forcing. The graphic convention is the same as in Fig. 5.8, but the contour interval is 1 unit.

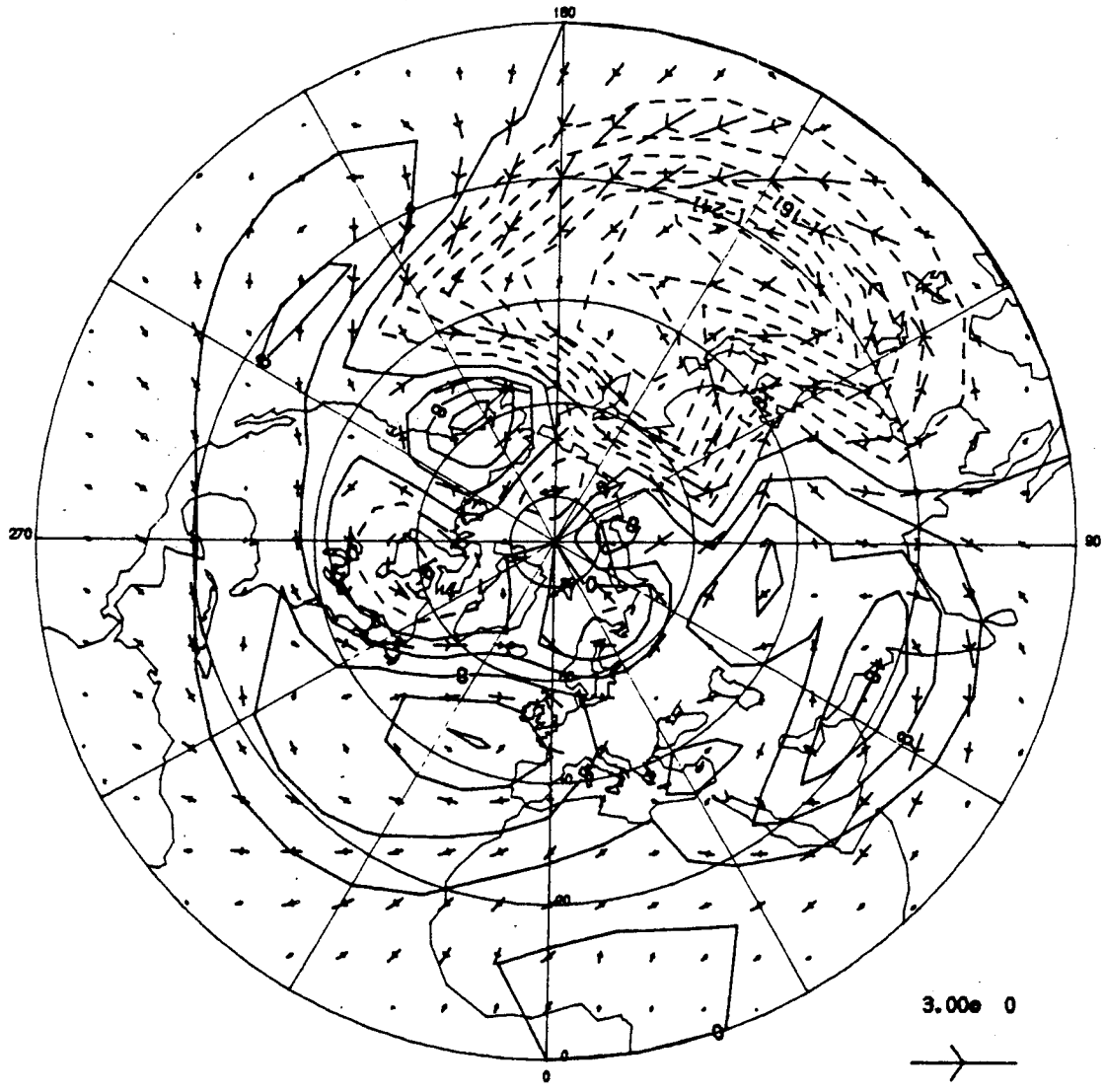

Fig.5.38 700 mb perturbation stream field as in Fig. 5.35, but for the nonlinear response. Contours are at intervals of 5 units.

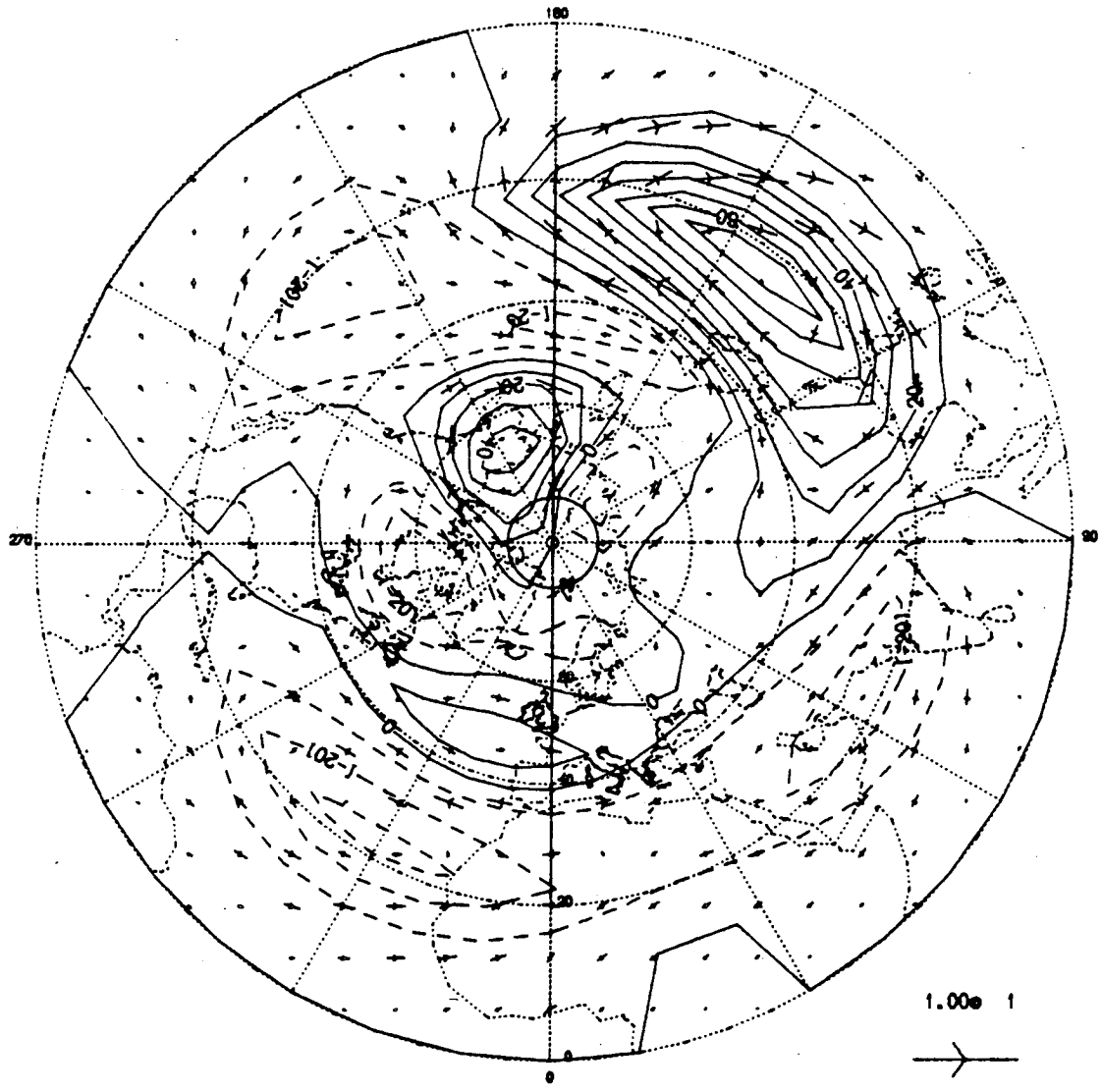

Fig. 5.39 200 mb perturbation stream field as in Fig. 5.36, but for the nonlinear response. Contours are at intervals of 10 units.

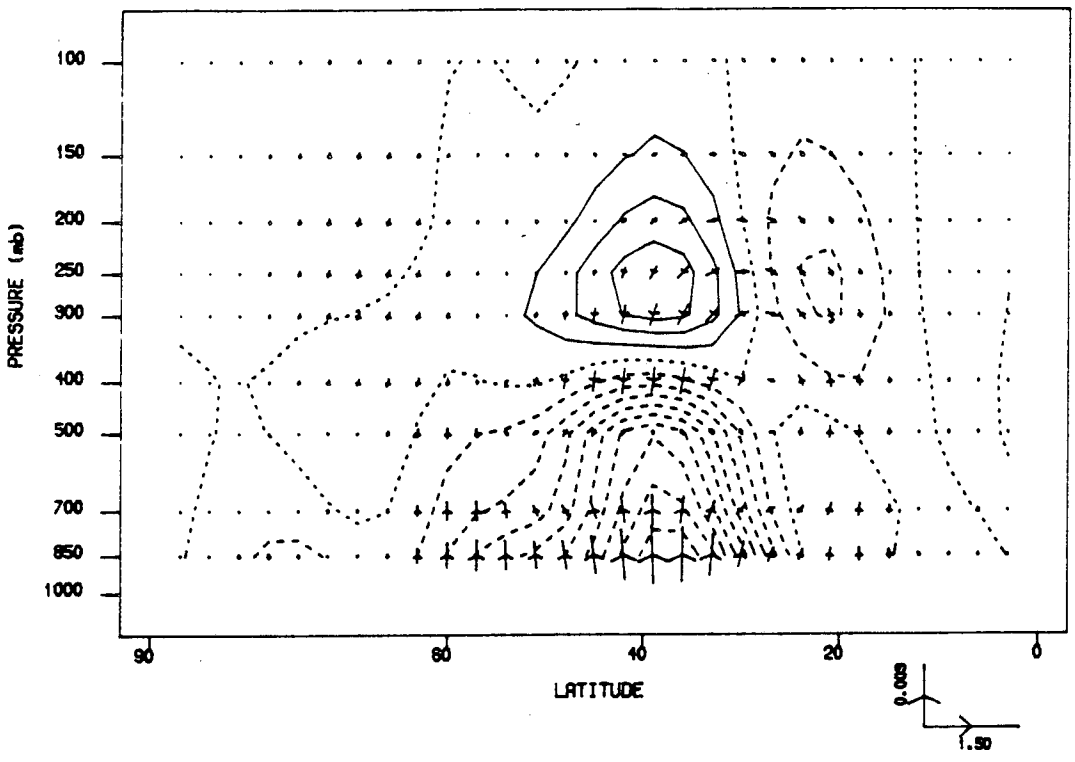

Fig. 5.40 EP cross-section as in fig. 5.37, but for the nonlinear response.

CHAPTER 6

LINEAR RESPONSE TO LARGE SCALE TOPOGRAPHY AND DIABATIC HEATING

The simple experiments for idealized orographic and thermal forcing described in the previous chapter give us a basis for understanding the steady response to the more complicated actual topography and diabatic heating. Now we go a step further to investigate the response to the actual topography in the Northern Hemisphere and the actual diabatic heating for January 1979 by using the linear model described in detail in chapter 3. This is discussed first for the two different categories of forcing separately (sections 6.1 and 6.2), and then for their combination (section 6.3).

6.1 Linear Response to Northern Hemispheric Topography

In the first place, we consider the pure orographic forcing where the Northern Hemisphere smoothed topography on the ECMWF FGGE grid is used to obtain a spectral representation of the actual topography (for a discussion of the influence of zonal resolution on the representation of the Northern Hemispheric topography, refer to Section 6.3.3). It is well known that the predominant large scale mountains in the Northern Hemisphere are the Tibetan Plateau, Rocky Mountains and the Greenland Plateau. In

Figs. 6.1 and 6.2 are shown the perturbation stream fields at the 700 mb and 200 mb levels for the linear response to actual Northern Hemispheric topography. The middle and high latitude response is dominated by zonal wavenumber two and has an evident barotropic component (the phase is almost independent of height), but the low latitude response at the upper level is much stronger than that at the lower level. From Fig. 6.2 we can see four major circulation systems at the 200 mb level in middle and low latitudes: two anticyclonic regions are located in the Atlantic, the northern and western Pacific, and two cyclonic areas in Eurasia, the eastern Pacific and North America. Fig. 6.3 is a longitudinal cross-section of perturbation geopotential height at 45°N which shows two major troughs at about 120°E and 90°W and two major ridges at about 150°W and 20°W. The troughs and ridges incline gently to the west with increasing of height. The upstream ridge and downstream trough of the Tibetan Plateau appear clearly at the lower levels. The vertical velocity at this section is displayed in Fig. 6.4, showing the two main centres of rising air over the Pacific and the eastern coast of North America, and two centres of sinking air over the Europe and the eastern Asia. The upslope and downslope current is also clear over the Tibetan Plateau.

From wave activity maps it is possible to distinguish three wavetrains propagating mainly eastward, equatorward and upward (see, e.g., Fig. 6.5). They may be related to the three large scale mountains in the Northern Hemisphere, and

the wave train originated to the north and east of the Tibetan Plateau is both more intense and more extensive than the others. The associated EP flux pattern (Fig. 6.6) is similar to that in Fig. 5.8 for an idealized mid-latitude topographic forcing. These diagnostics suggest that the major orographic forcing of the stationary planetary waves results from the Tibetan Plateau, while the Rocky mountains and Greenland Plateau seem to be of secondary importance.

In order to study further the relative importance of these three large scale mountains to the orographically forced stationary waves two experiments have been made: One removes the topography in North America, i.e., before transforming the surface geopotential height from grid point value to a spectral expression, we reset the values at those points which are located in North America equal to zero; Another removes the topography in Greenland in the same way. When the North American topography is removed, the major circulation systems influenced are the eastern Pacific cyclone and the Atlantic anticyclone. For example, at 200 mb level (Fig. 6.7) the former displaces westward with a centre at 150°W and the latter displaces eastward with a centre at 0°E, the intensity of both systems is weakened by about one third. The other systems are almost unchanged. When Greenland's topography is removed, both the anticyclonic circulation over Greenland and the cyclonic circulation to the west at 200 mb level (Fig. 6.8) are weakened by a half. and the anticyclonic circulation over the Atlantic is also weakened by one third.

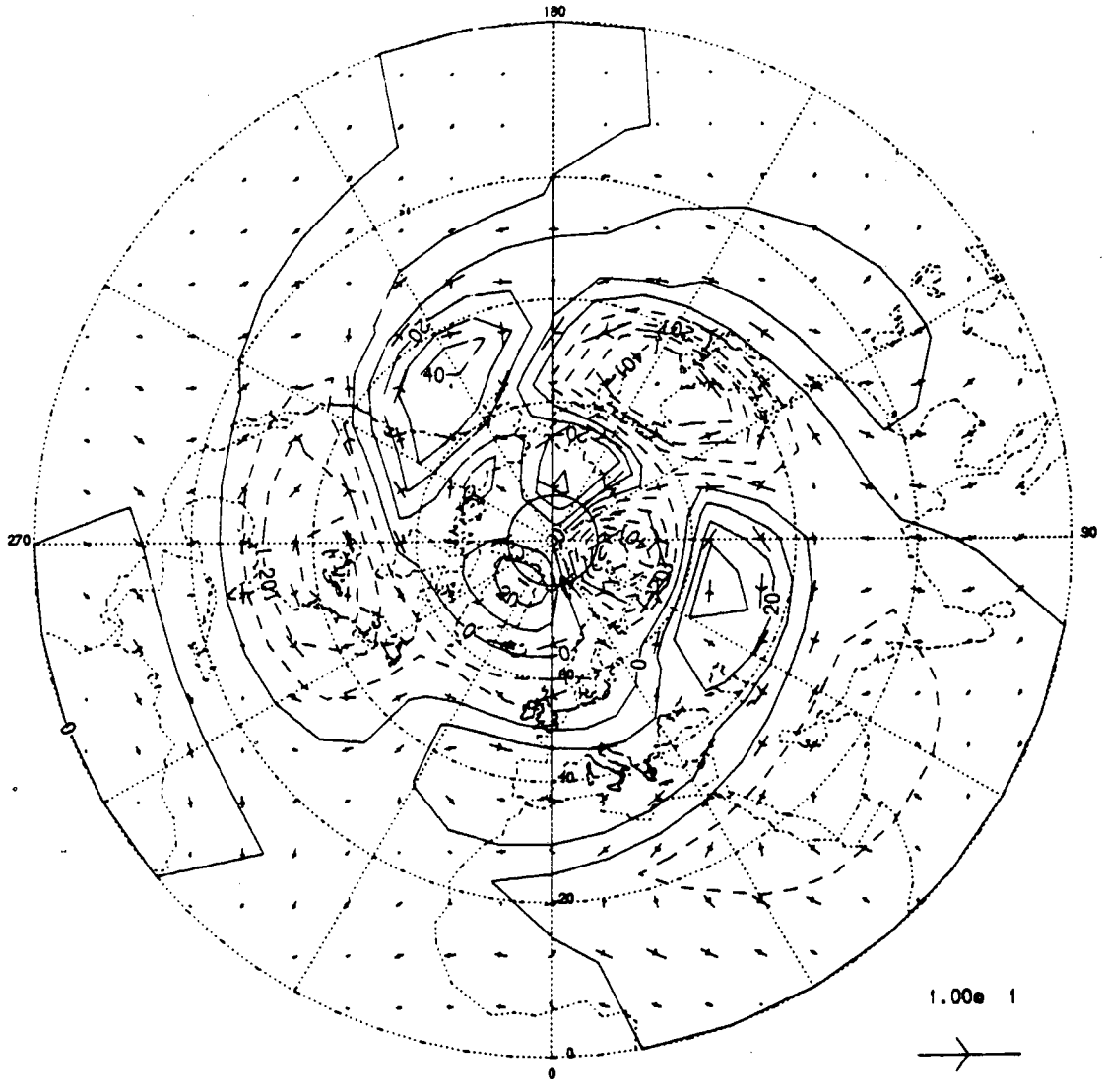

Fig. 6.1 700 mb perturbation stream field for the linear response to the Northern Hemispheric topography. Contours represent the perturbation streamfunction/($10^5 m^2 s^{-1}$) with an interval of 10 units.

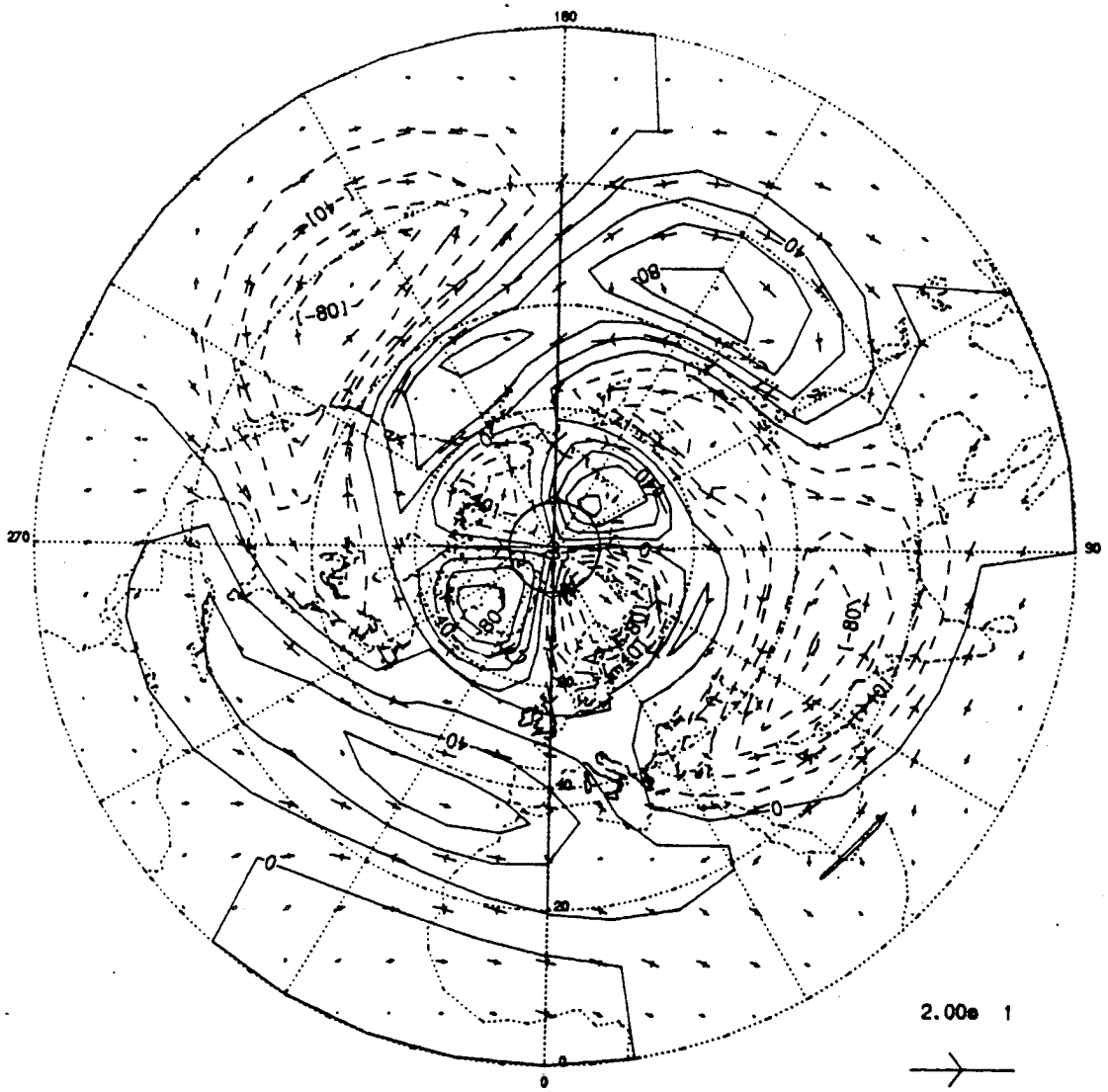

Fig. 6.2 As Fig. 6.1, but for 200 mb. Contours are at intervals of 20 units.

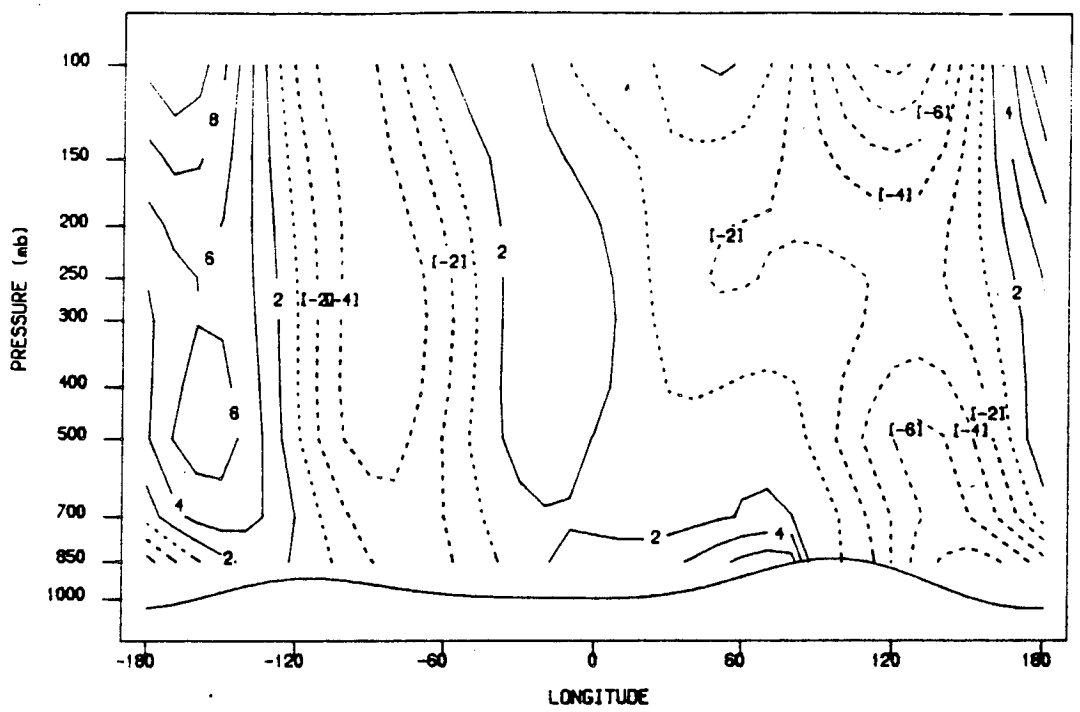

Fig. 6.3 Longitudinal cross-section of perturbation geopotential height at 45°N for the linear response to the Northern Hemispheric topography. Contour interval is 2 dam.

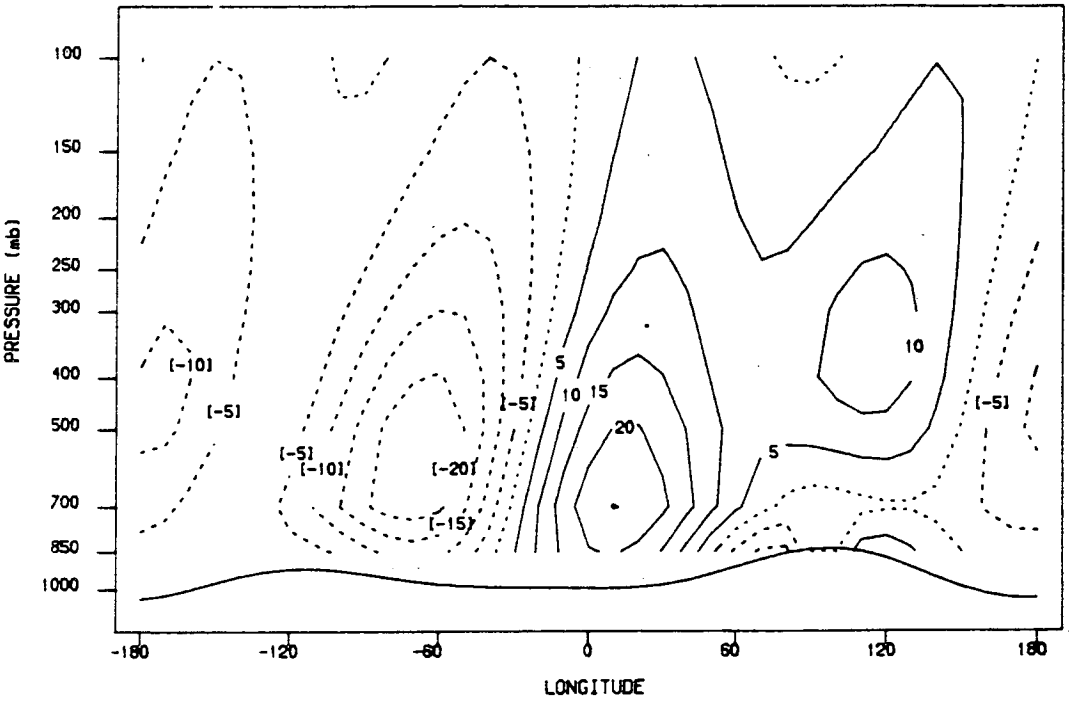

Fig. 6.4 As Fig. 6.3, but for perturbation vertical velocity. Contour interval is 5 mbd^{-1}.

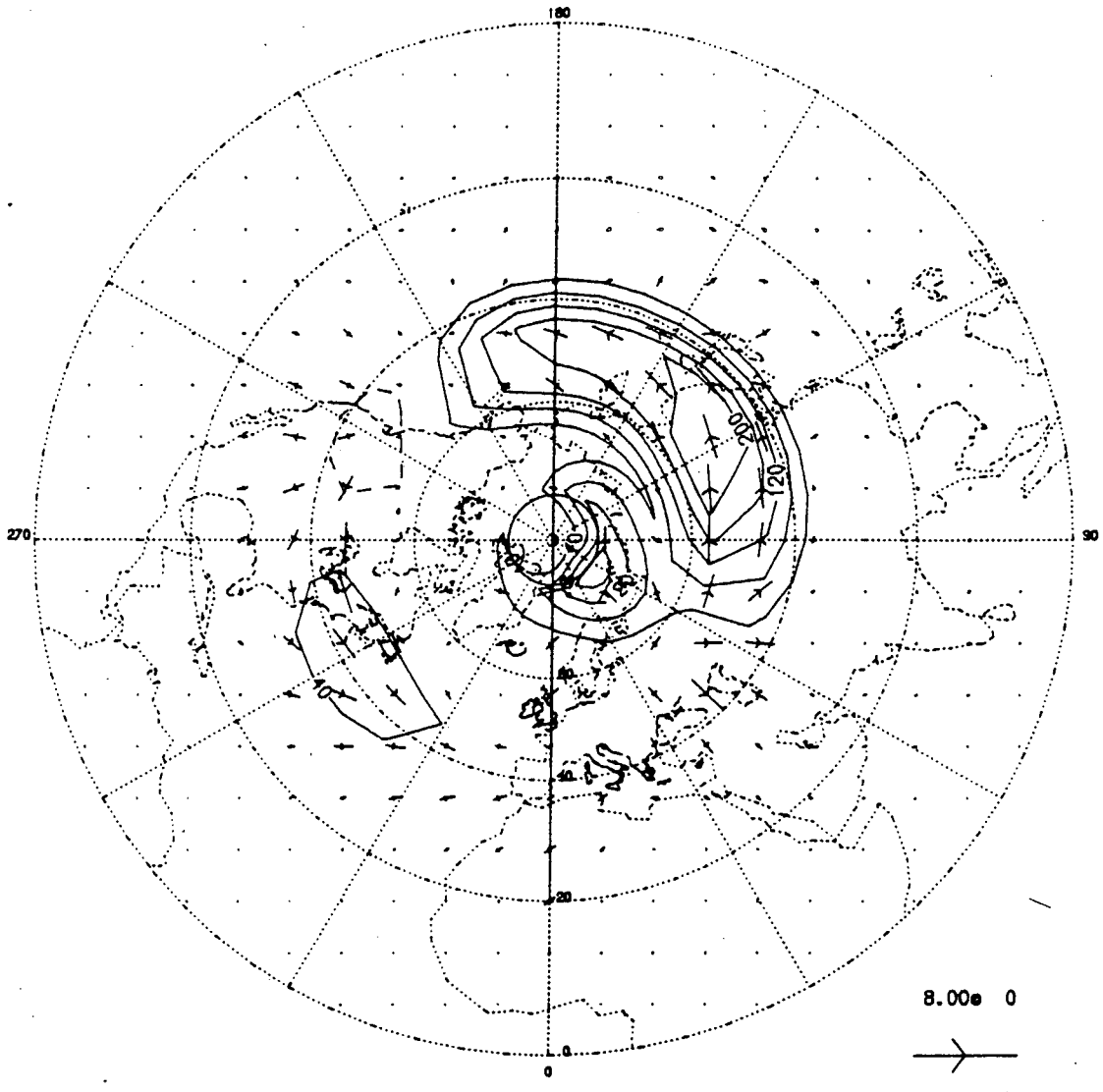

Fig. 6.5 Wave activity flux **F** at 850 mb for the linear response to the Northern Hemispheric topography. The graphic convention is the same as in Fig. 5.6, but the contour interval is 40 units.

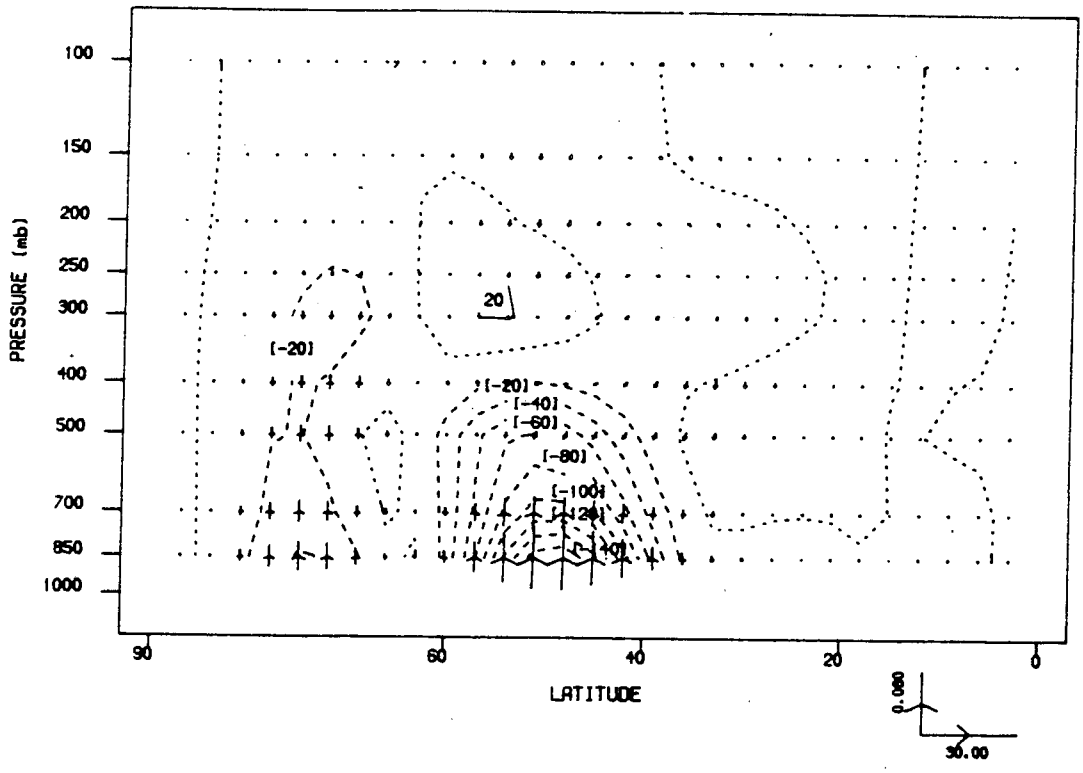

Fig. 6.6 EP cross-section for the linear response to the Northern Hemispheric topography. The graphic convention is the same as in Fig. 5.8, but the contour interval is 20 units.

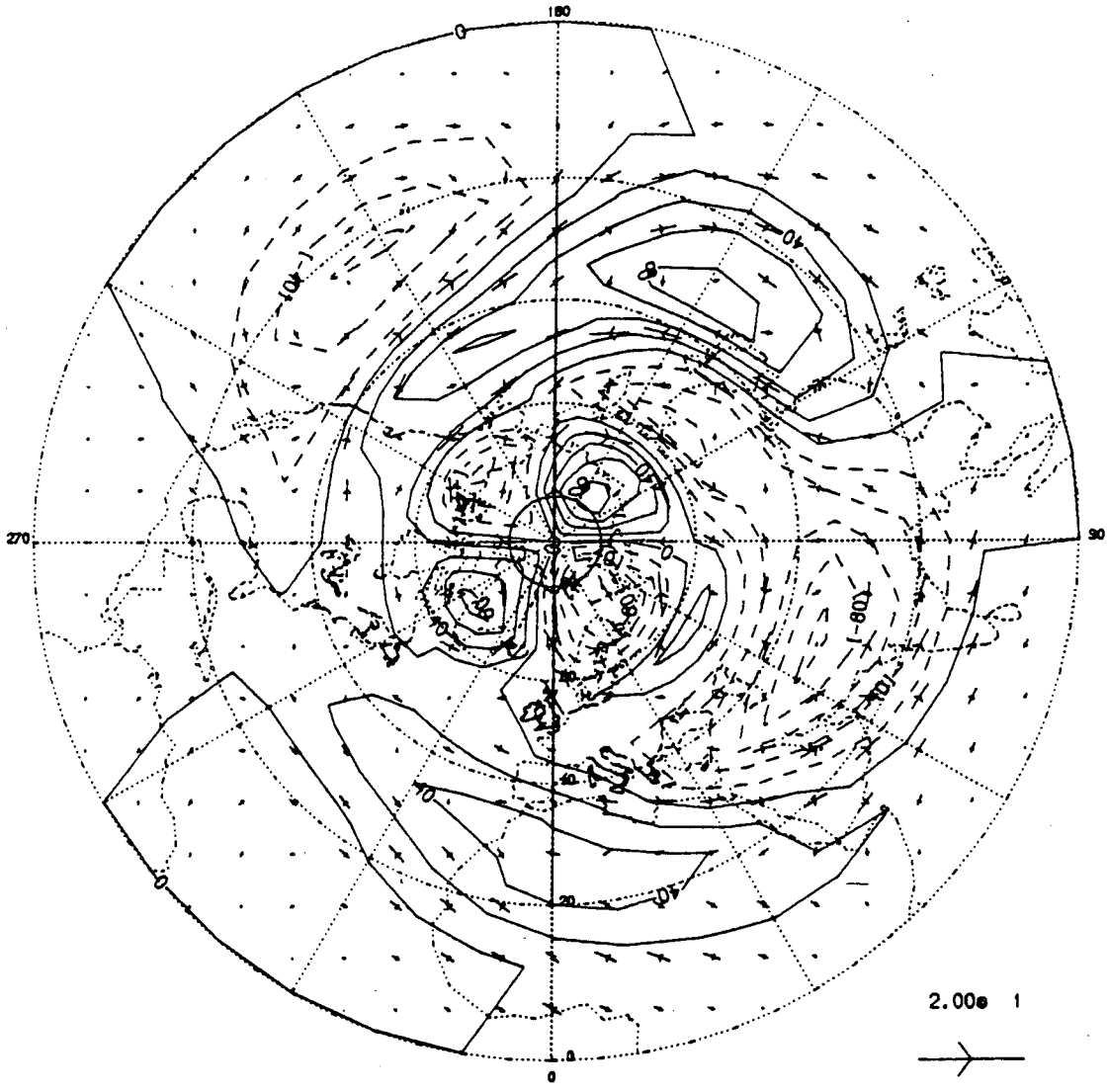

Fig. 6.7 200 mb perturbation stream field as in Fig. 6.2, but the topography of North America is removed.

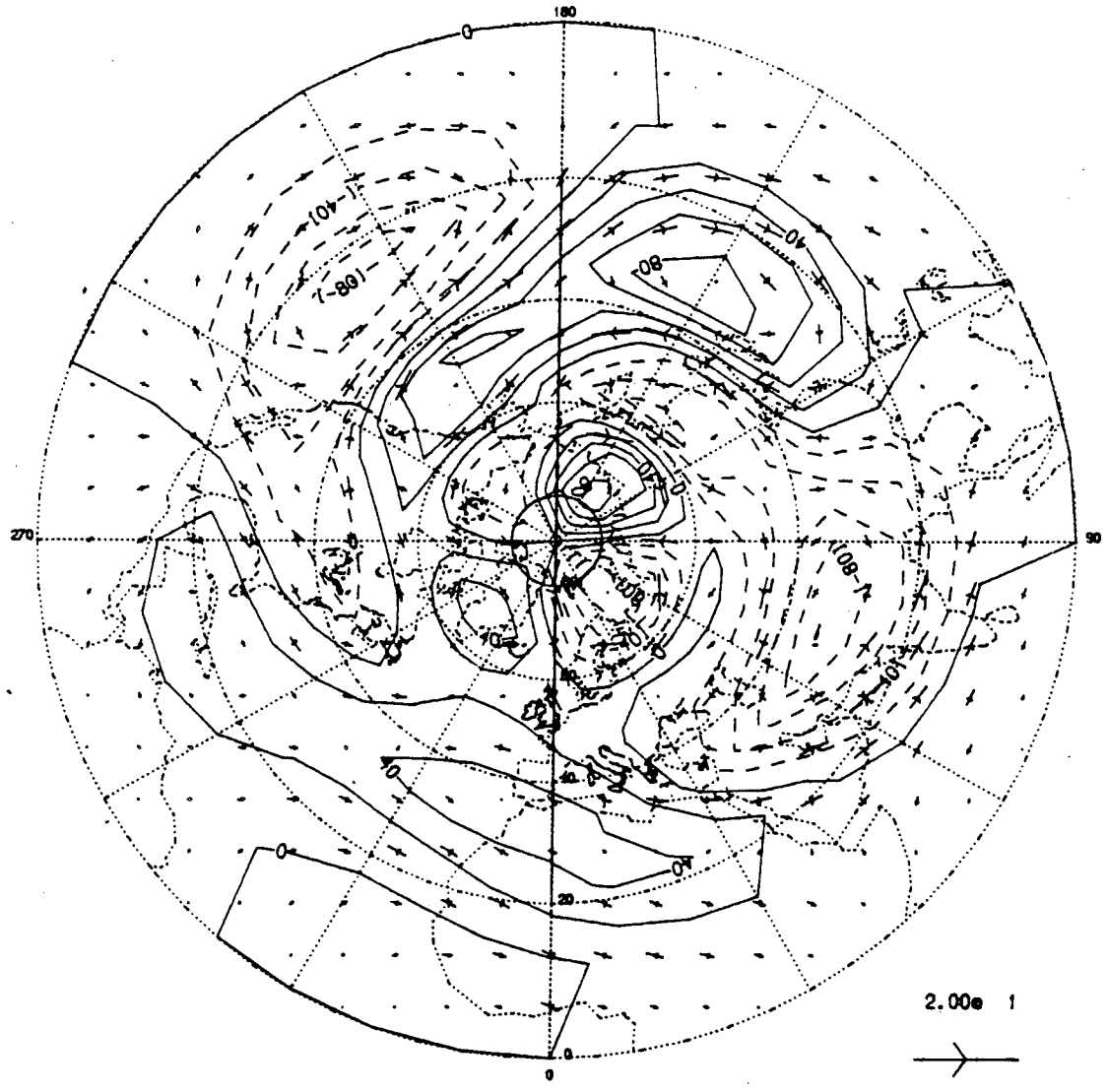

Fig. 6.8 200 mb perturbation stream field as in Fig. 6.2, but the topography of Greenland is removed.

Other systems are little affected. These experiments confirm that the Rockies and the Greenland Plateau are of secondary importance on the maintenance of orographically forced stationary waves in the Northern Hemisphere compared with the Tibetan Plateau.

6.2 Linear Response to Diabatic Heating in January 1979

The problem of thermal forcing is complicated by the dependence of the response on the vertical and horizontal structure of the diabatic heating field. In order to calculate the response of a model atmosphere to actual diabatic heating in winter, we need a three-dimensional distribution of heating rates. The vertically integrated heating rates for January 1979 prepared from NMC FGGE Level IIIa operational data set and also ECMWF FGGE Level IIIb analysis by Johnson et al (1985) are used as the horizontal distribution of diabatic heating and its vertical variation is given by the analytical expression (4 .13). The use of two data sets is in consideration of the fact that the actual diabatic heating distribution in the troposphere is difficult to calculate accurately. Therefore we will discuss the respective results using the heating fields derived from different data sources. Their similarity may contribute to a better confidence in the results.

6.2.1 Heating Field Derived from FGGE IIIa Data

The horizontal variation of the mean diabatic heating rate in January 1979 derived from FGGE IIIa data is illustrated in Fig. 6.9. The major heat sources are found in the following areas: a) Along the ITCZ over the Pacific, b) the North Pacific and c) the eastern coasts of North America and the North Atlantic. The diabatic cooling covers larger areas than the heat sources. As we might expect, the longitudinal variation of heat sources and sinks reflects mainly the spatial distribution of precipitation and surface heat fluxes.

The perturbation stream fields at the 700 mb and 200 mb levels for the linear response to this diabatic heating are shown in Figs. 6.10 and 6.11 respectively. At low-levels there are two cyclonic and two anticyclonic circulation systems mainly over the oceans and the continents in correspondence with the horizontal distribution of heat sources and sinks. At upper level these systems are reversed. The amplitude of this thermally forced wave is comparable to that forced by the Northern Hemisphere topography. A longitudinal cross-section of perturbation geopotential height at 45°N is presented in Fig. 6.12, showing two ridges around 130°W and 0°E and two troughs around 135°E and 60°W. The trough over eastern Asia is much more intense than that over the eastern coast of North America. Another noteworthy feature in Fig. 6.12 is

the obvious westward tilt of phase with height. Compared with topographic forcing, we find that the response to the thermal forcing has a stronger baroclinic nature.

The wave activity flux (see, e.g. , Fig. 6.13) shows two distinct wavetrains over the North Pacific and the North Atlantic. Both are spreading eastward and upward, but their meridional propagation is in opposite directions. This can be understood from the horizontal distribution of diabatic heating (Fig. 6.9). There is a quite strong heat source over the tropical Pacific, while a quite extensive heat sink is found over the tropical Atlantic. Therefore the Pacific wavetrain propagates poleward and the Atlantic wavetrain equatorward. This wave activity flux pattern suggests that the longitudinal variation of diabatic heating in the tropical region has significant influence on the stationary planetary wave in middle and high latitudes. In addition there is a downward flux in northern Asia at 850 mb, but all vertical flux turns upward at 700 mb and above (not shown here).

The associated EP flux (Fig. 6.14) is also quite different to that for actual topographic forcing (Fig. 6.6). The former has a stronger vertical flux at upper levels than the latter, and evident convergent regions of EP flux are found in the middle and upper troposphere as well as in the lower stratosphere in Fig. 6.14. This supports the suggestion in section 5.3.1, that is, the thermal forcing in the troposphere makes a considerable contribution to the maintenance of the vertically propagating stationary

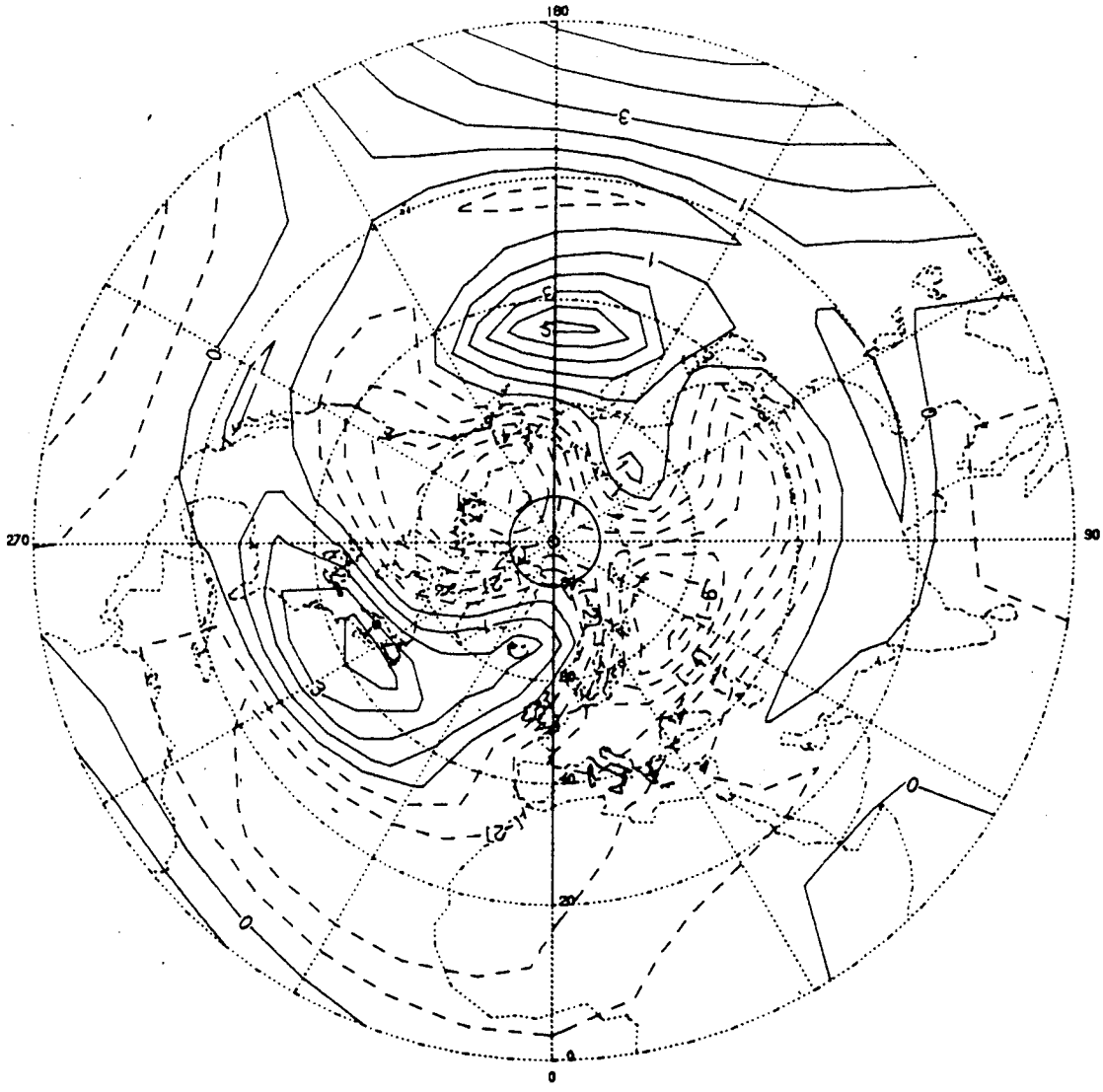

Fig.6.9 The horizontal distribution of vertically integrated diabatic heating in January 1979 derived from FGGE IIIa data by Johnson. The original data is on 2.5°x2.5° grid points, which have been transformed into a spectral expression with truncation indices M=3 and J=11. Contour interval is 0.5 Kd^{-1}.

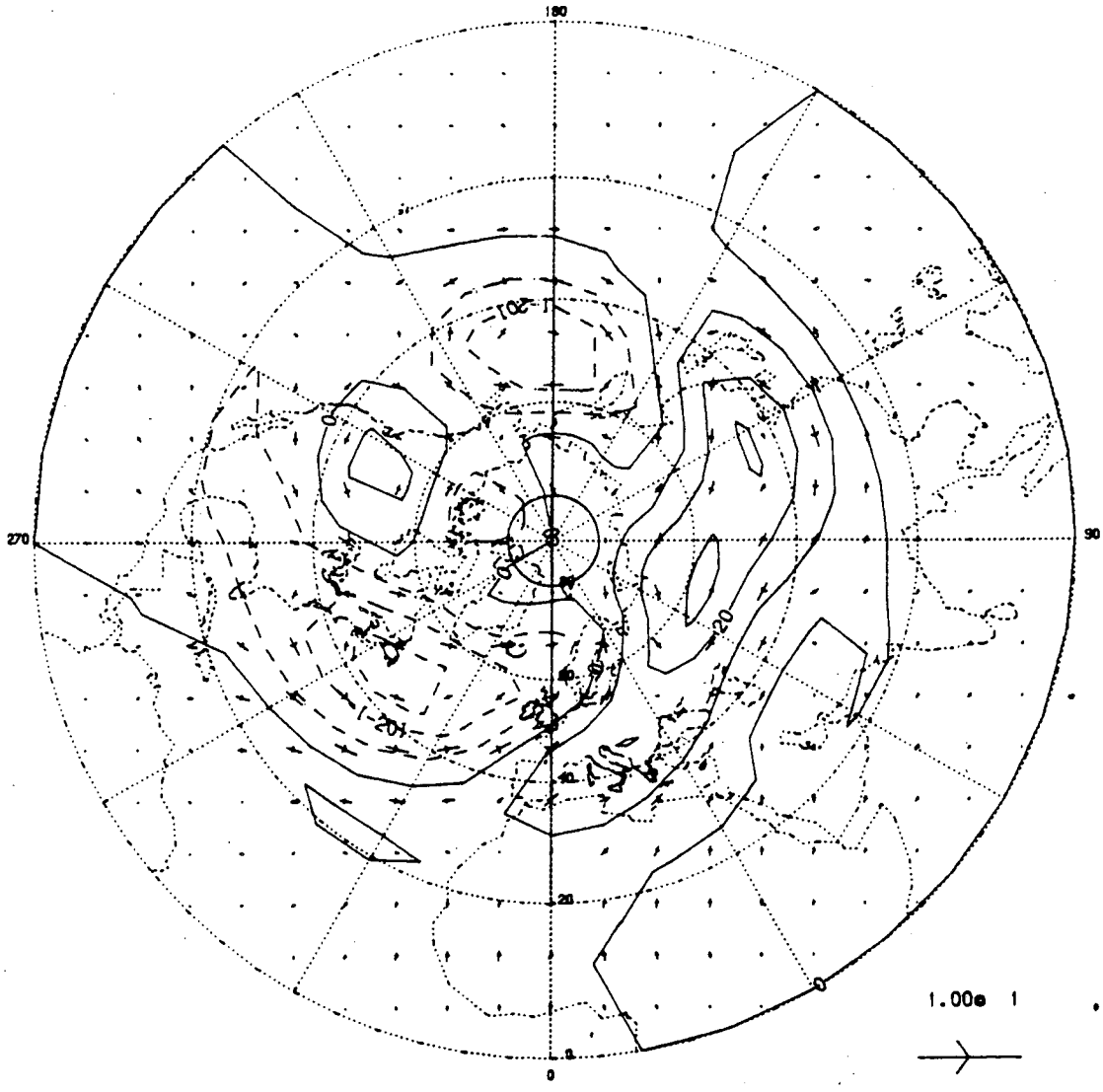

Fig. 6.10 700 mb perturbation stream field for the linear response to the actual diabatic heating field derived from FGGE IIIa data. Contours represent the perturbation streamfunction/($10^5 m^2 s^{-1}$) with an interval of 10 units .

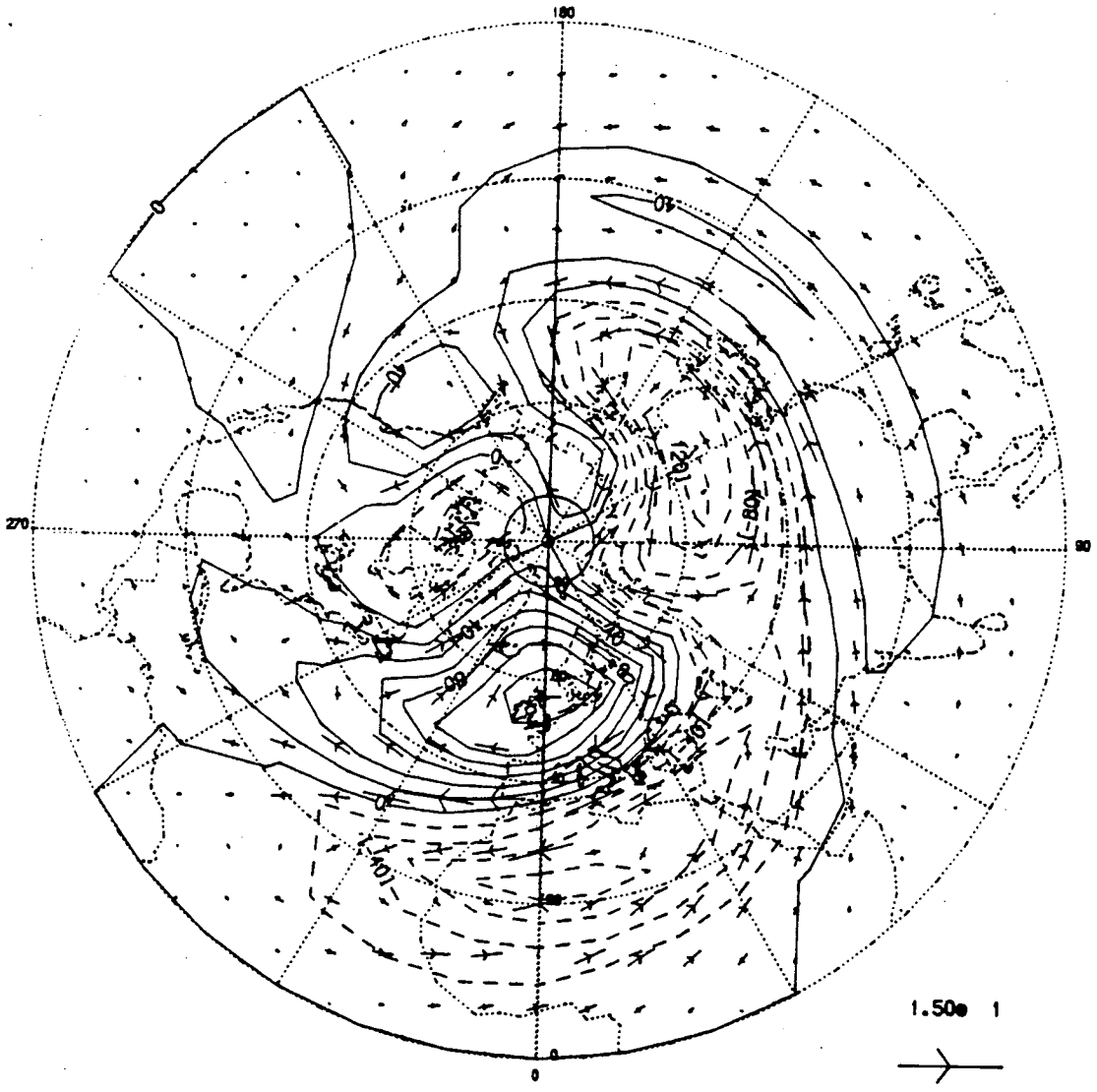

Fig. 6.11 As Fig. 6.10, but for 200 mb. Contours are at intervals of 20 units.

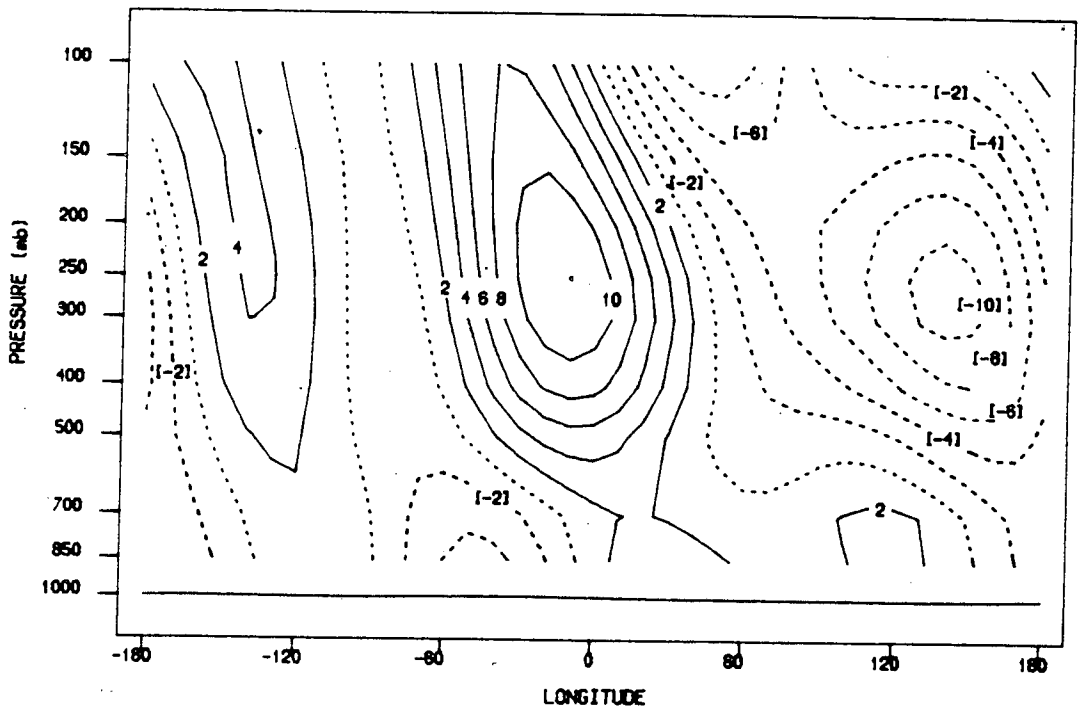

Fig. 6.12 Longitudinal cross-section of perturbation geopotential height at 45°N for the linear response to the diabatic heating field derived from FGGE IIIa data. Contour interval is 2 dam.

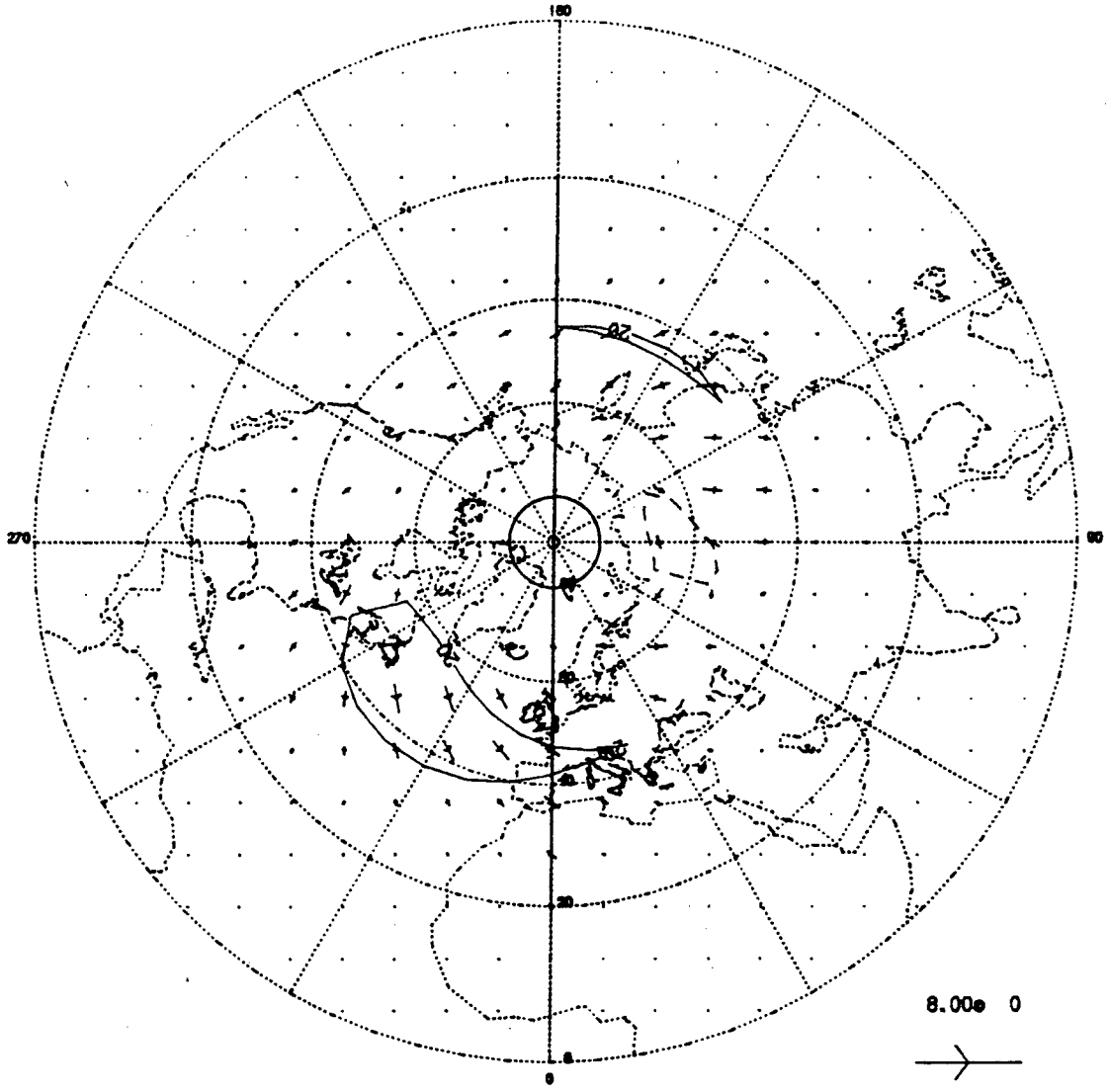

Fig. 6.13 850 mb wave activity flux as in Fig. 6.5, but for the linear response to the diabatic heating field derived from FGGE IIIa data. Contours are at intervals of 20 units.

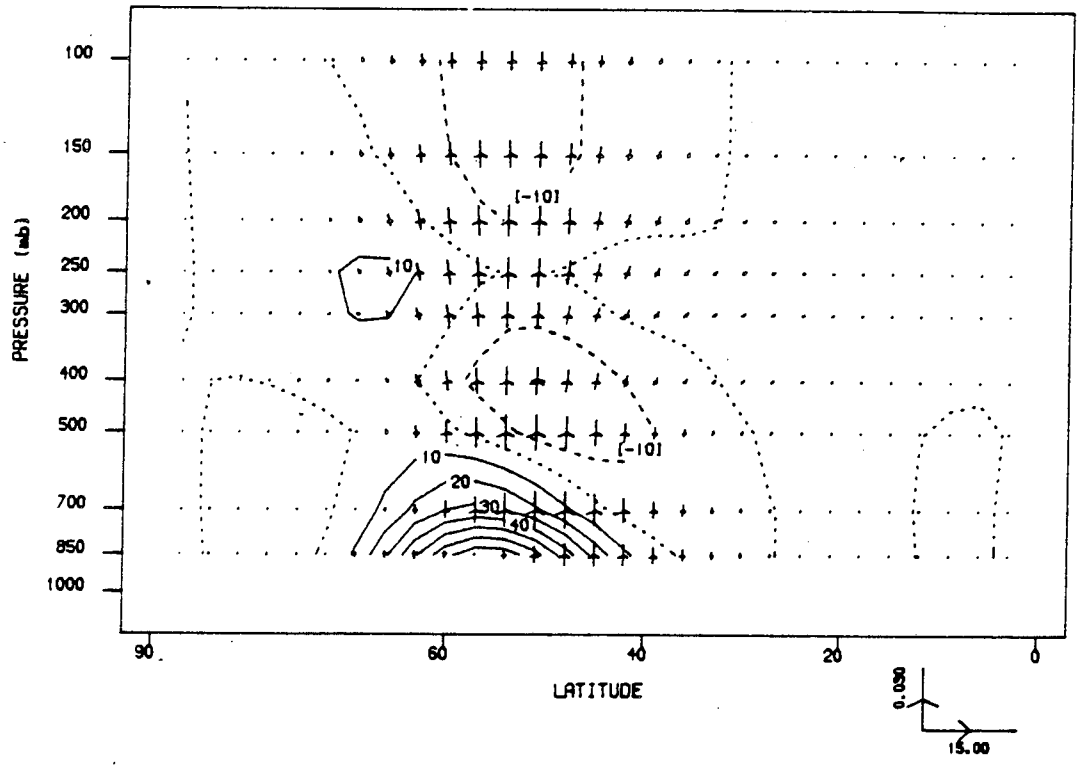

Fig. 6.14 EP cross-section for the linear response to the diabatic heating field derived from FGGE IIIa data. Contours are at intervals of 10 units.

planetary waves in the stratosphere. In the meridional direction the EP flux splits into two branches: the southern one points towards the equator and the northern one towards the pole.

6.2.2 Heating Field Derived from FGGE IIIb Data

An alternative representation for the vertically integrated mean diabatic heating in January 1979 was derived from ECMWF's Level IIIb analysis and illustrated in Fig. 6.15. The predominant features in Fig. 6.15 are in general consistent with those in Fig. 6.9, but with a more extensive tropical heat source (positive deviation from the zonal mean is still concentrated in the tropical Pacific) and a more intense heat source in the North Pacific.

The perturbation stream fields at the 700 mb and 200 mb levels for the linear response to this alternative heating field are shown in Figs. 6.16 and 6.17 respectively. The wave patterns shown in these figures are similar to those in Figs. 6.10 and 6.11, but the amplitude of different circulation systems is either intensified or weakened depending on their geographical location. The most significant difference is found in the Pacific, both low-level cyclonic and upper-level anticyclonic circulations are greatly intensified. In Figs. 6.18 and 6.19 are shown the wave activity fluxes at the 850 mb and 200 mb levels respectively. The main difference for the wave propagation

is also found over the Pacific. As previously mentioned the linear response to the FGGE IIIa heating field displays a poleward meridional propagation of wave activity over the Pacific at the 850 mb, 700 mb and 500 mb levels, only a weak equatorward propagation found at the 200 mb level (not shown here). But for the FGGE IIIb heating field there is an evident equatorward propagation of wave activity over the Pacific at the 500 mb level and above. This may result from the more intense heat source over the northern Pacific and the relatively weaker heat source (refer to the deviation from the zonal mean) over the tropical Pacific. The associated EP cross-section is shown in Fig. 6.20, which is also similar to Fig. 6.14 except with weaker convergence at middle and upper levels.

6.3 Linear Response to Topography and Diabatic Heating

We consider further the linear response to combined orographic and thermal forcing, i.e., both the Northern Hemisphere topography and mean diabatic heating rate in January 1979 are included in the model. This solution is simply a linear superposition of the linear solutions for the pure orographic and the pure thermal forcing. As in the previous section, we will discuss the linear response to the Northern Hemispheric topography combined with FGGE IIIa and FGGE IIIb heating fields separately.

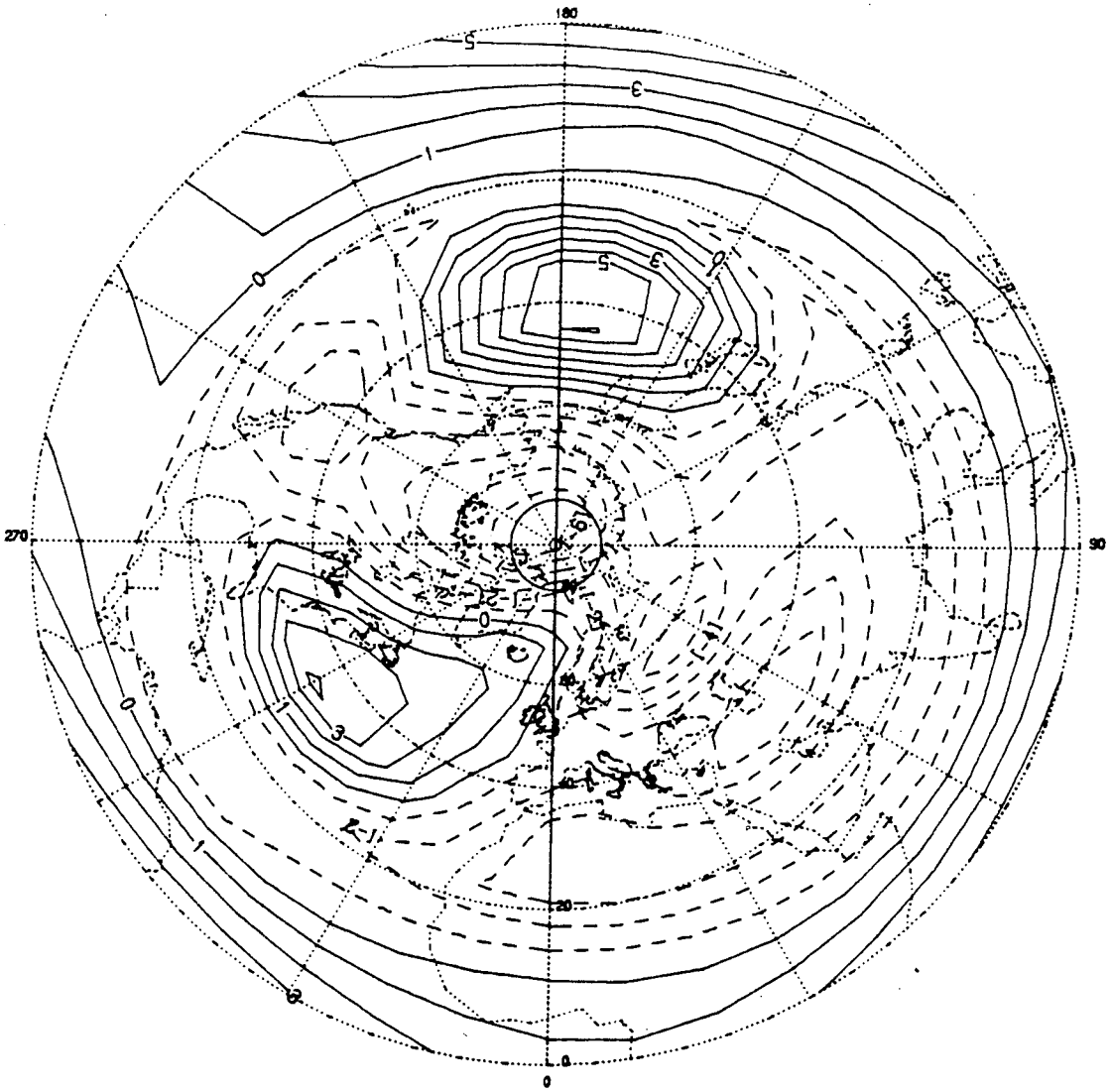

Fig. 6.15 The horizontal distribution of diabatic heating as in Fig. 6.9, but derived from FGGE IIIb analysis. The original data is on 1.875°x1.875° grid points and transformed into a spectral expression with the same resolution as in Fig. 6.9. Contour interval is 0.5 Kd^{-1}.

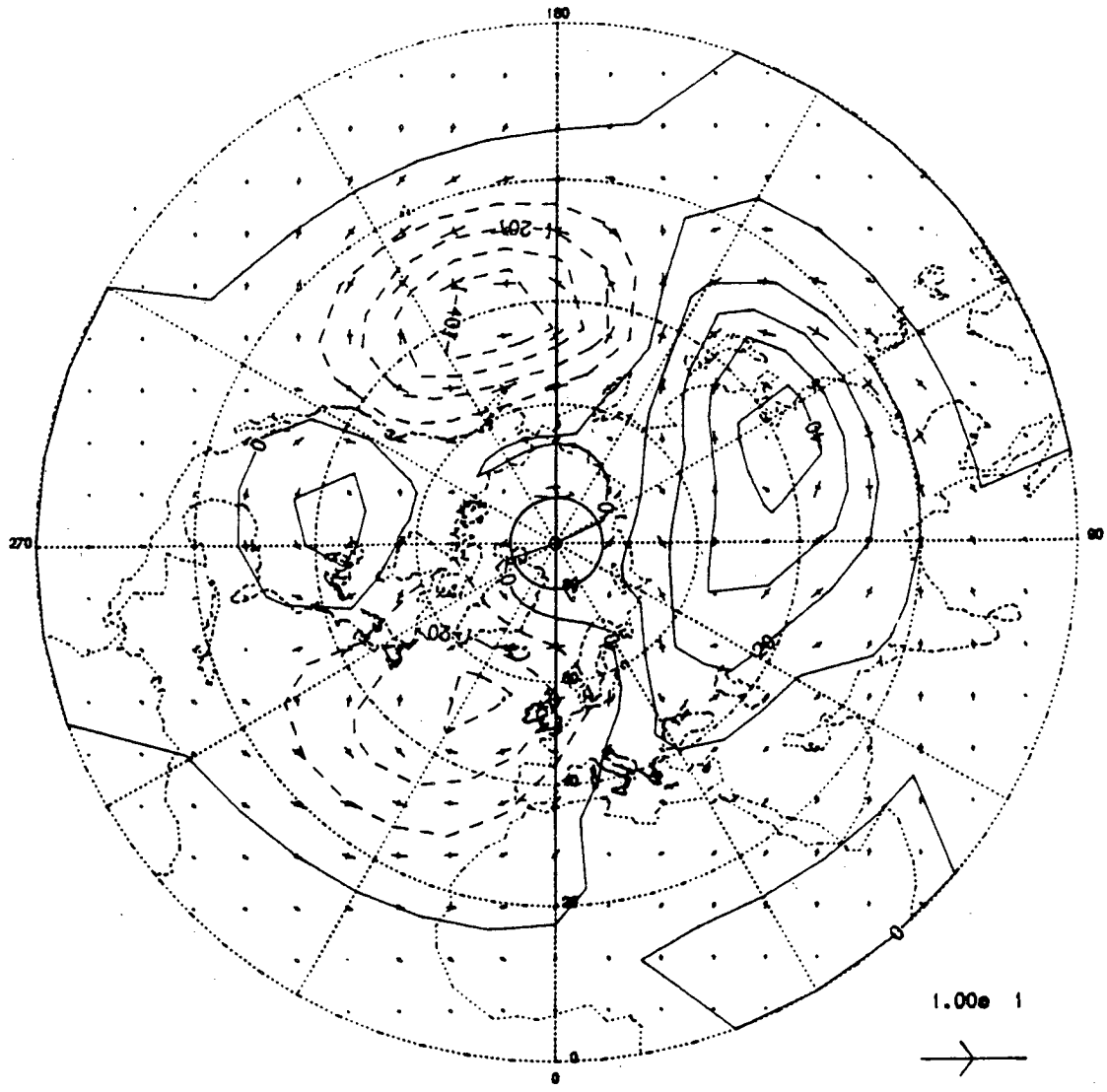

Fig. 6.16 700 mb perturbation stream field as in Fig. 6.10, but for the diabatic heating derived from FGGE IIIb data.

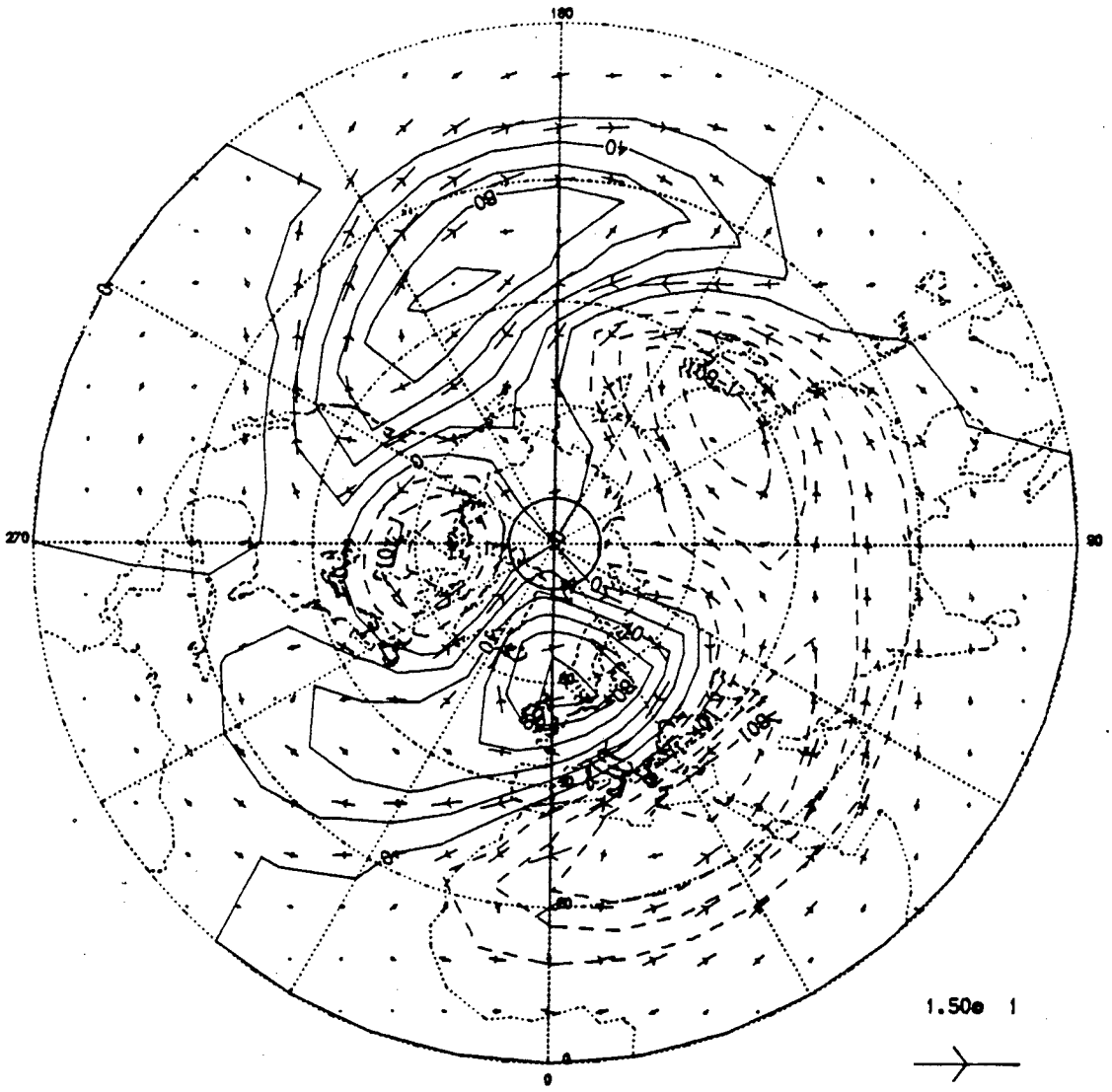

Fig. 6.17 200 mb perturbation stream field as in Fig. 6.11, but for the diabatic heating derived from FGGE IIIb data.

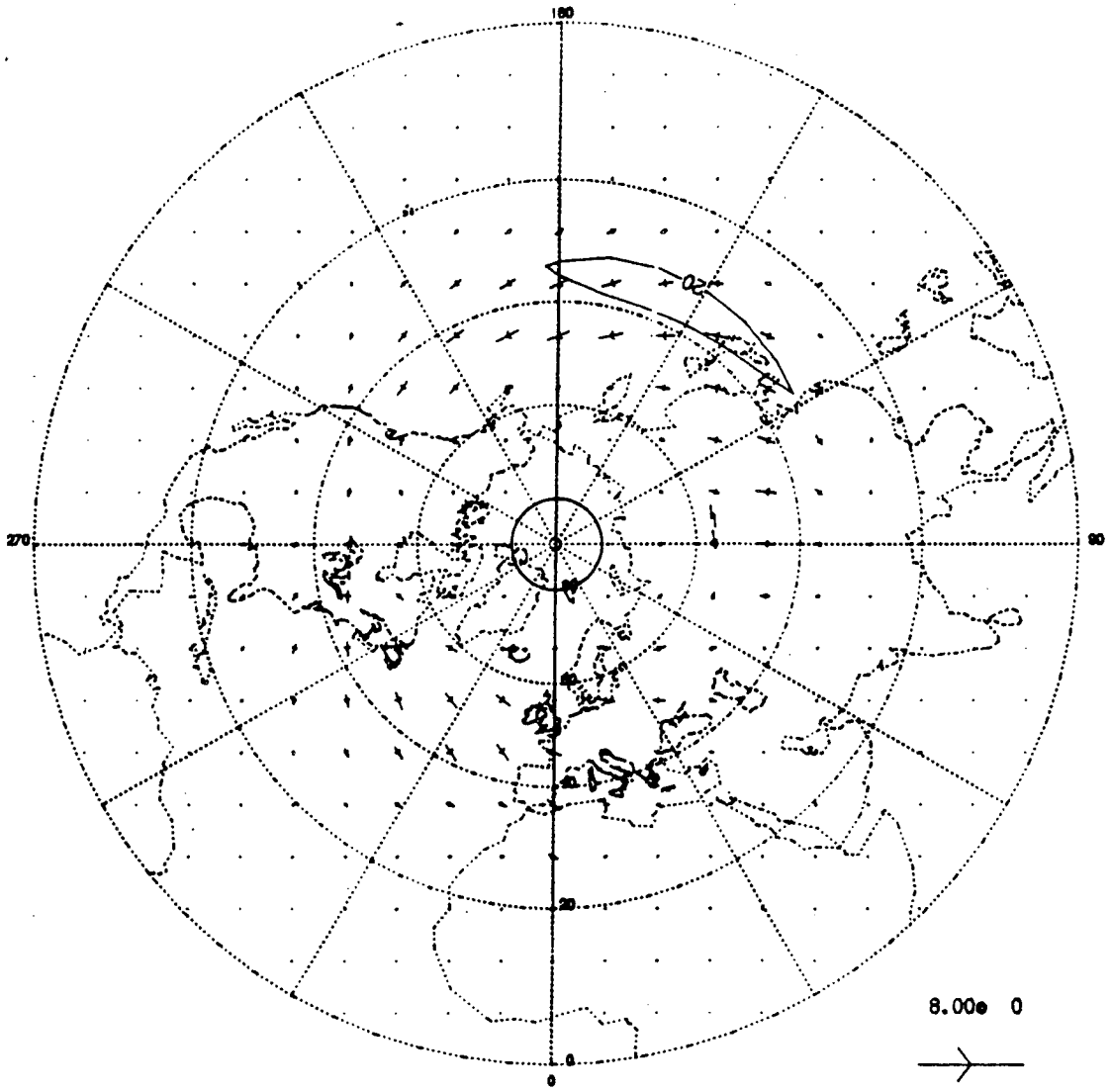

Fig. 6.18 850 mb wave activity flux as in Fig. 6.13, but for the diabatic heating derived from FGGE IIIb data.

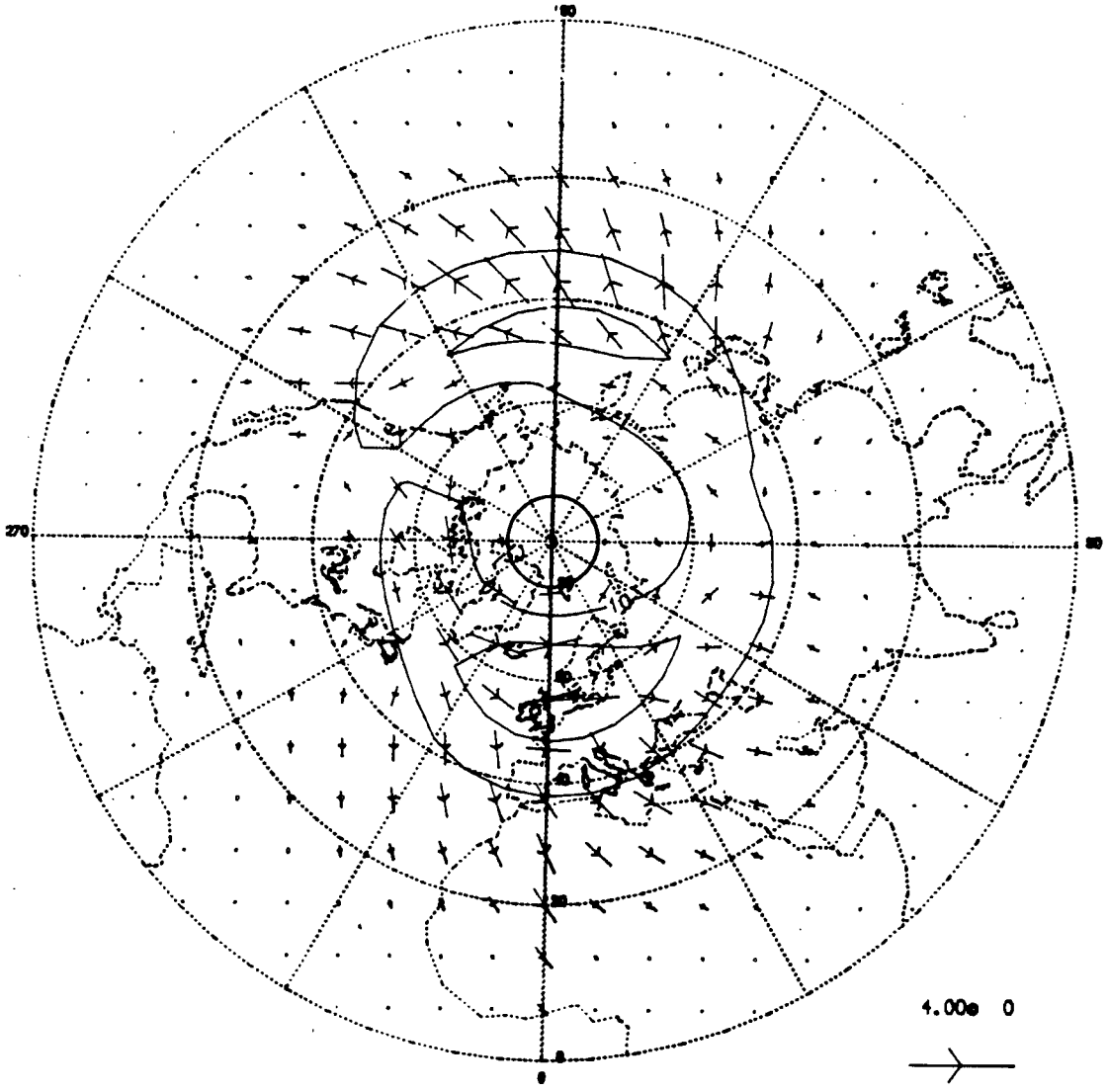

Fig. 6.19 As Fig. 6.18, but for 200 mb level. Contours are at intervals of 10 units.

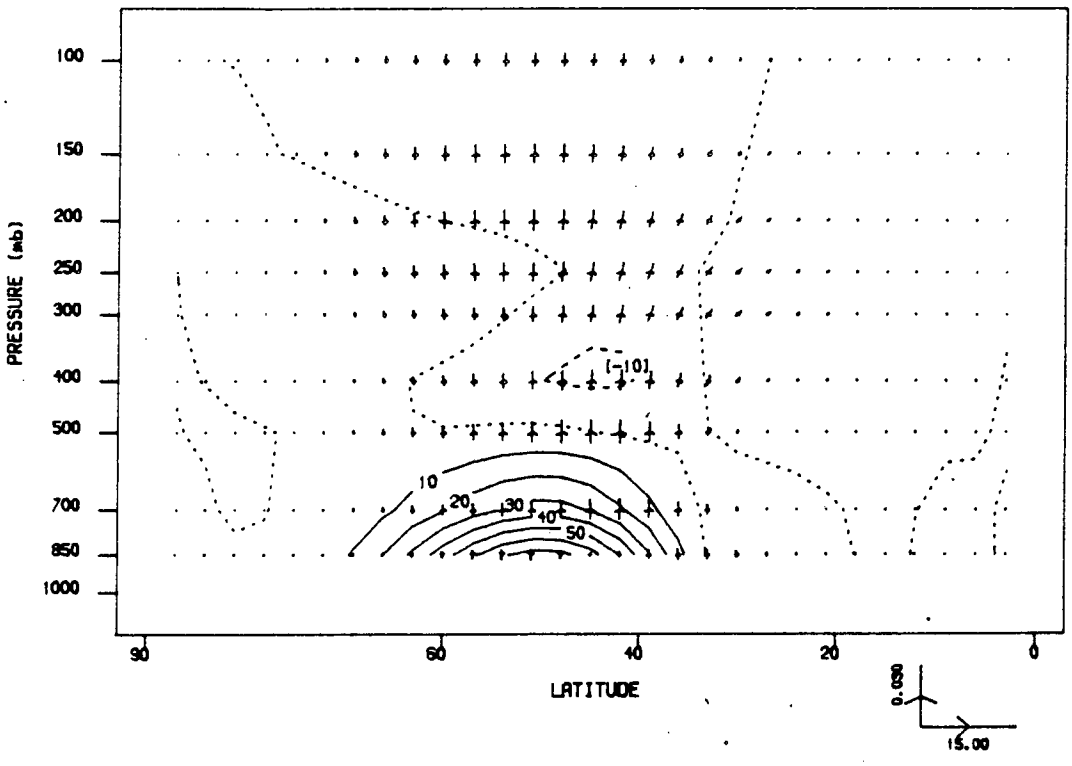

Fig. 6.20 EP cross-section as in Fig. 6.14, but for the diabatic heating derived from FGGE IIIb data.

6.3.1 Topography and FGGE IIIa Heating Field

In Figs. 6.21 and 6.22 are shown the corresponding perturbation stream fields at the 700 mb and 200 mb levels respectively. The circulations in high latitudes at the 700 mb level are mainly contributed from the orographic forcing except for the cyclonic circulation between 150°W and 90°W, where the stationary wave exerted by topography has a weaker intensity than that by thermal forcing. Both the orographic and the thermal forcings made a comparable contribution to the stationary waves in middle latitudes at the 700 mb level. At upper levels the relative importance of these two categories of forcing depends upon the geographical position of the circulation system. In general, we may consider them to be of equal importance. This can be seen from a comparison between Figs. 6.2, 6.11 and 6.22, or from the longitudinal cross-sections at a particular latitude. The longitudinal cross-section of perturbation geopotential height at 45°N is shown in Fig. 6.23, in which the trough in eastern Asia and the ridge in the eastern Pacific result from both the orographic and thermal forcing (compare with Figs. 6.3 and 6.12). The thermal forcing made a substantial contribution to the ridge near the west coast of Europe, while the ridge located to the west of the Tibetan Plateau at the low levels is clearly induced by the topography.

It is not the intention of this study to simulate the observed wintertime stationary waves accurately. However,

it is of interest to compare these results with the observations. Two maps for the statistics of observed stationary waves in winter are presented here. One is the Northern Hemisphere climatological mean January distribution of stationary wave geopotential height at the 200mb level (Fig. 6.24), which is photocopied from the paper of Wallace (1983) and originally based on the Atlas of Crutcher and Merserve (1970), digitized, spatially and temporally smoothed and archived on magnetic tape in the NCAR data library. Another is the Northern Hemisphere 6-year climatological wintertime (December-February) distribution of stationary wave streamfunction at the 250 mb level (Fig. 6.25), which is provided by B. J. Hoskins (personal communication, 1986) and is based on ECMWF analyses. All the major features displayed in these two figures are in good agreement. They appear in individual winters with only relatively minor year to year variations in structure (Wallace, 1983).

Comparing Fig. 6.22 with Figs. 6.24 and 6.25, we find that the pattern of stationary waves at the 200 mb level simulated by this linear model is fairly consistent with the observation, but the following deficiencies are evident in the model results:

a) The anticyclonic circulation over the western Pacific is relatively too weak compared with the middle latitude circulation systems.

b) The cyclonic circulation centred at 60°E, 35°N is relatively too strong.

c) The cyclonic circulation over the eastern tropical Atlantic and North Africa is severely weakened.

d) In high latitudes both the cyclonic circulation between 175°W and 90°W, and the anticyclonic circulation between 105°E and 175°W are displaced westward, and the latter has too large an extreme value of perturbation streamfunction.

The inaccurate representation of the actual wintertime diabatic heating and the Northern Hemispheric topography due to the low resolution used in the model as well as the lack of transient effects included explicitly in the model may be partly responsible for these deficiencies. Certainly, we should not forget the possibility that there might have been evident differences in the forcing condition between a particular month and a long period on which the climatological statistics are based. However, in the next chapter we will show that the nonlinearity is an important factor in simulating these circulation systems in low and high latitudes.

A longitudinal cross-section of perturbation vertical velocity at 45°N (Fig. 6.26) shows that the sinking air is mainly concentrated over the Eurasian Continent at this latitude circle, and rising air occurs elsewhere.

The wave activity fluxes at the 850 mb and 500 mb levels are shown in Figs. 6.27 and 6.28 respectively. There are two major wavetrains propagating upward, eastward and mainly equatorward from eastern Asia across the North Pacific and from eastern North America across the North

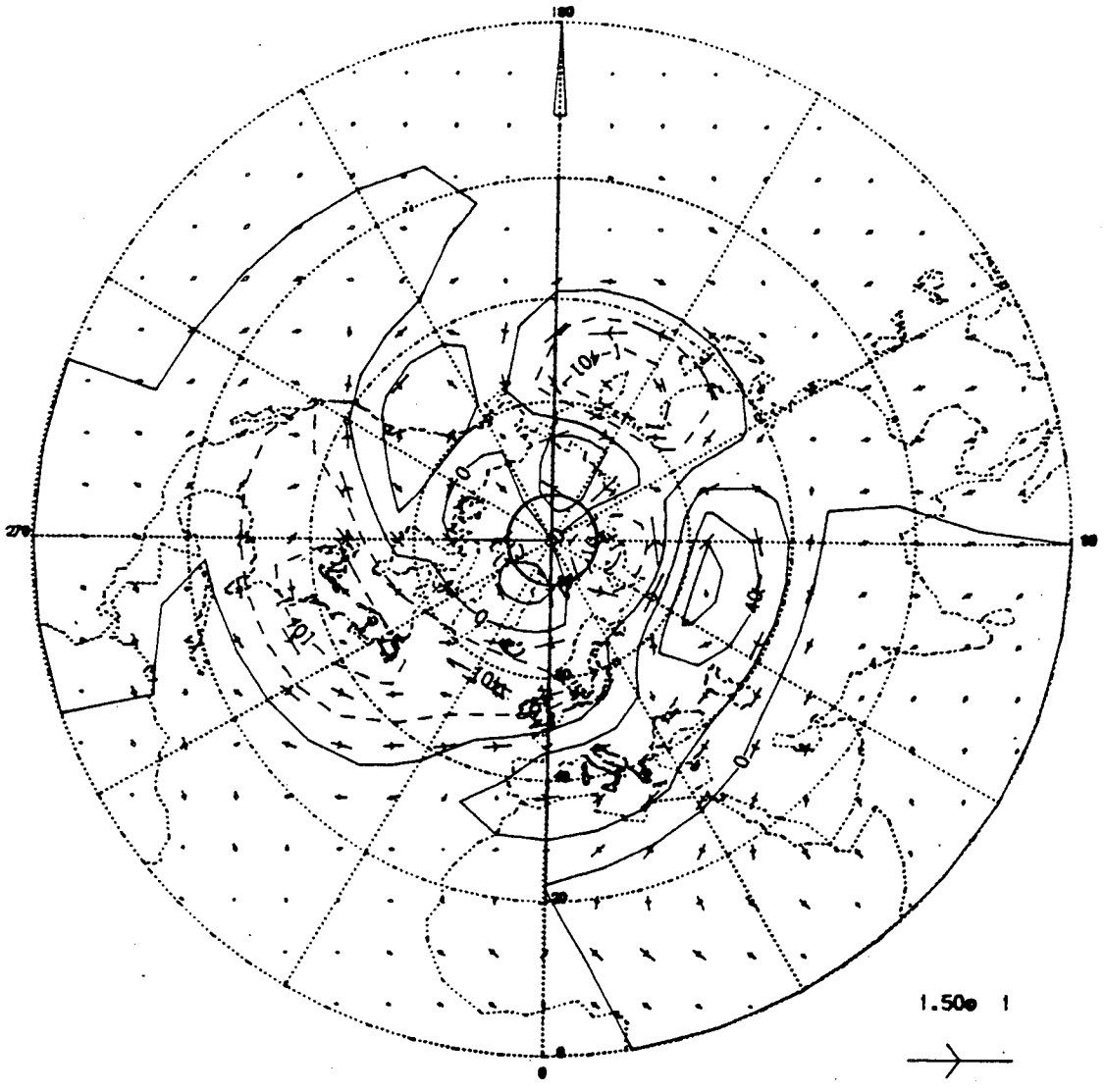

Fig. 6.21 700 mb perturbation stream field for the linear response to the Northern Hemispheric topography and the diabatic heating field derived from FGGE IIIa data. Contours represent the perturbation streamfunction/($10^5 m^2 s^{-1}$) with an interval of 20 units.

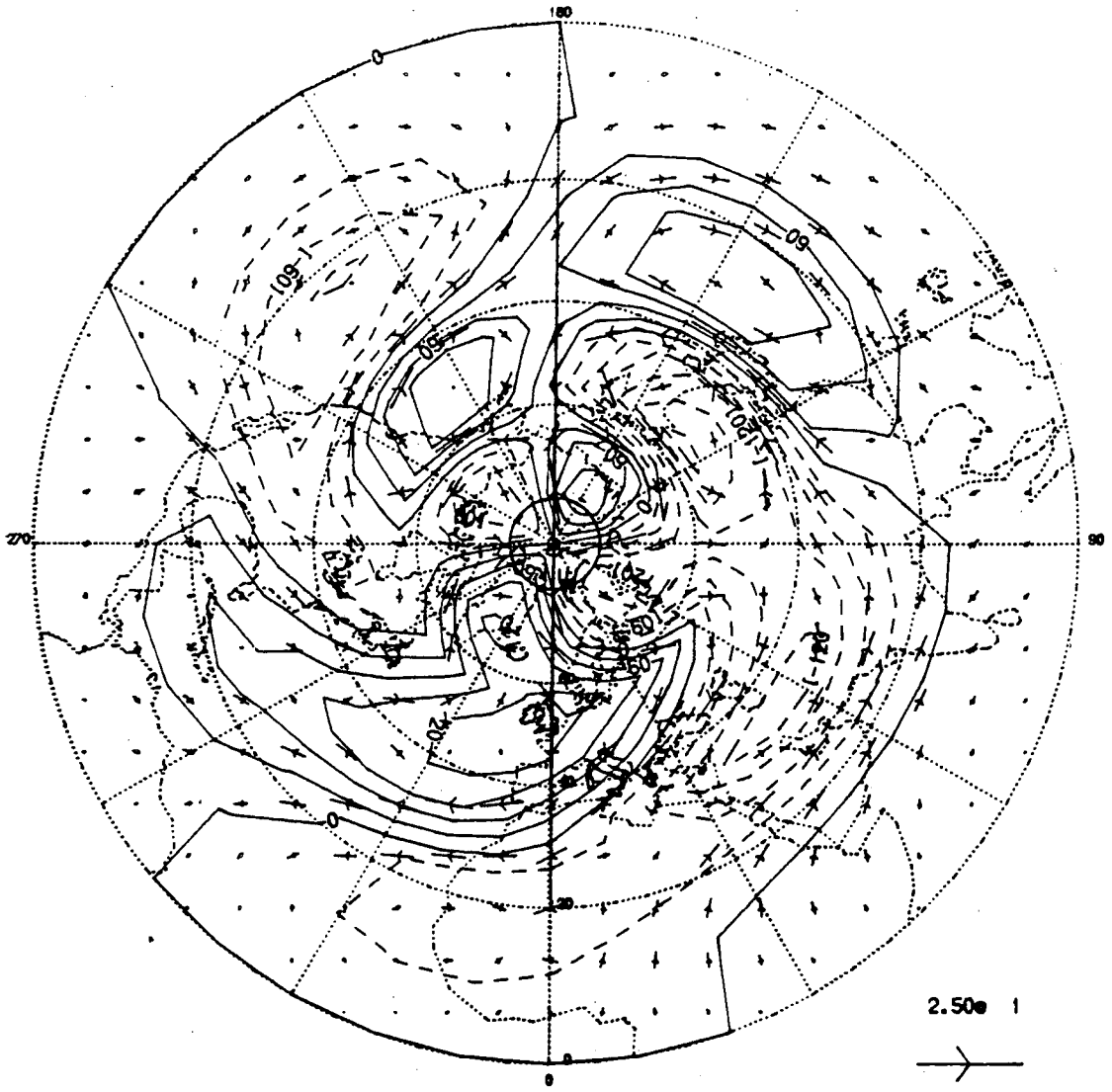

Fig. 6.22 As Fig. 6.21, but for 200 mb. Contours are at intervals of 30 units.

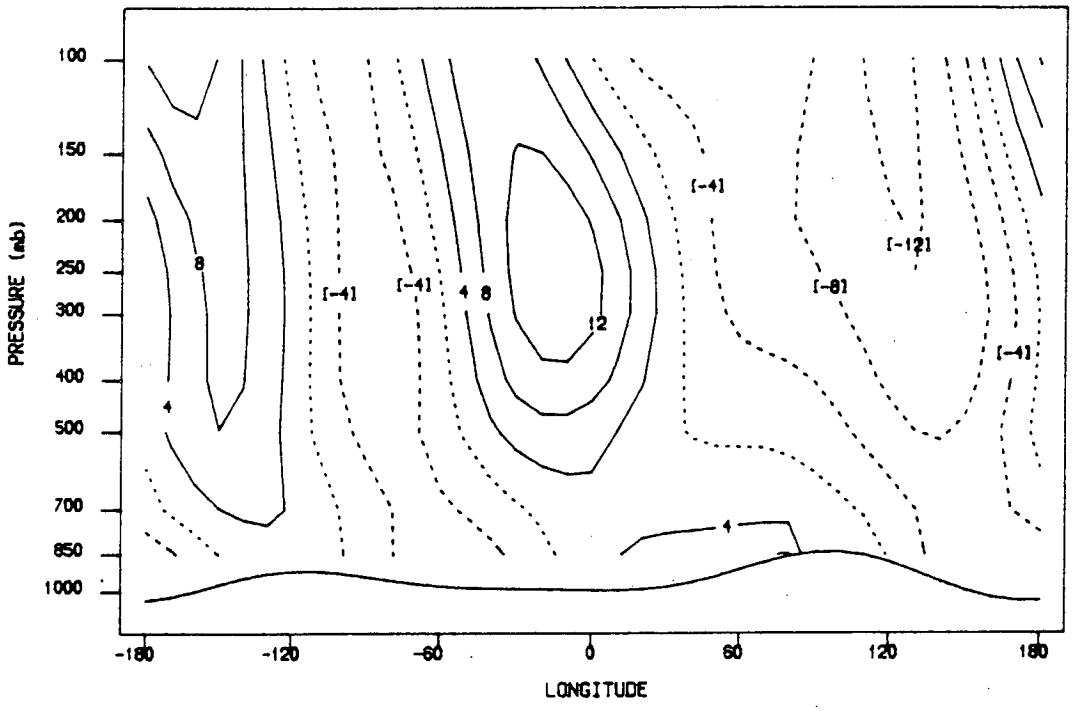

Fig. 6.23 Longitudinal cross-section of perturbation geopotential height at 45°N for the linear response to the Northern Hemispheric topography and the diabatic heating field derived from FGGE IIIa data. Contour interval is 4 dam.

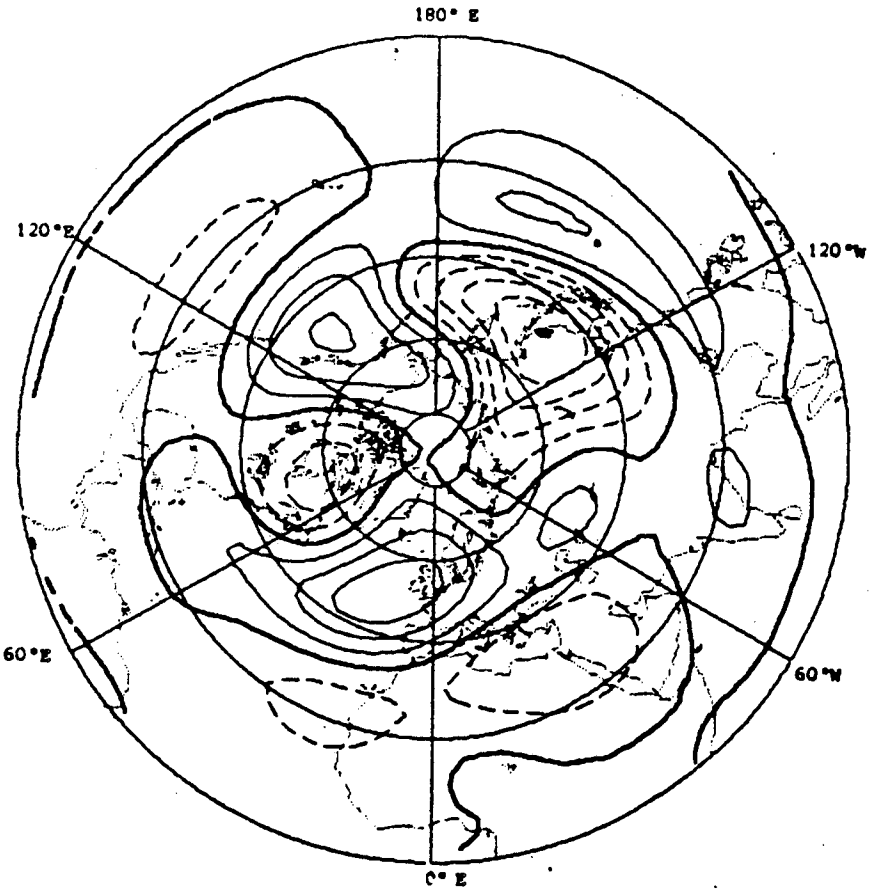

Fig. 6.24 Northern Hemisphere climatological mean January distribution of stationary wave geopotential height at the 200 mb level. Photocopied from the paper of Wallace (1983). Contour interval is 6 dam. The zero contour is thickened; positive contours are solid and negative ones are dashed. Lines of latitude and longitude are drawn every 20° and 60°, respectively.

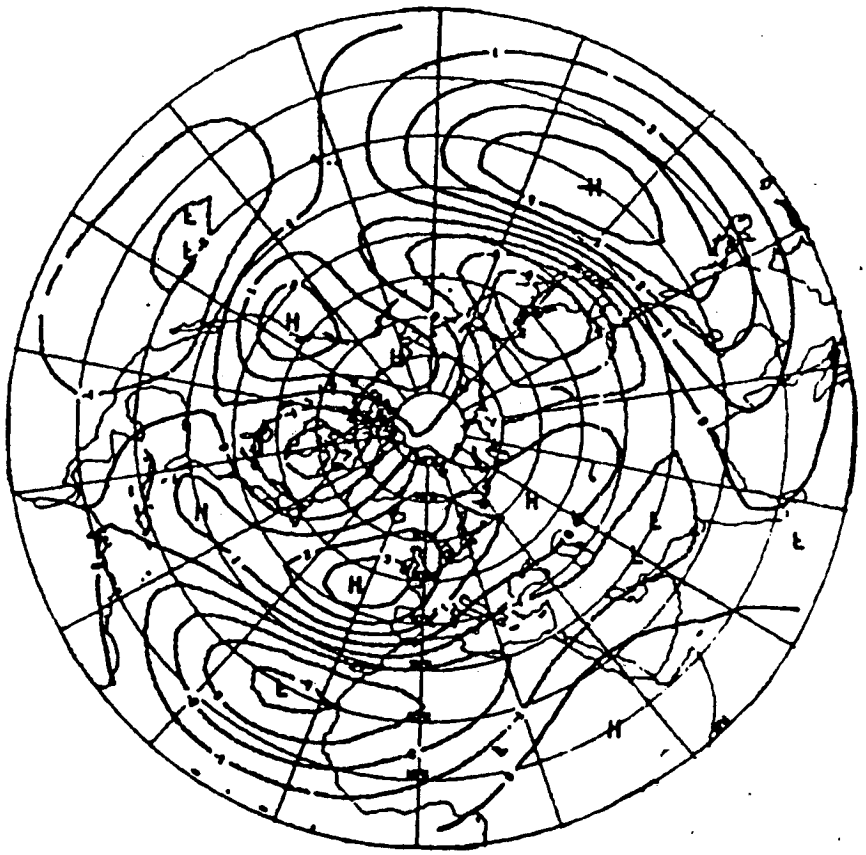

Fig. 6.25 Northern Hemisphere 6-year climatological December-February distribution of stationary wave streamfunction at the 250 mb level. Provided by B. J. Hoskins. Lines of latitude and longitude are drawn every 10° and 20°, respectively.

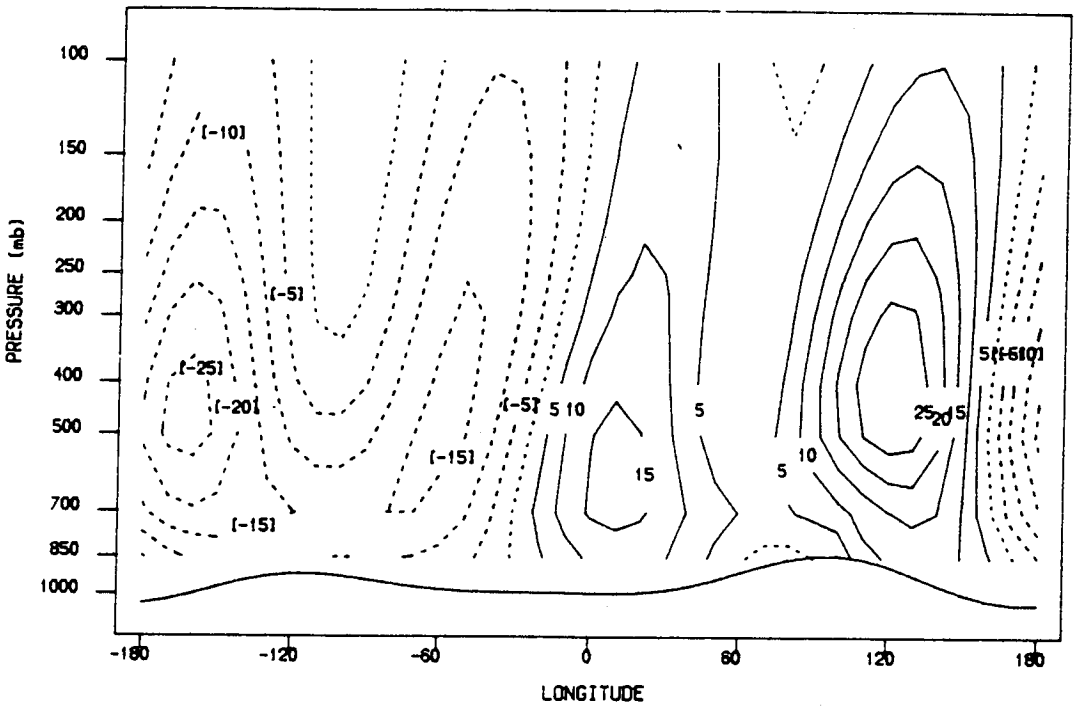

Fig. 6.26 Longitudinal cross-section of perturbation vertical velocity at 45°N for the linear response to the Northern Hemispheric topography and the diabatic heating derived from FGGE IIIa data. Contour interval is 5 mbd^{-1}.

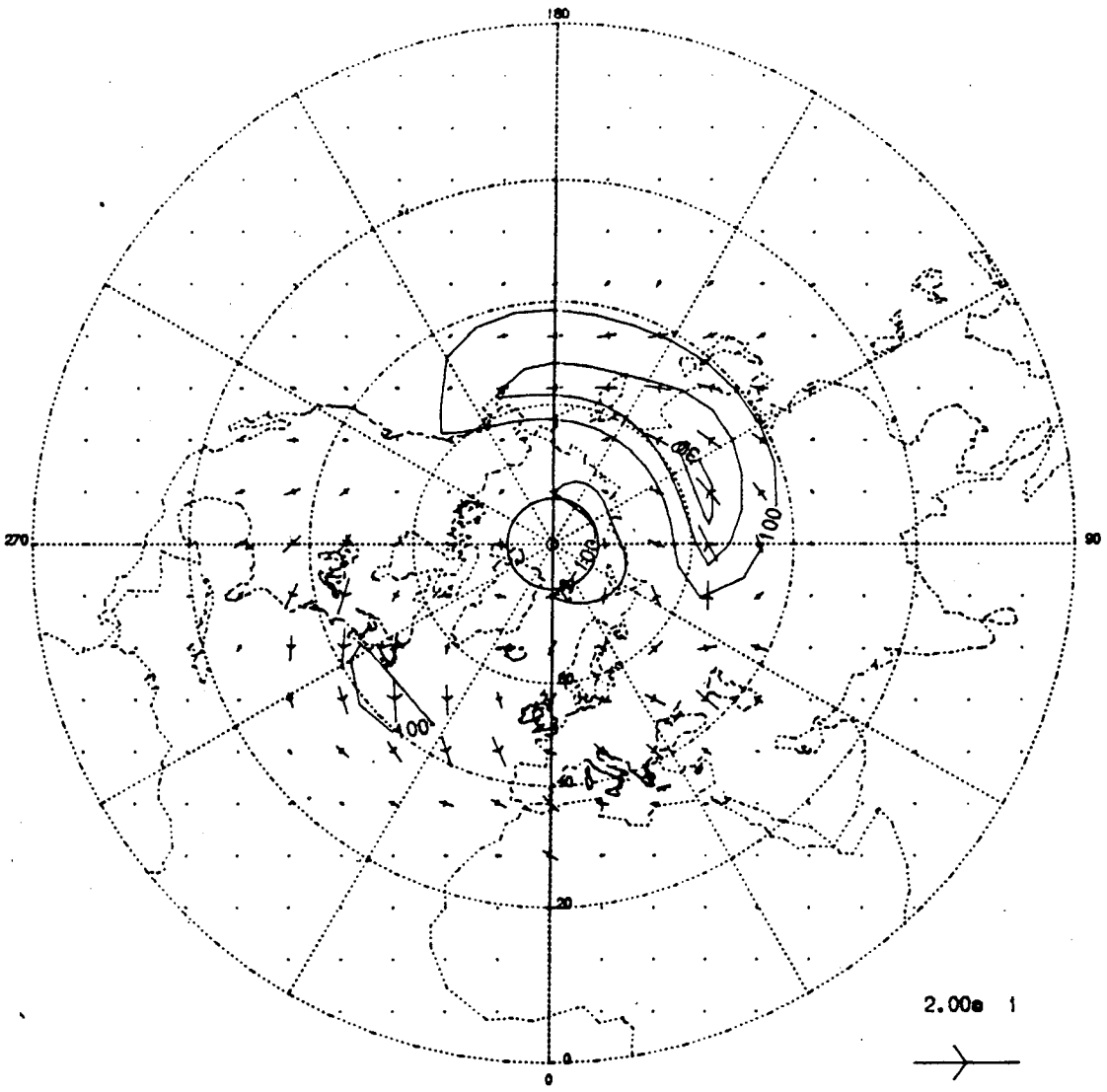

Fig. 6.27 850 mb wave activity flux for the linear response to the Northern Hemispheric topography and the diabatic heating field derived from FGGE IIIa data. The graphic convention is the same as in Fig. 5.6, but contour interval is 100 units.

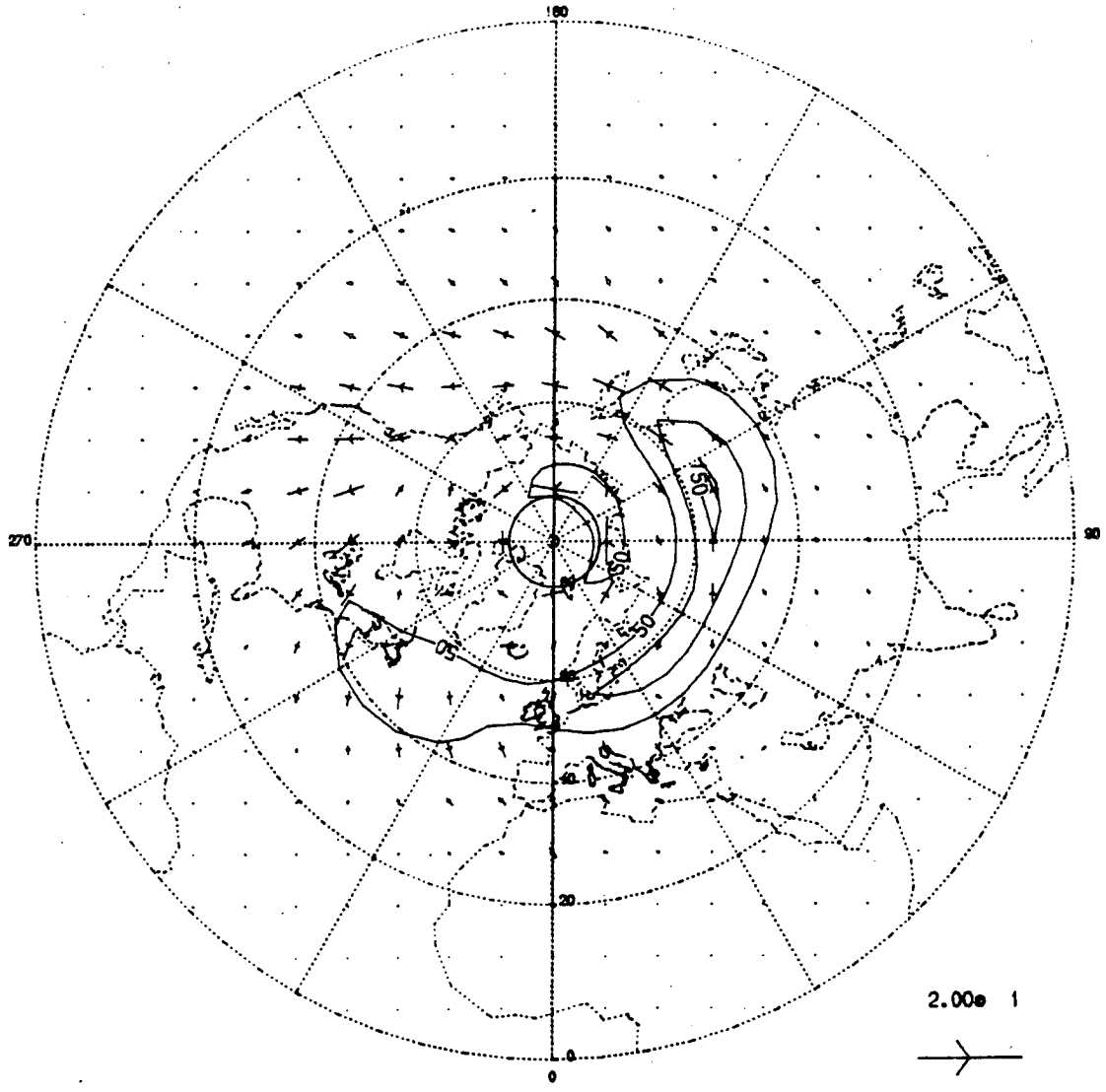

Fig. 6.28 As Fig. 6.27, but for the 500 mb. Contours are at intervals of 50 units.

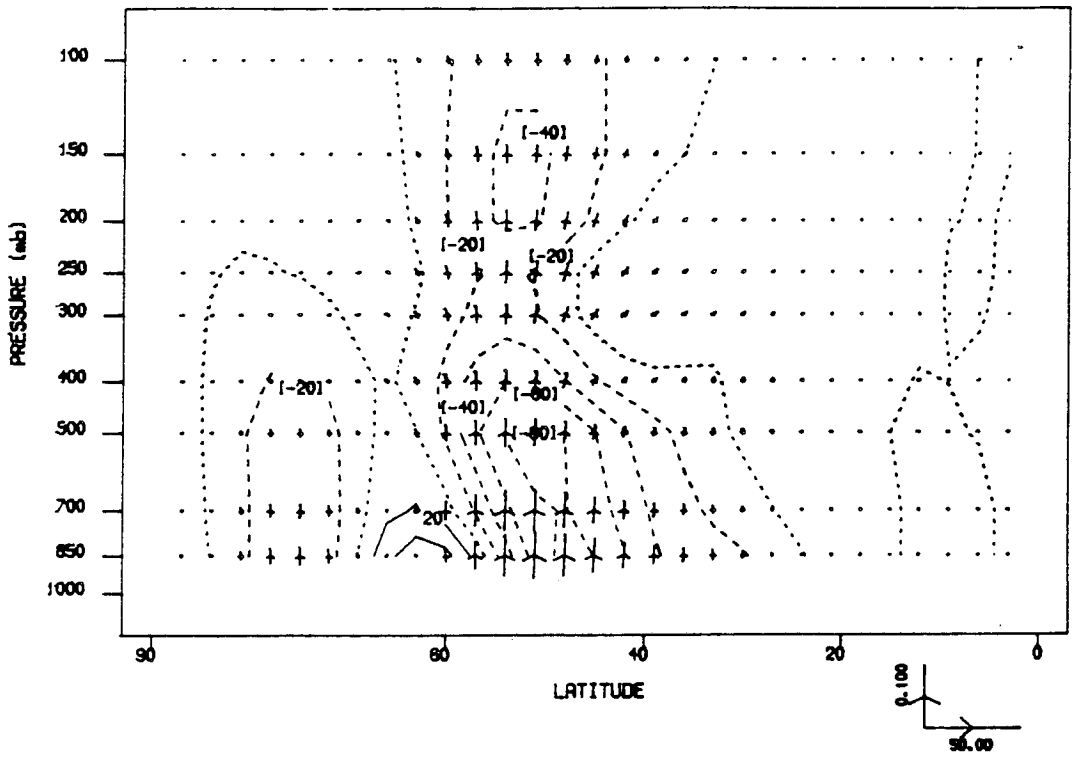

Fig. 6.29 EP cross-section for the linear response to the Northern Hemispheric topography and the diabatic heating field derived from FGGE IIIa data. Contour interval is 20 units.

Atlantic. The North Pacific wavetrain is both more intense and more extensive than that in the North Atlantic. From the calculations for the pure orographic forcing and the pure thermal forcing, it is found that at low levels the North Pacific wavetrain is predominantly originated by orographic forcing, in particular, the Tibetan Plateau plays the most important role, while the thermal forcing makes relatively more contribution to the North Atlantic wavetrain than to the North Pacific wavetrain. Above 500 mb (e. g., at 200 mb level, not shown here), the individual contributions to the wave activity flux from both the orographic and the thermal forcing are comparable. Fig. 6.29 is the corresponding EP cross-section. The EP flux in the lower troposphere is predominantly determined by orographic forcing, while the EP flux in the middle and upper troposphere depends on both the orographic and the thermal forcing.

6.3.2 Topography and FGGE IIIb Heating Field

As discussed in section 6.2.2, when the FGGE IIIb vertically integrated heating field is used as an alternative representation of the actual diabatic heating the linear response to the combined orographic and thermal forcing gives a similar wave pattern, but some significant differences are found in the Pacific Ocean. For example, at the 700 mb level (Fig. 6.30) there is an anticyclonic circulation between 20°N and 40°N over the western Pacific

associated with a cyclonic circulation to the west. These systems do not appear in Fig. 6.21, where the FGGE IIIa heating field is used. The 200 mb perturbation stream field (Fig. 6.31) is also similar to its counterpart for the FGGE IIIa heating field, only the amplitude of some wave patterns is changed. Comparing these results with observations (Fig. 6.25) shows that this linear solution still has the deficiencies mentioned in the previous section, particularly failing to simulate the cyclonic circulation over the eastern tropical Atlantic and North Africa.

The influence on the wave activity flux is not significant and not shown here. The corresponding EP cross-section is displayed in Fig. 6.32, showing a weaker convergence of EP flux in the middle and upper levels between 40°N and 60°N and a stronger source of EP flux in the middle troposphere centred around 37°N.

6.3.3 A Zonal Resolution Test

As previously mentioned, in this study we only calculate the response to ultra-long waves, i.e., only zonal wave numbers 1, 2 and 3 are considered, partly because they are most important for stationary planetary waves, partly because the computational resource available is limited for the nonlinear model, which has a high requirement of computer storage and CPU time. However, in contrast to the nonlinear model, the linear model has the advantage of much lower requirements in computational aspects.

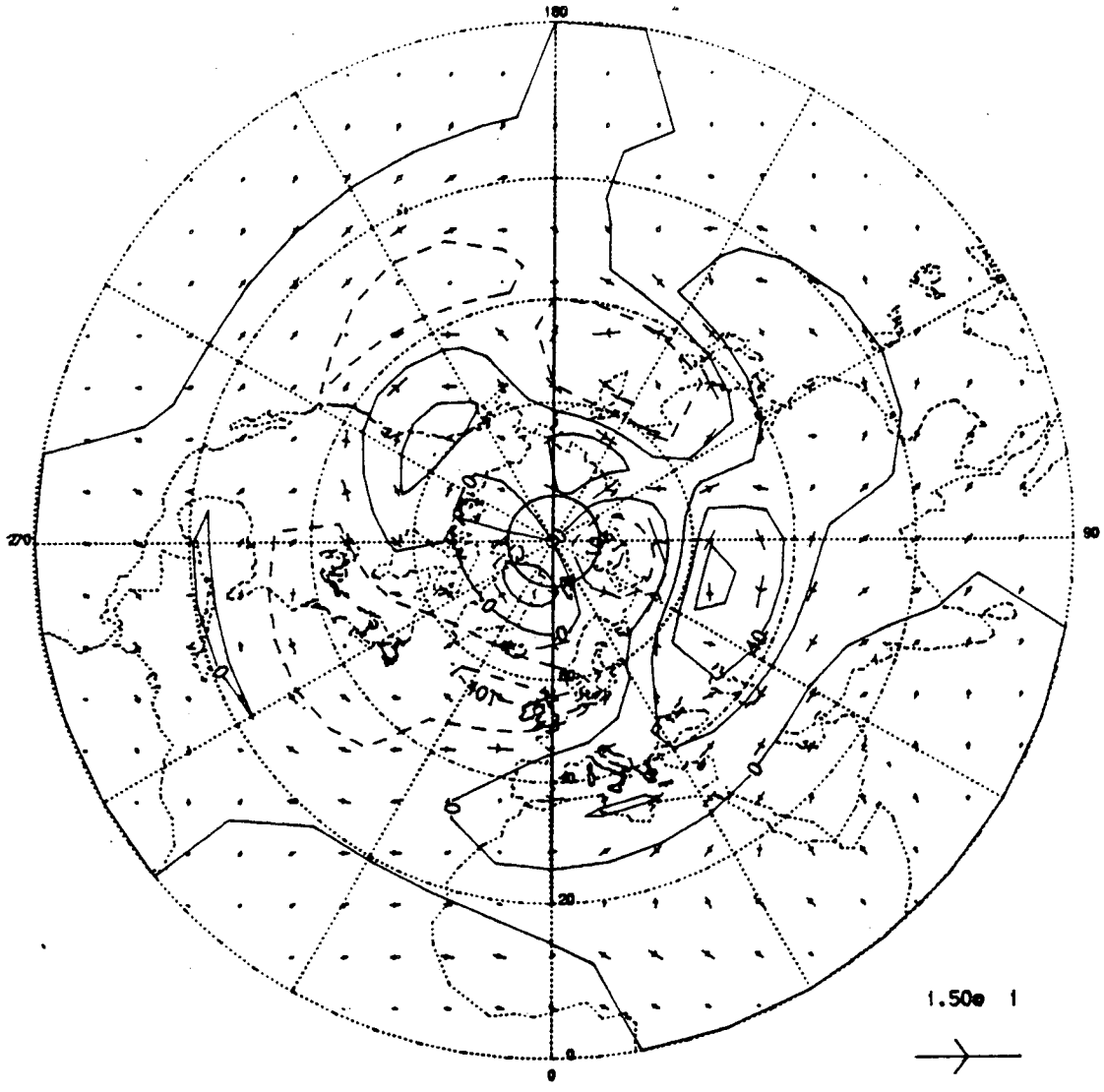

Fig. 6.30 700 mb perturbation stream field as in Fig. 6.21, but the diabatic heating field is derived from FGGE IIIb data.

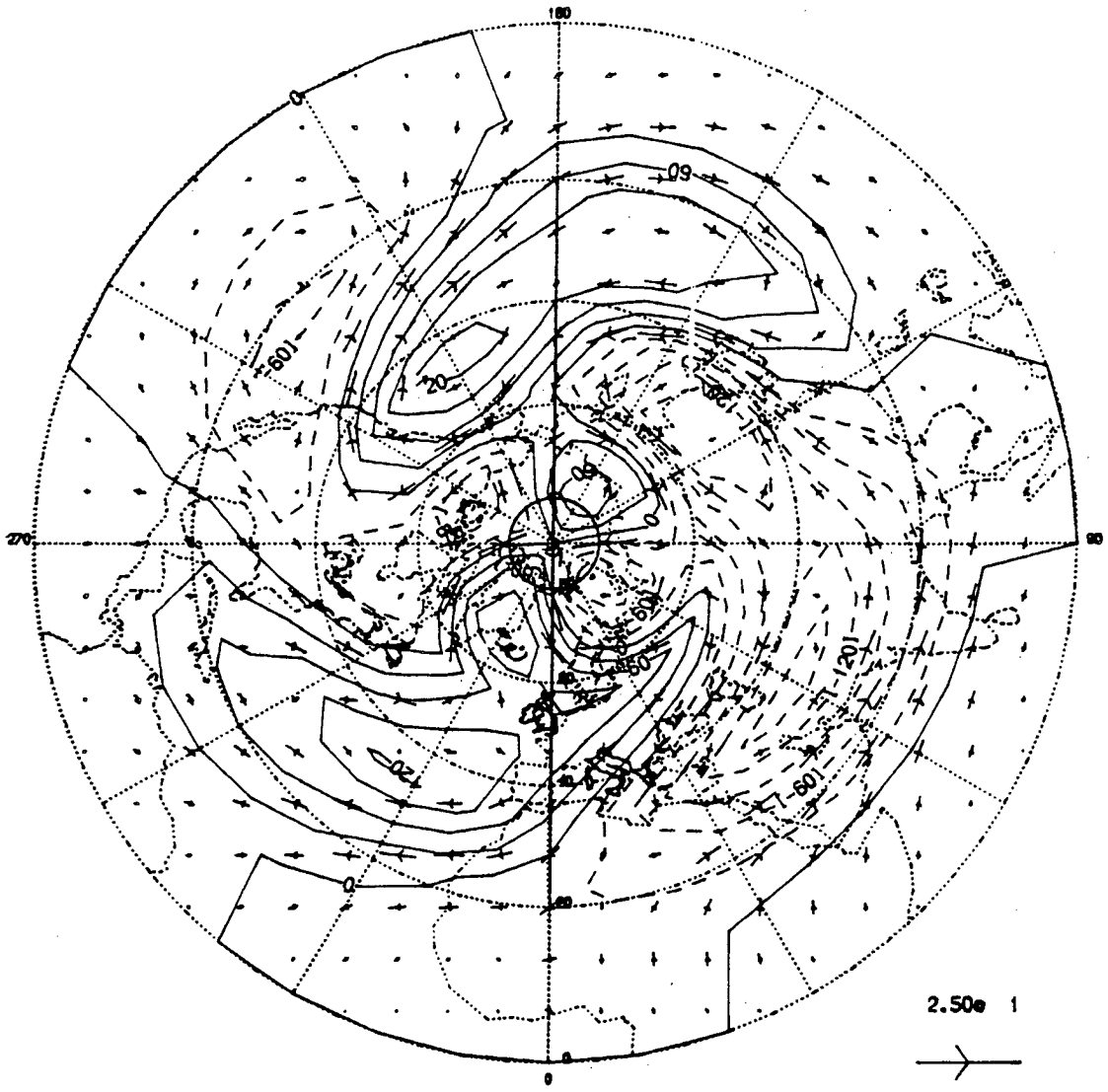

Fig. 6.31 200 mb perturbation stream field as in Fig. 6.22, but the diabatic heating field is derived from FGGE IIIb data.

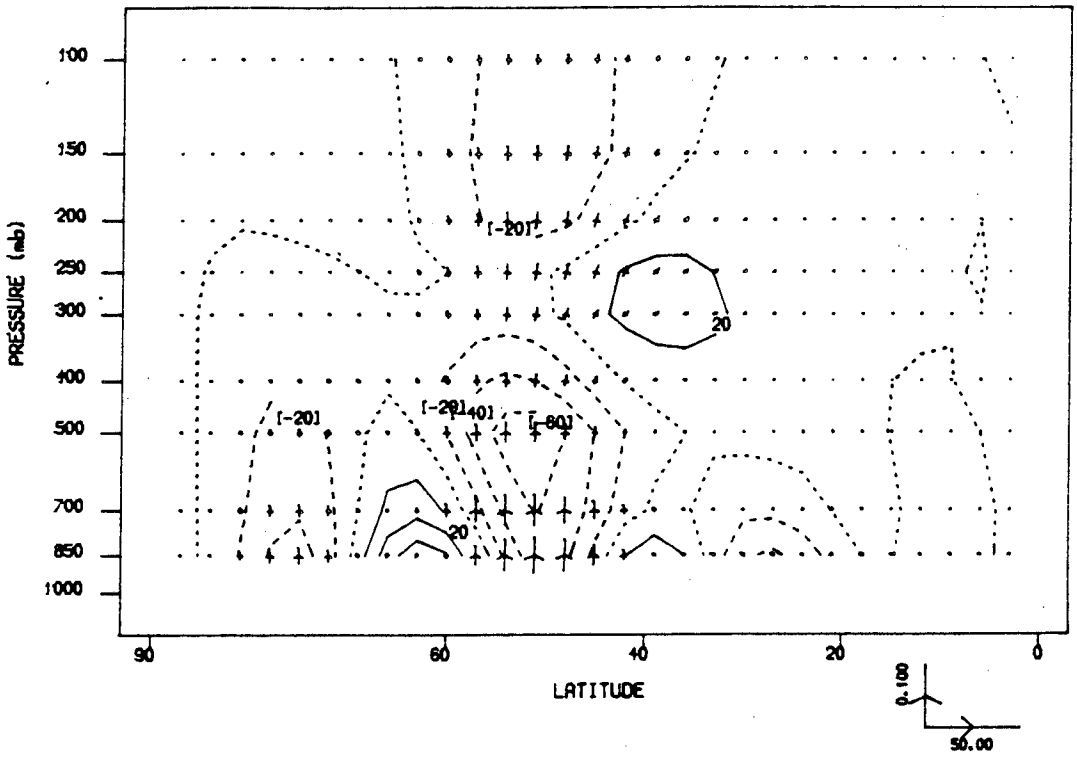

Fig. 6.32 EP cross-section as in Fig. 6.29, but the diabatic heating field is derived from FGGE IIIb data.

Therefore a zonal resolution test was carried out to see if significant differences might result from the inclusion of higher wavenumbers. In this experiment both the meridional and vertical resolutions remain unchanged, but the zonal resolution comprises wavenumbers up to nine. The forcing functions correspond to those used in section 6.3.1, that is, both Northern Hemispheric topography and diabatic heating derived from FGGE IIIa data are included in the linear model.

The perturbation stream fields at the 200 mb level superposed for wavenumbers up to six and nine are shown in Figs. 6.33 and 6.34 respectively. The perturbation wave patterns displayed in these two figures are very similar to those in Fig. 6.22, where only wavenumbers up to three are superposed. Comparing these results with the observations (see, Fig. 6.25), there are some improvements achieved. Firstly, the anticyclonic circulation over the western Pacific is enhanced after inclusion of higher wavenumbers, which is more realistic; next, the cyclonic circulation over the eastern tropical Atlantic and North Africa is evidently enhanced, which is also closer to the observed wintertime climatological stationary wave pattern. The cyclonic circulation centred previously at 60°E, 35°N is displaced slightly eastward and has a stronger intensity, this deviates from observed stationary waves even further. There is no improvement found for the simulation in high latitudes. In addition, the cyclonic circulation over eastern North America is represented better by inclusion of higher zonal wavenumbers.

The improved wave simulations described above are connected with a more realistic representation of the Northern Hemispheric topography and diabatic heating by inclusion of higher zonal wavenumbers in the model. In order to see the influence of zonal resolution on the representation of the Northern Hemispheric topography in terms of truncated series of spherical harmonics, the horizontal distribution of surface geopotential height for zonal wavenumbers up to three and nine are shown in Fig. 6.35 and Fig. 6.36 respectively. It is obvious that the inclusion of higher wavenumbers produces more realistic topography, especially for mountains with a smaller horizontal scale, such as the North African mountains, the Greenland Plateau and the Rocky mountains. Fig. 6.37 shows the horizontal distribution of vertically integrated diabatic heating in January 1979, as in Fig. 6.9, but here zonal wavenumbers up to nine are included. We can identify smaller scale structures in Fig. 6.37, which are not visible in Fig. 6.9.

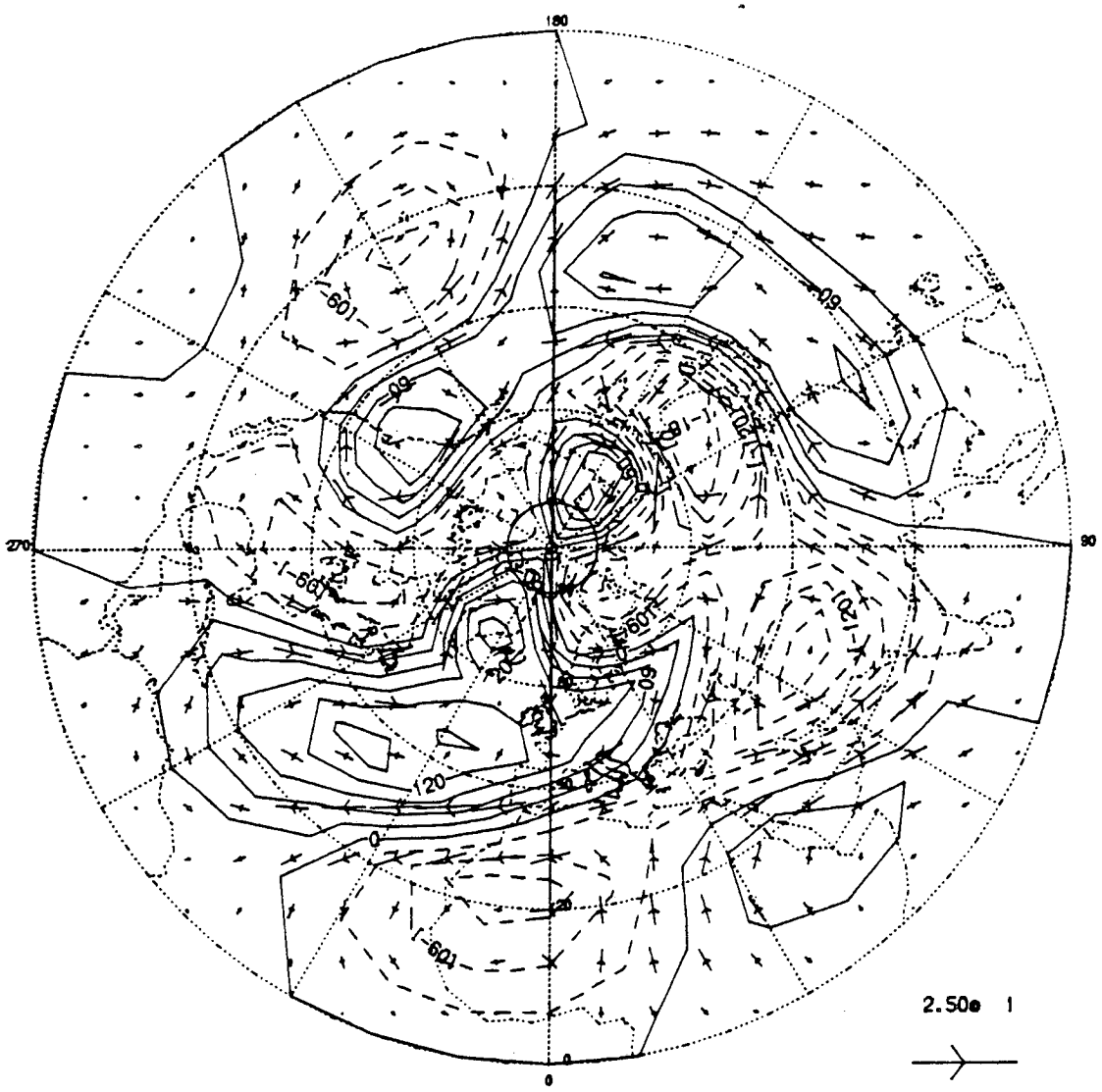

Fig. 6.33 200 mb perturbation stream field as in Fig. 6.22, but for wavenumbers up to six.

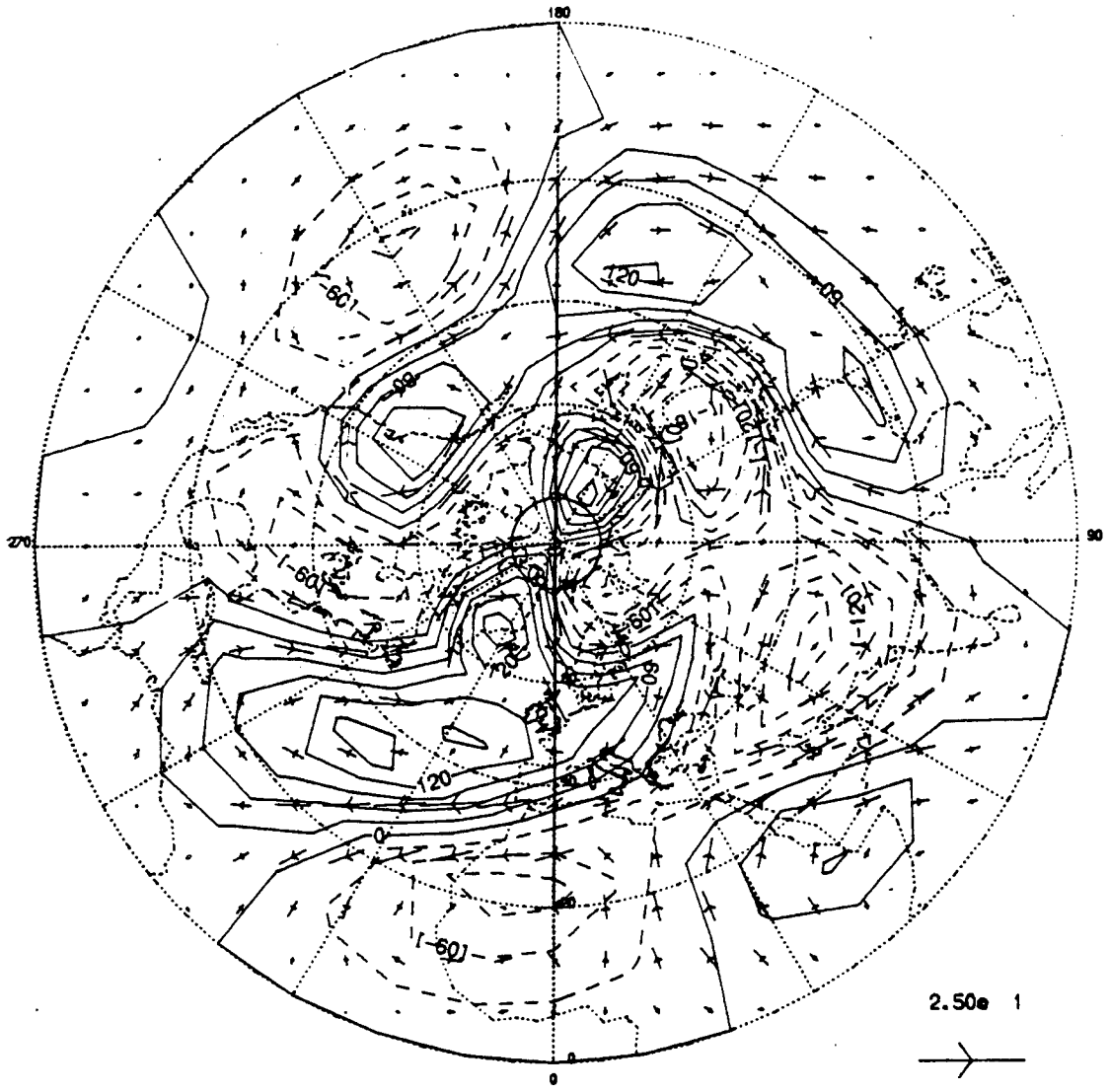

Fig. 6.34 200 mb perturbation stream field as in Fig. 6.22, but for wavenumbers up to nine.

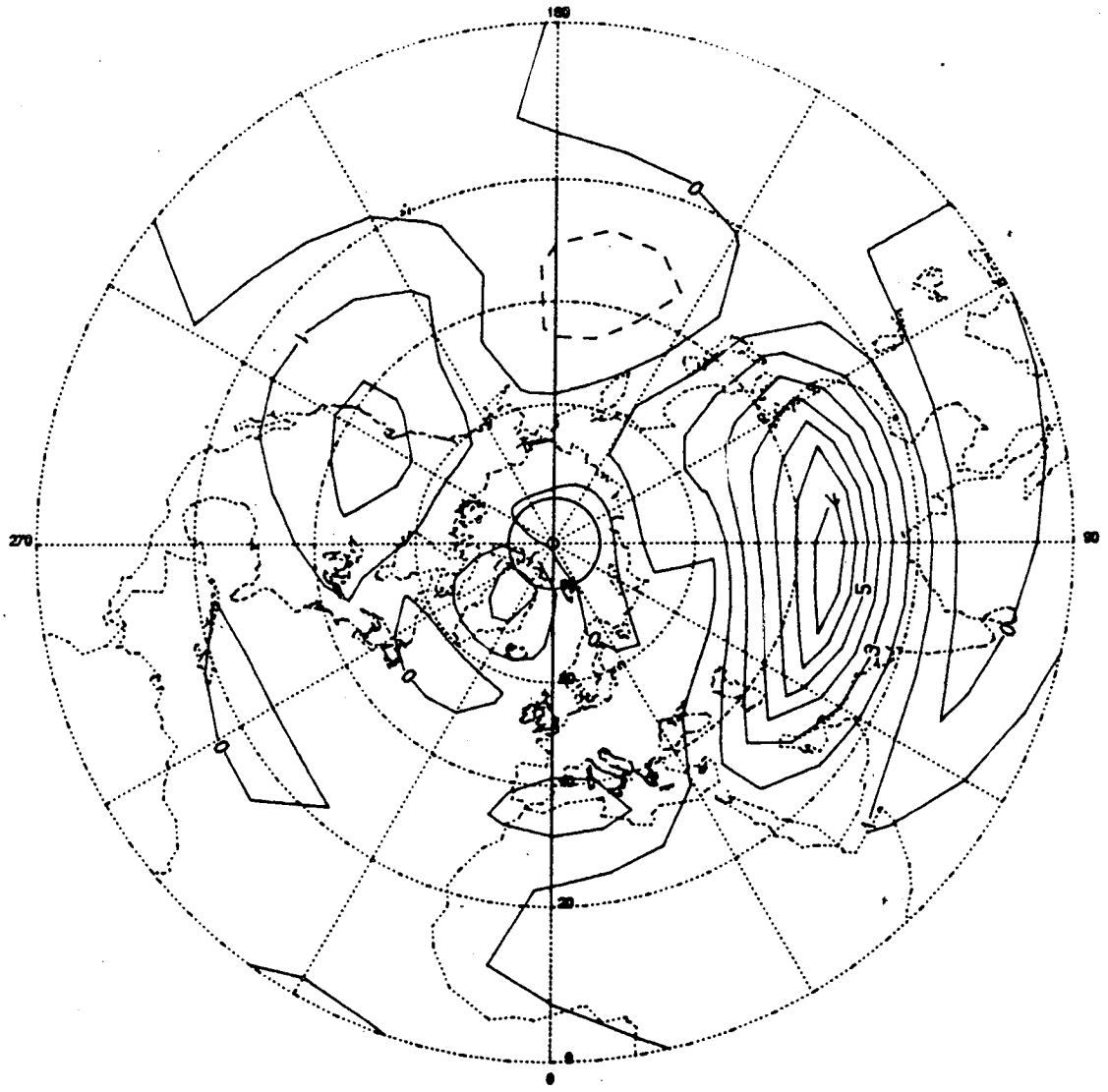

Fig. 6.35 The horizontal distribution of surface geopotential height for the Northern Hemispheric topography. The original data is on 1.875°x1.875° grid points, which have been transformed into a truncated series of spherical harmonics with truncation indices M=3 and J=11. Contours represent topography height/(300m).

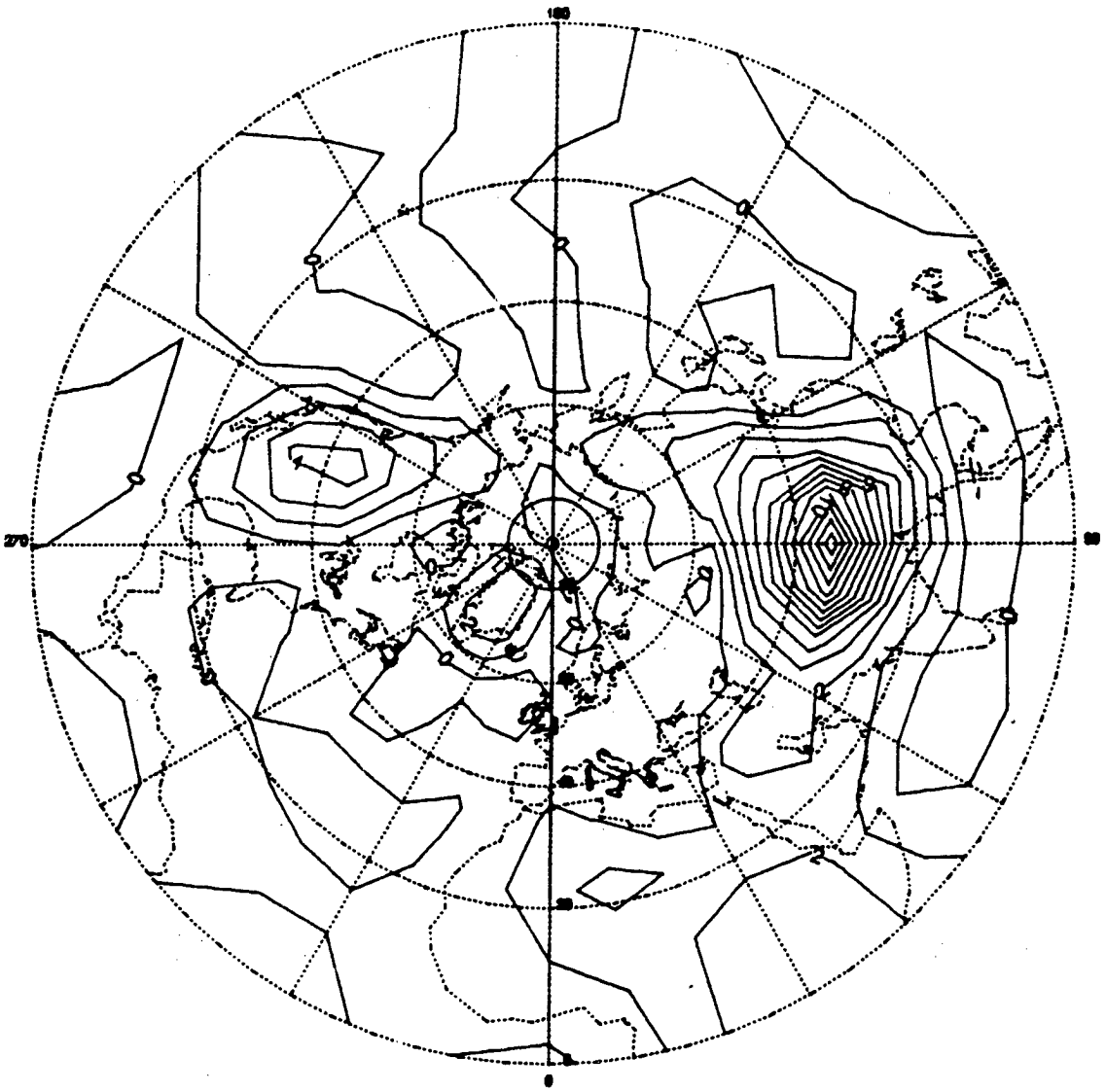

Fig. 6.36 As Fig.6.35, but with M=9.

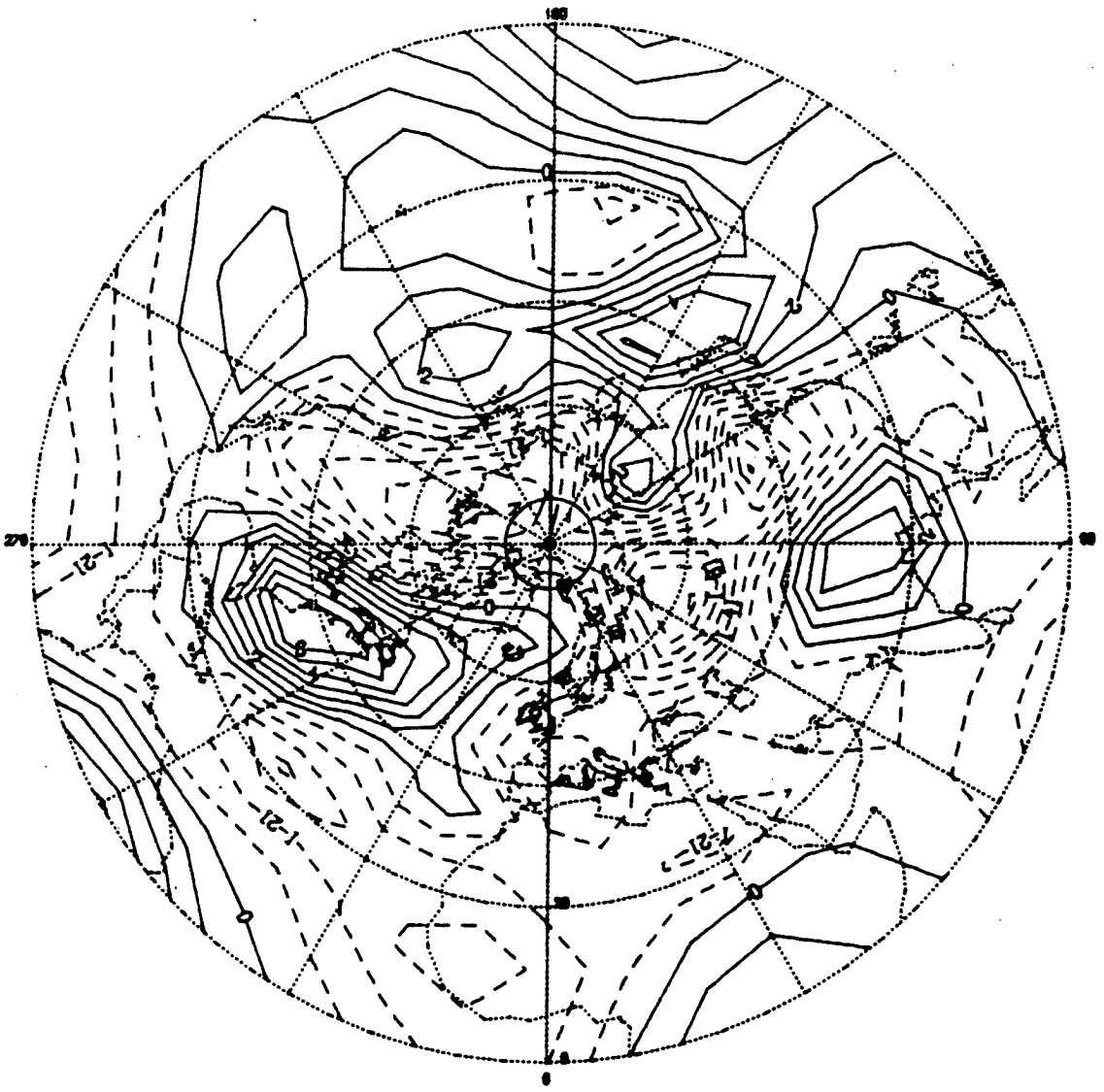

Fig. 6.37 As Fig. 6.9, but with M=9.

CHAPTER 7

NONLINEAR RESPONSE TO LARGE SCALE TOPOGRAPHY AND DIABATIC HEATING

The linear calculations of the response to large scale Northern Hemispheric topography and the actual wintertime diabatic heating, as described in the previous chapter, are interesting because of their suggestive similarity with the observed climatological stationary wave patterns despite some evident deficiencies in both amplitude and geographic position of the simulated waves. However, the equations governing the linear model are clearly a great simplification of the real atmospheric behaviour. The velocity components of finite amplitude disturbances in the real atmosphere are often of comparable magnitude to the mean zonal flow. In this case one of the basic assumptions for the perturbation method breaks down, namely, the terms in the governing equations which involve products of perturbation variables become significant. This is particularly evident in some areas such as the polar and tropical regions where the zonally averaged basic flow is weak while the stationary waves induced by local and remote forcing are relatively strong. It should be noted that the strong nonlinearity in a limited region influences other parts of the global circulation by means of various interaction processes in the atmosphere. As a step closer to reality, in this chapter we look for the response to the

actual topography and diabatic heating again by using the nonlinear primitive equation model described in chapter 2. In a similar way to the previous chapter, we will first consider the two different categories of forcing separately (sections 7.1 and 7.2), and then for their combination (section 7.3). Our attention is mainly directed to the differences between the nonlinear and linear response.

7.1 Nonlinear Response to Northern Hemispheric Topography

In Figs. 7.1 and 7.2 are shown the perturbation stream fields at the 700 mb and 200 mb levels for the nonlinear response to the Northern Hemispheric topography. At 700 mb the nonlinear response has a similar wave pattern to the linear one, but with an enhanced amplitude in general. At 200 mb the difference between the linear and nonlinear response is more complicated. In the polar region the nonlinear response is weakened except the anticyclonic circulation over Greenland, which is considerably intensified. The most significant changes take place in an extensive region from the eastern Atlantic to the east coast of Asia. Over the Atlantic there is an extensive anticyclonic circulation in the linear response (see Fig. 6.2), the eastern half of which is now replaced by a weak inverse circulation. Farther east the previous strong cyclonic circulation over the Middle East and India is greatly weakened and displaced south-eastward, whereas a quite intense and extensive anticyclonic circulation appears to

the northwest. The downstream cyclonic circulation is also enhanced. In chapter 5 we made a similar comparison between the linear and nonlinear response for the idealized orographic forcing, but the changes described here are more dramatic than before. This suggests that the nonlinearity of the response to the actual Northern Hemispheric topography is very significant.

The longitudinal cross-sections of perturbation geopotential height and vertical velocity are shown in Figs. 7.3 and 7.4 respectively. Fig. 7.3 shows two troughs and two ridges similar to Fig. 6.3 for the linear response, but the vertical structure of the disturbances in Asia and the West Pacific is obviously changed. In the linear case the upstream ridge and the downstream trough of the Tibetan Plateau at 45°N are mainly concentrated below the 500 mb level and the disturbance in the upper troposphere is relatively weak (see Fig. 6.3, also Fig. 6.1 and 6.2), but in the nonlinear case they pervade the whole troposphere with the maximum deviation value of geopotential height at about 250 mb. In the region further upstream, the trough at North America is also considerably intensified. Fig. 7.4 shows two main centres of rising air over the eastern Pacific and the Atlantic, and two centres of sinking air over North America and eastern Asia. This differs from the linear counterpart evidently (see Fig. 6.4).

The wave activity flux at 850 mb (Fig. 7.5) shows two main wavetrains, one is over eastern Asia and the Pacific, another over North America and the North Atlantic. The

former is much stronger and related to the Tibetan Plateau, the latter with the Rocky mountains. The North American wavetrain shows more evidence of splitting with one branch propagating north-eastward and the other south-eastward. These two wavetrains have their linear counterparts (see Fig. 6.5), but with a stronger meridional component in the nonlinear case. In addition, a maximum of the vertical flux can be found to the west of Greenland. It may not be related only to the Greenland Plateau, the nonlinear interaction is more important as discussed later. Comparison with Fig. 6.5 suggests that the wave activity flux in high latitudes for the nonlinear case differs dramatically from that for the linear case. This is also seen from the EP cross-section (Fig. 7.6), where the vertical flux at the low level in high latitudes is considerably weakened.

The two experiments which were performed in section 6.1 for the purpose of studying the relative importance of the three large scale mountains of the Northern Hemisphere to the orographically forced stationary waves were repeated using the nonlinear model. In the linear case, the major circulation systems influenced by removing the North American topography are confined to middle latitudes. but in the nonlinear case its influence involves a more extensive area. For example, at the 200 mb level (Fig. 7.7), the previous anticyclonic circulation over the tropical Atlantic (see Fig. 7.2) has almost disappeared and the cyclonic circulation over the eastern tropical Pacific is also

weakened. A more interesting thing occurs in high latitudes, that is, the previous quite strong anticyclonic circulation over Greenland is greatly weakened (the maximum in the perturbation streamfunction has decreased by about a half). A longitudinal cross-section of perturbation geopotential height at 45°N is shown in Fig. 7.8. Comparison of Fig. 7.3 and Fig. 7.8 shows that the topography of North America, among which the predominant mountains are the Rockies, makes a substantial contribution to the maintenance of the trough in North America as well as the associated ridge upstream at this latitude circle.

When the topography of Greenland is removed, both the anticyclonic circulation over Greenland and the inverse circulation to the west at the 200 mb level (Fig. 7.9) are weakened. It is noteworthy that the maximum in the perturbation streamfunction over Greenland is decreased only by about one third, which is less than the decrease caused by removing the North American topography. On the 850 mb wave activity flux map (not shown here), when the North American topography is removed the previously mentioned maximum vertical flux to the west of Greenland disappears, while it is only greatly weakened when the Greenland Plateau is removed. This suggests that the wave activity flux from mid-latitudes and its nonlinear interaction with the waves induced locally are important in determining the wave activity flux pattern in high latitudes, thus affecting the stationary waves there. As to the maintenance of orographically forced stationary

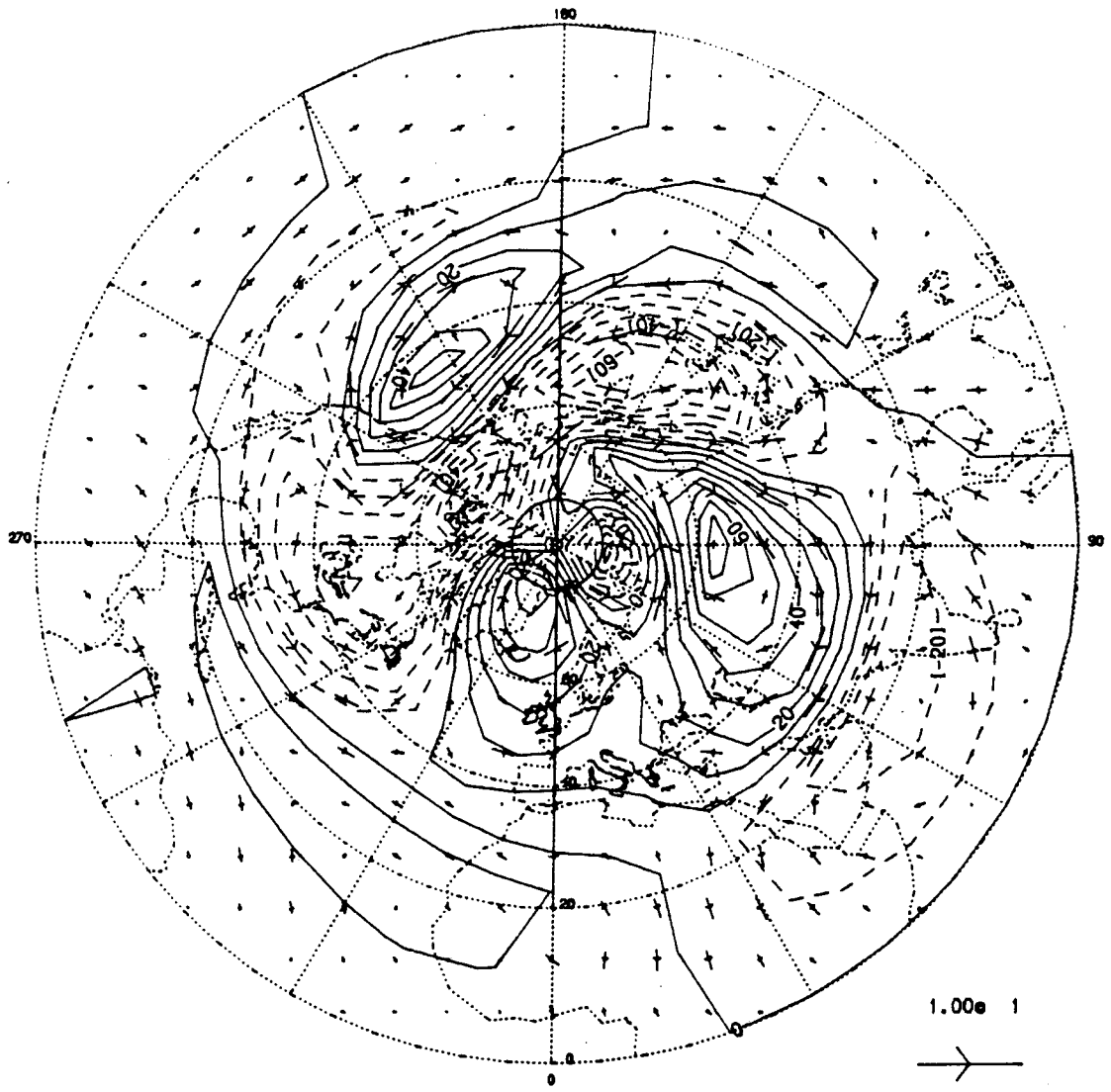

Fig. 7.1 700 mb perturbation stream field as in Fig.6.1, but for the nonlinear response.

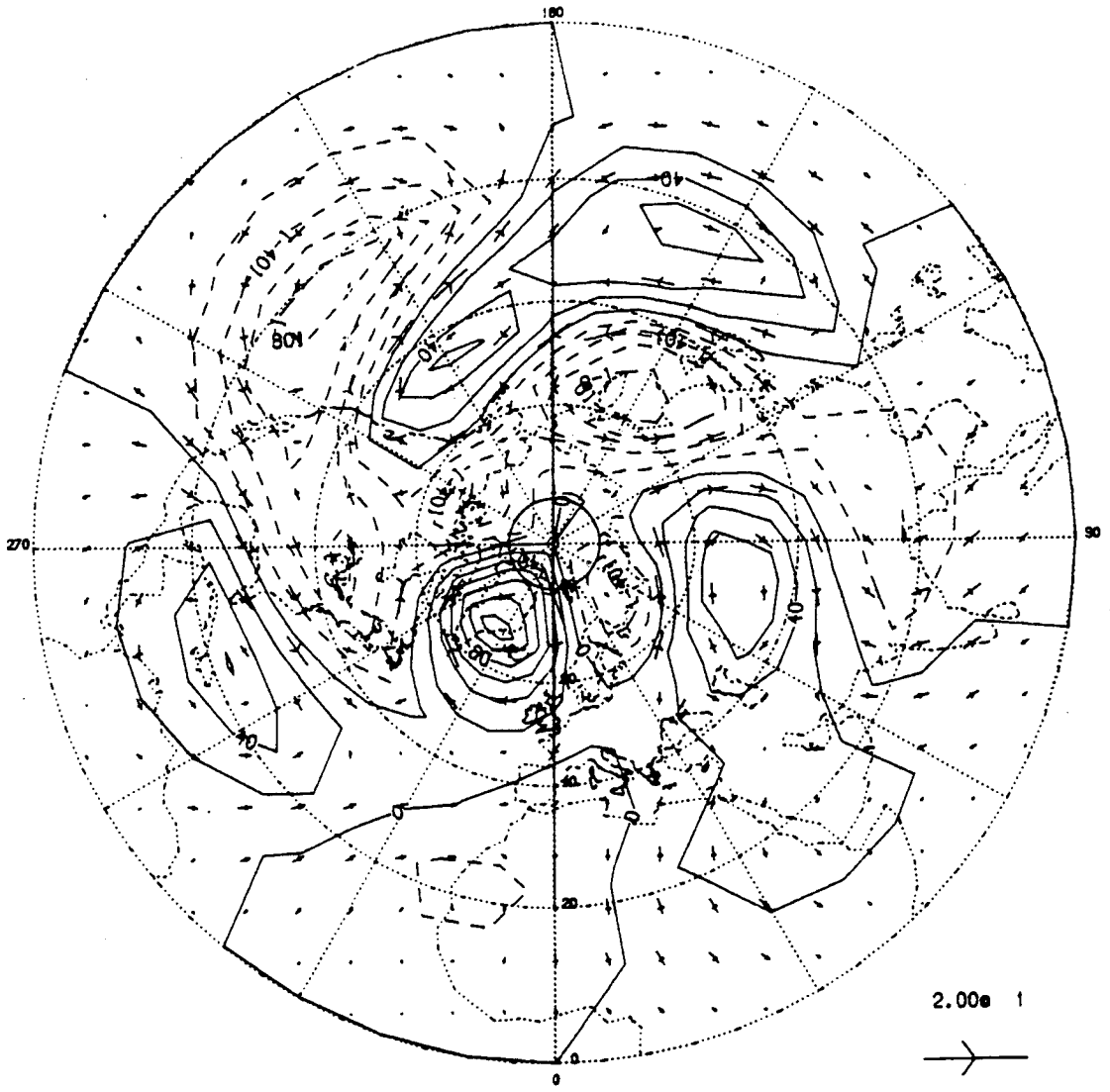

Fig. 7.2 200 mb perturbation stream field as in Fig.6.2, but for the nonlinear response.

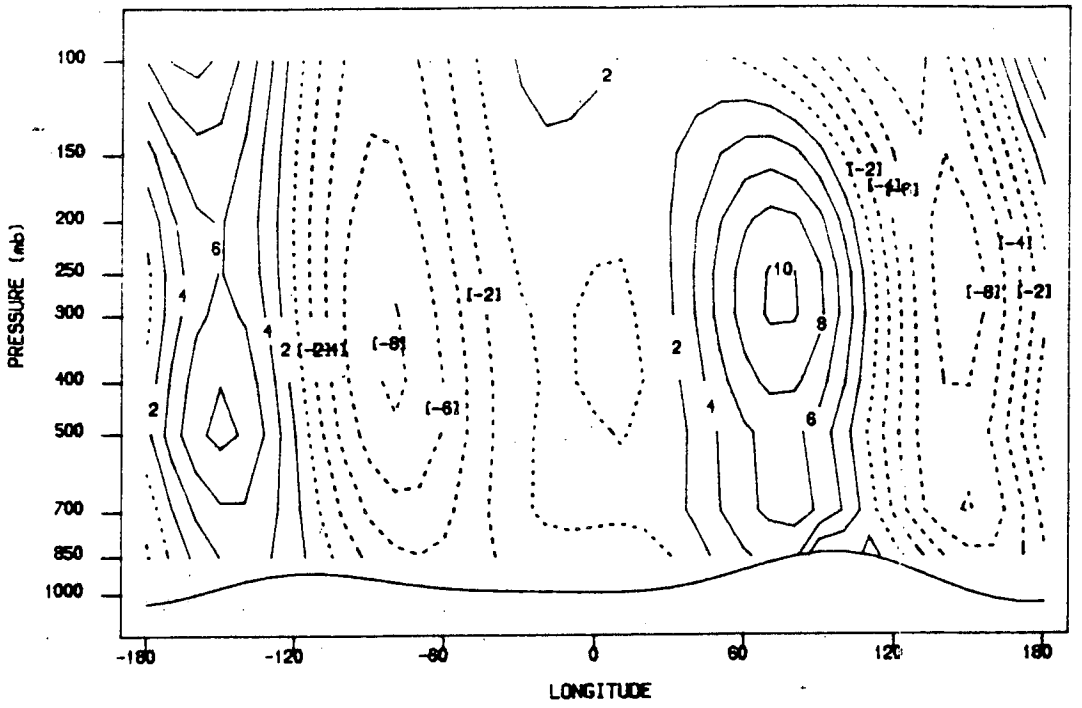

Fig. 7.3 Longitudinal cross-section of perturbation geopotential height at 45°N as in Fig. 6.3, but for the nonlinear response.

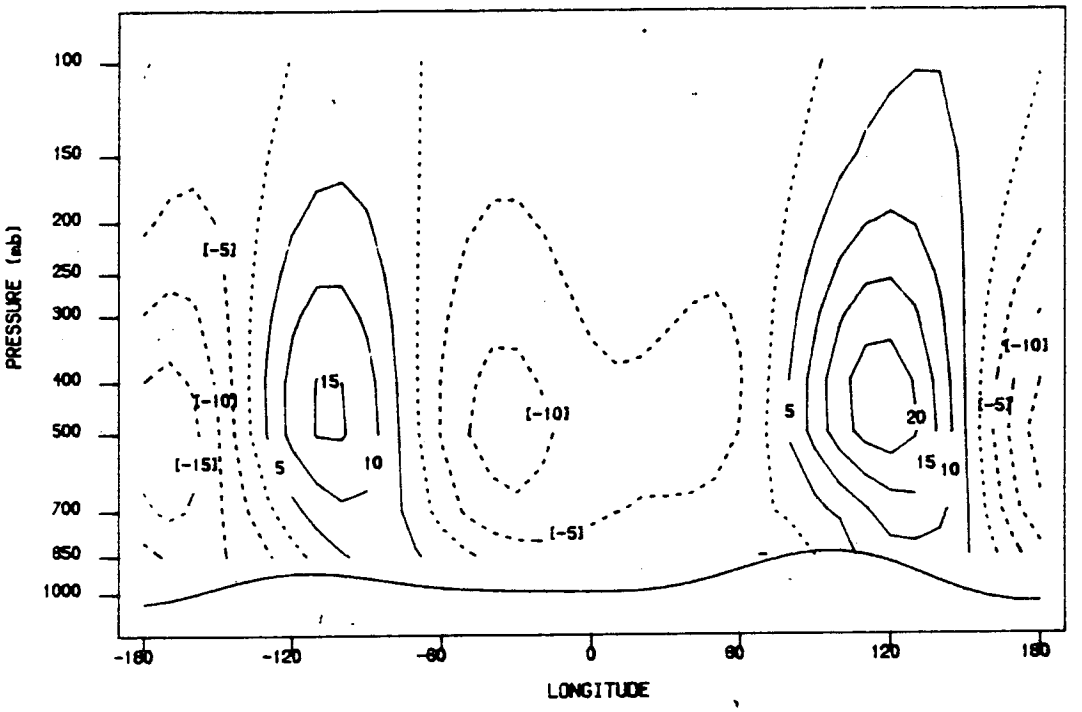

Fig. 7.4 Longitudinal cross-section of perturbation vertical velocity at 45°N as in Fig. 6.4, but for the nonlinear response.

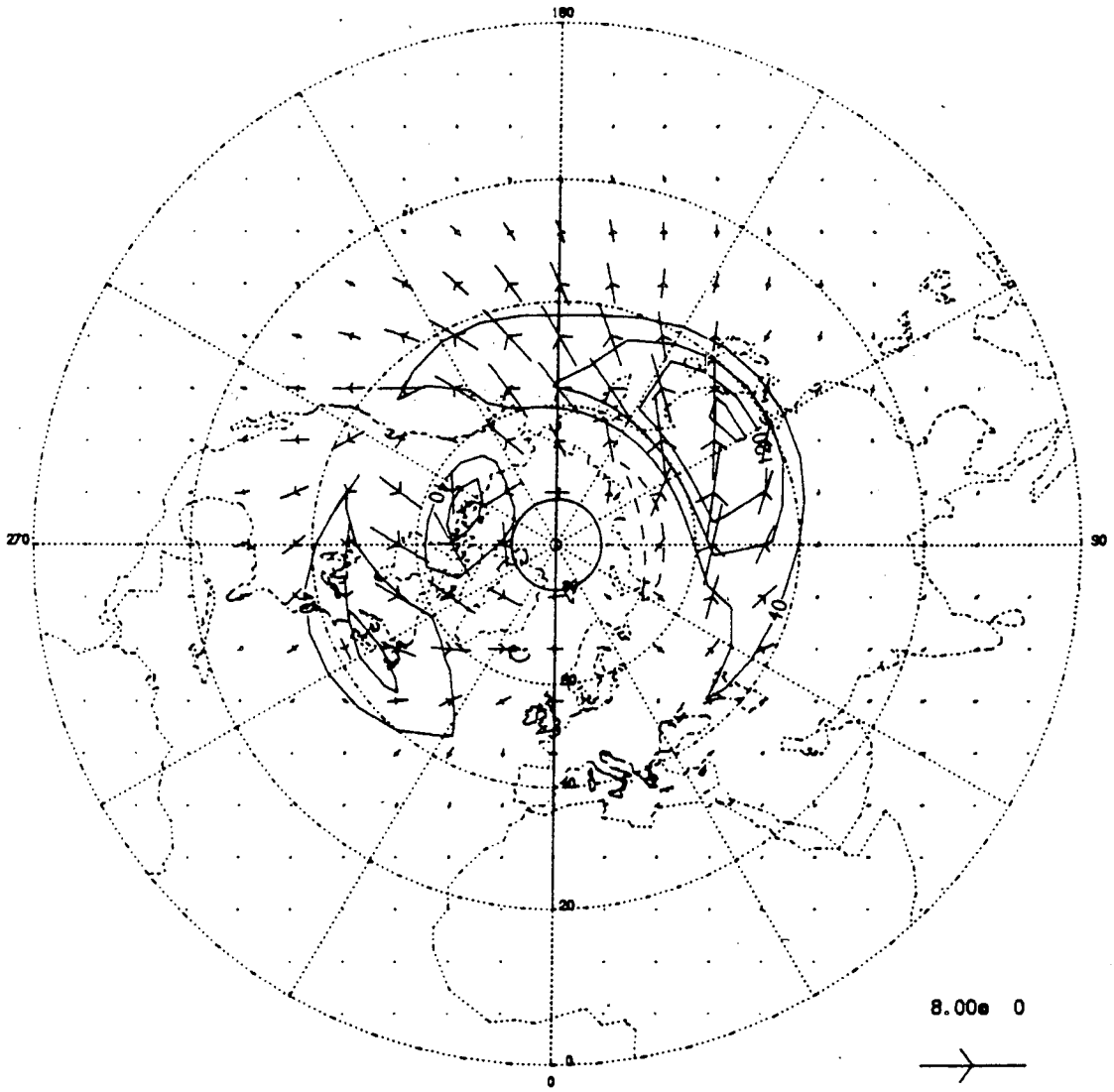

Fig. 7.5 Wave activity flux F at 850 mb as in Fig. 6.5, but for the nonlinear response.

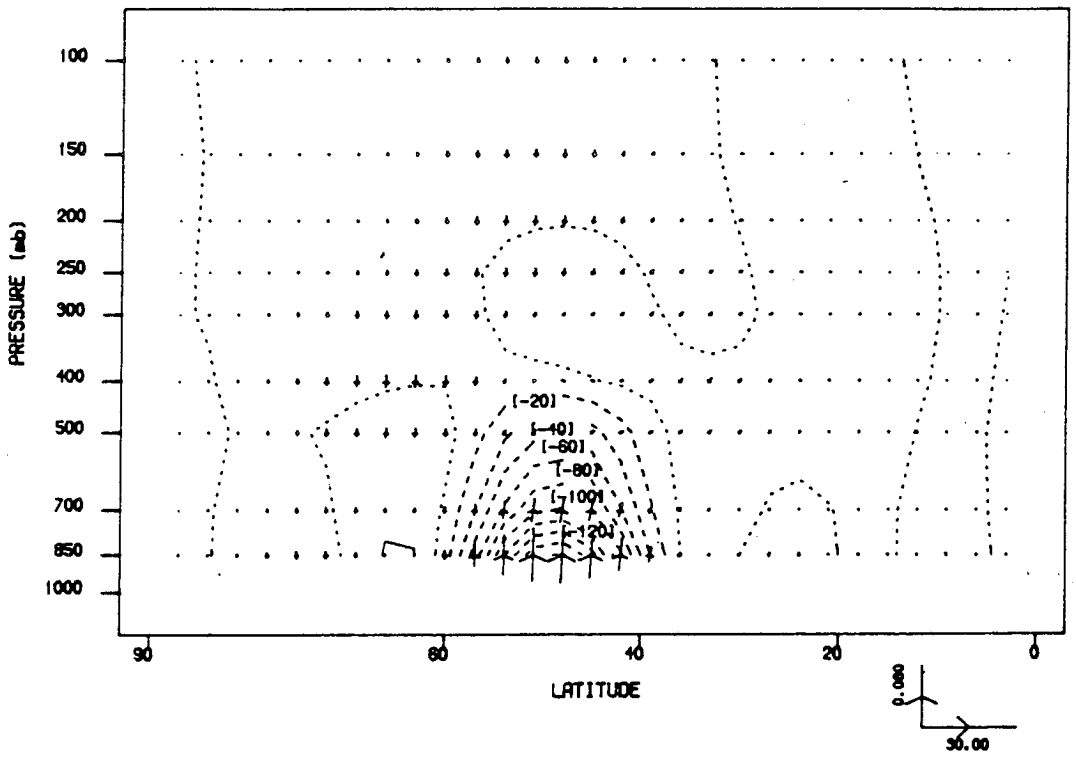

Fig. 7.6 EP cross-section as in Fig. 6.6, but for the nonlinear response.

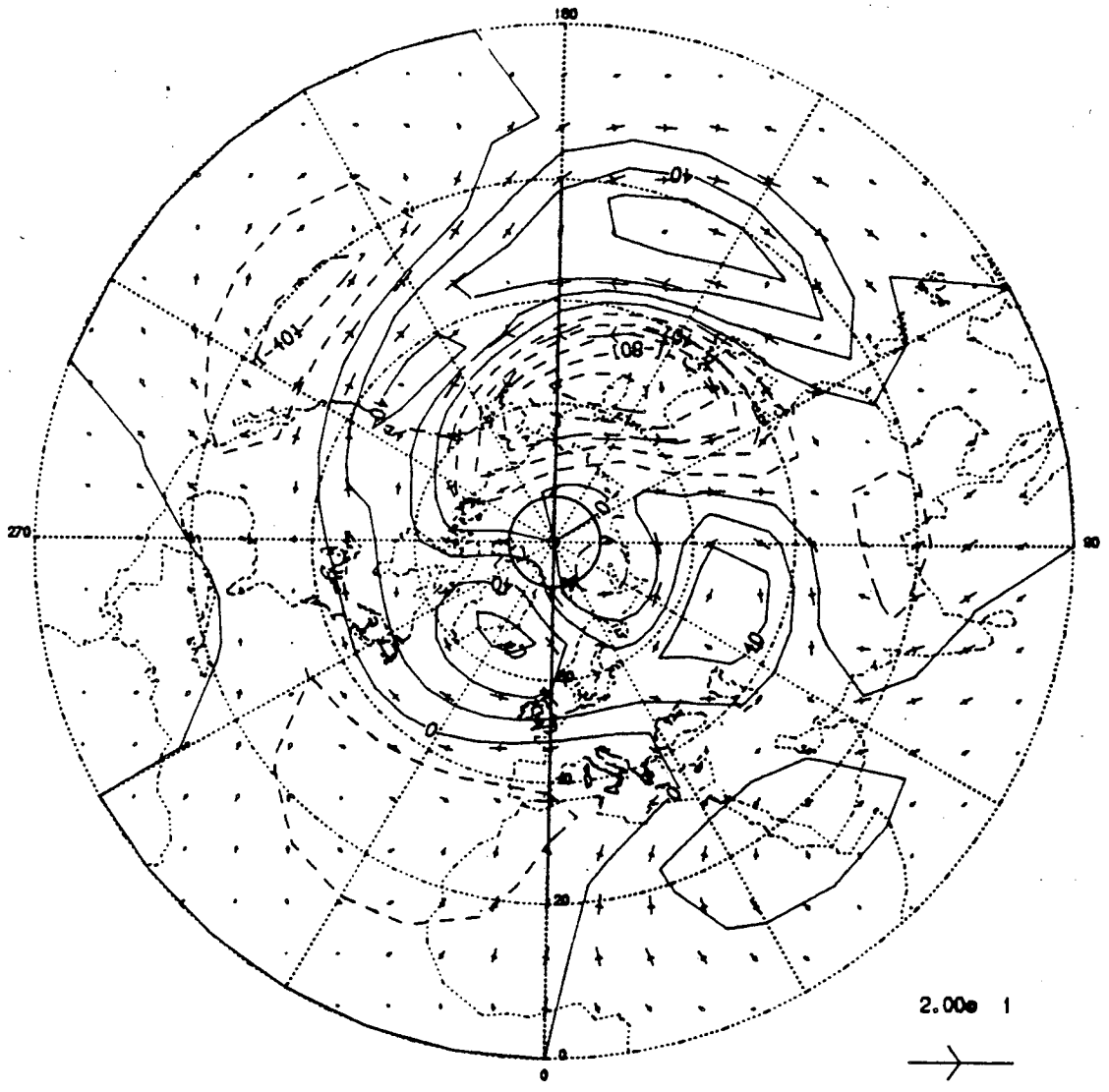

Fig. 7.7 As Fig. 7.2, but the topography of North America is removed.

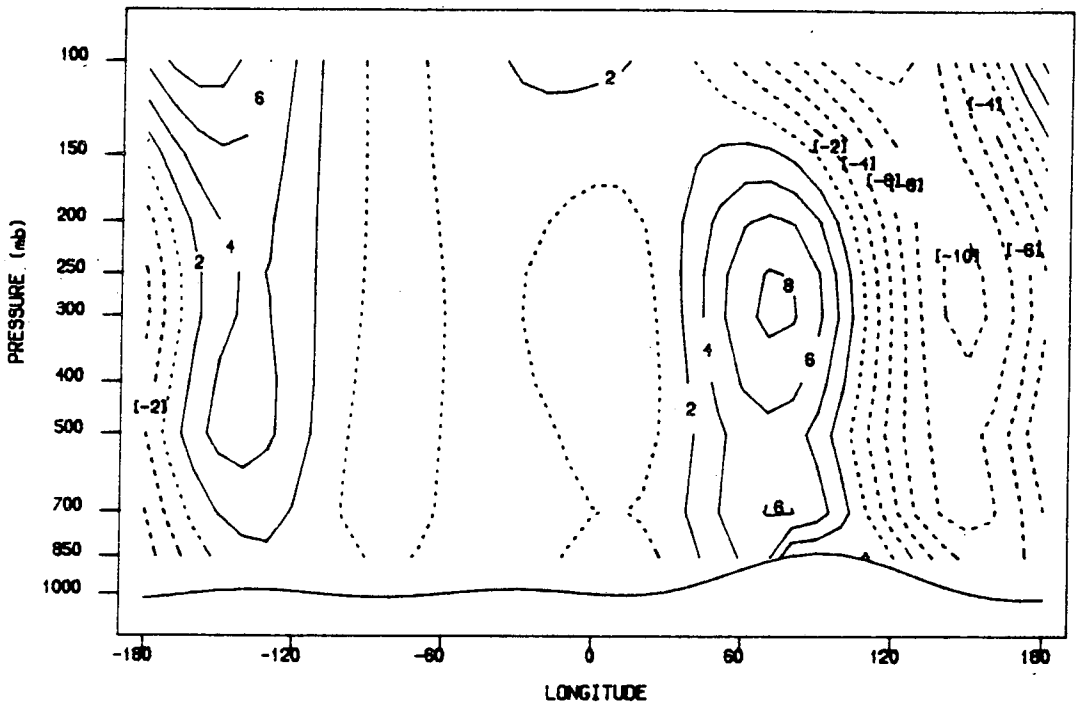

Fig. 7.8 As Fig. 7.3, but the topography in North America is removed.

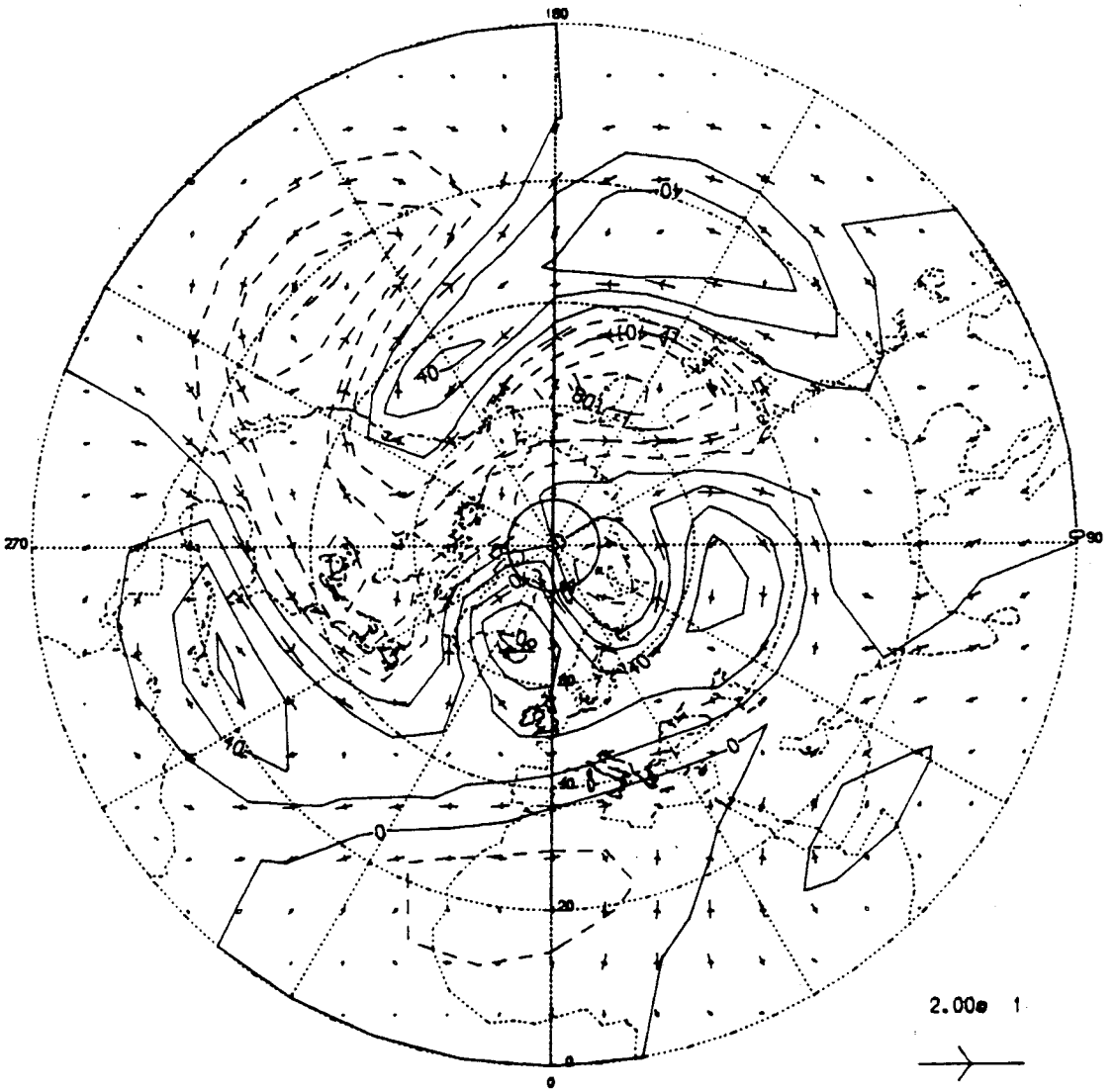

Fig. 7.9 As Fig. 7.2, but the topography of Greenland is removed.

waves in the whole Northern Hemisphere, these nonlinear calculations show that the Rockies and the Greenland Plateau are still of secondary importance compared with the Tibetan Plateau.

7.2 Nonlinear Response to Diabatic Heating in January 1979

For the idealized thermal forcing in middle latitudes where the zonal mean basic flow is relatively strong, we found that the influence of nonlinearity on the wave patterns at the 850 mb and 200 mb levels is not evident (section 5.3). But the geographic distribution of diabatic heating in the real atmosphere is much more complicated than that idealized case, hence it is expected that the nonlinear interaction may be more significant for the more realistic thermal forcing. In this section we discuss the nonlinear response to the mean diabatic heating in January 1979. Similar to the previous chapter, the heating fields derived from different data sources will be considered separately.

7.2.1 Heating Field Derived from FGGE IIIa Data

The 700 mb perturbation stream field for the nonlinear response to the FGGE IIIa heating field (Fig. 7.10) has a similar wave pattern in middle latitudes to that for linear response, but with a much larger amplitude. The nonlinear response in high and low latitudes produce some wave

patterns which cannot be seen clearly in the linear case. At the 200 mb level the nonlinear response (Fig. 7.11) in both high and low latitudes is also stronger than the linear one, while in middle latitudes the main difference is found in the eastern Pacific and North America. Fig. 7.12 is a longitudinal cross-section of perturbation geopotential height, which shows similar structure to the linear solution (Fig. 6.12) except between 180°E and 60°W. These comparisons suggests that the nonlinearity for the response to the actual diabatic heating in the wintertime is also significant, particularly in high and low latitudes.

It is interesting to compare the nonlinear response to the wintertime actual thermal forcing with that to the Northern Hemispheric orographic forcing. We find that both responses have comparable amplitude, this implies they are equally important for the maintenance of the stationary planetary waves in wintertime. The difference in vertical structure of the induced wave patterns for these two categories of forcing is evident. For example, comparison between the longitudinal cross-sections (Fig. 7.3 and 7.12) shows that the response to the actual thermal forcing has more baroclinic nature than that to the actual orographic forcing.

The wave activity flux for actual thermal forcing (FGGE IIIa) at the 850 mb level is shown in Fig. 7.13. The major features of the wave activity propagation displayed in this figure are, in general, consistent with those in Fig. 6.13, but the former has much larger magnitude than the latter.

As an extreme example, the maximum vertical flux for the Pacific wavetrain increases by a factor of five over its linear counterpart. The wave activity flux at the 200 mb level (not shown here) has also a similar pattern to the linear one but with a smaller magnitude, the maximum vertical flux decreases by about 50%. In addition, the downward flux at 850 mb for the linear response has completely disappeared in the nonlinear case, where all vertical fluxes are upward. As discussed in section 6.2.1, in the nonlinear case the North Pacific wavetrain is still propagating poleward in the meridional direction and the North Atlantic wavetrain equatorward, showing the important effect of the longitudinal variation of diabatic heating in the tropical region.

Compared with the linear response, the vertical component of wave activity flux for the nonlinear response increases in the lower levels and decreases in the upper levels. This must be reflected in the corresponding EP cross-section. Fig. 7.14 reveals a much more intense and extensive vertical EP flux at the lower levels and a slightly weakened vertical EP flux at high levels than in Fig. 6.14 for the linear case, thus there is a much stronger convergence of EP flux in the middle troposphere at mid-latitudes in Fig. 7.14 than in Fig. 6.14. This means that the interaction between the mean flow and the stationary waves simulated by the nonlinear model is more significant than by the linear model. On the other hand, compared with the orographically forced waves (refer to Fig. 7.6), the

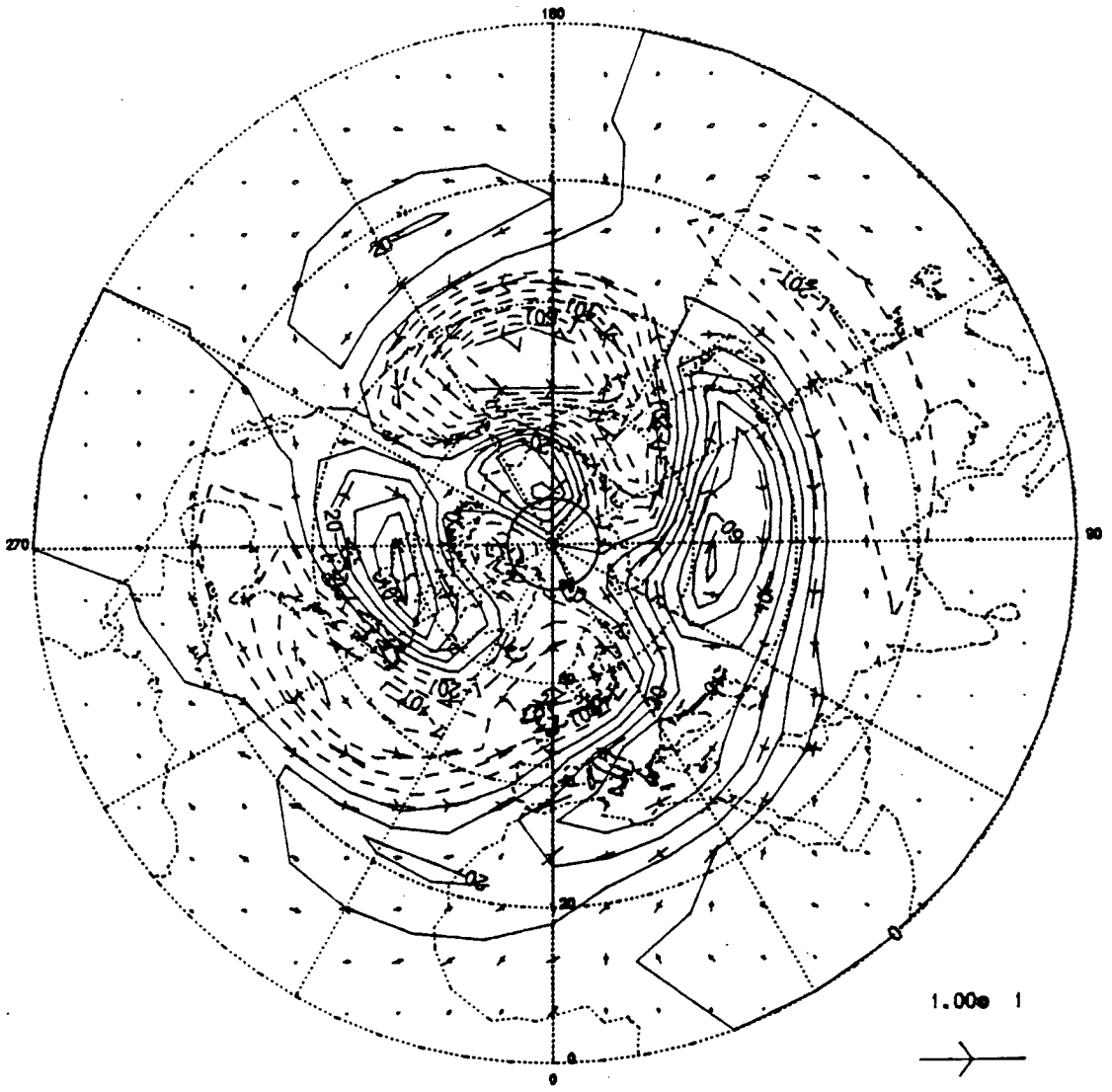

Fig. 7.10 700 mb perturbation stream field as in Fig.6.10, but for the nonlinear response.

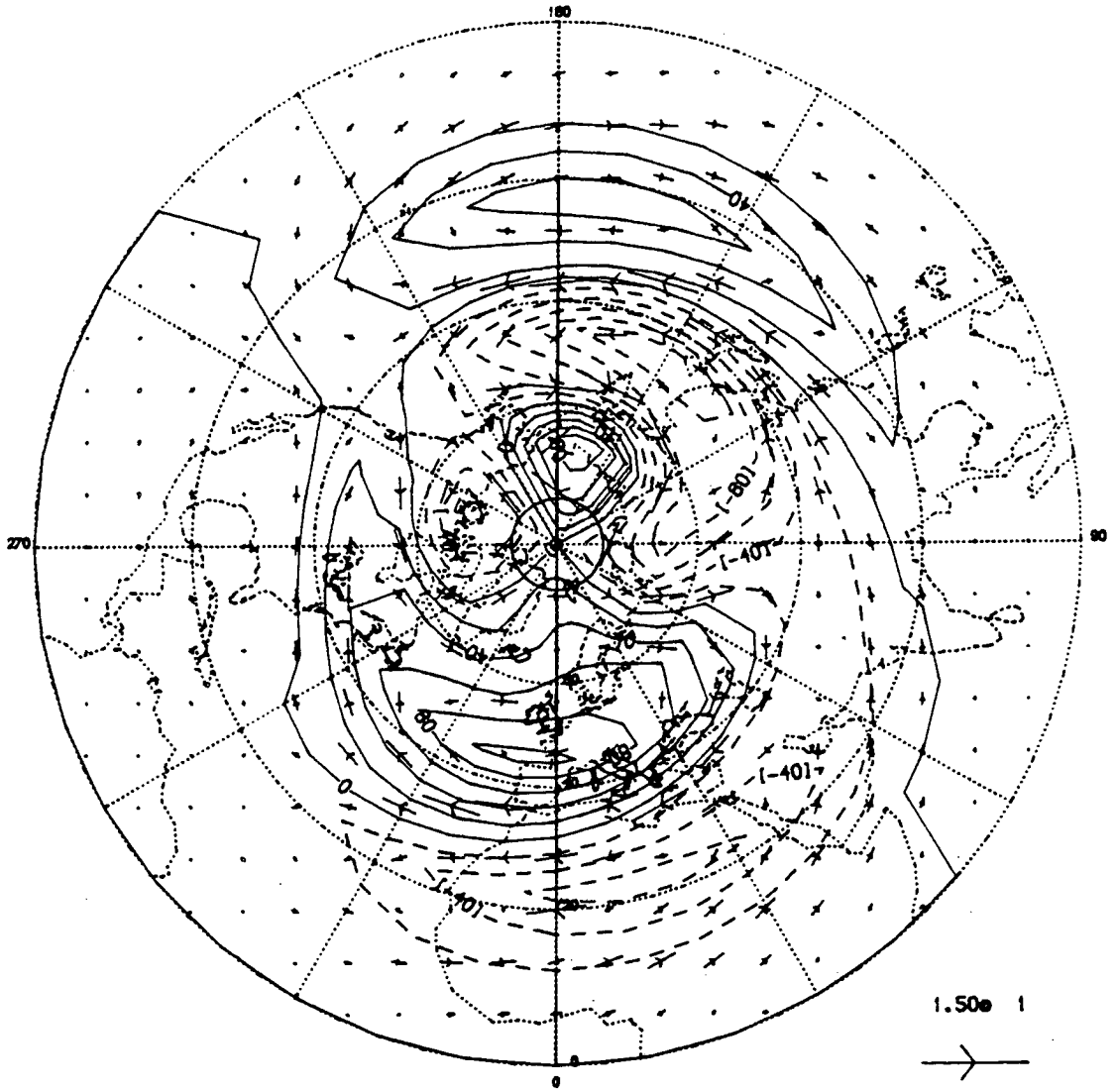
180
270
90
0
-40
-80
-120
-160
-200
-240
-280
-320
-360
-400
-440
-480
-520
-560
-600
-640
-680
-720
-760
-800
-840
-880
-920
-960
-1000
-1040
-1080
-1120
-1160
-1200
-1240
-1280
-1320
-1360
-1400
-1440
-1480
-1520
-1560
-1600

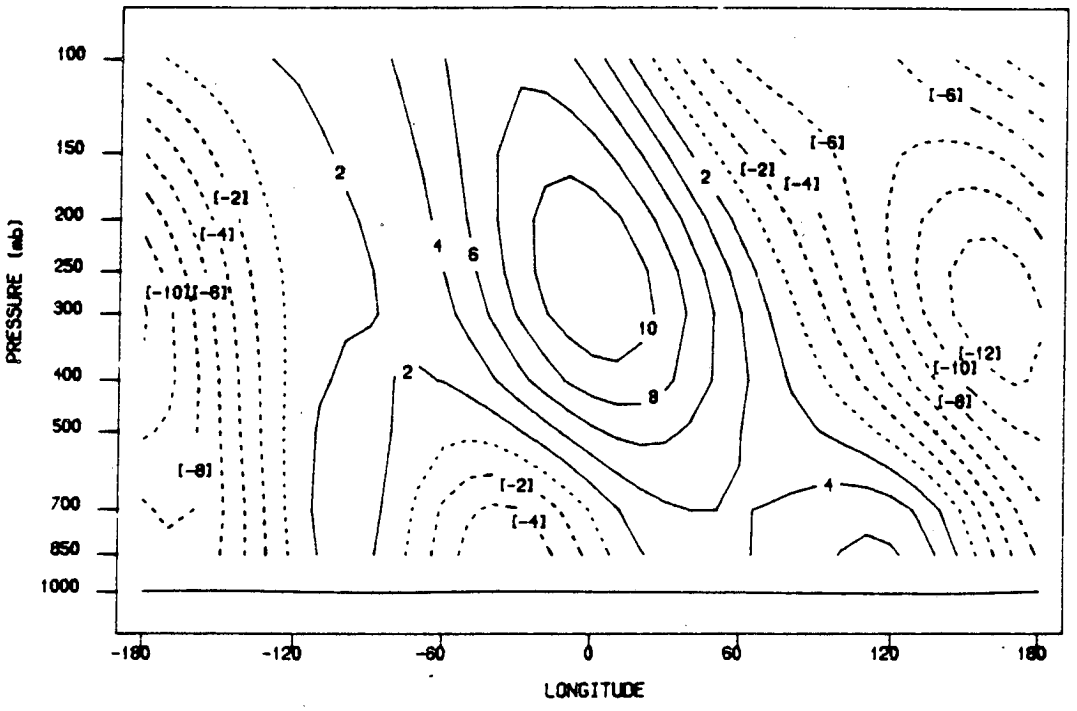

Fig. 7.12 Longitudinal cross-section of perturbation geopotential height at 45°N as in Fig. 6.12, but for the nonlinear response.

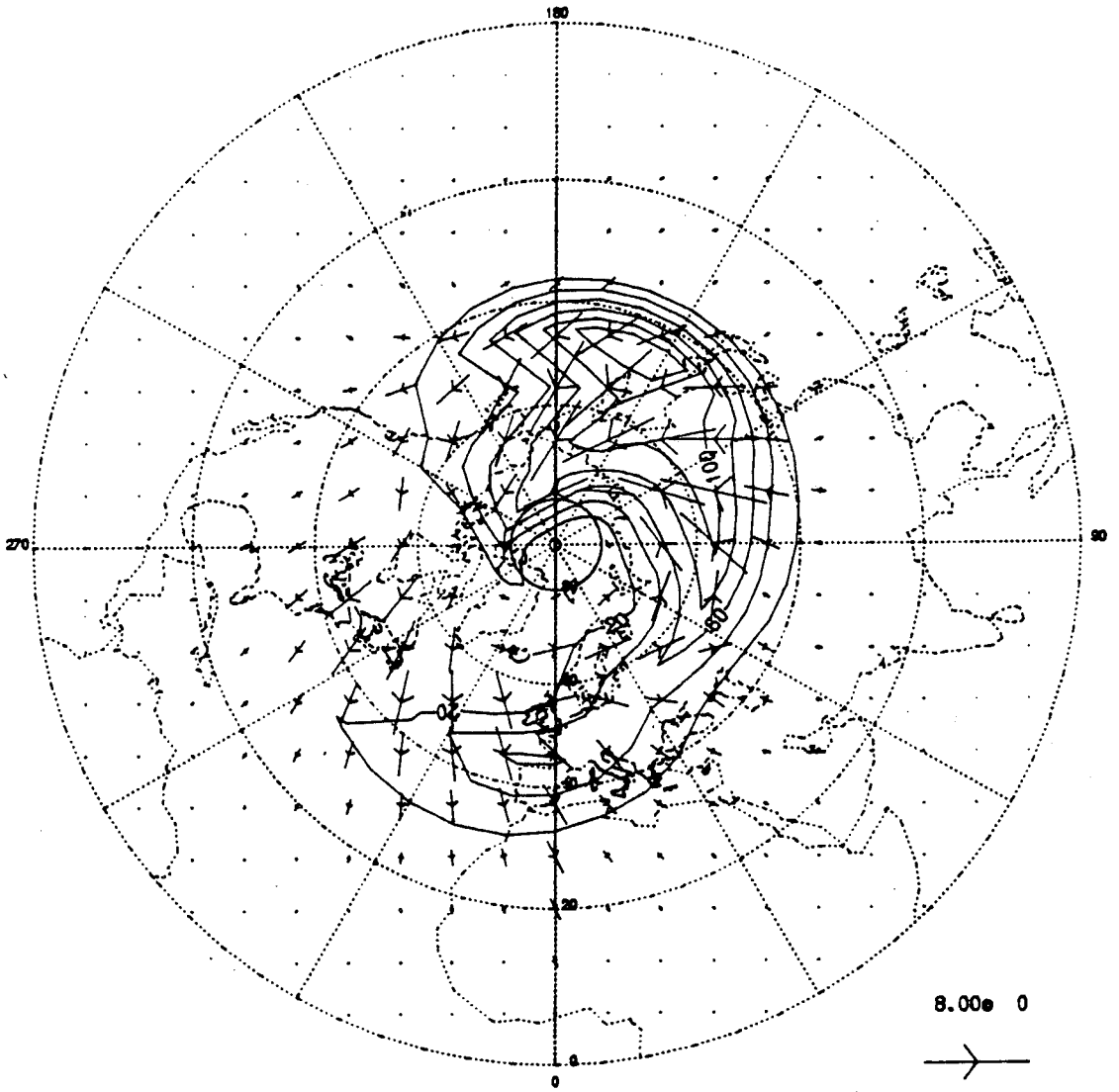

Fig. 7.13 Wave activity flux **F** at 850 mb as in Fig. 6.13, but for the nonlinear response.

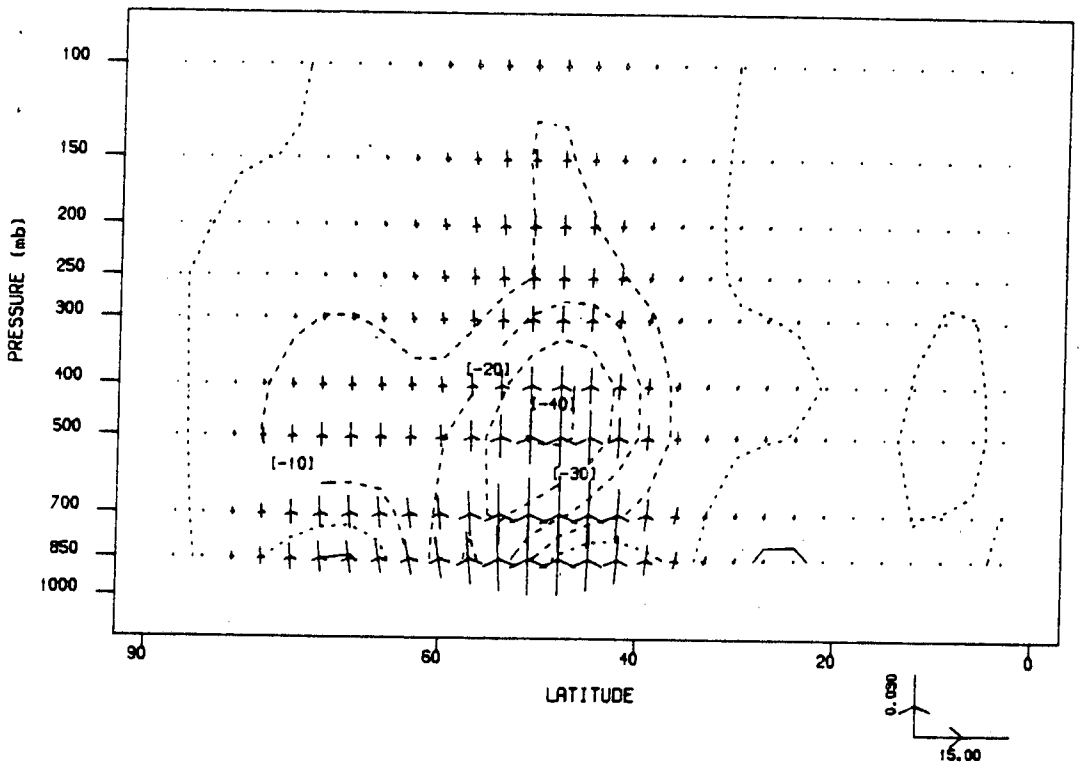

Fig. 7.14 EP cross-section as in Fig. 6.14, but for the nonlinear response.

major convergent region of EP flux for the response to the thermal forcing is located at the higher levels. Their contributions to the maintenance of the vertically propagating stationery planetary waves in the stratosphere are comparable, as discussed on the previous chapter for the linear case.

7.2.2 Heating Field Derived from FGGE IIIb Data

In Figs. 7.15 and 7.16 are shown the perturbation stream fields for the nonlinear response to the diabatic heating, which is derived from FGGE IIIb data, at the 700 mb and 200 mb levels. Firstly, we compare these figures with Figs. 7.10 and 7.11 where the FGGE IIIa heating field is used. The 700 mb response in Fig. 7.15 differs that in Fig. 7.10 evidently. The predominant systems in Fig. 7.15 are the cyclonic circulation over the Pacific and the anticyclonic circulation over Eurasia, ~~but in Fig. 7.10 the former is much weaker and the latter does not exist~~ they are more extensive than their counterparts in Fig. 7.10. The circulation systems in the other areas displayed in Fig. 7.10 are either weakened or have disappeared in Fig. 7.15. Therefore it looks as if the low level wave patterns produced by different data set are quite different. However, at the 200 mb level their difference is less evident. In order to see the vertical structure of the wave pattern in middle latitudes, a longitudinal cross-section of perturbation geopotential height at 45°N is displayed in Fig. 7.17. Comparing Fig. 7.17 with Fig. 7.12 shows the troughs and

ridges produced by the two data sets are in general agreement. Secondly, we compare Fig. 7.15 and 7.16 with their linear counterparts (i.e., Fig. 6.16 and 6.17). At the lower level the response in the Pacific and Eurasia is considerably more intense in the nonlinear case than in the linear case. The extreme values of perturbation streamfunction in this region are now approximately double what they were in the linear case. In addition, the polar region response is also much stronger. At the upper level a quite strong anticyclonic circulation has developed with a centre at 65°N, 165°W in the nonlinear case, showing a much stronger wave propagation poleward in the meridional direction than in the linear case.

The corresponding wave activity fluxes at the 850 mb and 200 mb levels are shown in Fig. 7.18 and 7.19. Similar to the previous section for the FGGE IIIa heating field, the lower level flux is much larger than in the linear case in both horizontal and vertical directions. A quite strong convergence of EP flux is also found in the middle levels at mid-latitudes (Fig. 6.20). The extreme value of the convergence of EP flux in the nonlinear case is tripled compared with the linear case.

7.3 Nonlinear Response to Topography and Diabatic Heating

Unlike the linear case, the nonlinear solution for the combined orographic and thermal forcing is not a simple linear superposition of the separate nonlinear solutions for

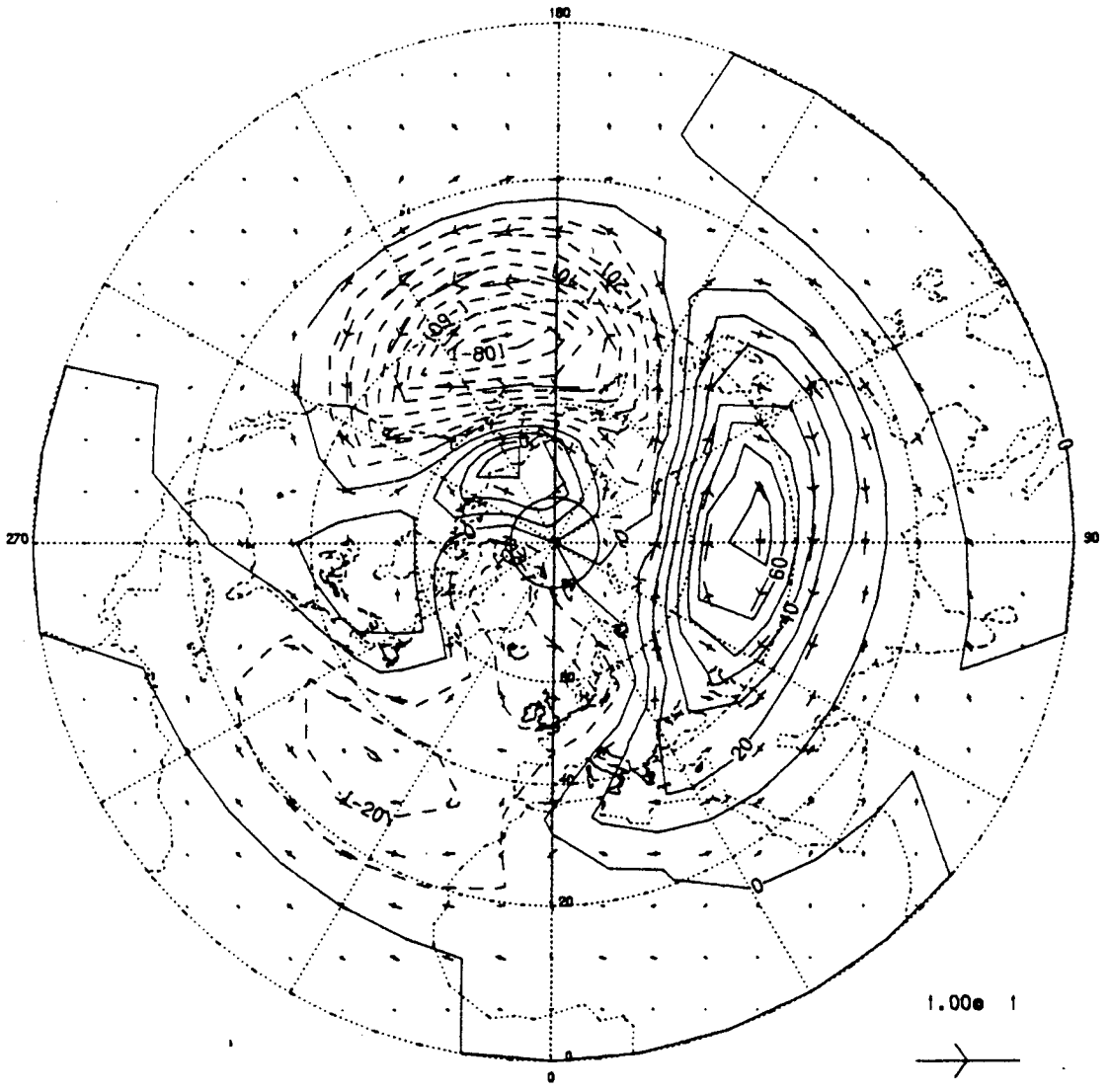

Fig. 7.15 700 mb perturbation stream field as in Fig. 6.16, but for the nonlinear response.

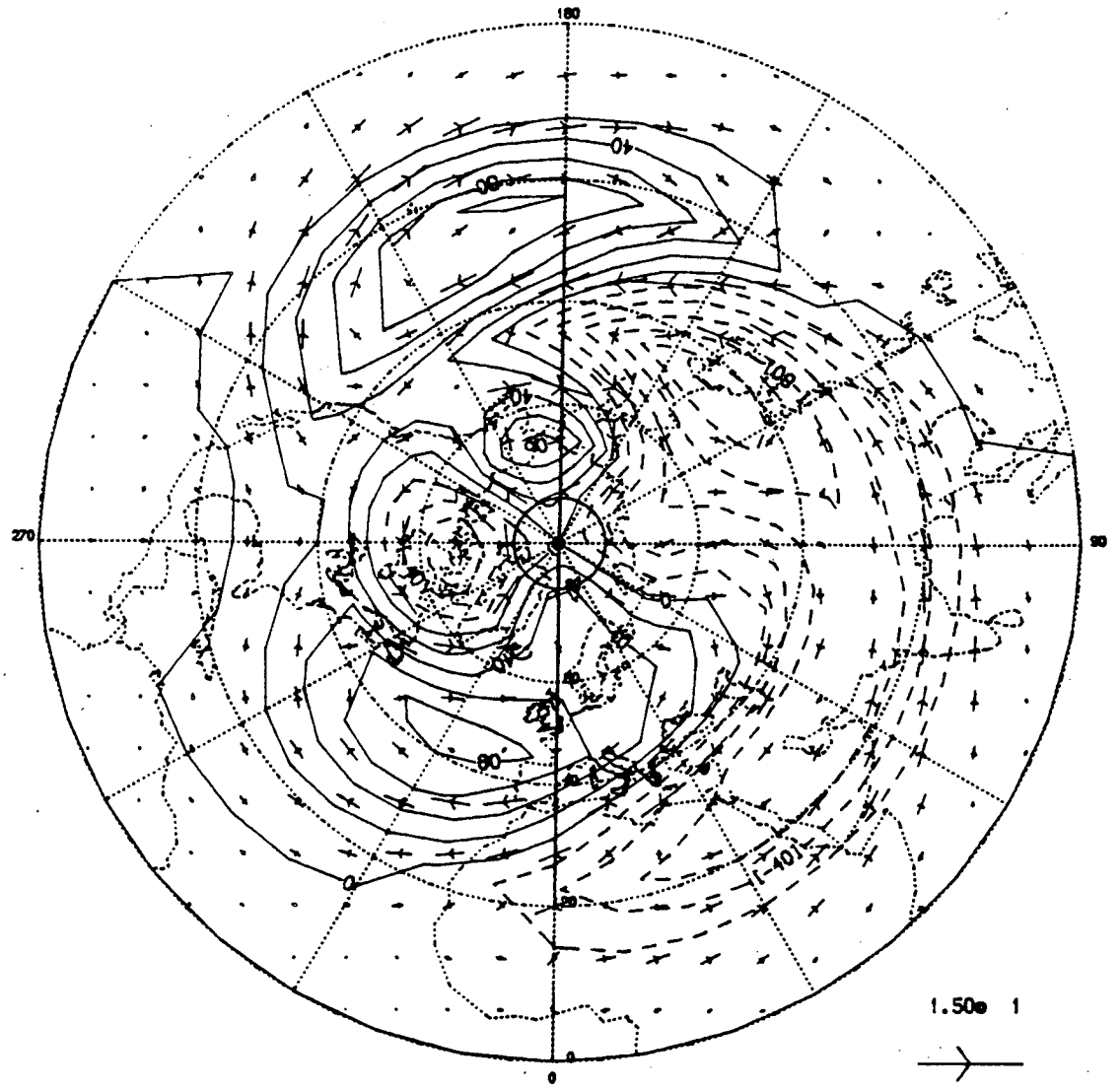

Fig. 7.16 200 mb perturbation stream field as in Fig. 6.17, but for the nonlinear response.

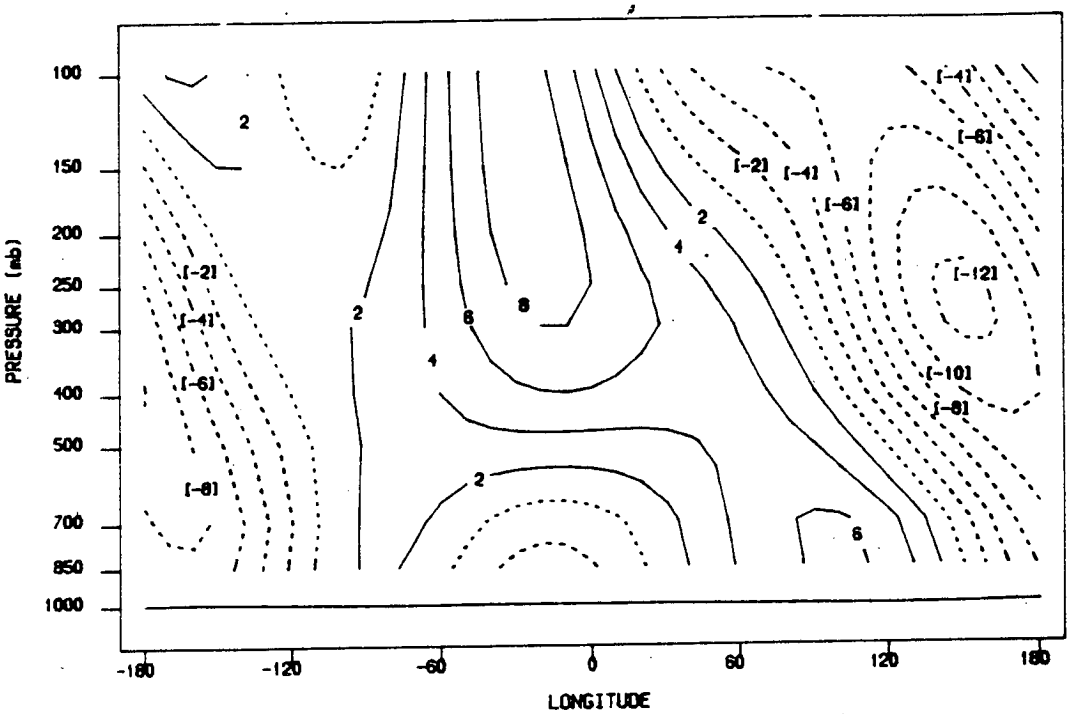

Fig. 7.17 Longitudinal cross-section of perturbation geopotential height at 45°N as in Fig. 7.12, but for the FGGE IIIb heating field.

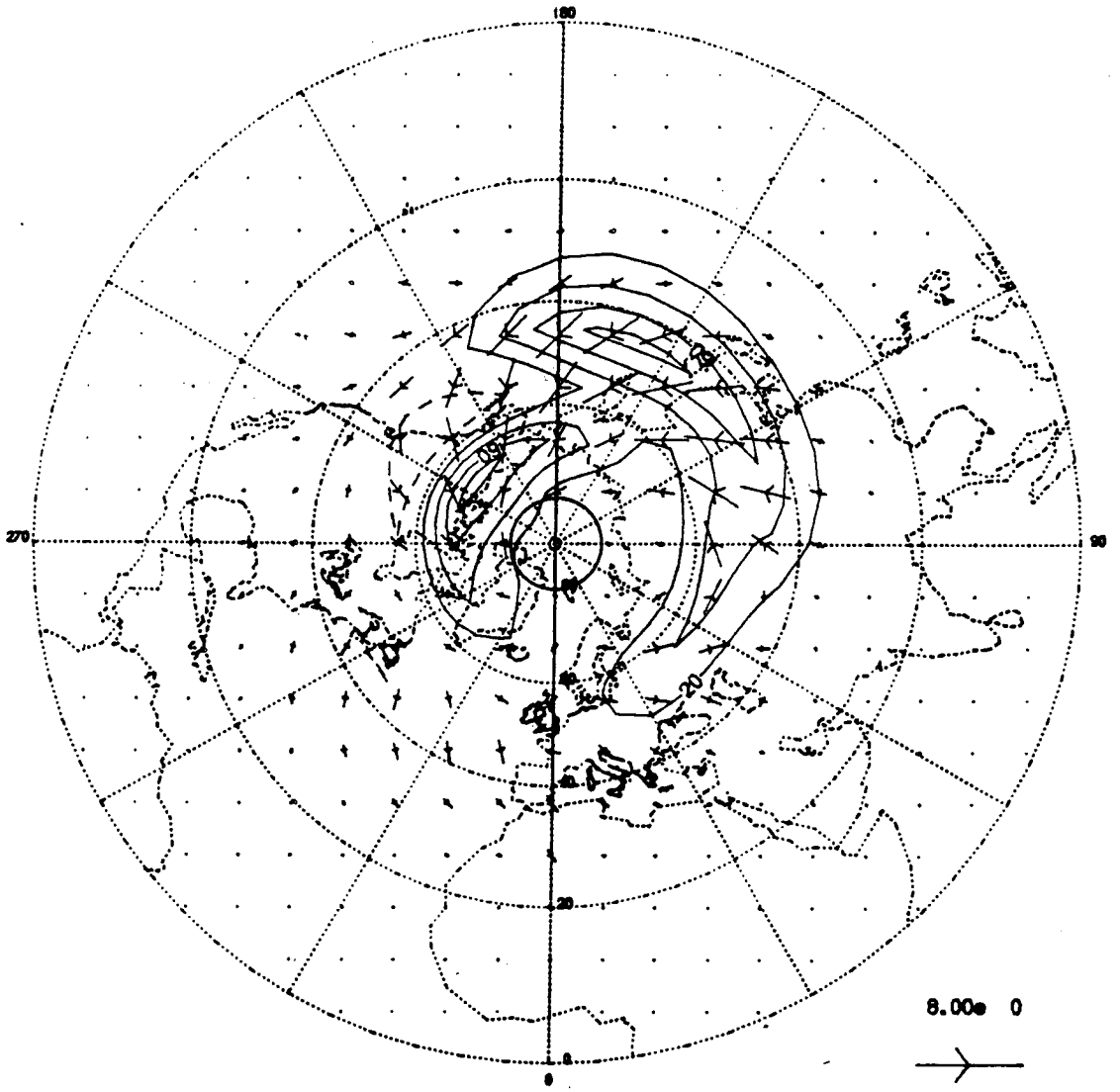

Fig. 7.18 Wave activity flux **F** at 850 mb as in Fig. 6.18, but for the nonlinear response.

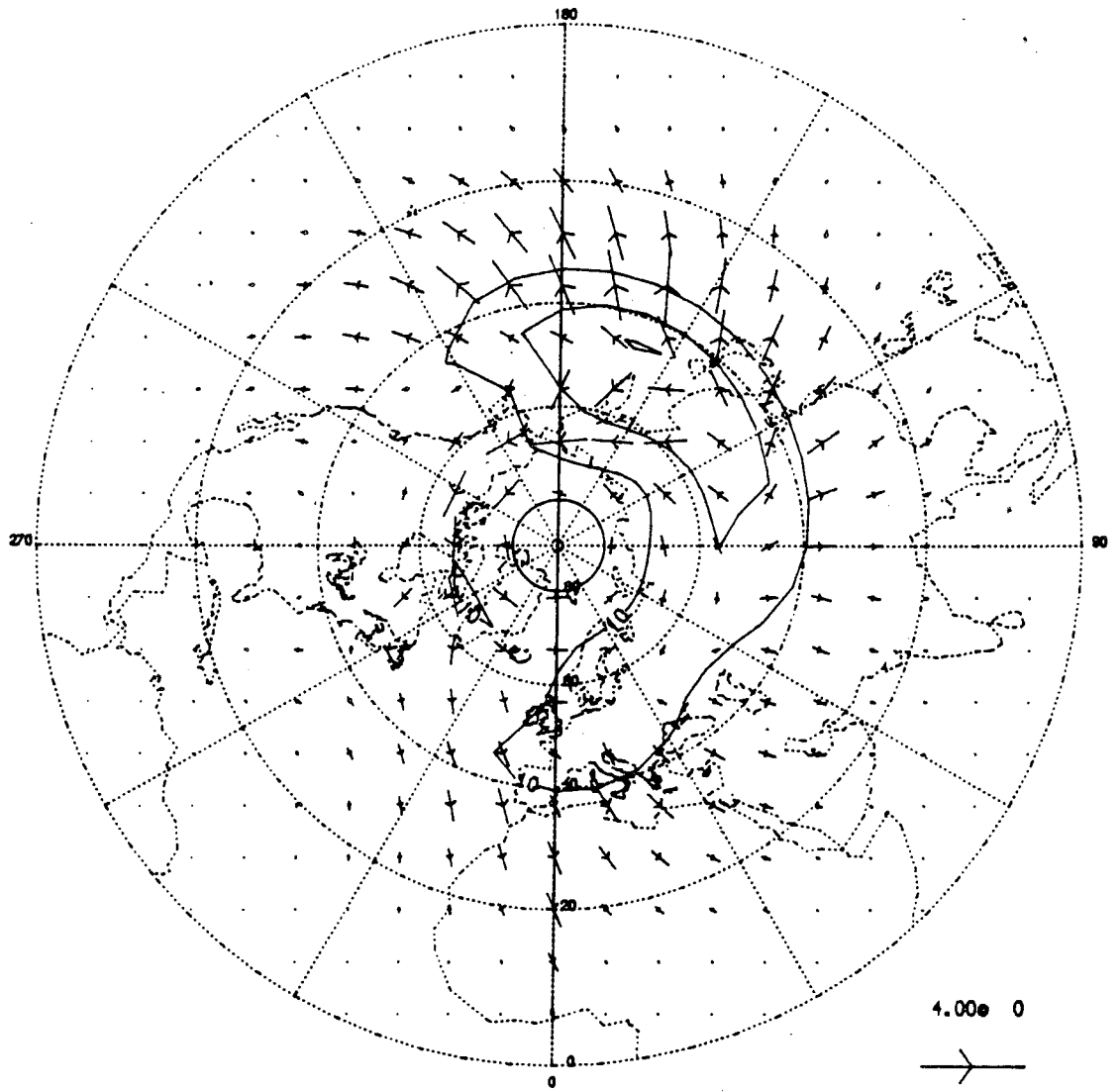

Fig. 7.19 Wave activity flux **F** at 200 mb as in Fig. 6.19, but for the nonlinear response.

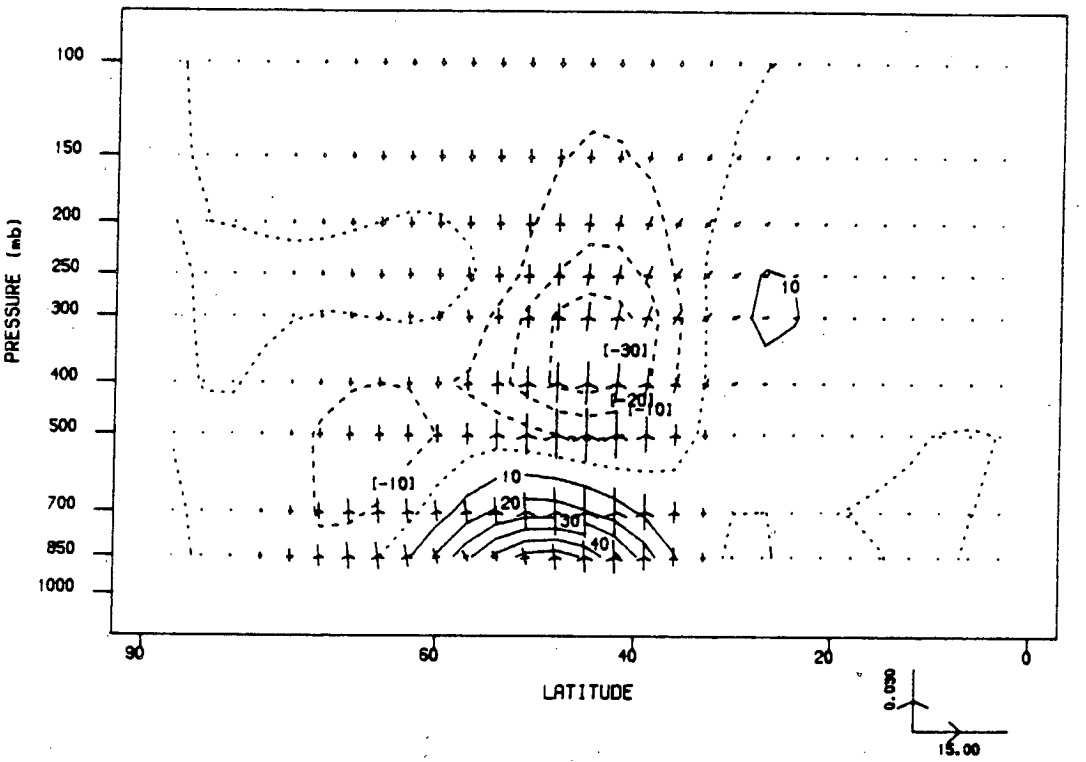

Fig. 7.20 EP cross-section as in Fig. 6.20, but for the nonlinear response.

the pure orographic and the pure thermal forcings. These forcing functions must be inserted into the nonlinear model simultaneously. The results for the Northern Hemispheric topography in combination with the FGGE IIIa or the FGGE IIIb heating field are described separately.

7.3.1 Topography and FGGE IIIa Heating Field

In Figs. 7.21 and 7.22 are shown the perturbation stream fields at the 700 mb and 200 mb levels for the nonlinear response to the Northern Hemispheric topography in combination with the FGGE IIIa heating field. As we may expect from the previous experiments, at the lower level the nonlinear response is greatly enhanced compared with the linear one, especially in high and low latitudes. Even in middle latitudes the extreme value of the perturbation streamfunction for most circulation systems increases more than 100%. At the upper level the difference between nonlinear and linear responses is also evident. In order to show what improvements have been achieved by inclusion of the nonlinear interaction, we may review the deficiencies of the linear response, which were discussed in section 6.3.1, as follows.

a) The anticyclonic circulation over the western Pacific, which appears too weak in the linear response, is considerably intensified in the nonlinear case and looks more realistic compared with the observed 6-year climatological stationary waves (Fig.

6.25).

b) The cyclonic circulation located in the Middle East and to the North of India, which is too strong and appears unrealistic in the linear response, is greatly weakened in the nonlinear case and, in general, consistent with the observation.

c) The cyclonic circulation over the eastern tropical Atlantic and North Africa, which appears very weak in the linear response (the extreme value of perturbation streamfunction is slightly more than 10% of the observed value), is evidently enhanced in the nonlinear case. The extreme value of perturbation streamfunction for this circulation reaches up to 1.5×10^3 $m^2 s^{-1}$ (the observed value for the 250 mb pattern is about $2.0 \times 10^3 m^2 s^{-1}$). This may be considered as a substantial improvement for the model simulation.

d) Finally, this nonlinear solution still cannot realistically simulate the observed climatological stationary waves in high latitudes. The reasons for this deficiency have not been investigated fully. From the numerical experiments which have been done, it is believed that the inaccurate representation of the actual wintertime diabatic heating is partly responsible. For example, the anticyclonic circulation located poleward of 60°N and between 120°E and 150°W is too strong and clearly displaced eastward. This mainly results from the

thermal forcing (see Fig. 7.11). If the alternative heating field derived from FGGE IIIb data is employed a better result may be obtained (see Fig. 7.16). In the next section it is shown that the nonlinear response to the Northern Hemispheric topography in combination with the FGGE IIIb heating field does give a better representation for the high latitude wave pattern.

The first three nonlinear effects discussed above are significant improvements in the response characteristics of the model. Therefore it is apparent that the nonlinearities are of primary importance in the response of the model atmosphere to the actual topography in combination with the actual diabatic heating.

In middle latitudes at the 200 mb level the difference between the nonlinear and linear response is less evident. In Fig. 7.23 is shown a longitudinal cross-section of perturbation geopotential height at 45°N. For convenience of comparison, another corresponding longitudinal cross-section based on observations in the winter season is shown in Fig. 7.24, which is adapted from Lau (1979b) and derived from 11 years of NMC operational analyses. Comparison between Figs. 7.23 and 7.24 shows that the major troughs and ridges at this latitude circle predicted by this nonlinear model are in their correct locations. The vertical phase structure of the geopotential height perturbations displayed in Fig. 7.23 is characterized by a distinct westward tilt with height, which is also

reasonable. The amplitude of the perturbations in these two figures is not coincident. There is nothing surprising about it because the steady-state solution, with no effect of transient waves explicitly included, differs from the time mean of a time varying solution. It is certainly possible that some other reasons exist which may affect the amplitude. For example, the dissipation parameters are important for the simulated wave amplitude as shown in the sensitivity experiments of section 5.1.3. Comparing Fig. 7.23 and 7.24 with Fig. 6.23 suggests that the nonlinear response is closer to observations than the linear response even in middle latitudes.

In comparing Fig. 7.22 with Fig. 7.2 (for the pure orographic forcing) and Fig. 7.11 (for the pure thermal forcing), we also note that the mid-latitude topography, especially the Tibetan Plateau (compare further with Figs. 7.7 and 7.9), makes a substantial contribution to the maintenance of the cyclonic circulation over the eastern tropical and sub-tropical Pacific as well as the inverse circulation over the western Pacific at the 200 mb level. These upper level systems are usually considered to be associated with the large scale longitudinal circulation over the tropical Pacific, which is often referred to as the 'Walker Circulation'. It is here suggested that the orographic forcing in mid-latitudes plays an important role on the planetary scale motions in the tropics.

A longitudinal cross-section of perturbation vertical velocity at 45°N is shown in Fig. 7.25, which is

characterized by rising motion over the oceans and sinking motions over the continents. The vertical motion over eastern Asia and the Pacific is evidently stronger than over the other regions at this latitude circle. Compared with the linear case (Fig. 6.26), the rising (sinking) over the Pacific (Europe) is considerably enhanced (weakened), and the vertical motion over North America is reversed. This example shows that the vertical velocity, which is associated with the irrotational (divergent) component of the horizontal flow, is very sensitive to the nonlinearity.

In Figs. 7.26 and 7.27 are shown the wave activity fluxes at 850 mb and 500 mb respectively. The wave propagation characteristics shown in these figures are, in general, consistent with those in the linear case, but with evidently larger magnitude. For example, the maximum of the vertical flux at the 850 mb level for both the Pacific and the Atlantic wavetrain are doubled compared with the linear case. The meridional propagation of wave activity is also more evident. From the view of computation, the change in wave activity flux **F** results from the variation of the spatial structure of the forced stationary waves, especially the horizontal and vertical gradient of perturbation streamfunction are important factors in determining the **F**. As mentioned in section 4.1.1, the conservation relation for F (Plumb, 1985) is derived from the linearized geostrophic equations. In the nonlinear case we may render it valid by incorporating the nonlinear effects into the source term. Therefore the evident

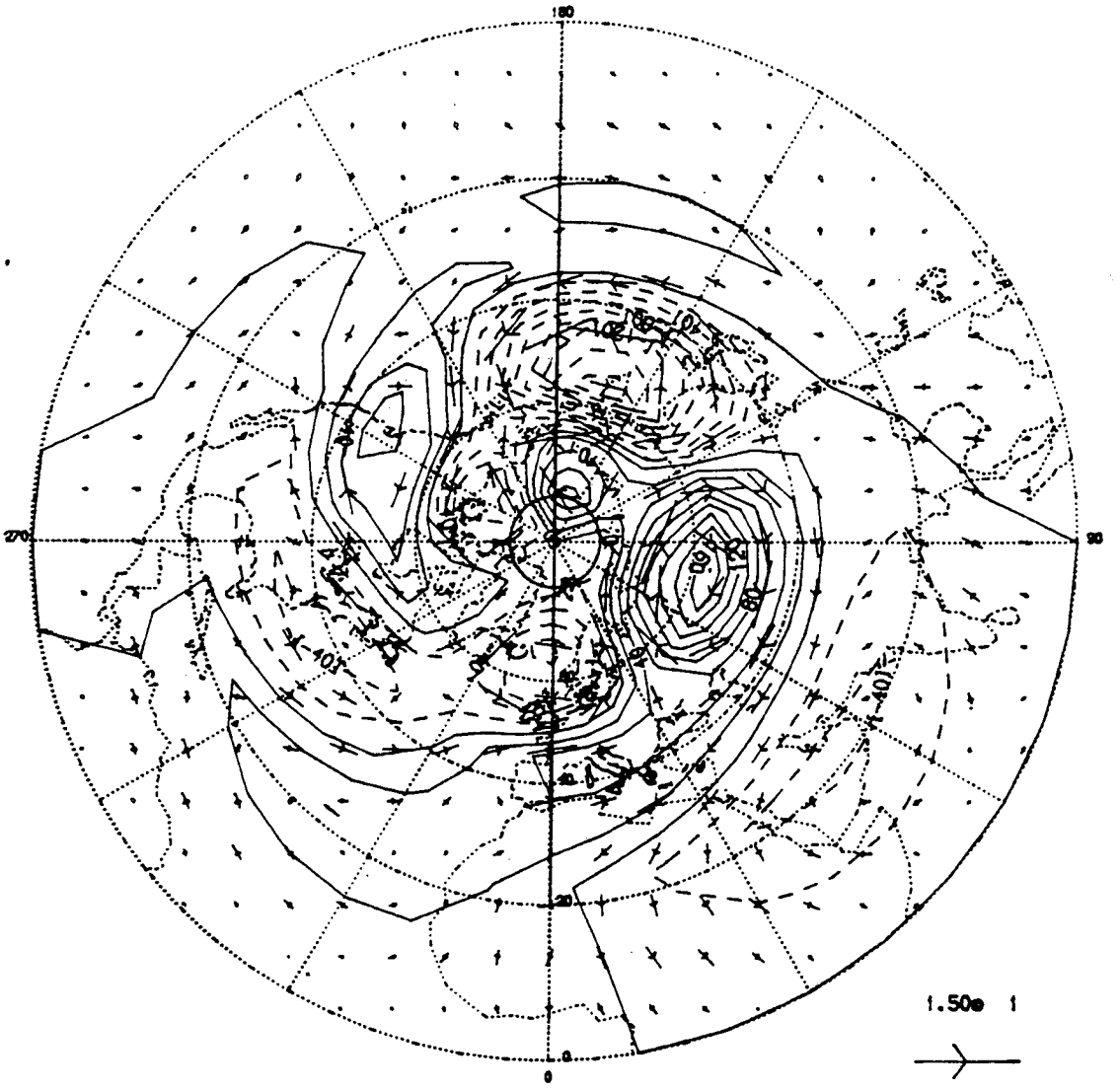

Fig. 7.21 700 mb perturbation stream field as in Fig. 6.21, but for the nonlinear response.

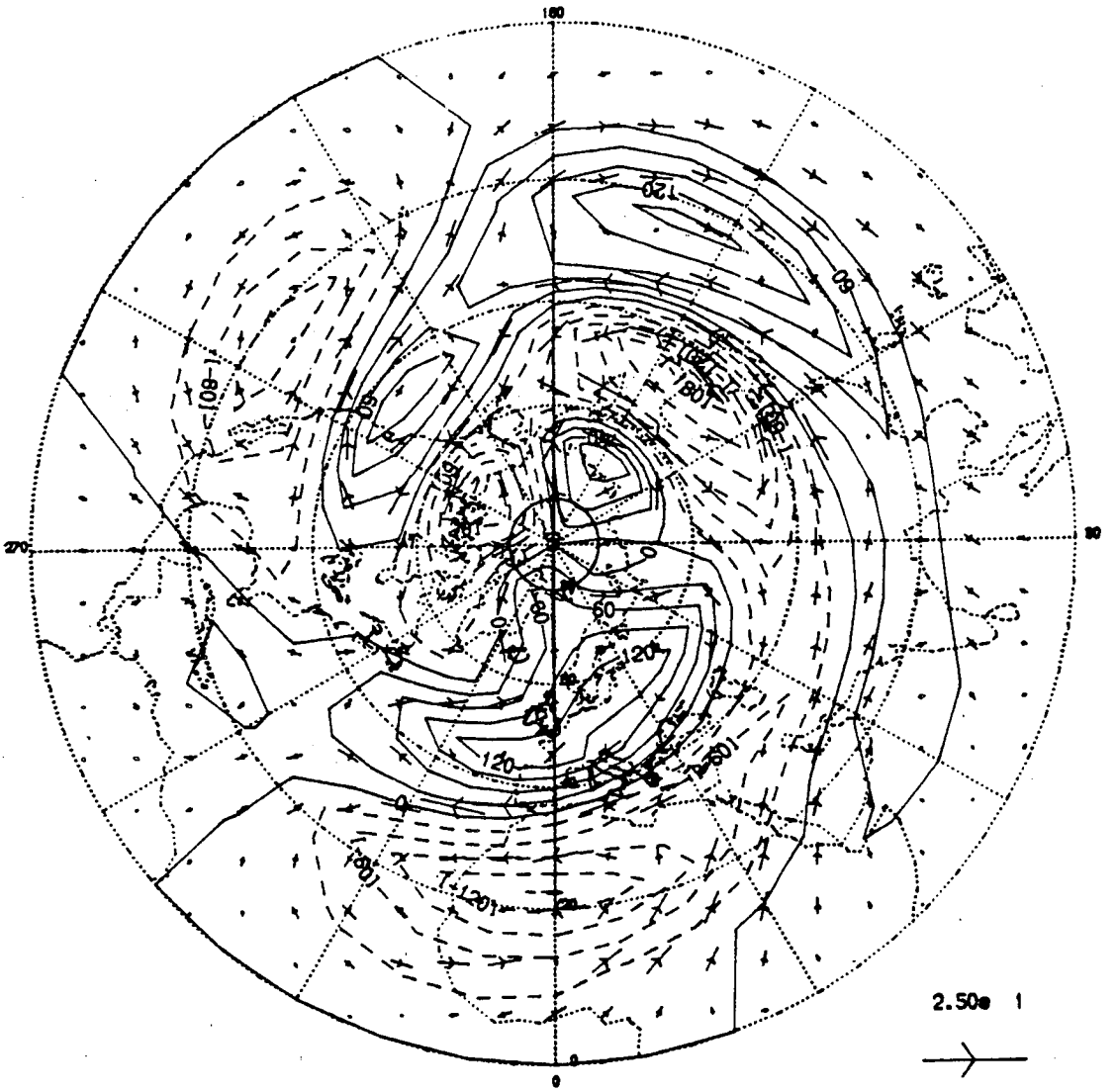

Fig. 7.22 200 mb perturbation stream field as in Fig. 6.22, but for the nonlinear response.

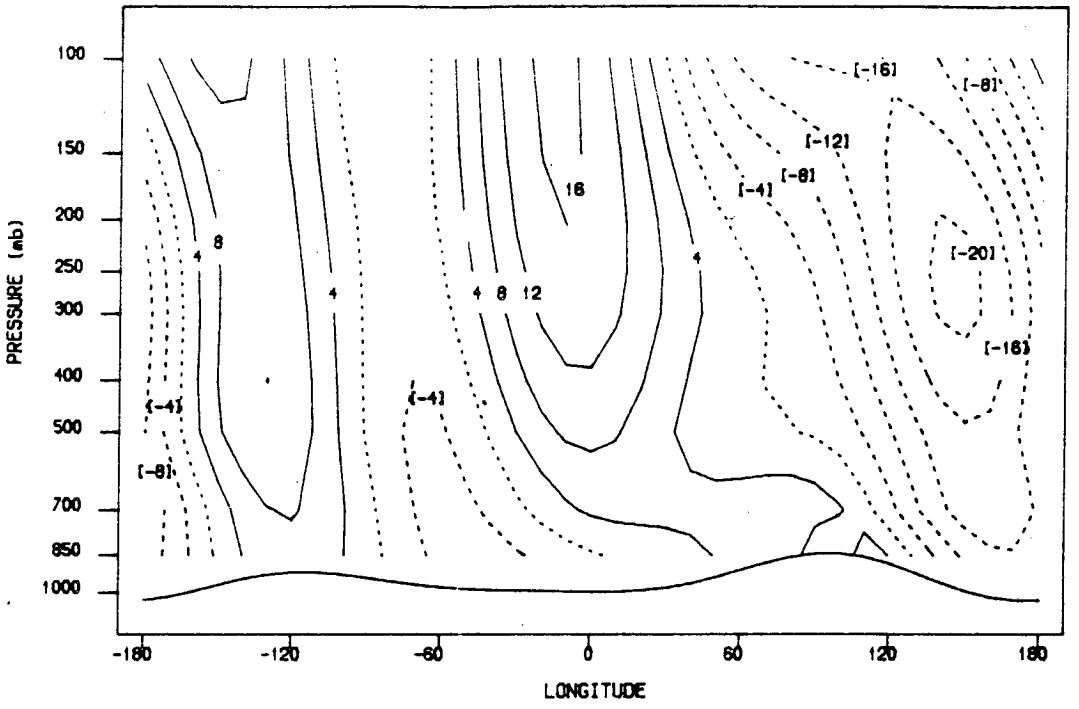

Fig. 7.23 Longitudinal cross-section of perturbation geopotential height at 45°N as in Fig. 6.23, but for the nonlinear response.

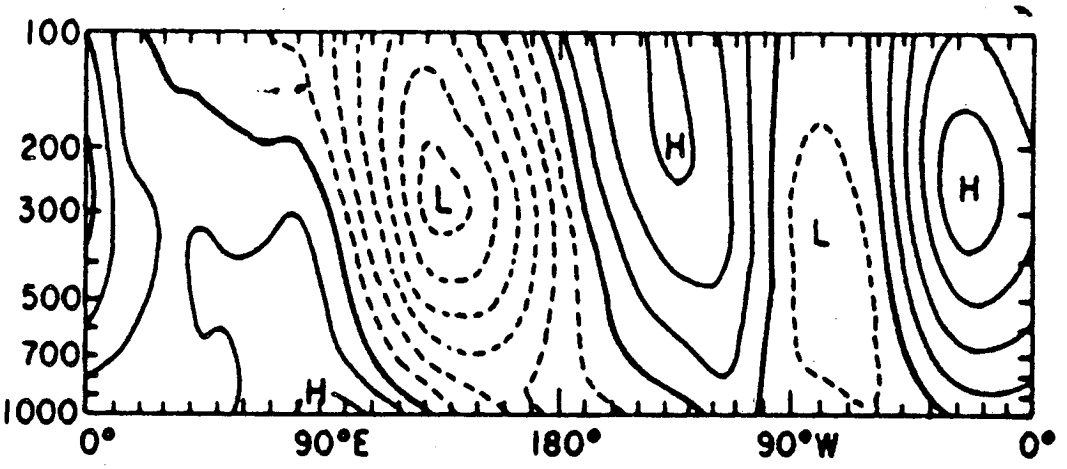

Fig. 7.24 Longitudinal cross-section of perturbation geopotential height at 45°N for the winter season, derived from 11 years of NMC operational analyses, adapted originally from Lau (1979b), photocopied from Wallace (1983). Contour interval is 5 dam; the zero contour is thickened.

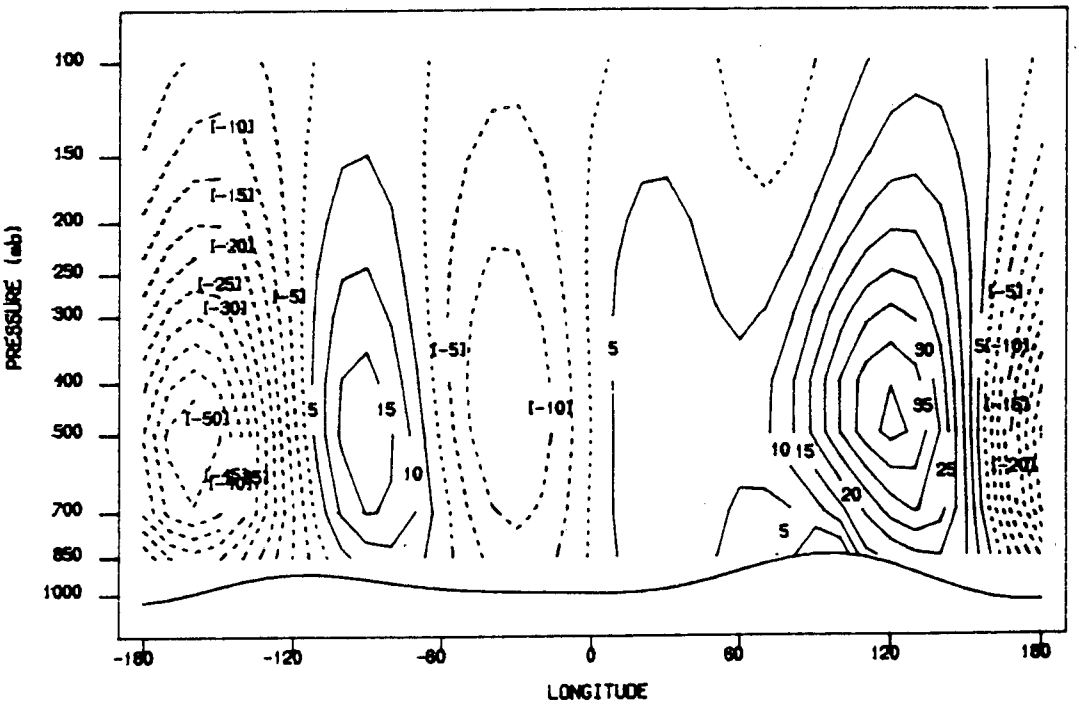

Fig.7.25 Longitudinal cross-section of perturbation vertical velocity at 45°N as in Fig. 6.26, but for the nonlinear response.

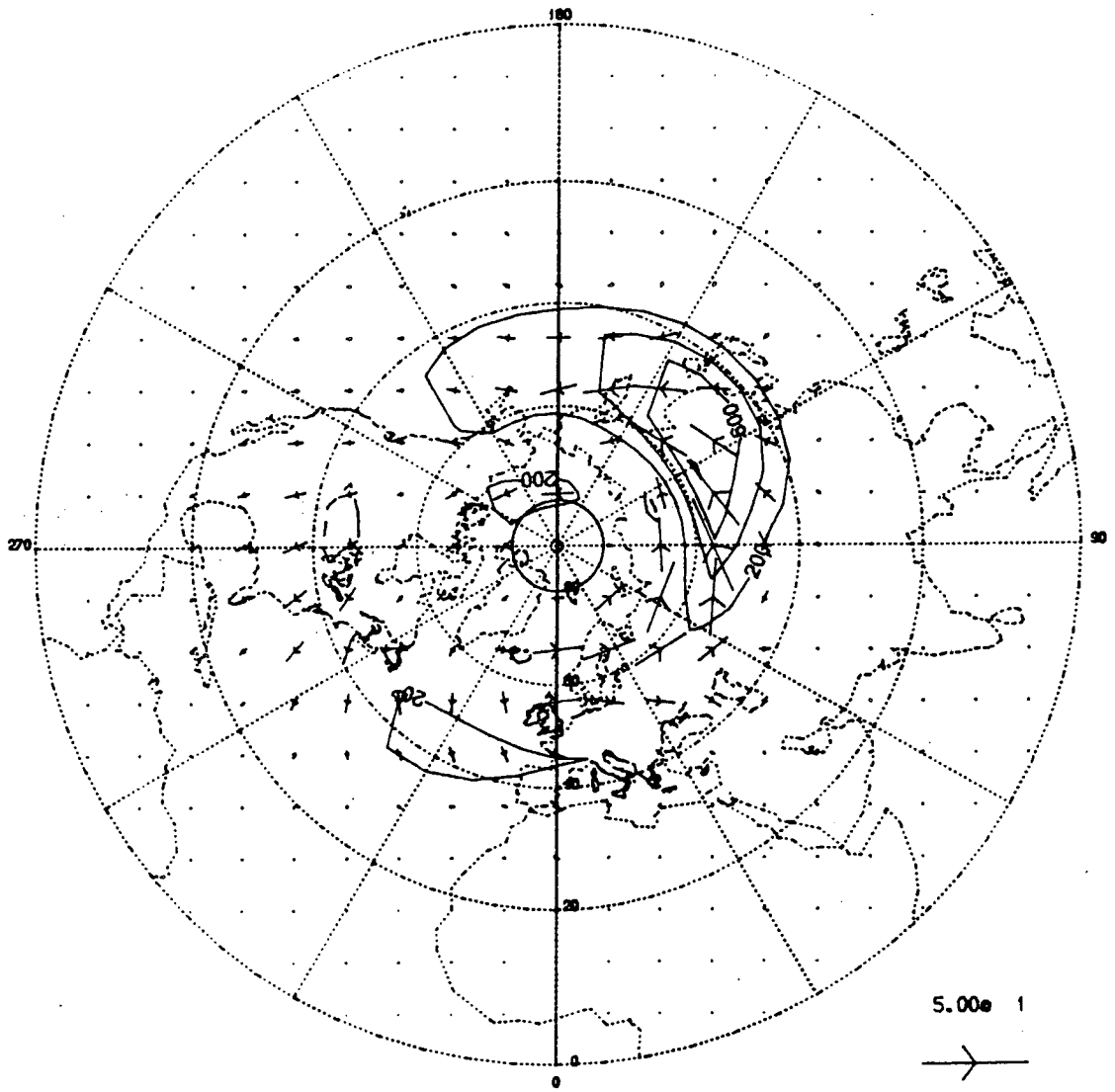

Fig. 7.26 Wave activity flux **F** at 850 mb as in Fig. 6.27, but for the nonlinear response. Contours are at intervals of 200 units.

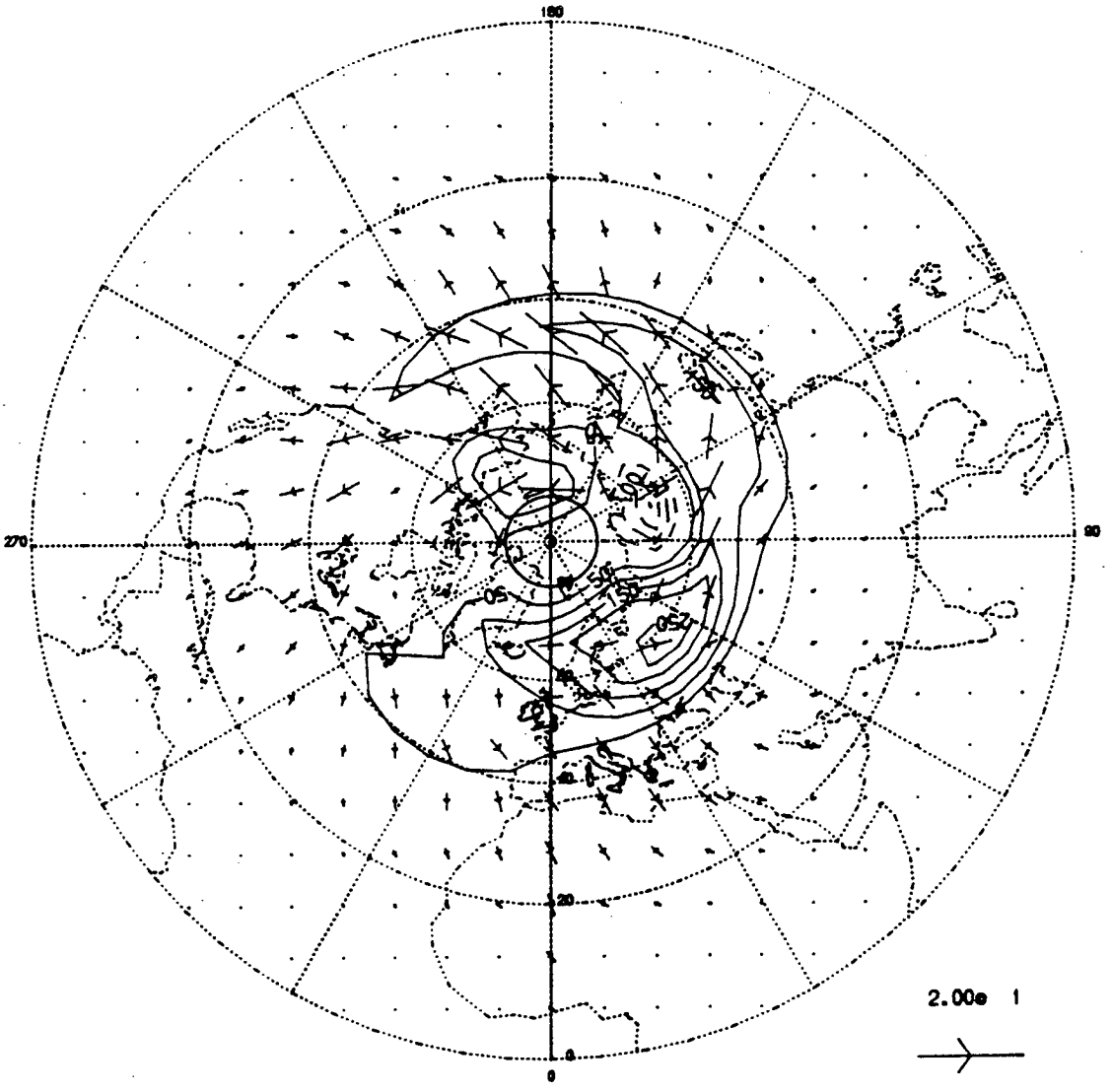

Fig. 7.27 Wave activity flux **F** at 500 mb as in Fig. 6.28, but for the nonlinear response.

difference of F between the nonlinear and linear response implies that the nonlinearity is significant.

The corresponding EP cross-section is shown in Fig. 7.28. The pattern of EP flux in middle latitudes is, in general, consistent with that for the linear case (Fig. 6.29), but the vertical flux is greatly enhanced at the low levels and associated with a much larger convergence of EP flux in the lower and middle troposphere. A source of EP flux appears in the upper troposphere between 40°N and 50°N , which results obviously from the inclusion of nonlinear effect in the model because no evidence is found in the linear case for this upper troposphere source. The pattern of EP flux and the associated divergence in high latitudes for the nonlinear case differs from the linear case evidently. These diagnostic analyses suggest again that the nonlinearity is significant for the response to the Northern Hemispheric topography, and also that the interaction between mean flows and the stationary waves simulated by the nonlinear model is much stronger than by the linear model.

7.3.2 Topography and FGGE IIIb Heating Field

In Figs. 7.29 and 7.30 are shown the perturbation stream fields at the 700 mb and 200 mb levels for the nonlinear response to the Northern Hemispheric topography in combination with the mean diabatic heating in January 1979, which is derived from FGGE IIIb data. Compared with

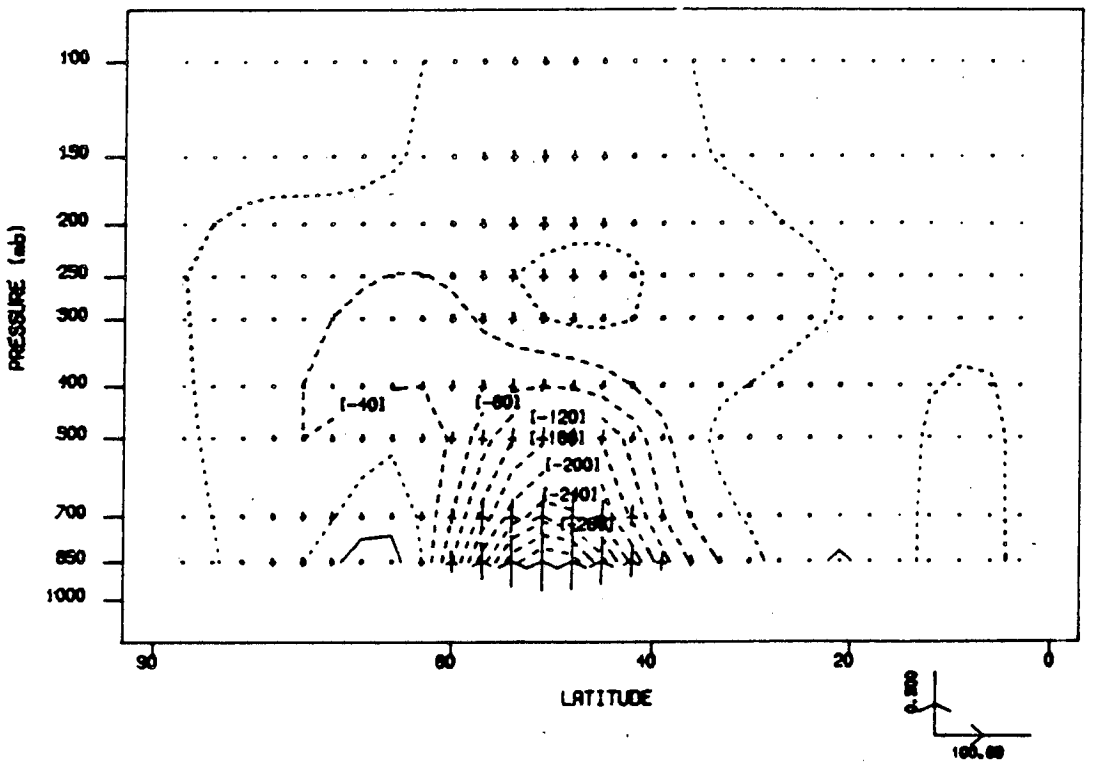

Fig. 7.28 EP cross-section as in Fig. 6.29, but for the nonlinear response. Contour interval is 40 units.

the linear counterparts (Fig. 6.30), the lower level response is obviously enhanced. Compared with the observed climatological stationary waves (Fig. 6.25), substantial improvements are also achieved for the 200 mb perturbation stream field not only in low and middle latitudes as described in the previous section, but also in high latitudes where Fig. 7.30 gives better results than Figs. 6.22, 6.31 as well as 7.22.

The corresponding EP cross-section (Fig. 7.31) is similar to Fig. 7.28 where the diabatic heating field is derived from FGGE IIIa data. Comparison for the EP cross-section between the linear (Fig. 6.32) and nonlinear (Fig. 7.31) case support the suggestions discussed in the previous section.

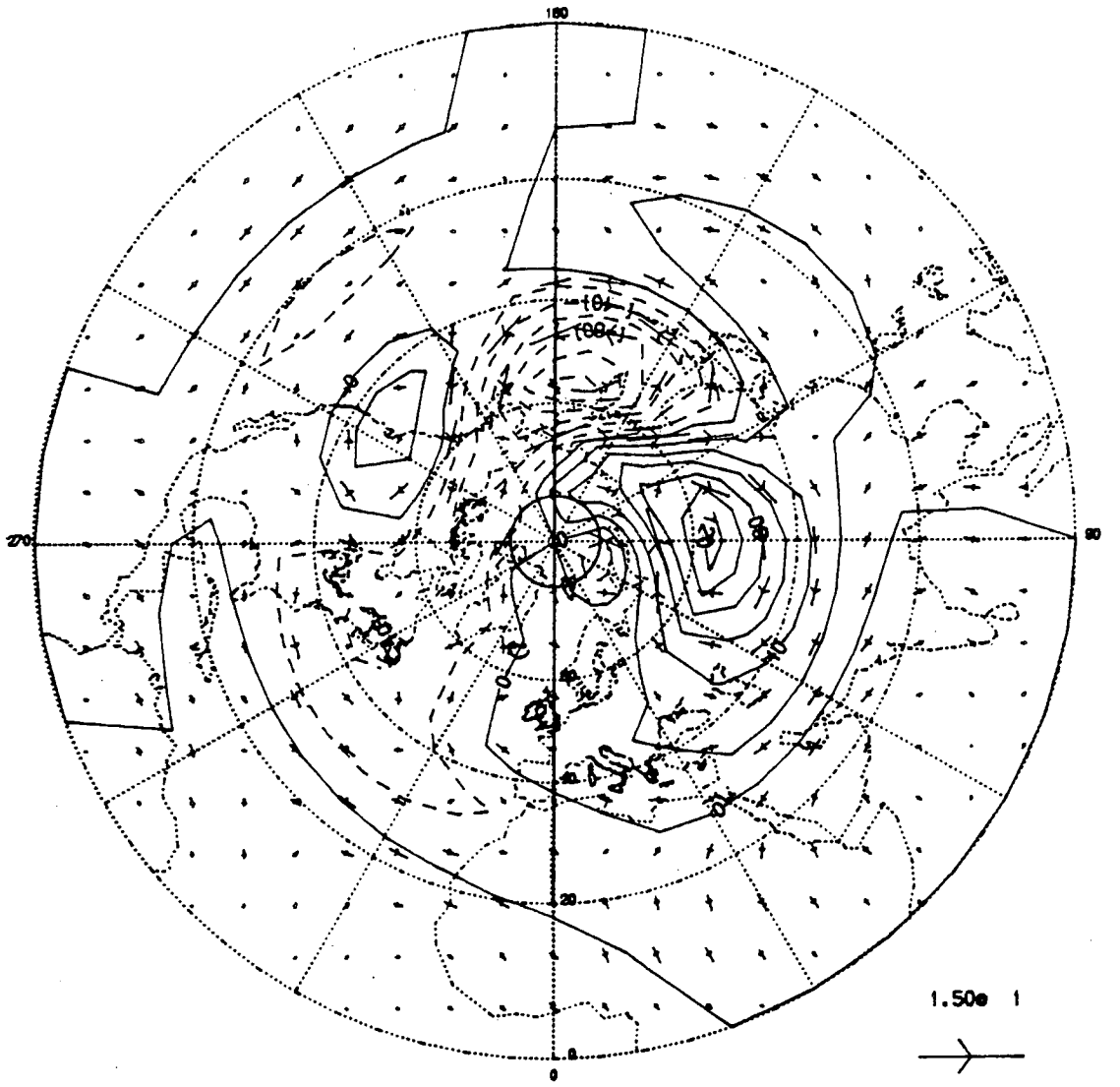

Fig. 7.29 700 mb perturbation stream field as in Fig. 6.30, but for the nonlinear response.

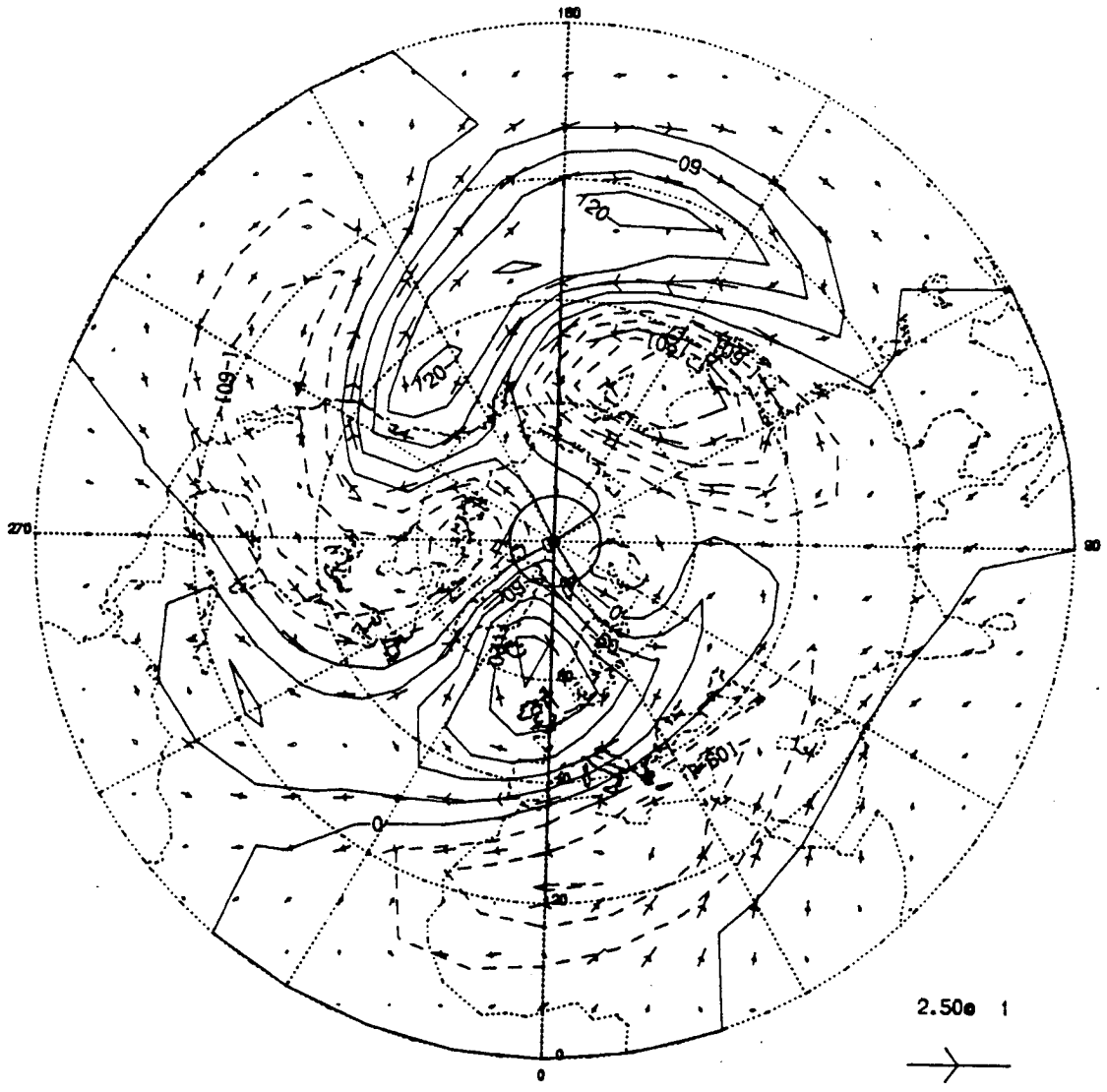

Fig. 7.30 200 mb perturbation stream field as in Fig. 6.31, but for the nonlinear response.

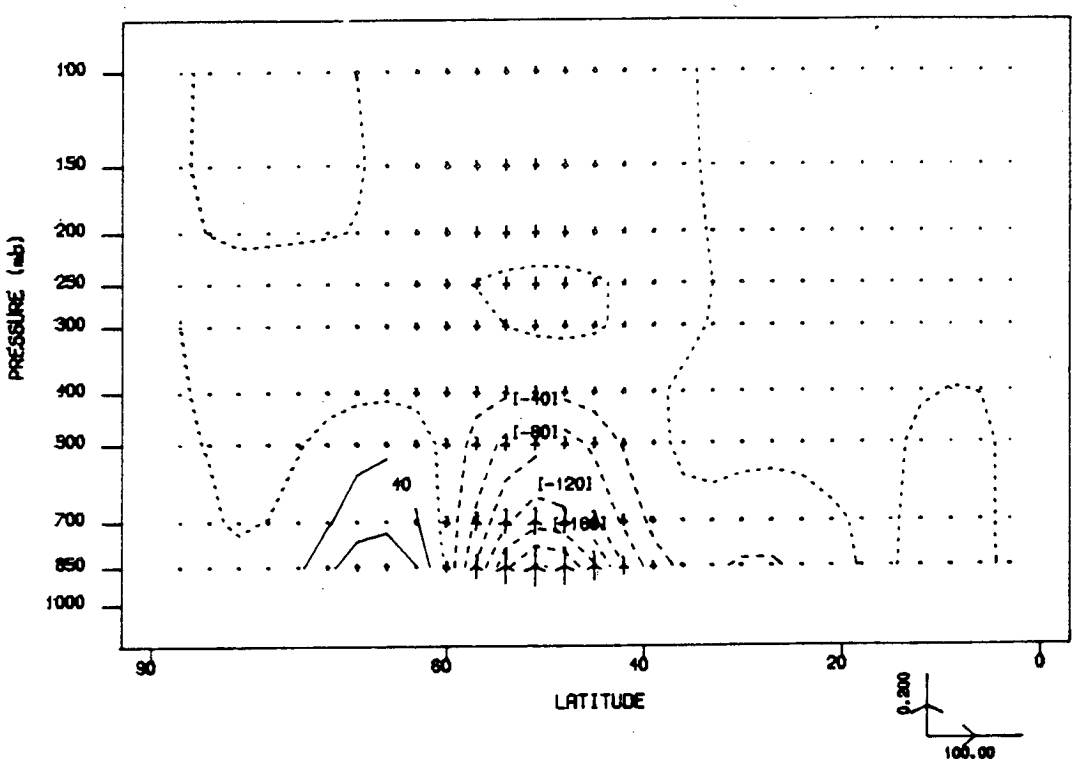

Fig. 7.31 EP cross-section as in Fig. 6.32, but for the nonlinear response. Contour interval is 40 units.

CHAPTER 8

CONCLUSIONS

8.1 Summary

In this study, the response of a model atmosphere to large scale topography and stationary diabatic heating has been investigated using linear and nonlinear steady-state, baroclinic primitive equation models, in which Rayleigh friction, the effect of Newtonian cooling and biharmonic horizontal diffusion are included, and the vertical as well as the horizontal structure is described by truncated series of analytic orthogonal functions. The transform method is used to evaluate the nonlinear terms in the governing equations. The steady-state, convergent, nonlinear solution is obtained by using Newton-Raphson iteration.

Observations of the atmosphere and the modelling results from previous authors have shown that the vertical propagation of wave activity is important for stationary planetary waves with small zonal wavenumber. In order to investigate the vertical as well as the horizontal propagation, a three-dimensional wave activity flux, which was derived by Plumb (1985) for linear, quasi-geostrophic stationary waves on a zonal flow, is used as a diagnostic for both the linear and nonlinear solutions. In addition, the EP cross-section has also been used as a diagnostic not only for the vertical and meridional propagation of the

wave activity, but also for the interaction between waves and mean flow.

The main conclusions from the numerical experiments which have been done in this study may be summarized as follows.

(1) The linear theory of stationary waves is based on two basic assumptions, i.e., the basic state variables must themselves satisfy the governing equations when the perturbations are set to zero, and the perturbation fields must be small enough so that all terms in the governing equations which involve products of the perturbation variables can be neglected (see, e.g., Holton, 1979). The linear solutions calculated in this study show that this simple technique is ideally suited for qualitative analysis of the characteristics of the stationary waves induced by large scale topography and diabatic heating. However, the linear theory is a great simplification of the real atmospheric behaviour. The horizontal velocity of the stationary waves in the real atmosphere is often of comparable magnitude to the mean zonal flow and thus the basic assumptions of the perturbation theory break down, i.e., the interaction between waves and mean flow become important and the nonlinear terms in the governing equations cannot be neglected. This is particularly true in some areas, such as the polar and tropical regions, or the lower troposphere in mid-latitudes, where the zonally averaged basic flow is relatively weak. On the other hand, the significant nonlinearity in a limited region may have a

further influence on the remote response in terms of various complicated interaction processes in the atmosphere. The great difference revealed in the comparisons between the linear and nonlinear response either to the orographic forcing or to the thermal forcing shows that the nonlinearities are significant provided the forcing has a comparable intensity to that in the real atmosphere. The experiments for the idealized forcing suggest that the nonlinear effect is more evident when the forcing region is situated in high or low latitudes.

(2) The wave pattern produced by the linear response to the Northern Hemispheric topography and diabatic heating, which is derived for January 1979 either from the NMC FGGE IIIa operational data or from the ECMWF FGGE IIIb analysis, is consistent with the observed climatological stationary waves on the whole, but also with some evident deficiencies as described in section 6.3. In contrast, the corresponding nonlinear response makes a significant improvement over these deficiencies. The nonlinear model does produce more realistic stationary waves in the winter season than the linear model with the same resolution. This fact suggests, from another point of view, that the nonlinearities are of primary importance in simulation of the stationary waves in the real atmosphere.

(3) The diagnostic analyses in this study show that the wave activity flux is a useful diagnostic of the three-dimensional propagation of the stationary wave activity, and also a useful diagnostic of the nonlinearities.

The wave activity is a quantity based on linearized quasi-geostrophic equations. When we use it as a diagnostic for the nonlinear model experiment, or for the observational data, we must bear in mind the effect of nonlinearity. Some sources or sinks of wave activity flux may result from, or partly from, the nonlinear effect. Since the evaluation of the wave activity flux involves the three-dimensional structure of the perturbation stream field, i.e., the vertical as well as the horizontal gradient of the perturbation streamfunction, in certain circumstances it is more sensitive to the nonlinear effects than the streamfunction itself.

(4) When zonal averages are taken, the wave activity flux reduces to the EP flux, which is also useful because it is a measure of net wave propagation in both vertical and meridional directions and its divergence is a direct measure of the total forcing of the zonal mean state by the stationary waves. Compared with the linear case, the vertical component of EP flux for the nonlinear response to the Northern Hemispheric topography and the actual diabatic heating in the winter season is considerably enhanced at low levels and associated with a much larger convergence of EP flux in the lower and middle troposphere. This implies the interaction between the mean flow and the stationary waves simulated by the nonlinear model is much stronger than by the linear model. Therefore the nonlinearity is also important for investigating wave propagation and the interaction between the zonal mean

flow and the stationary waves.

In addition, the evident difference of wave activity fluxes (or EP fluxes) between the linear and nonlinear responses suggests also that the nonlinear effects play an important role in determining the three-dimensional structure of stationary waves.

(5) The numerical experiments for the response to some idealized topography, where the topography of North America or Greenland is removed from the whole Northern Hemispheric topography, show that the Tibetan Plateau plays the most important role in the maintenance of orographically forced stationary waves in the winter season, while the forcing by the orographic effect of the Rocky mountains or the Greenland Plateau seems to be of secondary importance.

(6) The middle latitude orographic forcing, especially that by the Tibetan Plateau, makes a substantial contribution to the maintenance of the cyclonic circulation over the eastern tropical and sub-tropical Pacific as well as the inverse circulation over the western Pacific in the upper troposphere. These upper level systems are usually associated with the Walker circulation. It is therefore suggested that the orographic forcing in mid-latitudes plays an important role on the maintenance of the planetary scale motions in the sub-tropics and tropics (but not in the equatorial region for this hemisphere model).

(7) The stationary waves induced by the actual thermal forcing have a comparable amplitude with those by the

Northern Hemispheric orographic forcing. We may hence consider these two categories of forcing are equally important for the maintenance of the wintertime stationary waves in the Northern Hemisphere.

(8) The response to the actual thermal forcing has a more baroclinic nature than that to the actual orographic forcing.

(9) The vertical structure of EP flux for the pure thermal forcing differs from that for the pure orographic forcing. Although the former usually has a smaller vertical component at the lower troposphere than the latter, they become comparable in the middle and upper troposphere. Both the thermal and orographic forcings make a substantial contribution to the maintenance of the vertically propagating stationary planetary waves in the stratosphere.

(10) The experiment for the response to an idealized diabatic heating in the tropical region shows that an isolated tropical heating produces not only a strong response in the tropical region itself, but also a quite strong extratropical response, which appears as a wavetrain propagating poleward as well as longitudinally, and suggests that the tropics may have a significant influence on the wintertime stationary waves in middle and high latitudes. This is also supported by the comparison between the responses which use the diabatic heating derived from the NMC FGGE IIIa operational data or, alternatively from the ECMWF FGGE IIIb analysis. The

longitudinal variation of diabatic heating in the tropical region has different characteristics in these two heating fields, and the corresponding wave patterns in high latitudes simulated by the nonlinear model are quite different. The directions of meridional propagation of the wave activity for the Pacific wavetrain and the Atlantic wavetrain at the low levels in the pure thermal forcing case (as discussed in section 6.2.1) are reversed, this provides additional evidence to support the above suggestion.

8.2 Possible Extensions

A number of extensions to this study are possible. The contribution from the tropical diabatic heating to the maintenance of the stationary waves in middle and high latitudes could be further investigated by using a separating technique, which has been employed to investigate the relative importance of the three large scale mountains of the Northern Hemisphere to the orographically forced stationary waves.

Since the pioneering work of Charney and Eliassen (1949), the stationary response to forcing in the Northern winter have been investigated by many authors although there are still some uncertainties which require further study. However, there are relatively few studies on the response to the forcing in summer. The zonally averaged basic flow in summer is much weaker than in winter. It is therefore

expected that the nonlinear effect may be more evident in the summer simulation than in this study. The nonlinear model developed here should be suitable for investigating the stationary waves in the summer season.

In the linear model a predefined zonal mean basic state is used and precludes the interaction between mean flow and the waves. This constraint is relaxed in the nonlinear model, but the zonally averaged components of the nonlinear solution are still damped toward their initial state, i.e., the prescribed basic state for the linear model. It is possible to relax this constraint further in the nonlinear model and a flow varying in the zonal direction could be used as the basic state. This would allow waves propagating deeply into some tropical regions of weak westerlies. The inclusion of a zonally non-uniform basic flow is particularly interesting for investigating the tropical-extratropical interactions.

The nonlinear model, which was used to study the hemispherical structure and therefore prohibited the cross-equator propagation of stationary waves, has clear potential for further study by extension to global domain. For a global model, the asymmetric components about the equator must be included in the spherical harmonics expansions and some additional truncation relations are required as discussed by Eliasen et al. (1970).

An important deficiency of this study is that there is no effect of transient waves included in the model. The observed climatological stationary waves are a time-averaged picture. By neglecting the forcing due to the mean convergence of heat and momentum transports by

the smaller scale transient waves, it is impossible for us to simulate accurately the observed climatological stationary waves. It should be possible to obtain a more realistic result if the transient effects are properly introduced into the model.

Another deficiency is that the nonlinear model developed in this study is not economic, the high requirement for computational resources has imposed restrictions on the model resolution. Further study would also be worthwhile exploring a more reasonable specification of the dissipation parameters. A three-dimensional diabatic heating field derived from observational data is preferable to the idealized vertical profile used in the study.

ACKNOWLEDGEMENTS

I would like to thank my supervisor, Dr C. N. Duncan, for his continual interest and invaluable advice in both science and language throughout this study. My thanks are due to Dr B. J. Hoskins for helpful discussions and suggestions on this work and for making Fig. 6.25 available to me. The help of Dr D. R. Johnson in providing the vertically integrated diabatic heating data is gratefully appreciated. I wish to thank the members of the Department of Meteorology, Edinburgh University, the Edinburgh Regional Computing Centre and the University of Manchester Regional Computer Centre for their assistance.

Many other people have made useful suggestions and provided helpful information to assist this research. My thanks for this help go to Drs A. J. Simmons, M. Tiedtke, B. Machenhauer, R. Daley, W. Bourke and many others.

I am greatly indebted to financial support of a WMO fellowship which enabled me to make this study, also to the Chinese State Meteorological Administration, and the Nanjing Institute of Meteorology for sending me to Britain to study, and to my former supervisor, Prof. Ji-jia Zhang, for his encouragement during this study.

Finally, I wish to acknowledge my wife, Zhi-qun Zhang, for her important support and typing this thesis.

APPENDIX A

LIST OF SYMBOLS

Only the principal symbols are listed. Symbols formed by adding primes, superscripted or subscripted indices are not listed separately. Boldface type indicates vector quantities. Where symbols have more than one meaning, the section where the second meaning is first used is indicated in the list. the matrix symbols also use boldface types in the text and are not listed here.

a	Radius of the earth
e	Base of the natural logarithm
f	(1) $\equiv 2\Omega\sin\varphi$, Coriolis parameter;
	(2) A function (section 2.5.4)
g	Gravitational acceleration
i	(1) An integer;
	(2) Square root of minus one (section 2.3.1)
j	Total wave number
k, l	Vertical wave number
m	Zonal wave number
n	Total wave number, $n-\|m\|$ is the number of zeros of $P_{m,n}(\mu)$ between the poles
q	$\equiv \ln P_s$, logarithm of surface pressure
t	Time
u	Zonal component of velocity (eastward)
v	Meridional component of velocity

x_i	Sample points for Gauss-Legendre quadrature
w_i	Weighting coefficients for Gauss-Legendre quadrature
z	$\equiv -H\ln(P/P_s)$, vertical coordinate in log-pressure system
A	An arbitrary variable
$[A]$	Zonal mean of A
A^*	Deviation from the zonal mean [A]
$A^{(\lambda)}$	$=\partial A/\partial\mu$, zonal derivative of A
$A^{(\mu)}$	$=(\mu^2-1)\partial A/\partial\mu$, meridional derivative of A, multiplied by (μ^2-1)
$A^{(\sigma)}$	$=(\sigma^2-1)\partial A/\partial\sigma$, vertical derivative of A, multiplied by (σ^2-1)
C_p	Specific heat of dry air at constant pressure
$\mathbf{E}$	Eliassen-Palm (EP) wave flux
E_φ	Meridional component of EP flux
E_z	Vertical component of EP flux
$\mathbf{F}$	Three-dimensional wave activity flux
F_λ	(1) Zonal component of friction force per unit mass; (2) Zonal component of wave activity flux (section 4.1.1)
F_φ	(1) Meridional component of friction force per unit mass; (2) Meridional component of wave activity flux (section 4.1.1)
F_z	Vertical component of wave activity flux
G_k	Vertical derivative of K_k, defined by eq. (2.54)
H	Scale height

H_k Meridional derivative of normalized Legendre polynomial

$H_{m,n}$ Meridional derivative of normalized associated Legendre polynomial

I_k Integration of weighted Legendre polynomial, defined by eq. (2.57)

J Truncation index for total wave number

K_k Integration of normalized Legendre polynomial, defined by eq. (2.52)

K_t Decay rate of Newtonian cooling

L Truncation index for vertical wave number

M Truncation index for zonal wave number

N (1) Number of grid points;
(2) Buoyancy frequency (section 4.1.1)

P Pressure

P_o A standard constant pressure

P_k Normalized Legendre polynomial

$P_{m,n}$ Normalized associated Legendre polynomial

Q Diabatic heating per unit mass per unit time

R Gas constant for dry air

R_f Decay rate of Rayleigh friction

S Transformed vertical component of velocity, defined by eq. (2.11)

T Temperature

U Zonal component of velocity multiplied by the cosine of latitude

V Meridional component of velocity multiplied by the cosine of latitude

α Coefficient of biharmonic horizontal diffusion in the momentum equation

β $\equiv df/dt$, variation of the Coriolis parameter with latitude

κ $\equiv R/C_p$, ratio of gas constant to specific heat at constant pressure

λ Longitude

μ $\equiv \sin\varphi$, sine of latitude

ν Coefficient of biharmonic horizontal diffusion in the thermodynamic equation

ϱ_o A standard density

σ $\equiv 2P/P_s - 1$, vertical coordinate in σ system

$\dot{\sigma}$ $\equiv d\sigma/dt$, vertical component of velocity in σ system

τ e-folding diffusive time

φ Latitude

χ Velocity potential

ψ Streamfunction

ω $\equiv dP/dt$, vertical component of velocity in pressure system

Δ Divergence of EP flux for contouring in the EP cross-section

ϕ Geopotential

ϕ_s Surface geopotential

Ω Angular speed of rotation of the earth

∇ Hamiltonian operator

APPENDIX B

INDEX OF FIGURES

The following abbreviations are used in this index:

(L) Linear response

(NL) Nonlinear response

M Truncation index for zonal wavenumber

Horizontal Distribution of Forcing Function

Diabatic heating (FGGE IIIa), M=3, Fig. 6.9

Diabatic heating (FGGE IIIa), M=9, Fig. 6.37

Diabatic heating (FGGE IIIb), M=3, Fig. 6.15

Idealized topography in mid-latitudes, Fig. 5.1

Northern Hemispheric topography, M=3, Fig. 6.35

Northern Hemispheric topography, M=9, Fig. 6.36

Normalized associated legendre polynomial, Fig. 2.1

Observed climatological stationary waves

Longitudinal section at 45°N for ϕ^{*}, Fig. 7.24

Perturbation geopotential height, 200mb, Fig. 6.24

Perturbation streamfunction at 250 mb, Fig. 6.25

Response to

Actual thermal forcing in Jan. 1979 (FGGE IIIa)

EP cross-section, Figs. 6.14(L), 7.14(NL)

Longitudinal section at 45°N for ϕ^{*}, Figs. 6.12(L), 7.12(NL)

Perturbation stream field, 700mb, Figs. 6.10(L), 7.10(NL)

Perturbation stream field, 200mb, Figs. 6.11(L), 7.11(NL)

Wave activity flux, 850mb, Figs. 6.13(L), 7.13(NL)

Actual thermal forcing in Jan. 1979 (FGGE IIIb)

EP cross-section, Figs. 6.20(L), 7.20(NL)

Longitudinal section at 45°N for ϕ^*, Fig. 7.17(NL)

Perturbation stream field, 700mb, Figs. 6.16(L), 7.15(NL)

Perturbation stream field, 200mb, Figs. 6.17(L), 7.16(NL)

Wave activity flux, 850mb, Figs. 6.18(L), 7.18(NL)

Idealized orographic forcing in high latitudes

EP cross-section, Figs. 5.24(L), 5.25(NL)

Perturbation stream field, 200mb, Figs. 5.20(L), 5.22(NL)

Wave activity flux, 500mb, Figs. 5.21(L), 5.23(NL)

Idealized orographic forcing in mid-latitudes

EP cross-section, Figs. 5.8(L), 5.15(NL)

Longitudinal section at 35°N for ϕ^*, Figs. 5.4(L), 5.11(NL)

Longitudinal section at 35°N for ω^*, Figs. 5.5(L), 5.12(NL)

Perturbation stream field, 700mb, Figs. 5.2(L), 5.9(NL)

Perturbation stream field, 200mb, Figs. 5.3(L), 5.10(NL)

Wave activity flux, 850mb, Figs. 5.6(L), 5.13(NL)

Wave activity flux, 500mb, Figs. 5.7(L), 5.14(NL)

Sensitivity experiments, Figs. 5.16-5.19(L)

Idealized thermal forcing in low latitudes

EP cross-section, Figs. 5.37(L), 5.40(NL)

Perturbation streamfunction, 700mb, Figs.5.35(L), 5.38(NL)

Perturbation streamfunction, 200mb, Figs.5.36(L), 5.39(NL)

Idealized thermal forcing in mid-latitudes

EP cross-section, Figs. 5.31(L), 5.34(NL)

Meridional section at 135°E for **F**, Figs. 5.30(L), 5.33(NL)

Perturbation stream field, 700mb, Fig. 5.26(L)

Perturbation stream field, 200mb, Fig. 5.27(L)

Wave activity flux, 500mb, Figs. 5.29(L), 5.32(NL)

Northern Hemispheric topography

EP cross-section, Figs. 6.6(L), 7.6(NL)
Longitudinal section at 45°N for ϕ^*, Figs. 6.3(L), 7.3(NL)
Longitudinal section at 45°N for ω^*, Figs 6.4(L), 7.4(NL)
Perturbation stream field, 700mb, Figs. 6.1(L), 7.1(NL)
Perturbation stream field, 200mb, Figs. 6.2(L), 7.2(NL)
Wave activity flux, 850mb, Figs. 6.5(L), 7.5(NL)

N. H. topography, but removing topography of North America

Longitudinal section at 45°N for ϕ^*, Fig. 7.8(NL)
Perturbation stream field, 200mb, Figs. 6.7(L), 7.7(NL)

N. H. topography, but removing the Greenland Plateau

Perturbation stream field, 200mb, Figs. 6.8(L), 7.9(NL)

N. H. topography and actual diabatic heating (FGGE IIIa)

EP cross-section, Figs. 6.29(L), 7.28(NL)
Longitudinal section at 45°N for ϕ^*, Figs. 6.23(L), 7.23(NL)
Longitudinal section at 45°N for ω^*, Figs. 6.26(L), 7.25(NL)
Perturbation stream field, 700mb, Figs. 6.21(L), 7.12(NL)
Perturbation stream field, 200mb, Figs. 6.22(L), 7.22(NL)
Wave activity flux, 850mb, Figs. 6.27(L), 7.26(NL)
Wave activity flux, 500mb, Figs. 6.28(L), 7.27(NL)
Zonal resolution test, Figs. 6.33-6.34(L)

N. H. topography and actual diabatic heating (FGGE IIIb)

EP cross-section, Figs. 6.32(L), 7.31(NL)
Perturbation stream field, 700mb, Figs. 6.30(L), 7.29(NL)
Perturbation stream field, 200mb, Figs. 6.31(L), 7.30(NL)

Zonal mean flow in January 1979, Fig. 3.1

Zonal mean temperature in January 1979, Fig. 3.2

REFERENCES

Andrews, D.G. and M. E. McIntyre, 1976: Planetary waves in horizontal and vertical shear: the generalized Eliassen-Palm relation and the mean zonal acceleration. J. Atmos. Sci., 33, 2031-2048.

Ashe, S., 1979: A nonlinear model of the time-average axially asymmetric flow induced by topography and diabatic heating, J. Atmos. Sci., 36, 109-126.

Belousov, S. L., 1962: Tables of normalized associated Legendre polynomials. Pergamon Press, New York, 379pp.

Blackmon, M. L., 1976: A climatological spectral study of the 500 mb geopotential height of the Northern Hemisphere. J. Atmos. Sci., 33, 1607-1623.

Blackmon, M. L., J. M. Wallace, N.-C. Lau and S. L. Mullen, 1977: An observational study of the Northern Hemisphere wintertime circulation. J. Atmos. Sci., 34, 1040-1053.

Bolin, B., 1950: On the influence of the Earth's orography on the general character of the westerlies. Tellus, 2, 184-195.

Bourke, W., McAvaney, B., Puri, K. and R. Thurling, 1977: Global modelling of atmospheric flow by spectral methods. Methods in Computational Physics, vol.17. Academic Press. p267-324.

Charney, J. G. and A. Eliassen, 1949: A numerical method for predicting the perturbation of the middle latitude westerlies, Tellus, 1, 38-54.

Chervin, R. M., J. E. Kutzbath, D. D. Houghton and R. G. Gallimore, 1980: Response of the NCAR general circulation model to prescribed changes in ocean surface temperature. Part II: Mid-latitude and subtropical changes. J. Atmos. Sci., 37, 308-332.

Cooley, J. W. and J. W. Tukey, 1965: An algorithm for the machine calculation of complex Fourier series. Math. Comp., 19, 297-301.

Derome, J. and A. Wiin-Nielsen, 1971: The response of a middle-latitude model atmosphere to forcing by topography and stationary heat sources. Mon. Wea. Rev., 99, 564-576.

Dunkerton, T., C.-P. F. Hsu and M. E. McIntyre, 1981: Some Eulerian and Lagrangian diagnostics for a model stratospheric warming. J. Atmos. Sci., 38, 819-843.

Edmon, H. J., B. J. Hoskins and M. E. McIntyre, 1980: Eliassen-Palm cross sections for the troposphere. J. Atmos. Sci., 37, 2600-2616.

Egger, J., 1976a: The linear response of a hemispheric two-level primitive equation model to forcing by topography. Mon. Wea. Rev., 104, 351-364.

Egger, J., 1976b: On the theory of the steady perturbations in the troposphere. Tellus, 28, 381-389.

Egger, J., 1977: On the linear theory of the atmospheric response to sea surface temperature anomalies. J. Atmos. Sci., 34, 603-614.

Eliasen, E. and B. Machenhauer, 1970: On a numerical method for integration of the hydrodynamical equations with a spectral representation of the horizontal fields. Report No 2, University of Copenhagen, Institut for teoretisk meteorologi.

Elsaesser, H. W., 1966: Evaluation of spectral versus grid methods of hemispheric numerical weather prediction. J. Appl. Meteor., 5, 246-262.

Fletcher, R. and M. J. D. Powell, 1963: A rapidly convergent descent method for minimization. Computer Journal, 6, 163-168.

Frederikson, J. S. and B. L. Sawford, 1981: Topography waves in nonlinear and linear spectral barotropic models. J. Atmos. Sci., 36, 223-234.

Gill, A. E., 1980: Some simple solutions for heat-induced tropical circulation. Quart. J. R. Met. Soc., 106, 447-462.

Gill, P. E., W. Murray and M. H. Wright, 1981: Practical Optimization. Academic Press.

Grose, W. L. and B. J. Hoskins, 1979: On the influence of orography on large-scale atmospheric flow. J. Atmos. Sci., 32, 2082-2093.

Grose, W. L., W. T. Blackshear and R. E. Turner, 1984: The response of a non-linear, time-dependent, baroclinic model of the atmosphere to tropical thermal forcing. Quart. J. Roy. Meteor. Soc., 110, 981-1002.

Held, I. M., 1983: Stationary and quasi-stationary eddies in the extratropical troposphere: theory. Large-scale dynamical processes in the atmosphere. Ed. B. Hoskins and R. Pearce, Academic Press, p127-168.

Hendon, H. H. and D. L. Hartmann, 1982: Stationary waves on a sphere: sensitivity to thermal feedback. J. Atmos. Sci., 39, 1906-1920.

Holton, J. R., 1979: An introduction to dynamic Meteorology. Second edition. Academic Press. New York, 391pp.

Hoskins, B. J. and D. J. Karoly, 1981: The steady linear response of a spherical atmosphere to thermal and orographic forcing. J. Atmos. Sci., 38, 1179-1196.

Huang, R. H. and K. Gambo, 1981: The response of a model atmosphere in middle latitudes to forcing by topography and stationary heat sources. J. Meteor. Soc. Japan, 59, 220-237.

———, 1982: The response of a hemispheric multi-level model atmosphere to forcing by topography and stationary heat sources. J. Meteor. Soc. Japan, 60, 78-108.

Jarraud, M. and A. J. Simmons, 1983: The spectral technique. ECMWF Seminar 1983: Numerical methods for weather prediction. Vol. 2. 1-59.

Johnson, D. R., R. D. Townsend and M. Y. Wei, 1985: The thermally coupled response of the planetary scale circulation to the global distribution of heat sources and sinks. Tellus, 37A, 106-125.

Karoly, D. J., 1980: Stationary planetary waves in the atmosphere. Ph. D. thesis, Reading University, 200pp.

Kasahara, A., 1966: The dynamical influence of orography on the large-scale motion of the atmosphere. J. Atmos. Sci., 23, 259-271.

Kasahara, A., T. Sasamori and W. M. Washington, 1973: Simulation experiments with 12-layer stratospheric global circulation model, I: Dynamical effect of the Earth's orography and thermal influence of continentality. J. Atmos. Sci., 30, 1229-1251.

Lau, N.-C., 1978: On the three-dimensional structure of the observed transient eddy statistics of the Northern Hemisphere wintertime circulation. J. Atmos. Sci., 35, 1900-1923.

———, 1979a: the structure and energetics of transient disturbances in the Northern Hemisphere wintertime circulation. J. Atmos. Sci., 36, 982-995.

———, 1979b: the observed structure of tropospheric stationary waves and the local balances of vorticity and heat. J. Atmos. Sci., 36, 996-1016.

Lau, N.-C. and J. M. Wallace, 1979: On the distribution of horizontal transports by transient eddies in the Northern Hemisphere wintertime circulation. J. Atmos. Sci., 36, 1844-1861.

Machenhauer, B. and E. Rasmussen, 1972: On the integration of the spectral hydrodynamical equations by a transform method. Report No. 3, University of Copenhagen, Institut for teoretisk meteorologi.

Machenhauer, B. and R. Daley, 1972: A baroclinic primitive equation model with a spectral representation in three dimensions. Report No 4, University of Copenhagen, Institut for teoretisk meteorologi.

Manabe, S. and T. B. Terpstra, 1974: The effects of mountains on the general circulation of the atmosphere as identified by numerical experiments. J. Atmos. Sci., 31, 3-42.

Namias, J., 1966: Nature and possible causes of the northeastern United States drought during 1962-1965. Mon. Wea. Rev., 94, 543-554.

Oort, A. H. and E. M. Rasmusson, 1971: Atmospheric circulation statistics. NOAA prof. Pap. 5, U.S. Dept. of Commerce, 323pp.

Opsteegh, J. D. and H. M. Van den Dool, 1980: Seasonal differences in the stationary response of a linearized primitive equation model: prospects for long-range weather forecasting? J. Atmos. Sci., 37, 2169-2185.

Orszag, S. A., 1970: Transform method for calculation of vector coupled sums: application to the spectral form of the vorticity equation. J. Atmos. Sci., 27, 890-895.

———, 1974: Fourier series on spheres. Mon. Wea. Rev., 102, 56-75.

Palmer, T. N., 1981: Diagnostic study of a wavenumber-2 stratospheric sudden warming in a transformed Eulerian-mean formalism. J. Atmos. Sci., 38, 844-855.

Platzman, G. W., 1960: The spectral form of vorticity equation. J. Meteor., 17, 635-644.

Plumb, R. A., 1985: On the three-dimensional propagation of stationary waves. J. Atmos. Sci., 42, 217-229.

Ratcliffe, R. A. S., 1968: Forecasting monthly rainfall for England and Wales. Met. Mag., 97, 258-270.

———, 1974: The use of 500 mb anomalies in long-range forecasting. Quart. J. Roy. Meteor. Soc., 100, 234-244.

Reiter, E. R., 1963: Jet stream meteorology. Chicago University Press, 515pp.

Rowntree, P. R., 1972: The influence of tropical east Pacific Ocean temperature on the atmosphere. Quart. J. Roy. Meteor. Sci., 98, 290-321.

Simmons, A. J., 1982: The forcing of stationary wave motion by tropical diabatic heating. Quart. J. Roy. Meteor. Sci., 108, 503-534.

Smagorinsky, J., 1953: The dynamical influence of large-scale heat sources and sinks on the quasi-stationary mean motion of the atmosphere. Quart. J. Roy. Meteor. Sci., 79, 342-366.

Van Loon, H., R. L. Jenne and K. Labitzke, 1973: Zonal Harmonic standing waves. J. Geophys. Res., 78, 4463-4471.

Wallace, J. M., 1983: The climatological mean stationary waves: observational evidence. Large-scale dynamical processes in the atmosphere. Ed. B. Hoskins and R.Pearce, Academic Press, p27-53.

Webster, P. J., 1981: Mechanisms determining the atmospheric response to surface temperature anomalies. J. Atmos. Sci., 38, 554-571.

Wu, G. X., 1984: The nonlinear response of the atmosphere to large-scale mechanical and thermal forcing. J. Atmos. Sci., 41, 2456-2476.

Yeh, T. C., 1950: The circulation of the high troposphere over China in the winter of 1945-1946. Tellus, 2, 173-183.